
Direct Amplification of Femtosecond Pulses

Moritz Ueffing



München 2018

Direct Amplification of Femtosecond Pulses

Moritz Ueffing

Dissertation
an der Fakultät für Physik
der Ludwig-Maximilians-Universität
München

vorgelegt von
Moritz Ueffing
aus Freiburg

München, den 08.01.2018

Erstgutachter: Prof. Ferenc Krausz

Zweitgutachter: Prof. Thomas Udem

Tag der mündlichen Prüfung: 07.03.2018

Zusammenfassung

Lasersysteme mit Millijoule Pulsenergie basieren auf Laserverstärkern, welche die Energie von bereit gestellten Primärquellen, modengekoppelten Oszillatoren, erhöhen. Aufgrund der hohen Spitzenleistungen der erzeugten Laserpulse und den daraus resultierenden hohen Intensitäten, implementieren moderne Lasersysteme die sog. „Chirped-Pulse Amplification“. Dies reduziert zwar die Spitzenleistung während des Verstärkungsprozesses, erfordert jedoch Einheiten für Streckung und Kompression vor und nach dem Verstärker. Das führt zu erheblichen Nachteilen des Systems: Zum einen verringern die erhöhte Komplexität und die langen Freistrah-Wege die Stabilität des Systems. Zum anderen müssen in Laserverstärkern mit hohen mittleren Leistungen Reflexionsgitter eingesetzt werden, die besonders teuer, groß und, trotz der technologischen Fortschritte, eine Verlustquelle in der Kompressionseinheit darstellen. Die resultierende hohe Komplexität solcher Verstärker stellt eine wesentliche Einschränkung für hochempfindliche Messungen dar und verhindert die Aufnahme von Messdaten über lange Zeiträume.

Die Konstruktion von Laserquellen, die den hohen Ansprüchen an Langzeitstabilität und Reproduzierbarkeit der Leistung genügen, verlangt eine konzeptionelle Vereinfachung der Laserarchitektur. Vor diesem Hintergrund behandelt diese Arbeit die ersten Schritte für die Implementierung von Verstärkerkonzepten, welche auf „Chirped-Pulse Amplification“ verzichten und ebnet den Weg für kompaktere, kosteneffiziente und benutzerfreundliche multi-Millijoule Lichtquellen mit hohen mittleren Leistungen.

Der entwickelte Yb:YAG thin-disk regenerative Verstärker erreicht eine Pulsenergie von 2 mJ bei einer Wiederholrate von 100 kHz mit 200 W mittlerer Leistung. Die Integration nicht-linearer optischer Effekte führt zu einer außergewöhnlichen Pulsdauer von 210 fs. Dies ist im Vergleich zu anderen Yb:YAG Systemen, die auf „Chirped-Pulse“ Verstärkung beruhen, um das 5-fache kürzer. Das Konzept der direkten Verstärkung von Femtosekundenpulsen wird in der Pulsenergie auf 6.6 mJ bei 5 kHz oder 10 kHz mittels eines neuartigen Hybridverstärkers skaliert.

Zudem werden die Pulse mit einer nicht-linearen Pulskompressionsstufe, die auf einer Argon gefüllten Multipasszelle beruht, verkürzt. Die Pulskompressionsstufe formt einen Wellenleiter, der jedoch nicht mittels einer optischen Faser implementiert wird. Vielmehr wird der Wellenleiter durch ein optisches Abbildungssystem realisiert, welches vergleichbare Bedingungen schafft. Durch die technische Analyse der nicht-linearen Prozesse wird es ermöglicht Pulse mit einer Pulsdauer von 37 fs bei 100 kHz Repetitionsrate, 1.9 mJ Pulsenergie, 35 GW Spitzenleistung und mehr als 190 W Durchschnittsleistung zu erzeugen.

Die entwickelte Technologie stellt den Grundstein für Ultrakurzzeitmesstechnik mit hohen Repetitionsraten im 100 kHz Bereich dar. Erstmals können sich Yb:YAG Laserverstärker als direkte Lichtquelle für Experimente in der Ultrakurzzeitphysik behaupten.

Abstract

Laser systems with pulse energies of a few millijoule are based on laser amplifiers to increase the energy of laser pulses produced by their primary sources, mode-locked laser oscillators. Due to the high peak powers of the produced pulses and the resulting high intensities in the amplifier, state of the art laser systems implement chirped-pulse amplification. This reduces the peak intensity during the amplification process but requires stretching and compression units before and after the amplifier, which evokes significant disadvantages. The increased complexity of the system and the long freely propagating beams compromise the stability of the system. Furthermore, high average power laser amplifiers need to implement reflective gratings, which are particularly expensive, large in size and, despite the technological advances, a source for power loss in the compression unit. The resulting complexity of chirped-pulse amplifiers constitutes a main limitation for high sensitivity measurements and impedes data acquisition over long time scales.

Building laser sources that satisfy the high demands on long-term stability and reproducibility of performance requires conceptual simplification of the architecture. Therefore, this thesis discusses the first steps in implementation of amplification concepts avoiding chirped-pulse amplification and paves the way towards more compact, cost-effective, and user-friendly multi-millijoule high-average power light sources.

The developed Yb:YAG thin-disk regenerative amplifier achieves a pulse energy of 2 mJ at a repetition-rate of 100 kHz with 200 W average power. The integration of non-linear optical processes leads to an exceptional pulse duration of 210 fs, which is 5-fold shorter than similar Yb:YAG systems that rely on chirped-pulse amplification. The concept of direct amplification of femtosecond pulses is scaled in pulse energy to 6.6 mJ at 5 kHz or 10 kHz with a novel hybrid-amplifier.

Furthermore, the output pulses are shortened with a non-linear compression stage based on an argon filled multi-pass cell. The compression stage builds a waveguide that, however, is not implemented with an optical fiber. Wave-guiding is realized with an optical imaging system that creates comparable conditions. The involved non-linear optical processes were understood, which results in a pulse duration of 37 fs at 100 kHz repetition-rate, 1.9 mJ pulse energy, 35 GW peak power and more than 190 W average power.

The developed technology builds the foundation for ultrafast metrology with high repetition-rate in the 100 kHz range. For the first time, Yb:YAG laser amplifiers embody high average power light sources applicable as direct drivers for ultrafast physics.

Contents

Zusammenfassung	v
Abstract	vii
Introduction	1
1. Optical Effects in Ultrashort Pulse Amplifiers	7
1.1. Maxwell's equations and the non-linear wave equation	7
1.2. Gauss-Hermitian beams	11
1.2.1. The TEM ₀₀ mode	12
1.2.2. The M ² -value	14
1.3. Laser pulses and dispersion	16
1.4. Non-linear optical phenomena	18
1.4.1. Sum-frequency generation	19
1.4.2. The Pockels effect	22
1.4.3. Self-phase-modulation and the Kerr effect	24
1.4.4. Ultrashort pulse characterization	27
2. Laser Pulse Amplifiers	29
2.1. Solid-state laser basics	29
2.1.1. Amplification of laser pulses	32
2.1.2. Resonators	33
2.1.3. Gain narrowing	35
2.1.4. Chaotic pulse energy	36
2.2. Yb:YAG thin-disk amplifiers	36
2.2.1. The thin-disk concept	36
2.2.2. Properties of Yb:YAG	38
2.3. Regenerative amplifiers	41
2.4. Multi-pass amplifiers	44
3. Non-linear Thin-Disk Regenerative Amplifiers	47
3.1. The seed laser architecture and amplifier setup	48
3.2. Amplifier design considerations	51
3.2.1. Damage threshold of optics	51
3.2.2. Non-linear optical elements	54

3.3.	Beneficial resonators and limitations	55
3.3.1.	Large eigenmode resonators	56
3.3.2.	Imperfect optics in optical resonators	59
3.4.	The amplification process	61
3.4.1.	The influence of air	62
3.4.2.	Pulse evolution within the amplifier	63
3.4.3.	Self-focussing	70
3.5.	Pulse compression	74
3.5.1.	Grating compressor	74
3.5.2.	Chirped mirror compressor	75
3.6.	100 kHz non-linear regenerative thin-disk amplifier	76
3.6.1.	Laser design	76
3.6.2.	Performance	77
3.6.3.	Simple scaling of the repetition-rate	80
3.7.	Summary and conclusion	81
4.	Energy Scaling of Non-linear Thin-Disk Amplifiers	83
4.1.	The hybrid setup	84
4.2.	Non-imaging multi-pass amplifier	84
4.2.1.	Design	85
4.2.2.	Amplification and output	87
4.2.3.	Limitations and further design analysis	92
4.3.	Outlook	94
4.3.1.	Imaging multi-pass amplifier	94
4.3.2.	Summary	99
5.	Pulse Compression in Gas Filled Multi-pass Cells	101
5.1.	Introduction	102
5.2.	Simulation results	103
5.3.	Multi-pass cell setup	106
5.4.	Comparisson of different gases	107
5.5.	Beam quality	111
5.5.1.	Beam quality factor	111
5.5.2.	Spectral homogeneity of the beam	112
5.6.	Pulse compression after the multi-pass cell	114
5.6.1.	Optical wave-breaking and shock formation	116
5.6.2.	Differences between nitrogen and argon	118
5.7.	Scaling laws	121
5.8.	Conclusion	122
	Summary and Outlook	123

List of Publications	127
A. Split-Step model	129
A.1. Split-step method	129
A.2. Implementation	130
B. Resonator Calculation	133
C. Damage Threshold Calculation	137
D. Conversion of Parameters	139
D.1. The nonlinear refractive index	139
D.2. Gaussian laser pulses	139
E. Data Archiving	141
Bibliography	143
Acknowledgments	165

List of Figures

I.1. Summary of high-power Yb-doped laser systems	3
1.1. Measured higher order modes	15
1.2. Instantaneous frequency	16
1.3. chirped-pulse amplification	18
1.4. Sum frequency generation	20
1.5. Self-focusing	26
2.1. Laser principle	30
2.2. The concept of a thin-disk laser	37
2.3. Energy levels of Yb:YAG and temperature for different wavelengths	39
2.4. Cross sections of Yb:YAG	40
2.5. Amplification cycles within a regenerative amplifier	42
2.6. Interferometric switch	43
2.7. 4f-imaging	45
3.1. Amplifier setup	49
3.2. SH-FROG measurement of seed pulse	50
3.3. Damage threshold setup	52
3.4. Damage threshold measurement	53
3.5. Schematic picture of a Gaussian beam	58
3.6. Changing resonator mode	59
3.7. Monte-Carlo simulation for optical resonators	61
3.8. Resonator used to analyze the influence of air	62
3.9. Fourier limits in air and vacuum	63
3.10. Resonator used to analyze the pulse evolution	64
3.11. Spectra and FROG traces for different round trips	65
3.12. Pulse duration and temporal field	66
3.13. Fourier limit and pulse energy	67
3.14. Spectral intensity and phase of a 5 mJ pulse	70
3.15. Focal point shift depending on energy	72
3.16. Picture of the Pockels cell	73
3.17. Transmission grating compressor and shortest pulse	74
3.18. Heat distribution and GDD of the chirped mirror compressor	75
3.19. Picture of the chirped mirror compressor (picture: Thorsten Naeser)	76
3.20. Resonator eigenmode of under the influence of self-focusing	77

3.21. Measured stability of the system	78
3.22. FROG trace behind the chirped mirror compressor	79
3.23. Bifurcation at 100 kHz	79
3.24. Different repetition-rates.	80
4.1. The hybrid amplifier concept	84
4.2. Schematic overview of the hybrid amplifier	85
4.3. Picture of the multi-pass system	86
4.4. Power measurement of multi-pass and regenerative amplifier	88
4.5. Power stability and spectra of regenerative and multi-pass amplifier	89
4.6. SH-FROG measurement of 6.6 mJ output pulses	91
4.7. Beam caustic and fluences of the non-imaging system	92
4.8. Beam caustic and corresponding fluences of the imaging system	95
4.9. Image of the imaging system	97
4.10. Setup to compensate astigmatism	98
4.11. Characterization of the astigmatism	99
5.1. Calculated spectral inhomogeneity in lateral direction	104
5.2. Calculated beam quality factor vs. propagation distance	105
5.3. Schematic picture of the setup	106
5.4. Beam caustic	107
5.5. Measured input beam caustic and picture of plasma channels	108
5.6. 20 dB spectral bandwidth depending on the pressure	110
5.7. Measurement of the beam quality factor in argon	111
5.8. Measured homogeneity	112
5.9. Characterization of the spectral homogeneity	113
5.10. SH-FROG measurement of the output pulse	114
5.11. Illustration of optical wave-breaking	117
5.12. Effects resulting from the Raman response of nitrogen	119
5.13. Spectra of nitrogen and argon	120
5.14. Laser architecture for high repetition-rate attosecond metrology	124
A.1. Scheme: Numerical beam propagation	130
B.1. The “CavityCalculator”	133

List of Tables

1.1. Second order non-linear polarization	21
1.2. Summary of important Pockels cell crystals	22
2.1. Properties of selected laser materials	40
3.1. Non-linear refractive indices	55
3.2. Resonator parameters	60
4.1. Non-linear lengths	90
5.1. Non-linear properties of selected gases	109
B.1. ABCD-Matrices	135

Acronyms

AOI angle of incidence

AR anti-reflection

ASE amplified spontaneous emission

BBO β -Ba (BO₂)₂

CEP carrier-envelope-phase

CM chirped mirror

CPA chirped-pulse amplification

CW continuous-wave

DFG difference-frequency generation

DKDP KD₂PO₄

FROG frequency-resolved optical gating

FS fused-silica

FTL Fourier transform limit

FWHM full width at half maximum

GDD group delay dispersion

GRENOUILLE “grating-eliminated no-nonsense observation of ultrafast incident laser light e-fields”

GVD group velocity dispersion

HR high-reflective

MPC multi-pass cell

NIR near infrared

OPCPA optical parametric chirped-pulse amplification

PEPC plasma electrode Pockels cell

RMS root mean square

RoC radius of curvature

RT round trip

RTP rubidium titanyl phosphate

SF self-focusing

SFG sum-frequency generation

SH-FROG second-harmonic frequency-resolved optical gating

SPIDER spectral phase interferometry for direct electric-field reconstruction

SPM self-phase modulation

SVEA slowly varying envelope approximation

TEM transverse electromagnetic mode

TFP thin-film polarizer

TGG terbium gallium garnet

Ti:Sa Ti:Sapphire

TOD third order dispersion

YAG yttrium aluminium garnet

Introduction

Light is the source for life on earth and fascinates mankind since the early stages of their evolution. Description of light and efforts to understand the underlying processes reach back to ancient scientists and philosophers. In the beginning people considered the human eye as emitting device that actively scans the environment, which is of course far away from the insight that we have today. The first characterization of light that comes close to today's picture has been handed down by Aristotle who, ~350 BC, first stated that light is a phenomenon send out by objects, which is then detected by the human eye. This hypothesis had been rigorously proven more than 1000 years later by Alhazen [1] whose considerations paved the way to modern optics. It took, however, more than 800 years until Maxwell finally summarized results from experimental findings of several physicists into a set of four equations [2], which build the foundation for describing electromagnetic waves as it is today.

Since the 19th century this formalism embodies the “classical” view of light as a wave that propagates through space and time. With the advent of quantum mechanics, Albert Einstein had to go beyond Maxwell's continuous description and interpreted light as a particle with discrete energy to explain the photoelectric effect [3]. His findings caused wide ranged consequences and yielded the theoretical prediction of a process that allows light amplification by stimulated emission of radiation (LASER) [4]. The first demonstration of a laser by Theodore Maiman [5] was a success and the starting point for human made light sources with outstanding capabilities. Lasers emit light in confined – nearly diffraction limited – beams that easily achieve intensities high enough to reveal the anharmonic nature of the potential, bound electrons in matter are exposed to. The anharmonic potential manifests in non-linear optical responses of media such as second harmonic generation that was demonstrated shortly after the presentation of the first laser [6]. Thus, lasers and the available highly intense light sources gave birth to the field of non-linear optics. Ever since ground breaking physical effects originate from experiments based on laser sources with advanced parameters.

The basic functionality of lasers lies in the discrete quantum nature of electronic transitions in matter. Consequently, lasers tend to operate at well defined frequencies that emit light continuously, which makes them ideal tools for frequency resolved optical measurements. However, time resolved measurement techniques rendering electronic motion visible need temporarily confined events to allow sampling of the process on the underlying time scale. Luckily, it has quickly turned

out that lasers also operate in pulsed mode. The synchronization of longitudinal resonator modes opened the way for producing light flashes on the picosecond or femtosecond time scale. In 1964 “mode locking” was realized with an active modulation of losses inside the laser’s resonator [7]. The breakthrough in creating laser pulses on the femtosecond (“ultrashort”) time scale was the discovery of passive mode locking techniques [8] and their fundamental understanding [9–15]. Methods exploiting non-linear optical effects and using them as saturable absorbers such as semiconductor saturable amplitude modulators (SESAMs) [16, 17] and Kerr-lens mode locking [15, 18] further shortened the pulse duration to the sub 100 fs time scale and yielded the shortest events created by human kind, so far. The femtosecond duration of the light pulses opened access to time resolved spectroscopy on molecules and chemical processes for the first time and was honored with the Nobel prize in 1999 [19].

Electronic motion on the atomic time scale is three orders of magnitude faster and demands even shorter events. During the last two decades laser sources have been committed that emit pulses merely a few optical cycles ($T_{\text{one cycle}}=2.7$ fs @ $0.8 \mu\text{m}$) in length, which are best described by the underlying electric field rather than their envelope. The steep rise of the electric field gives access to time resolutions far less than the time scale of one optical light cycle and triggered the development of experiments with attosecond time resolution [18, 20]. Few-cycle pulses for attosecond science have so far been based on Ti:Sapphire (Ti:Sa) laser systems providing mJ-scale pulses with spectral bandwidths supporting pulse durations of typically less than 5 fs. Pulse energies on the millijoule scale are achieved in chirped-pulse amplification (CPA) [21] systems that amplify pulses provided by mode locked oscillators. Subsequent non-linear pulse compression in hollow core fibers [22] generates pulses of less than 4 fs duration [23, 24] and are the back bone of attosecond metrology [20].

Ti:Sa CPA systems constitute well developed light sources but are limited in average power to 10-40 W. This is caused by the large quantum defect, the resulting thermal issues [25] and the limited power of available pump light sources [26]. Therefore, the repetition-rates of millijoule Ti:Sa lasers are limited to ~ 10 kHz. Higher repetition-rates, however, would yield better statistics, shorter measurement times and paves the way towards rare events such as coincidence measurements and spectroscopy of low-cross-section systems [27, 28].

Overcoming the average power limitation of Ti:Sa systems whilst providing multi-millijoule few-cycle pulses is challenging and constitutes a major research topic in current laser development. Lasers with pulse repetition-rates between 100 kHz and 1 MHz that emit pulses with millijoule energy operate at hundreds of watts average power. In this context several laser architectures with advanced thermal properties based on fiber [29, 30], innoslab [31] and thin-disk [32] amplifiers have been demonstrated. Based on ytterbium ion doping these systems recently crossed the mark of 1 kW average power whilst delivering ultrashort laser pulses [31, 33–35]

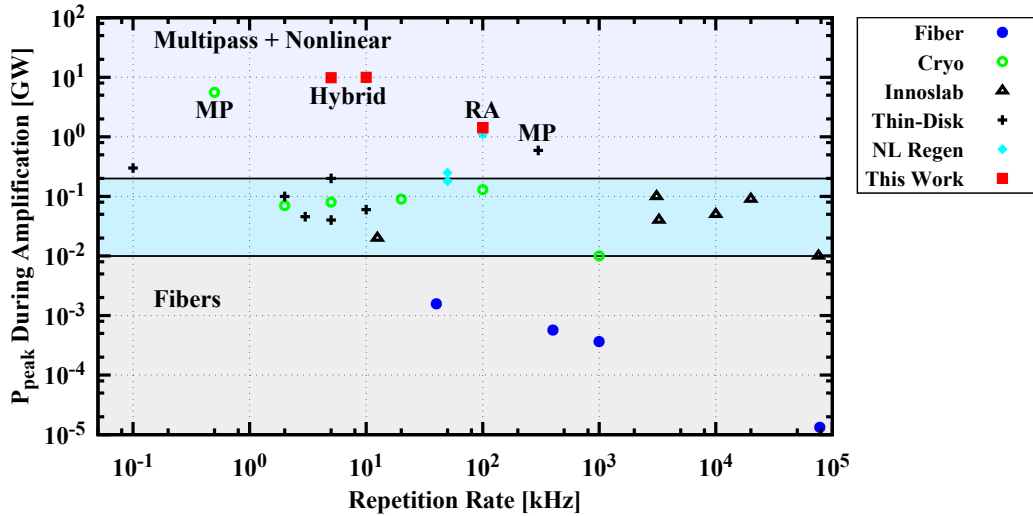


Figure I.1.: Summary of high-power Yb-doped laser systems. Peak power during amplification vs. repetition-rate of the amplifier. Note that all amplifiers exceeding 0.2 GW peak power are based on thin-disks. Peak powers are calculated, using the highest pulse energy after amplification before compression (gain narrowing included). Multipass (MP), Non-linear (NL). Sources: Thin-Disk [33, 35, 37–40]; Fiber [30, 34, 41–43]; Cryo-Cooled [44–51]; Innoslab [31, 52–56]; Non-linear Amplifiers [57, 58]

and thus have proven to outrange Ti:Sa systems in average power by far. However, ytterbium doped gain materials have narrower gain bands [36] than Ti:Sa and, therefore, generation of few-cycle pulses has remained challenging.

Based on the advantages of high energy ytterbium-based few-cycle lasers, this thesis focuses on the improvement and implementation of Yb:YAG thin-disk laser concepts aiming for high energy pulses at shortest possible pulse duration. Due to their cooling technology thin-disk lasers are one of the most important scalable concepts for high average power systems [59]. Moreover, the thin (~ 0.1 mm) gain medium allows for gigawatt peak powers during the amplification process at moderate beam diameters of a few millimeters. The scalability in peak power is a characteristic property of the thin-disk concept (Fig. I.1) and is beneficial for amplification of pulses to the multi-millijoule level. This advantage builds the basis for the work presented in this thesis that focuses on implementing the thin-disk concept without CPA. Omitting CPA avoids losses in the compression unit, leads to a cost-efficient, compact system and user-friendly system that is less sensitive to instabilities caused by stretching and compressing units. The direct amplification of femtosecond pulses leads to several challenges that are discussed in this document. It will be shown that it is possible to exploit non-linear optical effects during amplification providing intrinsically shortened pulses out of the Yb:YAG amplifier.

The achieved parameters of 210 fs pulse duration at 2 mJ pulse energy with 100 kHz repetition rate and 200 W average power are – to this day – unique properties of an Yb:YAG thin-disk regenerative amplifier. To generate even shorter pulses, a concept for non-linear spectral pulse compression of high-energy, high-average power laser systems is presented and both numerically and experimentally analyzed. The pulses of the non-linear amplifier are shortened by a factor of 5.6 to 37 fs that reach 35 GW peak power providing ideal parameters for further compression to the few-cycle regime. The implementation of this concept is – to the best of the authors knowledge – presented for the first time.

This thesis presents the concepts and results as follows:

- Chapter (1) summarizes from Maxwell's equations on the basic principles in non-linear optics and gives an overview on the effects that influence the amplified output pulses. In the first section of the chapter the wave equation for ultrashort pulses is derived, which is implemented in the developed simulation. The equation also builds the basis for further explanation of physical processes in the following chapters. The focus is set on basic parameters, values for specification and the measurement technique used for characterizing ultrashort laser pulses.
- Chapter (2) gives an overview to relevant properties of amplifiers and introduces the thin-disk concept, regenerative amplifiers and multi-pass amplifiers. Yb:YAG as gain medium is studied and further information on other materials are summarized to provide decent insight into the properties of Yb:YAG relative to Ti:Sa and other Yb-doped gain materials.
- Chapter (3) describes the properties of the developed system and explains the laser design choices, which are of importance. Special care is taken to show properties of the large mode resonators that need to be implemented to achieve the best possible performance. The presented data depicts the influence of air on the output pulses. The pulse evolution under the influence of non-linear optical effects during the amplification process is studied. Techniques to reach Fourier transform limited output pulses are presented and advantages and disadvantages are discussed. The chapter ends with the description of the developed non-linear 100 kHz repetition-rate amplifier and a detailed presentation of the achieved parameters.
- Chapter (4) investigates a new concept for energy scaling of a Yb:YAG thin-disk amplifier. The concept merges a regenerative amplifier with a thin-disk multi-pass amplifier reaching high overall gain in combination with pulse energies up to 6.6 mJ. The chapter describes a possible system for further pulse energy scaling above 10 mJ. This system is based on a relay imaging system, which is analyzed and necessary parameters for future implementation into the amplifier are given.

-
- Chapter (5) presents the implementation of an external non-linear compression stage for further pulse shortening of the developed 100 kHz amplifier. The implemented gas filled non-linear multi-pass pulse compression cell conveys properties known from hollow core fibers to a concept based on a wave guide formed by high-reflective mirrors. The peak power scalable concept allows spectral broadening whilst maintaining good beam quality and spectral homogeneity across the beam profile.

Chapter 1

Optical Effects in Ultrashort Pulse Amplifiers

This chapter intends to give detailed insight into the physics behind this thesis. It covers the main physical effects that describe the amplifier and the emitted laser pulses. To give an understandable introduction the starting point is set on Maxwell's equations that build the basis for the description of light waves. The first section depicts the path towards deriving the non-linear wave equation [Equ. (1.28)], that embodies the result as implemented in the applied numerical simulations, that are presented in chapters (3) and (5). The chapter continues to show the basic linear and non-linear optical effects necessary to describe the laser system. For this purpose, the non-linear wave equation is simplified to the essential parts putting focus solely on the effect of interest.

The chapter is thought to provide a good reference of the mathematics in a short version and allows reading the sections separately. For more details on this topic it is referred to [60, Ch. 13].

1.1. Maxwell's equations and the non-linear wave equation

Throughout this thesis the description of light as an electromagnetic wave forms the foundation upon which almost all observed optical phenomena can be reduced to. Maxwell's equations summarize the properties of electric and magnetic fields in their most fundamental character and relate the magnetic flux density \mathbf{B} , the magnetic field \mathbf{H} , the electric field \mathbf{E} and the electric displacement field \mathbf{D} to

$$\nabla \times \mathbf{E}_{rt} = -\frac{\partial \mathbf{B}_{rt}}{\partial t} \quad (1.1)$$

$$\nabla \times \mathbf{H}_{rt} = \frac{\partial \mathbf{D}_{rt}}{\partial t} + \mathbf{j} \quad (1.2)$$

$$\nabla \cdot \mathbf{D}_{rt} = \rho \quad (1.3)$$

$$\nabla \cdot \mathbf{B}_{rt} = 0 \quad (1.4)$$

where the indices of the fields denote their dependency on the space coordinate \mathbf{r} and the time coordinate t , ρ is the free charge density and \mathbf{j} is the free current density. In dielectrics the free charge density and the free current density vanish, so that $\rho = 0$ and $\mathbf{j} = 0$. Throughout this work only dielectrics are considered that further exhibit a negligible magnetization \mathbf{M}_{rt} leading to

$$\mathbf{H}_{rt} = \frac{1}{\mu_0} \mathbf{B}_{rt} - \mathbf{M}_{rt} = \frac{1}{\mu_0} \mathbf{B}_{rt} \quad (1.5)$$

where μ_0 is the vacuum permeability. The curl of (1.1) together with replacing the resulting curl of the magnetic flux density on the right with equation (1.2) leads to

$$\nabla \times (\nabla \times \mathbf{E}_{rt}) = -\frac{1}{\mu_0} \frac{\partial^2}{\partial t^2} \mathbf{D}_{rt}. \quad (1.6)$$

Using the identity $\nabla \times (\nabla \times \mathbf{E}_{rt}) = \nabla(\nabla \cdot \mathbf{E}_{rt}) - \nabla^2 \mathbf{E}_{rt}$ and dropping the first term on the right side [60, p. 71] the equation transforms to

$$-\nabla^2 \mathbf{E}_{rt} + \frac{1}{\epsilon_0 c_0^2} \frac{\partial^2}{\partial t^2} \mathbf{D}_{rt} = 0 \quad (1.7)$$

where the vacuum permittivity ϵ_0 , the speed of light in vacuum $c_0 = 1/\sqrt{\epsilon_0 \mu_0}$ is introduced and ∇^2 is the Laplace operator. For practical reasons it is helpful to separate the non-linear from the linear response of the medium so that the displacement field separates into [60]:

$$\mathbf{D}_{rt} = \epsilon_0 (\mathbf{1} + \boldsymbol{\chi}) \mathbf{E}_{rt} = \underbrace{\epsilon_0 (\mathbf{1} + \boldsymbol{\chi}^{(1)}) \mathbf{E}_{rt}}_{\mathbf{D}_{rt}^{(L)}} + \underbrace{\epsilon_0 \boldsymbol{\chi}^{(NL)} \mathbf{E}_{rt}}_{\mathbf{P}_{rt}^{(NL)}} = \mathbf{D}_{rt}^{(L)} + \mathbf{P}_{rt}^{(NL)}. \quad (1.8)$$

The tensor $\boldsymbol{\chi}^{(NL)}$ represents the magnitude of the non-linear susceptibility and is a function of the electric field. The wave equation in this notation is then [60]

$$-\nabla^2 \mathbf{E}_{rt} + \frac{\epsilon(\omega)}{c_0^2} \frac{\partial^2}{\partial t^2} \mathbf{E}_{rt} = -\frac{1}{\epsilon_0 c_0^2} \frac{\partial^2}{\partial t^2} \mathbf{P}_{rt}^{(NL)}, \quad (1.9)$$

where the non-linear polarization appears as source function for the electric field.

In most cases pulses emitted from lasers possess durations much longer than the time scale of a single cycle of an optical light field. Therefore, it is useful to separate the envelope of the pulse from the fast oscillating carrier frequency. Similar arguments apply for the spatial coordinate. The electric field and the non-linear polarization can be expressed as,

$$\mathbf{E}_{rt} = \mathbf{A}_{rt} e^{i(k_0 z - \omega_0 t)} + c.c. \quad (1.10)$$

$$\mathbf{P}_{rt}^{(NL)} = \mathbf{p}_{rt}^{(NL)} e^{i(k_0 z - \omega_0 t)} + c.c. \quad (1.11)$$

where *c.c.* denotes their complex conjugate and $k_0 = 2\pi n/\lambda_0$ with λ_0 and n being the wavelength of the light field and the refractive index at the carrier frequency.

As many physical quantities are known with respect to the frequency of an applied electric field rather than in the time domain – such as the permittivity $\epsilon(\omega)$ – the wave equation is more simply handled if the field is expressed in the frequency domain. The connection between both domains is given by the Fourier transformations

$$\mathbf{E}_{rt} = \frac{1}{2\pi} \int \mathbf{E}_{r\omega} e^{-i\omega t} d\omega \quad (1.12)$$

$$\mathbf{D}_{rt} = \frac{1}{2\pi} \int \mathbf{D}_{r\omega} e^{-i\omega t} d\omega \quad (1.13)$$

$$\mathbf{P}_{rt}^{(\text{NL})} = \frac{1}{2\pi} \int \mathbf{P}_{r\omega}^{(\text{NL})} e^{-i\omega t} d\omega \quad (1.14)$$

$$\mathbf{A}_{rt} = \frac{1}{2\pi} \int \mathbf{A}_{r\omega} e^{-i\omega t} d\omega. \quad (1.15)$$

Applying these relations to the wave equation (1.9) and assuming linear polarized light, the envelope $A_{r\omega}$ and the envelope of the non-linear polarization $p_{r\omega}^{(\text{NL})}$ fulfill the equation [60, 61]

$$\nabla^2 A_{r\omega} + 2ik_0 \frac{\partial A_{r\omega}}{\partial z} + [k^2(\omega) - k_0^2] A_{r\omega} = -\frac{\omega_0^2}{\epsilon_0 c_0^2} \left(1 + \frac{1}{\omega_0}(\omega - \omega_0)\right)^2 p_{r\omega}^{(\text{NL})}, \quad (1.16)$$

where $k^2(\omega) = \epsilon(\omega)\omega^2/c_0^2$ describes the dispersion relation, $k_0 := k(\omega_0)$ and the approximation [60]

$$E_{r\omega} = A(\mathbf{r}, \omega - \omega_0) + A^*(\mathbf{r}, \omega + \omega_0) \simeq A(\mathbf{r}, \omega - \omega_0) \quad (1.17)$$

was used. The assumption that $A_{r\omega}$ takes only non-vanishing values for frequencies in proximity to ω_0 is valid for fields that contain less than one octave bandwidth.

The introduced quantities relate to the intensity as

$$I(\mathbf{r}, t) = 2n_0\epsilon_0 c_0 |\mathbf{A}_{rt}|^2, \quad (1.18)$$

which also defines the fluence as the time integrated intensity

$$F(\mathbf{r}) = \int I(\mathbf{r}, t) dt. \quad (1.19)$$

The latter quantity describes the energy per unit area of the electric field, which is particularly useful if physical effects depend on the pulse duration and not only on the intensity of the laser pulse (Sec. 3.2.1).

Transformation of the wave equation into a first order differential equation with respect to the propagation coordinate z is beneficial for numerical field propagation. Centering the fields at the time coordinate zero is realized by introducing the

retarded time, which is achieved by shifting the time according to [60]

$$z' = z, \quad \tau = t - \frac{1}{v_g}z = t - k_1 z \quad (1.20)$$

$$\frac{\partial}{\partial z} = \frac{\partial}{\partial z'} - k_1 \frac{\partial}{\partial \tau} \quad \frac{\partial}{\partial t} = \frac{\partial}{\partial \tau}, \quad (1.21)$$

where $v_g = (\frac{\partial k}{\partial \omega})^{-1} = 1/k_1$ is the group velocity of the pulse. For further simplification the wave equation is transformed to the frequency domain. As the Fourier transformation converts the derivative with respect to time via

$$\partial_\tau \leftrightarrow -i(\omega - \omega_0) \quad (1.22)$$

the relations (1.21) translate into

$$\frac{\partial}{\partial z} = \frac{\partial}{\partial z'} + ik_1(\omega - \omega_0) \quad \frac{\partial^2}{\partial z^2} = \frac{\partial^2}{\partial z'^2} + 2ik_1(\omega - \omega_0) - k_1^2(\omega - \omega_0)^2 \quad (1.23)$$

which is the representation of the retarded time frame in the frequency domain. Implementing these results into the wave equation results in

$$\left[\nabla_\perp^2 + \frac{\partial^2}{\partial z'^2} + 2ik_0 \left(1 + \frac{k_1}{k_0}(\omega - \omega_0) \right) \frac{\partial}{\partial z'} - k_1^2(\omega - \omega_0)^2 - 2k_0k_1(\omega - \omega_0) + k^2(\omega) - k_0^2 \right] A_{r\omega} = -\frac{\omega_0^2}{\epsilon_0 c_0^2} \left(1 + \frac{1}{\omega_0}(\omega - \omega_0) \right)^2 p_{r\omega}^{(NL)}. \quad (1.24)$$

To obtain the final result $k(\omega)$ is written in a Taylor series [60]

$$k(\omega) = k_0 + k_1(\omega - \omega_0) + D; \quad D = \sum_{n=2}^{\infty} \frac{1}{n!} k_n (\omega - \omega_0)^n; \quad k_n = \left. \frac{\partial^n k}{\partial \omega^n} \right|_{\omega=\omega_0} \quad (1.25)$$

$$k^2(\omega) = k_0^2 + 2k_0k_1(\omega - \omega_0) + k_1^2(\omega - \omega_0)^2 + 2k_0D + 2k_1D(\omega - \omega_0) + D^2 \quad (1.26)$$

which transforms equation (1.24), after neglecting, D^2 , and applying the slowly varying envelope approximation (SVEA) [60],

$$\left| \frac{\partial^2 A}{\partial z^2} \right| \ll k \left| \frac{\partial A}{\partial z} \right|, \quad (1.27)$$

to the final result [60, 61]:

$$\left[\nabla_\perp^2 + 2ik_0 \left(1 + \frac{k_1}{k_0}(\omega - \omega_0) \right) \frac{\partial}{\partial z'} + 2k_0D \left(1 + \frac{k_1}{k_0}(\omega - \omega_0) \right) \right] A_{r\omega} = -\frac{\omega_0^2}{\epsilon_0 c_0^2} \left(1 + \frac{1}{\omega_0}(\omega - \omega_0) \right)^2 p_{r\omega}^{(NL)}. \quad (1.28)$$

This equation is implemented in the 2D-split step simulation that is used to illustrate properties of the pulse under the influence of non-linear optical effect in chapters (3) and (5). Integration of this equation into a numerical code is straight forward if the derivative with respect to z' is isolated. As the material properties carrying the information of dispersion are known in the frequency domain, these steps are usually applied in the frequency domain. The diffraction operator ∇_{\perp}^2 transforms to $-(k_x^2 + k_y^2) = -\mathbf{k}_{\perp}^2$ if the field is with

$$\mathbf{A}_{rt} = \frac{1}{(2\pi)^2} \int \int \mathbf{A}_{\mathbf{k}_{\perp}zt} e^{+i(k_x x + k_y y)} dk_x dk_y \quad (1.29)$$

transformed from spatial coordinates to the spatial frequency domain. Depending on the requirements the transformation of the field replaces the operators by their complementary variables (for more details see appendix A).

1.2. Gauss-Hermitian beams

The description of a laser beam is the topic of this section. It will be shown that laser beams are described by a group of functions that distinguish in their lateral intensity distribution. Furthermore, the beam quality and its measurement will be introduced providing an important tool for the further sections.

To discuss the properties of optical beams it is convenient to consider a monochromatic beam in vacuum which reduces equation (1.28) to the paraxial Helmholtz equation

$$\nabla_{\perp}^2 A(\mathbf{r}) + 2ik_0 \frac{\partial A(\mathbf{r})}{\partial z'} = 0. \quad (1.30)$$

This differential equation is solved by the Gauss-Hermitian beams that form a full set of orthogonal functions possessing an intensity distribution located to close proximity of the optical axis (paraxial approximation). In Cartesian coordinates these functions describe the field amplitude [62]

$$\begin{aligned} A(\mathbf{r}) = & A_0 H_l \left(\frac{\sqrt{2}x}{w(z)} \right) H_m \left(\frac{\sqrt{2}y}{w(z)} \right) e^{i(l+m)\xi(z)} \\ & \times \frac{w_0}{w(z)} \exp \left[-\frac{(x^2 + y^2)}{w^2(z)} \right] \exp \left[-ik \frac{(x^2 + y^2)}{2R(z)} \right] e^{i\xi(z)} \end{aligned} \quad (1.31)$$

with the two independent non-negative indices l and m being the order of the Hermitian polynomial. These polynomials fulfill the recursive relationship,

$$H_0(u) = 1 \quad (1.32)$$

$$H_1(u) = 2u \quad \text{and} \quad (1.33)$$

$$H_{k+1}(u) = 2uH_k(u) - 2kH_{k-1}(u) \quad (\text{Hermitian polynomials}). \quad (1.34)$$

The functions $w(z)$ and $R(z)$ describe the extension in space and define the curvature of the wave-fronts. The parameter $\xi(z)$ is the ‘‘Gouy phase’’, that describes an extra phase shift depending on the longitudinal coordinate.

1.2.1. The TEM₀₀ mode

Considering the mode with $l = m = 0$ equation (1.31) gives [62]

$$A(\mathbf{r}) = A_0 \frac{w_0}{w(z)} \exp \left[-\frac{(x^2 + y^2)}{w^2(z)} \right] \exp \left[-ik \frac{(x^2 + y^2)}{2R(z)} \right] e^{i\xi(z)} \quad (1.35)$$

$$I(\mathbf{r}) \propto |A_0|^2 \frac{w_0^2}{w^2(z)} \exp \left[-2 \frac{(x^2 + y^2)}{w^2(z)} \right] \quad (1.36)$$

where the intensity profile along the optical axis follows the function,

$$w(z) = \sqrt{w_0^2 + \frac{\lambda^2}{\pi^2 w_0^2} (z - z_f)^2}. \quad (1.37)$$

This is the $1/e^2$ waist radius of the beam, at position z from its minimum waist size at z_f . An equivalent notation is

$$w^2(z) = w_0^2 \left[1 + \left(\frac{z - z_f}{z_R} \right)^2 \right], \quad (1.38)$$

where the Rayleigh range

$$z_R = \frac{\pi w_0^2}{\lambda} \quad (1.39)$$

of the beam is introduced. This important quantity describes the distance from the focus, at which the waist enlarged by a factor of $\sqrt{2}$. The Rayleigh range sets the minimum mode size in relation to the beam divergence and quantifies this fundamental property of light beams. According to relation (1.37) the beam diverges with an angle of

$$\theta_0 = \frac{\lambda}{\pi w_0} \quad (1.40)$$

so that a beam with smaller waist diverges faster than a beam with larger waist. Longer wavelengths λ linearly increase the divergence θ_0 . For constant mode radius w_0 , this means that a light beam with shorter wavelength exhibits less divergence than a beam with longer wavelength.

Besides the intensity profile the beam further contains a phase term depending on $R(z)$, which describes the curvature of the phase fronts. It is related to the Rayleigh range z_R via the equation:

$$R(z) = z \left[1 + \left(\frac{z_R}{z - z_f} \right)^2 \right], \quad (1.41)$$

that reaches its minimum value at the Rayleigh range z_R . Obviously, the beam has a flat wavefront in the focus ($z = z_f$) and at infinite distance to it. Furthermore, the function

$$\xi(z) = \arctan \frac{z}{z_0} \quad (\text{Gouy Phase}) \quad (1.42)$$

describes an extra phase shift of π that accumulates during propagation through the focus and is named after its discoverer Léon Georges Gouy [63]. As the Gouy phase is not visible in intensity measurements, this quantity is very often hidden and appears only in special cases that depend on the actual phase of the beam. In describing optical resonators this quantity represents an equivalent description of the stability parameter (Sec. 2.1.2).

It is necessary to define a complex parameter, the “q-parameter”, to summarize the properties of the beam.¹ The parameter is defined as

$$q = (z - z_f) + iz_R \quad (1.43)$$

$$\Leftrightarrow \frac{1}{q} = \frac{1}{R(z)} - i \frac{2}{kw^2(z)} \quad (1.44)$$

and allows intuitive manipulation of the beam at given q . Propagation of distance d , for example, requires a simple addition of a real number to the q-parameter $q_{new} = q_{old} + d$. A lens with focal length f modifies just the curvature of the beam and addition of $1/f$ to $1/q$ produces a beam carrying the new, modified, properties. More generally, modification of the q-parameter is achieved with a simple matrix formalism that is known as the ABCD-Matrix or ray transfer matrix formalism. The 2x2 matrices [66] allow manipulation via the transformation

$$q_2 = \frac{Aq_1 + B}{Cq_1 + D}. \quad (1.45)$$

In context of resonator design (Sec. 2.1.2) this will be discussed in more detail.

As in most laser systems beam propagation takes place in isotropic media, the electric and magnetic field components in propagation direction vanish. Modes with this property are called transverse electromagnetic modes (TEMs) and are

¹Originally, this parameter needs to be introduced to avoid the pole of a spherical wave at $z=0$.

The well known method of shifting the parameter z to the complex plane $z \rightarrow z + iz_R$ solves this issue and naturally leads to the introduction of the Rayleigh length z_R [64, 65]

numbered accordingly TEM_{lm}. For several reasons that will be discussed shortly in this section, it is desirable to reach operation of the laser with its fundamental Gaussian TEM₀₀ mode.

1.2.2. The M²-value

An important quantity to describe the quality of a laser beam is the M²-value. This number sets the laser beam emitted from a laser source into relation to a perfect Gaussian TEM₀₀ mode. The M²-parameter is a measure of the space-beamwidth product that describes the divergence of a beam in relation to its waist size. Similarly to other complementary variables, that are connected via the Fourier transformation, the product of the beam divergence θ_0 and the beam width w_0 for an ideal Gaussian TEM₀₀ mode takes a minimum [67] with:

$$\theta_{0x}w_{0x} = \frac{\lambda}{\pi} \quad (1.46)$$

$$\theta_{0y}w_{0y} = \frac{\lambda}{\pi}. \quad (1.47)$$

The M²-factor now allows to quantify the deviation from the “diffraction limited” TEM₀₀ mode. The definition

$$\theta_x w_x = M_x^2 \frac{\lambda}{\pi} \quad \text{and} \quad (1.48)$$

$$\theta_y w_y = M_y^2 \frac{\lambda}{\pi} \quad (1.49)$$

with $M_x^2 \geq 1$ and $M_y^2 \geq 1$ reflects the properties of beams that deviate from the diffraction limit.

For a higher order Hermite-Gaussian mode it can be shown that [68, p. 242]

$$w_x = w_{0x} \sqrt{2l+1} \quad w_y = w_{0y} \sqrt{2m+1} \quad (1.50)$$

$$\theta_x = \theta_{0x} \sqrt{2l+1} \quad \theta_y = \theta_{0y} \sqrt{2m+1}. \quad (1.51)$$

With equations (1.48) and (1.49) the M²-value for a higher order mode gives

$$M_x^2 = \frac{\pi}{\lambda} \theta_x w_x = \frac{\pi}{\lambda} \theta_{0x} w_{0x} (2l+1) = (2l+1) \quad (1.52)$$

$$M_y^2 = \frac{\pi}{\lambda} \theta_y w_y = \frac{\pi}{\lambda} \theta_{0y} w_{0y} (2m+1) = (2m+1). \quad (1.53)$$

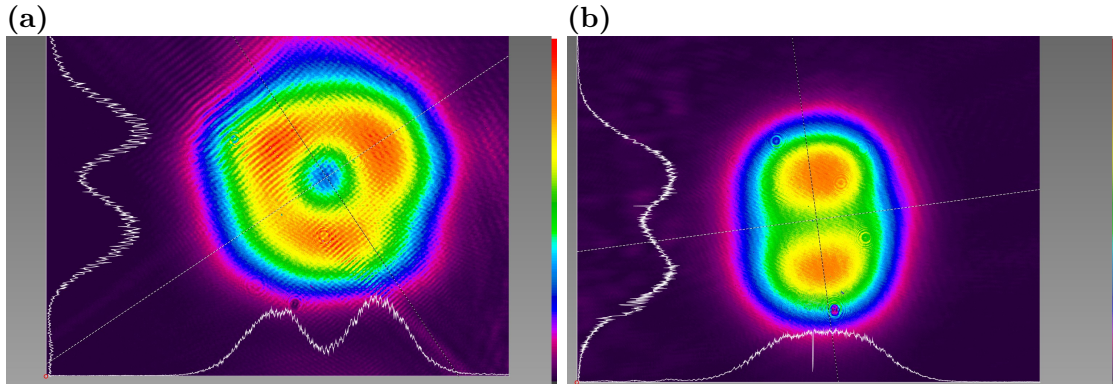


Figure 1.1.: (a) Measured “donut” mode and (b) mode close to TEM_{01}

The M^2 -factor reveals helpful as higher order modes and beam distortions show themselves in an increasing value. Anthony Siegman summarizes the M^2 -values for linear combinations of Gauss-Hermitian modes to [67]

$$M_x^2 = \sum_{l,m=0}^{\infty} (2l+1) |C_{lm}|^2 \quad \text{and} \quad (1.54)$$

$$M_y^2 = \sum_{l,m=0}^{\infty} (2m+1) |C_{lm}|^2 \quad (1.55)$$

$$1 = \sum_{l,m=0}^{\infty} |C_{lm}|^2 \quad (1.56)$$

allowing a quantification of the “beam quality” for arbitrary beams. The coefficients C_{lm} are the normalized amplitudes [Equ. (1.56)] of the TEM_{lm} modes. For example, the TEM_{10} mode has a $M_x^2 = 3$ and a $M_y^2 = 1$ revealing the enlarged space-beamwidth product in x-direction of this mode.

The beam quality factor for experimental data is determined by fitting the function

$$W^2(z) = W_0^2 + (M^2)^2 \frac{\lambda^2}{\pi^2 W_0^2} (z - z_f)^2 \quad (1.57)$$

to the recorded waist sizes at different positions z . Therefore, determining the beam quality of the laser requires the measurement of the laser beam at several different positions with a beam profiler. Due to the vanishing phase term in intensity measurements the simple conclusion that a Gaussian mode shape means the observation of a TEM_{00} mode is wrong. Generally, modes exist that seem fairly Gaussian, but are linear combinations of several Gauss-Hermitian beams exhibiting M^2 -values much larger than 1. Well designed laser systems can achieve M^2 -values

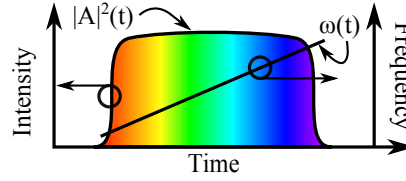


Figure 1.2.: Illustration of a pulse with raising instantaneous frequency

close to 1 but this value is easily exceeded if components inside the laser exhibit thermal lensing, the laser resonator design is incorrectly adjusted to the demanded constraints or other influences distort the beam. Figure (1.1) shows modes, that were measured with a beam profiler in a laser system not operating in the fundamental mode. The profile shown in (a) mode is to good extend a linear combination of the TEM_{01} and the TEM_{10} intensity profile. The recorded profile shown in (b) is close to the TEM_{01} mode exhibiting a contribution of the TEM_{00} mode, which leads to non-vanishing intensity in the center of the beam.

1.3. Laser pulses and dispersion

Laser pulses are temporarily confined events that are described by the time evolution of E_{rt} . Ignoring the spatial coordinate, the complex field of equation (1.10) can be expressed as

$$A(t) = |A(t)| e^{i\varphi(t)} \quad (1.58)$$

with $\varphi(t)$ being the time dependent phase of the field envelope. Adding the carrier frequency gives

$$\varphi_{tot}(t) = \varphi(t) - \omega_0 t, \quad (1.59)$$

which contains the full phase of the complex electric field. Taking the first derivative with respect to the time

$$\frac{d\varphi_{tot}(t)}{dt} = -(\omega_0 - \frac{d\varphi(t)}{dt}) = -\omega(t), \quad (1.60)$$

yields to the quantity that is known as the instantaneous frequency of the pulse. The derivative of the envelope's phase, $\frac{d\varphi(t)}{dt}$, describes the deviation of the frequency relative to the carrier frequency at a given time (Fig. 1.2).

The connection of time and frequency via the Fourier transformations (1.12)-(1.15) directly leads to a link of pulse duration and spectral bandwidth of the laser pulse. For a bandwidth limited pulse of duration τ and bandwidth $\Delta\nu = c_0\Delta\lambda/\lambda^2$,

where λ is the wavelength of the pulse and $\Delta\lambda$ the bandwidth in wavelengths, the time bandwidth product is constant with

$$\tau\Delta\nu = \tau\frac{c_0}{\lambda^2}\Delta\lambda = \text{const.} \quad (1.61)$$

Consequently, the shorter the laser pulse the broader its spectral bandwidth. Ultrashort laser pulses quickly possess spectral bandwidths that get affected by the frequency dependent refractive index of optical elements. As different frequencies contained within the laser pulse experience different refractive indices, spectral components separate from others and the pulse changes its shape and duration. These effects are summarized in the parameter D [Equ. (1.25)] that contains the Taylor expansion of $k(\omega)$ from the second term. The first order term in D has the magnitude k_2 , which is known as the group velocity dispersion (GVD). A positive value of k_2 leads to separation of the red from the blue spectral components due to a decreased velocity of the blue as compared to the red spectral components. A bandwidth limited input pulse influenced by this effect will stretch in time and possesses a red shifted leading and a blue shifted trailing edge. A negative k_2 does the opposite. The total amount of GVD that is introduced by an optical element after propagation of length L results in the group delay dispersion (GDD) of the pulse. The resulting frequency sweep of the pulse is also known as chirp. This influence of dispersive optical elements on laser pulses is often applied to manipulate the time structure of the pulse. In laser systems the method of chirped-pulse amplification (CPA) [21] implements this concept to reduce the pulse intensity and peak power during the amplification process by stretching the pulses prior to the amplification process. This is achieved by introducing either a positive or a negative dispersive optical element into the beam path. Being artificially stretched in time the pulses contain lower peak powers at equal pulse energy. The stretcher prior to amplification is usually designed to provide pulses with enough chirp to maintain the pulse duration roughly during the whole amplification process. After the pulses gained the desired energy the compressor unit that introduces the exact negative dispersion of the stretching unit removes the chirp from the high energy pulses. The shorter pulse duration then leads to a significant increase of peak power (Fig. 1.3).

The third order term of D results in third order dispersion (TOD) after propagating through a medium with length L . Depending on the sign of k_3 the output pulses exhibit pre- ($k_3 < 0$) or post- ($k_3 > 0$) pulses. Orders of D with $n > 3$ [Equ. (1.25)] generally cause symmetric and asymmetric pulse shapes for even and odd numbers of n , respectively. The energy of the pulse is then distributed in pedestals, pre- or post-pulses.

The process of introducing dispersion into a laser pulse is generally reversible as optical elements exist that provide both positive and negative coefficients. In the

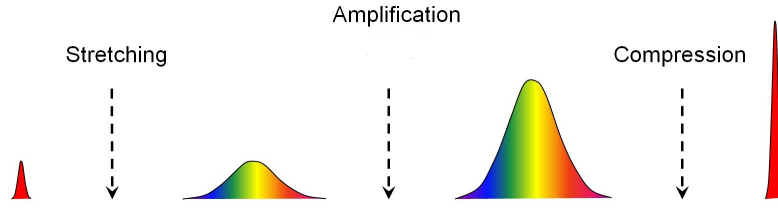


Figure 1.3.: Schematic illustration of the CPA principle with a negatively (blue arrives first) chirped pulse.

visible and near infrared (NIR) spectral range dielectrics usually exhibit positive k_2 and k_3 whilst negative values can be achieved optical elements specifically designed for this purpose such as chirped mirrors (CMs) [18, 69], grating or prism pairs.

1.4. Non-linear optical phenomena

Lasers provide nearly diffraction limited beams and their confined light bundles can easily exceed intensities of MW/cm^2 . At these intensities a variety of interesting phenomena unfolds that originate from the non-linear optical response of matter. The response of media then no longer depends on the material properties only, but are strongly influenced by the incident light wave. Once the laser intensity crosses the barrier to trigger non-linear optical processes effects reveal that nowadays constitute the bases for light manipulation, efficient generation of harmonics and light amplification [38].

Unlike the linear electronic response of matter, its non-linear behavior results from the anharmonic potential the charge carriers are exposed to. As the reset forces in such potentials are no longer linear with the displacement from the equilibrium position the polarized wave differs from the input driving field. From a simple classical oscillator model it can be derived that these processes are generally very fast. The time scale relates to the resonance frequency of the electronic response [60]. As this frequency is located in the ultraviolet spectrum – $\lambda_{\text{res}} \approx 200 \text{ nm}$ – non-linear optical processes occur on time scales

$$T = \lambda_{\text{res}}/c \approx 1 \text{ fs} \quad (1.62)$$

that are at the edge to the attosecond time scale. On all time scales that are considered here, this response can be considered as quasi instantaneous and the non-linear part of the susceptibility can be described by the Taylor expansion

$$\chi_{ij}(\mathbf{E}_{rt}) = \underbrace{\chi_{ij}^{(1)}}_{\chi^{(L)}} + \underbrace{\chi_{ijk}^{(2)}E_k + \chi_{ijkl}^{(3)}E_kE_l + \dots}_{\chi^{(NL)}(\mathbf{E}_{rt})} \quad (1.63)$$

with coefficients $\chi^{(n)}$ that describe the order of the non-linearity. In the following the non-linear coefficients can be considered frequency independent, which translates to an instantaneous response of the medium. In chapter (5) this assumption is partially dropped to explain the different behavior between argon and nitrogen in the multi-pass pulse compression cell.

Even though the topic is tremendously interesting and a variety of effects appear in this context, this section examines only the effects most relevant to this work. For a good overview over this topic it is referred to [60].

1.4.1. Sum-frequency generation

Considering the lowest order non-linear term of equation (1.63) yields non-linear optical effects of second order. As the second order susceptibility vanishes in centrosymmetric media [60] these effects are only visible in materials without an inversion center.

These effects are described by the interaction of two fields. The total field at a certain location within the medium is described by the sum of the field $\mathbf{E}^{(1)}$ with a second field $\mathbf{E}^{(2)}$. For simplicity the fields are considered without transverse components $\mathbf{E}_{rt} = \mathbf{E}(z, t)$. The total field within the nonlinear medium is given by

$$\mathbf{E}(z, t) = \mathbf{E}^{(1)}(z, t) + \mathbf{E}^{(2)}(z, t) \quad (1.64)$$

$$= \left(\mathbf{A}^{(1)}(z, t)e^{i(k_1z - \omega_1t)} + \mathbf{A}^{(2)}(z, t)e^{i(k_2z - \omega_2t)} + c.c \right) \quad (1.65)$$

where the complex fields are chosen with different carrier frequencies ω_1 and ω_2 . The third order non-linear susceptibility leads to a polarization

$$\tilde{P}_i^{(\text{NL})} = \sum_{ijk} \epsilon_0 \chi_{ijk}^{(2)} E_j^{(1)}(z, t) E_k^{(2)}(z, t) \quad (1.66)$$

$$\Leftrightarrow \tilde{P}^{(\text{NL})} = 2\epsilon_0 d_{eff} E^{(1)}(z, t) E^{(2)}(z, t), \quad (1.67)$$

that mixes the two waves. After carrying out the multiplication the equation shows that the susceptibility leads to sum-frequency generation (SFG), difference-frequency generation (DFG) and optical rectification (carrier frequency vanishes) (Tab. 1.1). The effective non-linear coefficient, d_{eff} , is often introduced to reduce the complexity of the notation. This quantity generally depends on the propagation direction of the beam relative to the crystal axis (see i.e. [70]).

The photon picture allows an intuitive interpretation of the processes. Considering SFG, for instance, the annihilation of the two fundamental photons creates a new photon with the sum of the energies (Fig. 1.4).

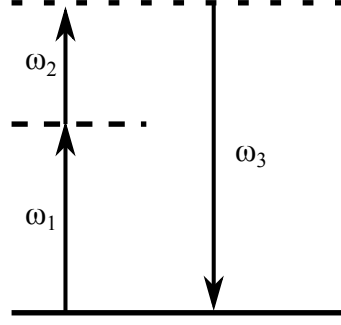


Figure 1.4.: Sum frequency generation in the photon picture.

The coupling between the three distinct fields directly reveals from equation (1.28). Considering three monochromatic plane waves of frequency ω_1 , ω_2 and $\omega_3 = \omega_1 + \omega_2$ the wave equation for each of the three fields simplifies to

$$2ik_i \frac{\partial}{\partial z'} A^{(i)}(z) = -\frac{\omega_i^2}{\epsilon_0 c_0^2} p^{(i)(NL)}(z) \quad (1.68)$$

where the second order susceptibility not only creates the field with frequency ω_3 , but also leads to mixing between the fundamental fields with the generated mixed frequency. The non-linear polarization for the SFG process (Tab. 1.1, No. 3) yields to the three coupled differential equations [71, p. 38]

$$\frac{\partial A^{(1)}}{\partial z} = i \frac{c_0 d_{eff} \omega_1}{n_{\omega_1} c_0} A^{(3)}(z) A^{(2)*}(z) e^{-i\Delta k z} \quad (1.69)$$

$$\frac{\partial A^{(2)}}{\partial z} = i \frac{c_0 d_{eff} \omega_2}{n_{\omega_2} c_0} A^{(3)}(z) A^{(1)*}(z) e^{-i\Delta k z} \quad (1.70)$$

$$\frac{\partial A^{(3)}}{\partial z} = i \frac{c_0 d_{eff} \omega_3}{n_{\omega_3} c_0} A^{(1)}(z) A^{(2)}(z) e^{i\Delta k z} \quad (1.71)$$

$$\Delta k = k_3 - (k_1 + k_2) \quad (1.72)$$

where $n_{\omega_i} = \sqrt{\epsilon(\omega_i)}$ is the refractive index of the medium at given frequency ω_i .

Assuming constant input fields in the undepleted regime ($A_1 = const.$, $A_2 = const.$), the solution for the field A_3 of the coupled system (1.69)-(1.71) is

$$A^{(3)}(z) = \frac{2i d_{eff} \omega_3 A^{(1)} A^{(2)}}{n_{\omega_3} c_0} \left(\frac{e^{i\Delta k z} - 1}{i\Delta k} \right) \quad (1.73)$$

and its intensity [Equ. (1.18)] is given by

$$I_3 \propto z^2 d_{eff}^2 \frac{\sin^2 \Delta k z / 2}{(\Delta k z / 2)^2}. \quad (1.74)$$

Nr.	$p^{(NL)}$	Frequency	Wavenumber	Name
1	$\epsilon_0 d_{eff} A^{(1)} A^{(1)} e^{i(2k_1 z - 2\omega_1 t)}$	$2\omega_1$	$2k_1$	SHG
2	$\epsilon_0 d_{eff} A^{(2)} A^{(2)} e^{i(2k_2 z - 2\omega_2 t)}$	$2\omega_2$	$2k_2$	SHG
3	$2\epsilon_0 d_{eff} A^{(1)} A^{(2)} e^{i((k_1+k_2)z - (\omega_1+\omega_2)t)}$	$\omega_1 + \omega_2$	$k_1 + k_2$	SFG
4	$2\epsilon_0 d_{eff} A^{(1)} A^{(2)*} e^{i((k_1-k_2)z - (\omega_1-\omega_2)t)}$	$\omega_1 - \omega_2$	$k_1 - k_2$	DFG
5	$\epsilon_0 d_{eff} A^{(1)} A^{(1)*}$	0	0	opt. rect.
6	$\epsilon_0 d_{eff} A^{(2)} A^{(2)*}$	0	0	opt. rect.

Table 1.1.: Terms of the second order non-linear polarization considering two initial fields at frequencies ω_1 and ω_2 . A_i^* represents the complex conjugate value of A_i .

Clearly, conversion to the sum frequency strongly depends on the phase mismatch Δk . The dependency of the generated field on the SINC-function leads to less conversion efficiency and continuous oscillations of the output intensity with respect to the propagation distance z for a non-vanishing phase mismatch. The physical explanation lies in the different phase velocities between the fundamental fields and the generated field. With proceeding propagation the emerging additional phase shift leads to destructive interference between field components that were generated at different positions within the medium. The condition

$$\Delta k = k_3 - k_1 - k_2 = \frac{2\pi n_{\omega_3}}{\lambda_3} - \frac{2\pi n_{\omega_1}}{\lambda_1} - \frac{2\pi n_{\omega_2}}{\lambda_2} = 0 \quad (1.75)$$

is known as phase matching, which from a quantum mechanical point of view is equivalent to the conservation of momentum

$$\hbar k_3 = \hbar k_1 + \hbar k_2 \quad (1.76)$$

of the three involved photons.

Phase matching generally requires birefringent crystals to achieve same phase velocities for the different frequencies. The crystal is cut with a defined angle to the optical axis to adjust the refractive index. Calculation of the angle to the optical axis is achieved with the equation [62, p. 64]

$$\frac{1}{n_\omega^2(\theta)} = \frac{\cos^2 \theta}{n_o(\omega)^2} + \frac{\sin^2 \theta}{n_e(\omega)^2} \quad (1.77)$$

that describes the refractive index of a uniaxial crystal along an arbitrary propagation direction with angle θ to the optical axis.

In this thesis SFG is used to characterize ultrashort pulses (Sec. 1.4.4).

ij	11	22	33	23,32	13,31	12,21
α	1	2	3	4	5	6
Mat.	Cut	Type	$r_{\alpha k}$ [pm/V]	V_{π} [kV]	λ [μm]	Sym.
BBO [73, 74]	Z	T	$r_{22} = 2.7$	12.5	0.2-3.5	3m
RTP [75, 76]	X	T	$r_{33} = 38.5$	2.2-2.6	0.35-4.5	mm2
	Y		$r_{33} = 35.0,$ $r_{23} = 12.5, r_{13} = 10.6$			
KDP [77]	Z	L	$r_{63} = 10.6$	14.5	0.18-1.45	2m
DKDP [77]	Z	L	$r_{63} = 23.6$	6.5	0.2-2.10	2m
LNB [77]	Z	T	$r_{22} = 6.8$	6.8	0.4-5.5	3m

Table 1.2.: Summary of important Pockels cell crystals and their properties. For the transverse Pockels cells (Type=T), the half wave voltages correspond to a $6 \times 6 \text{ mm}^2$ crystal with length 20 mm. For longitudinal Pockels cell (Type=L) crystals the voltage does not depend on the dimensions of the crystal.

1.4.2. The Pockels effect

The electro-optic effect, also known as Pockels effect, provides an important tool to switch and steer light through an optical setup. The effect causes a change of the refractive properties in non-centrosymmetric crystals if they are exposed to an electrostatic field. As nowadays electronics and computer systems control essentially all processes, the Pockels effect provides an effective interface between electronics and optics. Due to its fast response the refractive properties of the crystal follow directly the electric field as applied by the electronic components, that drive the process.

The description of the Pockels effect often bases on the impermeability tensor $\boldsymbol{\eta}$ that is the inverse of the permittivity tensor $\boldsymbol{\epsilon}$. The electric field and the displacement field are then related as

$$\mathbf{E} = \frac{1}{\epsilon_0} \boldsymbol{\eta}(\mathbf{E}) \mathbf{D}. \quad (1.78)$$

and a Taylor expansion of the impermeability tensor

$$\eta_{ij} = \eta_{ij}^{(0)} + r_{ijk} E_k^{(dc)} + \dots \quad i, j, k \in \{1, 2, 3\} \quad (1.79)$$

describes the Pockels effect with the first field dependent term, r_{ijk} . Due to the symmetry of the permittivity tensor [72, p. 666], the impermeability also fulfills the relation $\eta_{ij} = \eta_{ji}$. Thus, it is common to represent the tensor r_{ijk} with a contracted two dimensional notation $r_{\alpha k}$ where α takes the values listed in table (1.2).

Application of symmetry properties leads to vanishing components of $r_{\alpha k}$ and usually only several entries of the tensor remain that are of significance. Considering the example of β -Ba(BO₂)₂ (BBO), which is chosen as a material for the

Pockels cell inside the developed amplifier, it turns out that the crystal has a $3m$ symmetry. This class possesses only components of $r_{\alpha k}$ that are listed on the left of equation (1.80). Furthermore, the symmetry class possesses several identities [60, 71] so that the tensor simplifies to:

$$\begin{pmatrix} 0 & r_{12} & r_{13} \\ 0 & r_{22} & r_{23} \\ 0 & 0 & r_{33} \\ 0 & r_{42} & 0 \\ r_{51} & 0 & 0 \\ r_{61} & 0 & 0 \end{pmatrix} = \begin{pmatrix} 0 & -r_{22} & r_{13} \\ 0 & r_{22} & r_{13} \\ 0 & 0 & r_{33} \\ 0 & r_{51} & 0 \\ r_{51} & 0 & 0 \\ -r_{22} & 0 & 0 \end{pmatrix}. \quad (1.80)$$

With this tensor the impermeability tensor can be written as

$$\boldsymbol{\eta} = \begin{pmatrix} \eta_o - r_{22}E_2^{(dc)} + r_{13}E_3^{(dc)} & -r_{22}E_1^{(dc)} & r_{42}E_1^{(dc)} \\ -r_{22}E_1^{(dc)} & \eta_o + r_{22}E_2^{(dc)} + r_{13}E_3^{(dc)} & r_{42}E_2^{(dc)} \\ r_{42}E_1^{(dc)} & r_{42}E_2^{(dc)} & \eta_e + r_{33}E_3^{(dc)} \end{pmatrix} \quad (1.81)$$

describing the changes of crystal properties under the influence of an arbitrary electric field applied in $(E_1^{(dc)}, E_2^{(dc)}, E_3^{(dc)})$ direction. In case of BBO it can be stated that the coefficient $r_{51} = r_{42}$ is negligibly small [73] and the tensor for an applied field to the X-faces $(E_2^{(dc)} = 0)^2$ of the crystal calculates to

$$\boldsymbol{\eta} = \begin{pmatrix} \eta_o & -r_{22}E_1^{(dc)} & 0 \\ -r_{22}E_1^{(dc)} & \eta_o & 0 \\ 0 & 0 & \eta_e \end{pmatrix}, \quad (1.82)$$

which after a 45° rotation yields to

$$\boldsymbol{\eta}' = \begin{pmatrix} \eta_o - r_{22}E_1^{(dc)} & 0 & 0 \\ 0 & \eta_o + r_{22}E_1^{(dc)} & 0 \\ 0 & 0 & \eta_e \end{pmatrix}. \quad (1.83)$$

From this notation it is visible that BBO, or any other crystal with similar symmetry, becomes biaxial under the influence of the electric field. The different refractive indices

$$\Delta n = \frac{dn}{d\eta} \Delta\eta = -\frac{1}{2}n^3 \Delta\eta. \quad (1.84)$$

²To avoid issues with linear polarized light in either x- or y-direction the BBO Pockels cells are used with an electric field along the crystals X-direction. If the field is applied along the Y-direction, a linear polarized light beam oriented along one of the crystal X- or Y-axis would accidentally hit the eigenvector directions of the impermeability tensor even with applied electric field. This leads to an absolute phase shift but no polarization rotation.

then lead to a phase shift of the polarization eigenstates, which is given by

$$\Delta\varphi = \frac{2\pi n_o}{\lambda} \left(n_o + \frac{1}{2}n_o^3 r_{22} E^{(dc)} - n_o + \frac{1}{2}n_o^3 r_{22} E^{(dc)} \right) L \quad (1.85)$$

$$= \frac{2\pi}{\lambda} n_o^3 r_{22} E^{(dc)} L = \frac{2\pi}{\lambda} n_o^3 r_{22} \frac{U}{d} L \quad (1.86)$$

for a crystal of length L and thickness d . The quantity,

$$V_\pi = V(\Delta\varphi = \pi) = \frac{\lambda}{2} \frac{1}{r_{22} n_o^3} \frac{d}{L}, \quad (1.87)$$

which is known as half-wave voltage, corresponds to a rotation of the initial polarization by 90° . For $L=20$ mm and $d=6$ mm the resulting half-wave voltage of BBO is 12.5 kV (Tab. 1.2), which is large enough to cause break down in most gases. BBO is thus often implemented in a double pass configuration to reduce the voltage whilst allowing large apertures.

1.4.3. Self-phase-modulation and the Kerr effect

Due to the restriction of second order non-linear processes to non-centrosymmetric media third order processes are of increased importance being the lowest order non-linear processes in centrosymmetric media. The source for these non-linear effects is the third order susceptibility $\chi^{(3)}$ that leads to interesting effects fundamentally different as compared to the second order processes.

Besides other third order processes such as third harmonic generation or cross phase modulation (XPW) [78], for instance, the main focus is set on self-phase modulation (SPM) and self-focusing (SF) as these two processes dominate the performance of the laser system that is described in the next chapters.

The non-linear polarization [Equ. (1.8)] according to equation (1.63) for SPM and SF is

$$p_{rt}^{(NL)} = 3\epsilon_0 \chi^{(3)} A_{rt} A_{rt}^* A_{rt} \quad (1.88)$$

with A_{rt}^* being the complex conjugate electric field envelope. For a pulsed plane wave possessing a spectrum narrow enough to allow

$$\left(1 + \frac{k_1}{k_0} (\omega - \omega_0) \right) \approx \left(1 + \frac{1}{\omega_0} (\omega - \omega_0) \right) \approx 1, \quad (1.89)$$

the wave equation [Equ. (1.28)] is

$$\left[2ik_0 \frac{\partial}{\partial z'} + 2k_0 D \right] A_{r\omega} = -\frac{\omega_0^2}{\epsilon_0 c_0^2} p_{r\omega}^{(NL)}. \quad (1.90)$$

Note that this equation is still in the frequency domain. The non-linear polarization, however, is represented in the time domain, which requires the transformation into the time space. This is achieved using the equation (1.22), which simply transforms the dispersion D to \tilde{D} . The equation in the time domain is

$$\left[2ik_0 \frac{\partial}{\partial z'} + 2k_0 \tilde{D} \right] A_{rt} = -\frac{3\omega_0^2}{c_0^2} \chi^{(3)} A_{rt} A_{rt}^* A_{rt}, \quad (1.91)$$

which in rearranged form this gives

$$\frac{\partial}{\partial z'} A_{rt} = i\tilde{D} A_{rt} + i \frac{3\omega_0^2}{2k_0 c_0^2} \chi^{(3)} |A_{rt}|^2 A_{rt}. \quad (1.92)$$

The non-linear term obviously depends on the squared absolute value of the field envelope, which also defines the intensity [Equ. (1.18)]. The non-linear polarization allows intuitive interpretation if it is rewritten in terms of the intensity

$$\frac{3\omega_0^2}{2k_0 c_0^2} \chi^{(3)} |A_{rt}|^2 = \frac{\omega_0}{c_0} \frac{3}{4} \frac{\chi^{(3)}}{\epsilon_0 n_0^2 c_0} I(\mathbf{r}, t) = \frac{\omega_0}{c_0} n_2 I(\mathbf{r}, t) \quad (1.93)$$

and the non-linear refractive index n_2 is introduced as:

$$n_2 = \frac{3}{4} \frac{\chi^{(3)}}{\epsilon_0 n_0^2 c_0}. \quad (1.94)$$

This result illustrates that the non-linear polarization leads to a phase shift³ that depends on the intensity of the pulse. Being intensity dependent this phase shift will vary across the pulse following the intensity profile in time and space. In this context two processes are distinguished: SPM is the process that results from the time dependent intensity of the laser pulse. SF or self-defocussing are the counterparts in the spatial domain. The characteristic propagation length obtained from the differential equation (1.92) for both effects is defined as the inverse coefficient obtained in equation (1.93),

$$L_{NL} = \frac{c}{\omega_0 n_2 I}. \quad (1.95)$$

For the majority of materials the non-linear refractive index is positive in the optical wavelength range leading to an increased optical density of materials for higher intensities. The refractive index can thus be written as

$$n = n_0 + n_2 I(\mathbf{r}, t). \quad (1.96)$$

³see figure (3.12b), that shows almost no change of the intensity profile whilst the phase follows the intensity profile

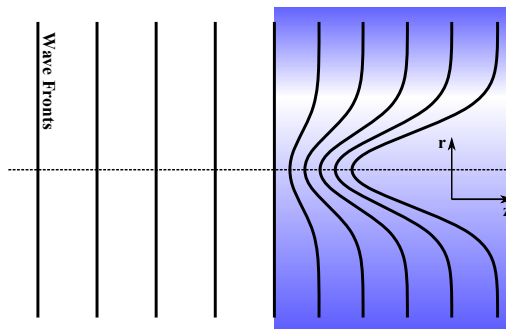


Figure 1.5.: Illustration of self-focusing. The wavefronts of a beam with Gaussian intensity profile bend due to the higher refractive index in the center of the beam.

Both effects can be prevented with a flat top profile in time (for SPM) or space (for SF) as the non-linear polarization would lead to a constant phase shift that is unimportant to the laser pulse characteristics. However, the temporal and spatial profiles often differ from a flat top shape leading to non-linear phase shifts in both time and space. Considering for example the Gaussian TEM₀₀ mode, the central part of the beam is delayed due to the positive value of n_2 . The wavefronts adjust to the Gaussian intensity of the laser mode (Fig. 1.5). Such deteriorations of the wavefronts lead to SF of the laser pulse and as the resulting wavefronts are not spherical, the mode will differ from the ideal diffraction limited beam. The latter is an increase of the M²-value of the laser beam, which is certainly an undesirable effect. In the worst case SF causes catastrophic focusing of the laser beam and if not willingly introduced leads to damage of expensive optics. The temporal phase shift in the time domain that is caused by a chirp-free pulse of the laser leads to an increase of its spectral bandwidth. SPM is widely used to produce octave spanning laser pulse spectra that allow pulse compression to single cycle durations (i.e. [22, 24]).

A quantity that is often used to describe the amount of non-linear phase accumulated by a pulsed laser beam within a medium of length L is the B-Integral:

$$B := \frac{2\pi}{\lambda} \int_0^L n_2 I dz. \quad (1.97)$$

A value of $B > 1$ describes a measure for non-linear phase distortions that alter the pulsed laser beam. The B-Integral allows quick estimation of design parameters of laser systems and reflects if non-linear phase shifts significantly affect the laser pulse. However, as this quantity embodies a strong simplification of the non-linear processes, it loses its meaning in describing laser pulses that benefit from significant non-linear phase shifts. An accurate description of the laser pulse requires the characterization of both the temporal intensity profile and the temporal phase or the spectral intensity and the spectral phase.

1.4.4. Ultrashort pulse characterization

Manipulating ultrashort laser pulses by introducing dispersion and non-linear phase shifts requires tools for accurate measurement of the affected light pulse. An effective description of the electric field is governed by the field intensity and its phase. Standard electronic devices such as photo diodes or CCDs, however, have only access to the intensity of the pulse and time resolution of modern electronics does not exceed the ~ 10 ps scale. As ultrashort light pulses range from picosecond to attosecond durations, electronic devices fail as tools to measure ultrashort pulses directly. Therefore, characterization of these events requires extra efforts and more sophisticated techniques.

The description of events in the time domain relies on sampling of the process on fractions of its duration. This is usually achieved with a “gate”, that cuts out a fraction of the event at a specific time and gives a signal proportional to the observable of interest. Temporal information is gained by moving the gate to different temporal positions relative to the event. With ultrashort laser pulses this gate needs to be an ultrashort laser pulse itself as shorter events are not available. The signal between the laser pulse and the gate is created using non-linear optical processes as they provide a fast mechanism to mix both parts together. The mixing of laser pulses with time delayed replica to imprint information on a light field allows for detection with a (slow) electronic device. Most common methods to measure ultrashort light pulses are autocorrelation, frequency-resolved optical gating (FROG), spectral phase interferometry for direct electric-field reconstruction (SPIDER), “grating-eliminated no-nonsense observation of ultrafast incident laser light e-fields” (GRENOUILLE) and streak cameras.⁴

Techniques such as autocorrelations and FROGs use a gate function, $g(t)$, to sample the electric field, $E(t)$. The chosen non-linearity defines the gate $g(t)$. The difference between the two devices is just the detection of the produced signal [80],

$$E_{sig}(\tau) = g(t - \tau)E(t). \quad (1.98)$$

As the autocorrelation measures the time integrated (slow detector) intensity of the generated signal field the resulting signal, as seen by the detection system is:

$$I_{auto}(\tau) \propto \int_{-\infty}^{\infty} |g(t - \tau)E(t)|^2 dt. \quad (1.99)$$

In case of FROG the measurement of the spectrum of the signal field yields to,

$$S_{FROG}(\tau, \omega) \propto \left| \int_{-\infty}^{\infty} g(t - \tau)E(t)e^{+i\omega t} dt \right|^2, \quad (1.100)$$

⁴A good overview over measurement techniques can be found in [79–82].

that describes a spectrum depending on the delay parameter τ . It can be shown that the spectrum of $E_{sig}(\tau)$, $S(\tau, \omega)$, provides the information to retrieve the phase and the intensity via a retrieval algorithm [80]. In contrast to FROG, the phase retrieval from the autocorrelation is impossible, which stems from the 1D-phase retrieval problem [79].

Considering now the special case of SFG as basic non-linearity used for pulse measurement, the gate function according to (1.4.1) is $g(t) = E(t)$ and the function

$$S(\tau, \omega) \propto \left| \int_{-\infty}^{\infty} E(t - \tau)E(t)e^{+i\omega t} dt \right|^2, \quad (1.101)$$

is the mathematical description of the second-harmonic frequency-resolved optical gating (SH-FROG). The auto-correlation trace can be calculated from the FROG trace $S_{FROG}(\tau, \omega)$ by integration over the spectrum:

$$I_{auto}(\tau) \propto \int S_{FROG}(\tau, \omega) d\omega. \quad (1.102)$$

A SH-FROG obviously uses the spectrogram of the sum frequency between the pulse with its time delayed copy. The advantage of shifting the measurement frequency to the second harmonic mainly lies in a good contrast. Furthermore, the second order process requires less intense pulses than a third order process. Only the phase matching condition [Equ. (1.75)] puts a constraint on the crystal thickness (Sec. 1.4.1), that needs to be thin enough to allow phase matching across the whole spectrum of the pulse.

Pulse characterization with a SH-FROG is a powerful tool to characterize pulses and their development under increasing non-linear optical phase shifts in the amplifier (Chap. 3) and the non-linear compressor (Chap. 5). However, even though SH-FROG allows retrieval of the pulse and its phase, there still exists one ambiguity, which results from the symmetry of the spectrogram meaning that $S(\tau, \omega) = S(-\tau, \omega)$. This symmetry leads to an undetermined time direction of the retrieved electric field. Luckily, most of the time the sign of the chirp is known due to extra information gathered from the properties of the materials the pulse was passing prior to the measurement. In the optical and NIR part of the spectrum materials usually exhibit normal dispersion ($k_2 > 0$). Including this information allow quick determination of the sign of the phase if other contributions with negative dispersion can be excluded. However, the time symmetry of the SH-FROG spectrogram often helps to distinguish good from corrupted measurements, because asymmetry of the spectrogram indicates issues during the measurement.

Chapter 2

Laser Pulse Amplifiers

Laser pulse amplifiers constitute a major technology to reach pulse energy levels that are not directly available with laser oscillators.¹ As the interest of this thesis lies on the construction of optical devices delivering multi-millijoule light pulses with durations < 1 ps, the only path towards reaching this goal is the amplification of existing light pulses within a laser amplifier.

Laser amplifiers manifest in a variety of technical implementations having their own area of application. To give a better understanding this chapter introduces the mechanics behind laser operation. It presents two common amplifier types and reviews their features. Because lasers appear in a rich variety of implementations, gain media and underlying mechanisms that contain gas, semiconductor, dye and solid-state lasers discussion is limited to solid-state lasers only. The main focus is thereby set on the thin-disk concept and Yb:YAG as gain material that constitute the backbone of this thesis.

2.1. Solid-state laser basics

The basic description of light that propagates through a medium of length L is given by Lambert-Beer's law

$$I(L) = I_0 e^{-(N_1 - N_2)\sigma L} \quad (2.1)$$

that describes the attenuation of light with initial intensity I_0 . The quantities N_1 and N_2 describe the population of the lower and upper state and σ is the cross section for the process. Considering this law it unfolds that light can not only be absorbed but also be amplified if the condition $N_1 - N_2 < 0$ is achieved. This condition is called population inversion and describes the basic mechanism of laser operation. The possibility to amplify light was first stated by Albert Einstein who described this process on the basis of rate equations based on the occupation of electronic states that are populated and depopulated via two basic mechanisms.

¹Other techniques such as enhancement cavities, for instance, increase the pulse energy by coherent pulse stacking with an external laser resonator (see i.e. [83]).

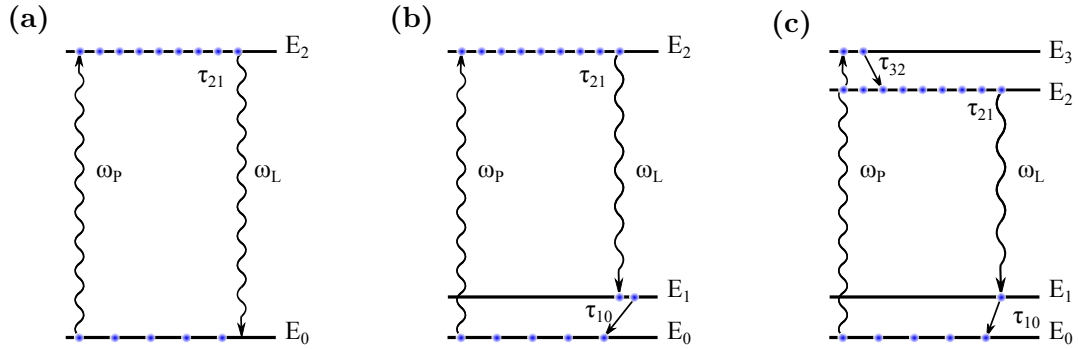


Figure 2.1.: Illustration of a two level medium (a), a three level laser (b) and a four level laser (c).

The first is stimulated emission and stimulated absorption. The second constitutes a spontaneous decay channel that effects all involved states except for the ground state. Laser materials are most commonly described as three or four level systems. This description is valid for almost all laser materials.

Solid-state lasers describe a family of materials that achieve laser operation via doping of a crystal or ceramic and are distinguished from semi-conductor lasers. Doping of these materials is achieved by replacing ions of the host material with ions of similar size but different electronic properties. The resulting artificial defects can exhibit electronic states that allow laser operation. As solid-state lasers need to be transparent to the laser radiation these materials are dielectrics, which are usually pumped optically using flash lamps or laser radiation.

In the following the basic mechanisms are illustrated on the basis of a solid-state laser material that exhibits three energy levels (Fig. 2.1b). The involved energy states of this system are the ground state with energy E_0 , the lower laser level E_1 and the upper laser level E_2 . Transitions between these states can occur both radiative or non-radiative. Laser materials possess the property that at least one transition is radiative meaning that the transition happens by emitting one photon of defined energy. In the picture of a three level laser shown in figure (2.1b) this transition is from state E_2 to E_1 and the emitted photon carries the energy

$$E_{\text{photon}} = E_2 - E_1 = \hbar\omega_L; \quad \omega_L = \frac{2\pi c}{\lambda_L}, \quad (2.2)$$

where \hbar is Planck's constant, ω is the angular frequency of the photon, λ_L its wavelength and c is the speed of light. To allow this transition the medium must be excited to the upper laser level. This process is often referred to as “pumping” and is often realized electronically or optically. As the energy difference for the transition from the ground state to the upper laser level is larger than the energy of the emitted photon, not all energy that is put into the system is extracted by

the lasing photon. This energy difference is called “quantum defect” and is usually transferred in form of heat to the laser material. As solid-state lasers are pumped optically, the quantum defect directly calculates from the energy difference between pump and laser photon energies.

The dynamics of the involved processes are described by rate equations that contain all involved states and form a coupled system of differential equations. For the three level laser of figure (2.1b) this system is

$$\frac{dN_2}{dt} = +W_{02}N_0 - W_{20}N_2 - W_{21}N_2 - \frac{N_2}{\tau_{sp}}; \quad \frac{1}{\tau_{sp}} := \frac{1}{\tau_{21}} + \frac{1}{\tau_{20}} \quad (2.3)$$

$$\frac{dN_1}{dt} = +W_{21}N_2 - W_{12}N_1 - \frac{N_1}{\tau_{10}} + \frac{N_1}{\tau_{21}} \quad (2.4)$$

$$\frac{dN_0}{dt} = -W_{02}N_0 + W_{20}N_2 + \frac{N_1}{\tau_{10}} + \frac{N_2}{\tau_{20}}. \quad (2.5)$$

The increase in population of the upper laser level is determined by the rate W_{02} describing the number of photons per second that are excited from the ground state to the upper laser level. The transition rate [62, p.220]

$$W_{ij} = \sigma_{ij} \frac{I}{\hbar\omega} \quad (2.6)$$

is equal to the cross section for the transition multiplied by the photon flux $I/\hbar\omega$ given by the intensity I and the photon energy $\hbar\omega$. Decay of states is defined by all possible transitions that reduce the population. These transitions happen both via stimulated emission and spontaneously with the decay rates τ_{ij} . The spontaneous decay time is often summarized in an effective value τ_{sp} . The signs of the terms on the right of the equation correspond to population (+) and depopulation (−) of the energy level. All transitions of one level appear on the population of corresponding level to conserve the total amount of involved states $N = N_1 + N_2 + N_3 = \text{const}$.

From basic quantum mechanical considerations it can be shown that the transition probabilities W_{ij} and W_{ji} are equal [62, p.218]. This leads to equal transition probability in both directions. Applying this to a two level system (Fig. 2.1a) the equilibrium $dN_k/dt = 0$ upper state population is given by:

$$N_2 = \frac{1}{1 + \frac{1}{\tau_{sp}W_{02}}} N_0. \quad (2.7)$$

Obviously infinite pump power and thus infinite W_{02} leads to an upper state population that is at most equal to the lower state population. The upper state population is then given by $N_2 + N_0 = 2N_2 = N$ and reaches half the total number of states N . Therefore, population inversion in two level systems is impossible and at least a third level needs to be involved.

Laser materials can possess more than 3 level allowing for increased efficiency and lower lasing threshold as neither the upper laser level nor lower level is effected by the pump radiation. A common example is the 4 level system (Fig. 2.1c). Best performance in such systems is achieved if the lifetimes of the upper level E_3 and the lower laser level E_1 are short compared to the lifetime of the level E_2 . This maximizes the inversion as the population of the laser level E_2 is directly populated with the pump radiation but not influenced by stimulated emission by the pump radiation. The level E_1 is nearly empty in this situation as depopulation to the ground state is fast. Unfortunately, these materials exhibit at least one additional non-radiative transition, which leads to a higher quantum defect and causes increased thermal load during operation. In high power systems this can significantly reduce the performance.

2.1.1. Amplification of laser pulses

A laser amplifier uses the described mechanism to amplify light, that falls into the spectral amplification bandwidth of the gain medium.

In contrast to oscillators that are build to amplify spontaneous emitted light within an optical resonator, amplifiers require an existing light source to boost its power. The increase in power P_1 after amplification relative to the power P_0 before amplification is given by the gain,

$$G = \frac{P_1}{P_0} = P_0 e^{2\alpha L}. \quad (2.8)$$

The coefficient $2\alpha = N_2\sigma_{em}(\lambda) - N_1\sigma_{abs}(\lambda)$ is the gain or absorption coefficient, σ_{em} and σ_{abs} describe the emission and the absorption cross section of the laser medium [84]. Amplification of broad bandwidth laser pulses requires consideration of the spectral response of the gain medium, which is summarized by the wavelength dependent cross sections $\sigma_{em}(\lambda)$ and $\sigma_{abs}(\lambda)$.

Once inversion is created and a photon triggers ($\sigma(\lambda_{photon}) \neq 0$) the stimulated emission process, the number of excited states N_2V (V is the volume of the laser material) reduces by one whilst the lower level population N_1V simultaneously increases by the same amount. The energy difference is transferred to a second photon similar to the incident photon. This simple picture illustrates that energy is extracted from the gain medium only if the photon falls within spectral regions, in which the emission cross section does not vanish. Furthermore, amplification of a photon leads to reduced population inversion causing a decreased gain, G , if the energy within the medium is not restored. Consequently, the gain medium can store only a defined amount of energy that is:

$$E_{Stored} = \Delta N A L \hbar \omega \quad (2.9)$$

where $\Delta N = N_2 - N_1$ is the inversion density, A is the active area and L is the length of the gain medium.

The lifetime of the upper laser level influences the maximum inversion density and, thus, effects the stored energy directly. As spontaneously emitted photons fall within the amplification band of the laser gain medium these photons are amplified corresponding to a parasitic loss channel. Amplified spontaneous emission (ASE) is an unwanted mechanism that can significantly reduce the population inversion. In laser amplifiers with high gain and long effective optical path lengths in at least one direction of the active volume of the laser gain medium this effect can become significant and leads to lower output power of the laser [85, 86].

Regarding solid-state lasers, the doping concentration determines the number of ions per volume and constitutes an important tuning parameter. Large doping concentrations are desirable to achieve high gain in a small active volume. However, with increasing doping concentration the effective lifetime of the upper laser level reduces due to quenching effects [87] and, thus, leads to lowered gain. The trade-off between maximum doping concentration and secondary effects that lower the effective gain leads to the best performance.

Important characteristic parameters of gain media are the saturation intensity, I_{sat} and the saturation Fluence, F_{sat} ,

$$I_{sat} = \frac{\hbar\omega}{\tau_{sp}\sigma_e} \quad (2.10)$$

$$F_{sat} = I_{sat}\tau_{sp} = \frac{\hbar\omega}{\sigma_e} \quad (2.11)$$

$$\alpha = \alpha_0 \frac{1}{1 + \frac{I}{I_{sat}}}, \quad (2.12)$$

that are related to the emission cross section of the material, the photon energy and the effective life time τ_{sp} . The saturation intensity describes the intensity, at which the amplifier gain coefficient, α , will reduce to half of its low intensity or unsaturated value, α_0 . Being just a function of laser material properties these quantities relate fundamental material characteristics to design parameters of the laser amplifier.

2.1.2. Resonators

Resonators constitute the heart of oscillators, regenerative amplifiers and even interferometers [88]. Resonators exist in a rich variety of configurations containing important parameters that influence the characteristics of the amplifier.

The ABCD-matrix formalism [Equ. (1.45)] [66] provides a simple and fast method for calculating optical resonators (Appx. B) [84, 89]. The resonator design condition according to equation (1.45) is equivalent to requiring

$$q = \frac{Aq + D}{Cq + D}, \quad (2.13)$$

which is the eigenvalue equation for a stable resonator. The solutions to this equation [84, p. 816]

$$\frac{1}{q_{1,2}} = \frac{D - A}{2B} \pm \frac{1}{B} \sqrt{\left(\frac{A + D}{2}\right)^2 - 1}, \quad (2.14)$$

need to be complex to form a Gaussian beam according to equation (1.44). This leads to the inequality

$$-1 < \frac{A + D}{2} < 1 \quad (2.15)$$

that describes stable resonators. Interestingly the stability condition does not depend on the other parameters of the ABCD-matrix (B.1). The stability condition, however, states solely that a Gaussian beam according to the eigenmode equation (2.13) exists. Misalignment sensitivity in linear resonators with a variable element (i.e. thermal lens), however, relates to the coefficient $1/|C|$ [89]. It can be shown that linear resonators possess two stability regimes [89], that are defined according to their misalignment sensitivity parameter $1/|C|$ [89]. The condition $C = 0$ defines the stability edge $(A + D)/2 = +1$ of the resonator. Such resonators are prone to mechanical disturbances [89, 90]. The other edge defined by $B = 0$ exhibits higher stability against misalignment of optical elements [89].

Changing the refractive power of an optical element within the resonator leads to a change of the resonator matrix and thus to a change of $(A + D)/2$. At a certain point the resonator reaches the stability edge. In linear resonators, for any varying optical element with changing refractive power, two stable zones can be found that fulfill equation (2.15). These two zones are generally not connected meaning that transition from one zone to the other incorporates an unstable resonator configuration in between. It is, however, possible to connect them in special configurations [91]. The two zones are generally distinguished by the misalignment sensitivity parameter $1/|C|$ meaning that one stability zone is less prone to misalignment of optical elements than the other. Resonators running in the zone less prone to misalignment generally exhibit smaller beam waist on the end mirrors [91]. This is particularly problematic for high pulse energy operation.

The point of dynamical stability of the resonator relates to the mode waist $(1/e^2)$ on the variable element via [91]

$$\Delta(1/f) = \frac{2\lambda}{\pi} \frac{1}{w^2} \quad (2.16)$$

where $\Delta(1/f)$ describes the refractive power changes of the variable element that are acceptable for the stability condition (2.15). This implies that a large mode radius inevitably leads to higher sensitivity of the resonator with respect to changing refractive powers of optical elements. Therefore, resonators with large mode sizes, demanding operation in stability *zone II* to avoid small beam waists, require stabilized temperature and environment conditions to allow for stable operation.

Interestingly, the Gouy phase shift for one resonator round trip is given by the matrix elements A and D with [92]

$$\Delta\xi = \arccos\left(\frac{A+D}{2}\right) \quad (2.17)$$

leading to a connection between the stability condition and the longitudinal phase accumulation of the Gaussian beam within the laser resonator. As the Gouy phase is a measure for the propagation of the Gaussian beam through its focus the accumulation of this phase can be interpreted as the partial propagation of the beam through the focus. A Gouy phase shift corresponding to $\Delta\xi = 0$ can thus be interpreted as propagation similar to a plane wave with infinite lateral extension, which of course is no confined eigenmode solution. This stability edge is shown to be increasingly sensitive to misalignment which is expected whereas the misalignment sensitivity at other edge $((A+D)/2 = -1)$ does not diverge [90].

2.1.3. Gain narrowing

The spectral dependent cross sections lead to varying gain for photons of different frequency. In laser amplifiers photons with energy equal to the peak of the cross section exhibit highest gain, whilst photons with lower or higher wavelengths are less amplified. Repeated application of this wavelength dependent gain leads to spectral narrowing of the pulses. The reduction of the bandwidth depends on the overall gain and is known as “gain narrowing”. For an emission cross section that has a full width at half maximum (FWHM) bandwidth of $\Delta\omega_a$ and a Lorentzian profile, the bandwidth of the amplified output pulses,

$$\Delta\omega_{3dB} = \Delta\omega_a \sqrt{\frac{3}{10 \log_{10} G(\omega_a) - 3}}, \quad (2.18)$$

depends on the total gain $G(\omega_a)$ of the amplifier at the peak of the emission cross section at ω_a [84, p.281]. Gain narrowing in high gain amplifiers often leads to unwanted decrease of the spectral bandwidth of the output pulses causing an increase of the pulse duration after amplification, i.e. [35, 56].

2.1.4. Chaotic pulse energy

Resulting from the lifetime of the upper state laser level it may occur that the initial state of the gain medium is not fully restored before the next pulse arrives. This is strongly pronounced, if a pulse significantly depletes the population inversion whilst the following pulse arrives at times comparable to the lifetime of the upper state of the amplifying medium. In these amplifiers the energy of the output pulse depends on the inversion state influenced by all preceding pulses. These dynamics can lead to unpredictable inversion levels of the gain medium resulting in chaotic behavior of the output pulse energy. Depending on the initial parameters the pulse energy undergoes characteristic bifurcations and chaotic regimes [93, 94].

Several publications prove that stable operation of lasers in intermediate bifurcations is possible [95, 96]. However, operation in these regimes complies with other constraints on pump intensity, seed input energy and acceptable peak intensity during the amplification process.

Yb:YAG amplifiers operating with repetition-rates at ~ 0.1 MHz are less influenced by this effect. Instabilities appear only, if the seed pulse is coupled inefficiently to the resonator or the carried energy is $\ll 1$ nJ (Fig. 3.23).

2.2. Yb:YAG thin-disk amplifiers

Solid-state laser materials are most commonly used in a rod geometry and are pumped longitudinally. Due to the moderate heat conduction of most of the used materials, this geometry leads to radial symmetric temperature profile with highest temperature in the center of the rod. The inhomogeneous heat load causes stress and thermally induced changes of the refractive index (thermal lensing). The radial differences cause mode distortions ultimately leading to degradation of the laser beam quality. In approaching output powers of $\gg 10$ W concepts have been developed that reduce unfavorable thermal changes of the gain medium.

2.2.1. The thin-disk concept

In consequence of all these challenges discussed, nowadays, the most promising concepts in high average power lasers amplifiers are fiber laser [97], slab lasers [31], cryogenically cooled lasers [50] and thin-disk [32, 98] lasers. All concepts have proven to be well scalable in average power and crossed the 1 kW frontier during the last years [33–35, 50, 53].²

The thin-disk concept [32] allows for exceptional high peak powers (GW) during the amplification process. These devices reach this outstanding performance due to the thin amplification medium (usually < 200 μm) that allows reduction of

² [50] is actually a cryogenically cooled thin-disk laser

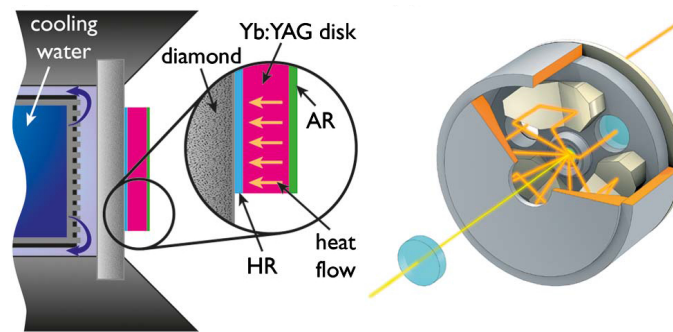


Figure 2.2.: The concept of a thin-disk laser. A heat sink (diamond/copper) cooled with water from the back side allows 1D-heat removal from the thin-disk. The thin-disk acts as an active mirror with an AR coated front and a HR coated back (left, Picture from [38]). Pump light cavity incorporating several passes to excite the thin-disk in the center of the setup (right, Courtesy of TRUMPF Laser GmbH).

non-linear optical phase introduced by the gain medium to a minimum. In view of reaching the ultimate limits in ultrashort pulse amplification, the thin-disk concept incorporates the basis of this thesis. The thermal management applied in the thin-disk concept relies on a 1D-heat flow reducing thermal lensing and stress induced changes of the gain medium to a minimum. A water cooled heat sink (usually copper/diamond) allows for efficient removal from the gain medium. The heat sink is attached to the high-reflective (HR) coated back side of the thin-disk. An anti-reflection (AR) reflection coating on the front of the thin-disk permits implementation of the gain medium as active mirror (Fig. 2.2). Due to the thin-gain material efficient pump light absorption is usually not possible within a single pass through the gain medium. In thin-disk lasers this is overcome with an imaging system that guides the pump beam several times over the thin-disk. To achieve efficient absorption and allow laser operation the coatings of the thin-disk match for both pump light and laser wavelengths [32].

As opposed to rod lasers this concept allows average power scaling by increasing the thin-disk and pump spot diameter. The essential mechanism and the 1D heat flow persists for lateral scaling. The most important limitation of this concepts constitutes ASE within the thin-disk [86] that increases the path length inside the gain medium for spontaneously emitted photons with increasing lateral extension of the pumped region. This ultimately leads to reduction of the effective upper state life time [99] and is particularly important for low repetition-rate lasers operating with saturated gain. Nevertheless, thin-disk lasers have crossed the kilowatt average power level whilst providing single-mode beams and ultrashort pulses [33, 35] The pulse energy reached values of more than 1 J at several hundreds of hertz [50]. Further scaling to several tens of kilowatt output power is considered to be possible [86, 98].

The thin laser gain medium of disk lasers puts higher requirements on the gain material as compared to other geometries, so that a

- high emission cross section σ_{em} ,
- long fluorescence lifetime τ_{sp} ,
- high tolerable doping concentration,
- high pump absorption cross section σ_{abs} and
- high mechanical strength

are favorable properties. The first three features directly effect the achievable gain of the thin-disk, which is necessary to reach significant gain within the ~ 0.1 mm thin gain medium. Same applies to pump light absorption. The higher the absorption cross section the lower the required amount of passes for efficient absorption. High mechanical strength of the laser material allows for high quality cutting, polishing and coating of the thin material. In addition, a robust material is necessary for attaching the material to the heat sink with high optical quality.

2.2.2. Properties of Yb:YAG

Laser materials exhibiting high thermal conductivity, a low thermal expansion coefficient and a low quantum defect are generally advantageous for operation in high power systems. Furthermore, excitation of the laser material with wavelengths that are accessible with commercial laser diodes allows highly cost efficient and reliable pumping of the medium. Yb-doped glasses, crystals or ceramics possess these advantages. Over the past decade, lasers based on Yb-doped materials have been repeatedly demonstrated with outstanding performance in a variety of different laser architectures. Partially, the success can be attributed to the superior properties of the Ytterbium ion.

The Yb³⁺-ion

The Yb³⁺ ion has a two level electronic structure with the $^2F_{7/2}$ ground state and the $^2F_{5/2}$ excited state. Under the influence of a surrounding crystal field, the two states split into four ($^2F_{7/2}$) and three ($^2F_{5/2}$) stark shifted sub-level (Fig. 2.3a), providing the necessary richness of energy states for laser operation [59]. The small energy splitting of the sub-level states results in a remarkably low quantum defect but also leads to thermal occupation of the lower stark manifolds. The occupation of the lower laser level (619 cm^{-1}), causes Yb-doped systems to require high pump intensities to reach inversion of the material and leads to higher laser threshold. The ever decreasing prices of laser diodes with kilowatts of average power, however, led to increasing success of Yb-doped laser materials over the past decade in a variety of configurations [29, 31, 98, 100].

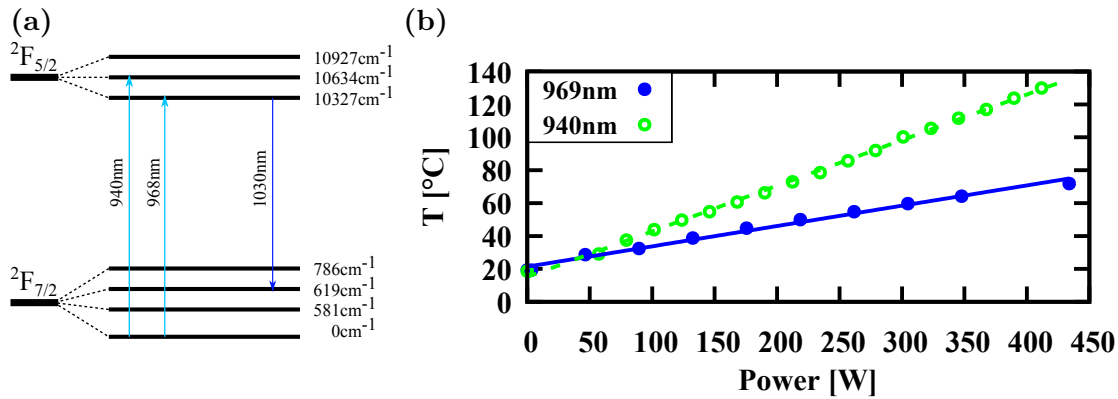


Figure 2.3.: (a) Energy levels of Yb^{3+} in yttrium aluminium garnet [102]. (b) Measured temperature vs. pump power of an Yb:YAG thin-disk pumped at 940 nm (dashed) and 969 nm (solid) with pump spot diameter of ~ 3.3 mm.

Yttrium aluminium garnet (YAG) as host material for Yb^{3+}

Nowadays, the most developed host material for the Yb^{3+} ion is YAG. The involved laser level for Yb:YAG are depicted in figure (2.3a). Yb:YAG possesses two pump bands that can be accessed with 969 nm and 940 nm InGaAs laser diodes that nowadays can provide output powers of more than 10 kW. The quantum defect for 940 nm and 969 nm amounts to 9% and 6%. Therefore, operation of Yb:YAG with 969 nm pump diodes allows decreasing the thermal load to a minimum. The transition is often referred to as “zero-phonon line” meaning the direct transition from the ground state to the excited state without the need for phonon excitation. Figure (2.3b) shows a temperature (FLIR A645sc IR-Kamera) measurement of a thin-disk pumped at the two different wavelengths under equal conditions. The narrow bandwidth of the zero-phonon line (Fig. 2.4b), however, requires more expensive wavelength stabilized diodes. Such diodes implement volume Bragg gratings that provide a selective feedback of a narrow band spectral component to force operation of the laser diode at this wavelength [101]. Wavelength stabilized diodes reach bandwidths of less than 0.5 nm and powers of several kilowatts.

Besides the beneficial spectroscopic properties of Yb:YAG it possesses a good thermal conductivity (Tab. 2.1) and the plain two level manifolds of the Yb-ion permit high doping concentrations without causing parasitic effects that reduce the effective life time of the upper laser level and thus the laser performance [103]. The YAG crystal is isotropic leading to simple optical usability of the crystal. Furthermore, the relatively large emission cross section and a long upper state lifetime support high gain, which makes the material an ideal choice for operation in thin-disk lasers. Because of the aforementioned properties, Yb:YAG is nowadays widely implemented in these laser architectures.

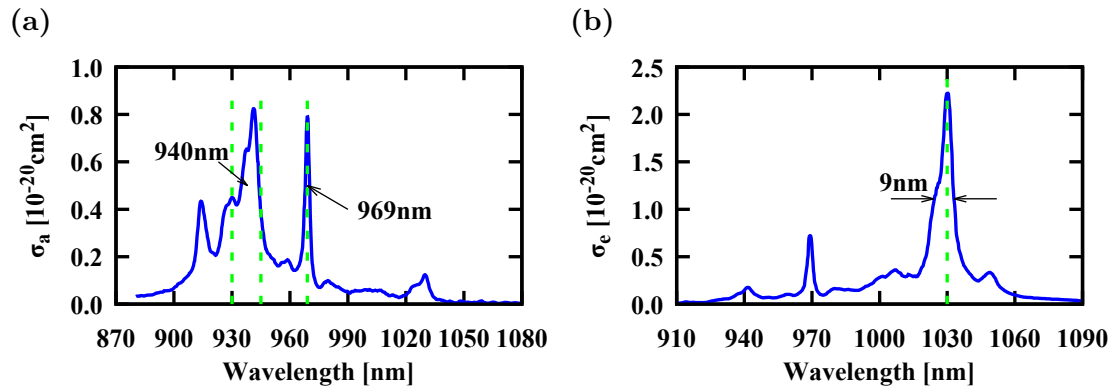


Figure 2.4.: Absorption (a) and emission (b) crosssection of Yb:YAG [36].

Material	λ_L [nm]	λ_p [nm]	σ_e [10^{-20}cm^2]	$\Delta\sigma_e$ [nm]	τ_{sp} [ms]	F_{sat} [J/cm^2]	κ [$\text{W}/\text{m} \cdot \text{K}$]
Yb:YAG	1030	940, 968	2.2	9	0.950	8.8	6 (10 %at.)
Yb:LuAG	1030	940, 968	2.8	5.5	0.985	6.9	7.5 (10 %at.)
Yb:Lu ₂ O ₃	1033	976	1.3	12.5	0.82	14.8	10.8 (3 %at.)
Yb:CaF ₂	1053	980	0.78	~40	1.9	24	5.4 (3 %at.)
Ti:Sa	800	532	41	>200	$3.2 \cdot 10^{-3}$	0.61	33 (0.1 %at.)

Table 2.1.: Properties of laser materials. λ_L : Central emission wavelength; λ_p : Pump wavelength; κ : Thermal conductivity; Sources Yb:YAG, Yb:LuAG [36], Yb:Lu₂O₃ [113, 114], Yb:CaF₂ [36, 115], Ti:Sa [116]. Elaborated list in [26].

Comments on other hosts and Ti:Sa

Other host materials such as ceramics [104], Lu₃Al₅O₁₂ (LuAG) [105–108] or Lu₂O₃ are promising candidates for kilowatt laser operation. Ceramic lasers are nowadays rarely found in high power ultra-short laser systems because of their immature optical quality [104]. Yb:Lu₂O₃ has been demonstrated to deliver ultra-short pulses of 740 fs duration at 140 W [109]. and recently ~500 fs at ~90 W were demonstrated [110]. The performance of this material is attributed [110] to the high thermal conductivity (2.1) and the low thermal expansion coefficient ($\alpha = 5.9 \cdot 10^{-6} \text{ 1/K}$ [111]), which are compared to YAG ($\alpha = 7 \cdot 10^{-6} \text{ 1/K}$ [112]) slightly superior. In addition, the emission bandwidth of Yb:Lu₂O₃ is larger and leads to shorter output pulses as compared to Yb:YAG. Table (2.1) summarizes selected laser materials for comparison.

It can be seen that Ti:Sapphire (Ti:Sa) is an outstanding material exceeding Yb:YAG in both heat conduction and emission cross section. However, the implementation of Ti:Sa in the thin-disk configuration for high power operation is challenging due to the requirement of high pump powers at 514-532 nm, which are

not easily available [26]. Moreover, the relatively small absorption cross section of Ti:Sa at these wavelengths requires intense pumping and/or a thicker medium that does not necessarily comply with the thin-disk concept. The large quantum defect contributes to significant heating of the gain material, which certainly limits performance even in thin-disk configuration [26, 117, 118].

As compared to Ti:Sa ultra-short Yb:YAG amplifiers suffer from a narrower amplification bandwidth. As a result millijoule level Yb:YAG laser amplifiers operating at room temperature usually provide gain narrowed pulses with 1-2 ps duration if no special efforts are being implemented. However, as demonstrated in mode locked Yb:YAG oscillators Yb:YAG supports pulses with ~ 100 -300 fs duration. Unfortunately, the pulse energy of oscillators is still limited to the $\sim 100 \mu\text{J}$ level and scaling towards the millijoule level is not within sight for the next decade [100]. Compensation of gain narrowing in amplifiers has been demonstrated by pre-shaping of the spectrum [119–121]. Exploiting non-linear optical effects during the amplification constitutes a method that broadens the bandwidth during the amplification process [57, 58, 122]. Despite the bandwidth limitation of Yb:YAG, pulse durations of 5 fs are possible – but not yet realized – with a non-linear compression stage after amplification (Chap. 5). This concept holds promise for producing single cycle pulses with several millijoule pulse energy at repetition-rates of ~ 100 kHz that will be discussed in chapter (5) of this thesis.

2.3. Regenerative amplifiers

Regenerative amplifiers represent a group of amplifiers that trap the pulse in a stable laser resonator to guide it through the amplification medium several times. An optical switch allows coupling of the pulses to the optical resonator. Due to the properties of the resonator, regenerative amplifiers support fundamental mode operation if the resonator is well designed. If this condition is met, any input beam will – on the expense of losses – adjust to the resonators eigenmode after a certain amount of round trips inside the laser resonator. Thus, regenerative amplifiers support intrinsically good beam quality factors, which is essential for most experimental applications.

Regenerative amplifiers can achieve enormous gain (10^9) because of the adjustable number amplification iterations through the gain medium. Depending on the desired repetition-rate of the laser amplifier it is possible to choose the duration of the amplification cycle until the gain medium is depleted or other constraints require an interruption of the amplification process.

The optical switch emerges as the most important part of regenerative amplifiers as in its absence coupling of pulses to the resonator would fail. Being indispensable, it constitutes a major object for design and optimization. Optical switches in state of the art regenerative amplifiers are implemented using electro-optically active

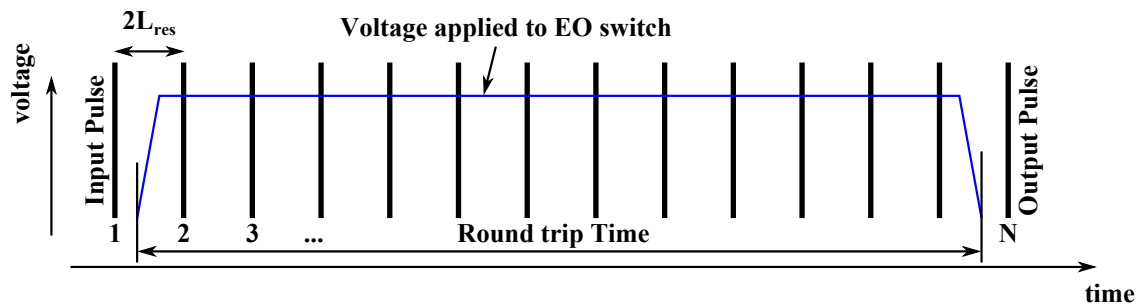


Figure 2.5.: Illustration of the amplification cycles within a regenerative amplifier. Switching of the electro optical switch traps the input pulse from the second cycle on.

crystals that exhibit the Pockels-effect. Such crystals allow changes of the polarization state by applying a voltage to the crystal. Together with a polarizer they permit beam path changes depending on the applied voltage. Obviously, an optical switch based on a crystal constitutes a transmissive optical element located within the optical resonator. Despite of anti-reflective coatings this element introduces at least two additional surfaces within the optical resonator leading to increased losses. In amplifiers reaching intensities that start non-linear optical processes the switch may contribute significantly to the non-linear phase shift and, therefore, to self-focusing (SF). SF can lead to damage of optical elements within the amplifier and certainly needs to be avoided. Thus, it is desirable to reduce the thickness of the crystal to a minimum. Depending on the Pockels cell crystal this condition leads to technical limitations of the the output energy of the amplifier caused by restrictions of the Pockels cell crystal.

The Pockels-effect is divided into two basic mechanisms that relate to the direction of the applied electric field relative to the propagation direction of the incident beam. If the electric field is applied longitudinally, the faces of electrodes need to be placed perpendicular to the optical beam path. As transmission of light through conductive materials is connected to large losses, electrodes for longitudinal Pockels cells have ring shapes allowing for transmission through their center. As the applied half wave voltage does not depend on the crystal length, these Pockels cells theoretically support short crystal lengths (< 1 mm). This would be particularly advantageous for high power ultra fast regenerative amplifiers. Unfortunately, ring electrodes in combination with large apertures and a thin crystals lead to inhomogeneous electric fields across the aperture of the crystal, which results in inhomogeneous polarization rotation and degraded contrast. Plasma electrode Pockels cells (PEPCs) solve this problem using a plasma across the crystal surface [123]. Based on KD_2PO_4 (DKDP) these devices are promising candidates for scaling the apertures of Pockels cells. However, to this day their use is limited to systems with low average powers due to the sol-gel [124] anti-reflection coating [125]. Transverse

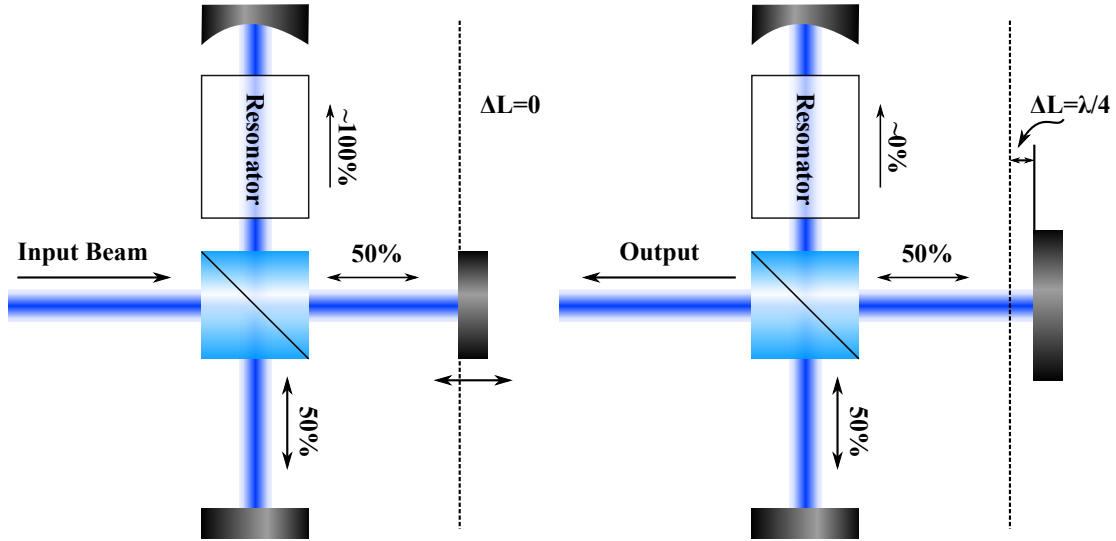


Figure 2.6.: Interferometric switch based on a Michelson interferometer as a part of a laser resonator.

Pockels cells allow usage of the full aperture of the crystal, but the length of the crystal determines the rotation of the polarization at given voltages. As the applied voltage needs to be below the breakdown, the crystal thickness has a minimum value that can not be easily reduced.

Alternatives to Pockels cell crystals are mechanical devices that allow switching without the necessity for transmissive elements. However, due to the speed of light these devices need to change the state within the time scale of one resonator round trip (10-100 ns). Ideas such as rotating wheels containing mirrors at certain positions to reflect the beam in and out of the resonator. These wheels need to rotate extremely fast $\sim 40000 \text{ min}^{-1}$ whilst the size of the mirror needs to be in the range of $\sim 100 \mu\text{m}$ [126]. These parameters put hard demands on the mechanics, vacuum conditions are required and the device is prone to optical damage due to the small aperture of the mirror.

Concepts based on interferometric switching grant another option but the short time to change the state of the switch applies to these devices as well. Assuming a Michelson interferometer within the resonator, the optical path length of one arm relative to the other requires a movement of $\lambda/4$ to switch one arm from constructive to destructive interference. The opposite applies to the other arm (Fig. 2.6). At $1 \mu\text{m}$ wavelength this corresponds to $250 \mu\text{m}$. The transition time of $t = 10\text{-}100 \text{ ns}$ then leads to an acceleration of $a = 2s/t^2 = 10^{10}\text{-}10^{12} \text{ m/s}^2$. The force applied to a $1/2"$ mirror with $m = 2g$ is $F = ma > 2 \cdot 10^7 \text{ N}$ and leads to a pressure of $> 39 \text{ GPa}$ exceeding the ultimate tensile or compression strength of glass

or even stainless steel by several orders of magnitude.³ Thus, implementation of an interferometric switch would rely on other techniques to change the relative optical path length of the interferometer arms. Clearly, this is leading back to the initial point of considering an electro-optical switch or a rotating wheel, for instance.

Having no alternative to replace the Pockels cell crystal several different common materials can be considered. A summary of these materials is given in table (1.2). The only suitable material for high power laser amplifiers is currently β -Ba(BO₂)₂ (BBO) permitting high average power, low Piezoelectric ringing and sufficient contrast [74, 77, 128]. Unfortunately, the crystal poses a high half-wave voltage 25 kV (Sec. 1.4.2) for a 12x12x20 mm³ crystal and apertures of high quality crystals are limited to these dimensions.

In thin-disk regenerative amplifiers, the Pockels cell crystal embodies the main source for non-linearities constituting the bottleneck of the amplifier device. Chapter (4) describes a method to circumvent this issue and explains a method for energy scaling of thin-disk regenerative amplifiers in the high peak intensity ($> 5 \text{ GW/cm}^2$) regime.

2.4. Multi-pass amplifiers

Multi-pass systems embody a group of laser amplifiers that rely on optical beam displacement to guide a beam several times through the gain medium. Beam guidance is usually achieved with high reflective mirrors. As every pass through the gain medium requires a new displaced path, such systems grow quickly in size and complexity with the number of required transitions. However, multi-pass amplifiers allow amplification without transmissive optics except for the gain medium and, hence, constitute the ultimate tool for amplification to high pulse energies. Particularly, the thin-disk concept reduces the amount of transmissive material and has been realized to the Joule level pulse energy [50, 129, 130] and at kilowatts average power [33]. Due to the low amount of material these amplifiers allow for amplification at exceptionally high peak intensities and do not necessarily require the implementation of chirped-pulse amplification (CPA) even at millijoule output pulse energies in thin-disk amplifiers.

Guidance of the beam thorough the gain medium can be distinguished into two different types:

1. Imaging Systems
2. Non-Imaging Systems.

³Carbon nanotubes would withstand these high demands [127]. But implementation of high reflective mirrors solely made of carbon nanotubes is rather difficult.

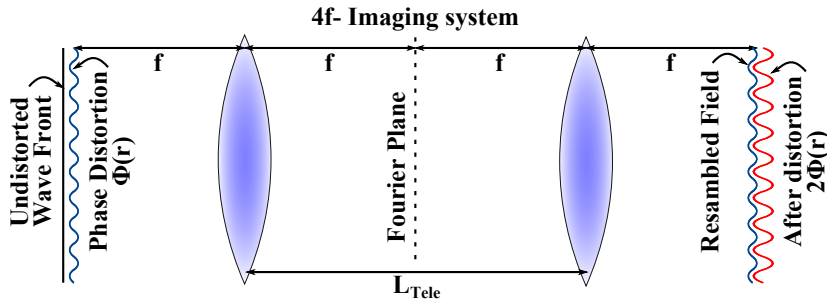


Figure 2.7.: Illustration of a 4f-imaging system with phase distortion. The undistorted input field accumulates phase distortions after propagation through the system.

Non-imaging systems guide the beam through the setup without implementing a special optical system. These systems solely rely on displacement of the beam such that the beam passes the gain medium several times. Imaging systems implement a more sophisticated optical system to transfer the beam to another position whilst keeping beam size and shape unchanged at a chosen plane. Similar to other optical imaging systems, the transfer is achieved with lenses or mirrors. Because of their recreational characteristics, these systems are often referred to as relay-imaging systems. Imaging systems have the advantage that distortions introduced at the imaging plane have no effect on the shape of the laser beam in the subsequent imaging planes. The constant beam shape at position of the gain medium then ensures a well defined overlap with the active region in the gain medium. Unfortunately, the beam is not only described by its shape but also by its wavefront and distortions introduced at the imaging plane will imprint on the wavefronts. Considering a 4f-imaging system (Fig. 2.7) propagation can be described by the Fourier transform at the “Fourier plane” and the field at the end of the system by the second application of this theorem. The two fold application yields to exact resemblance of the field behind the two lenses. The phase distortions $\phi_{dist_{p1}}(\mathbf{r})$ at one imaging plane will, therefore, be added to phase distortions $\phi_{dist_{p2}}(\mathbf{r})$ at the other. In case of systems that implement one and the same optic at the imaging planes of such optical setups, these distortions are equal and add up. The output field after two passes

$$A_{out_2}(\mathbf{r}) = A_{out}(\mathbf{r}) e^{i\phi_{dist}(\mathbf{r})} = A_{in}(\mathbf{r}) e^{2i\phi_{dist}(\mathbf{r})} \quad (2.19)$$

accumulates these distortions, which leads to degraded beam quality. This is visible in M^2 -measurements or directly visible if the beam profile is recorded at positions different from the imaging plane. Consequently, imaging multi-pass amplifiers that implement the gain medium at the imaging plane demand high quality optics to avoid beam quality degradation.

Considering a refractive element with focal length f_L on the left side of figure (2.7) the imprinted spherical wavefront appears on the right side of the system. The same focusing element will add the same phase to the existing beam and accumulation continues through the system. This phase leads to a beam that continuously grows on one imaging optic and focuses on the other and can lead to high fluences on at least one imaging optic (Fig. 4.8a). Often these systems implement corrections to compensate for accumulated focusing effects and resulting unwanted mode alterations. This is possible as refractive optics imprint well defined wavefront distortions that can be corrected by adjusting the telescope length L_{tele} . The condition $q_{out} = q_{in}$ in combination with the single elements of the optical system M_i

$$\prod_i M_i = \begin{pmatrix} A & B \\ C & D \end{pmatrix} \stackrel{!}{=} \pm \begin{pmatrix} 1 & 0 \\ 0 & 1 \end{pmatrix}. \quad (2.20)$$

is called q-preserving and implies preserved waist size and wavefront of the beam.

Chapter 3

Direct Amplification of Femtosecond Pulses in Non-linear Thin-Disk Regenerative Amplifiers

Ytterbium laser amplifiers have so far relied on chirped-pulse amplification (CPA) to deliver multi-millijoule pulse energies with gigawatt peak powers. These systems are usually conceived to avoid non-linear optical effects during the amplification process. CPA systems such as Ytterbium fiber laser amplifiers [30, 43], Yb:YAG thin-disk amplifiers [98, 131, 132] and Yb:YAG Innoslab amplifiers [31] deliver multi-millijoule pulse energies at repetition-rates from a few kHz to several hundred kHz. Additionally, cryogenic Yb:YAG amplifiers have proven to deliver multi-millijoule pulses [49] and recently crossed the joule pulse energy barrier [50]. These architectures provide pulse durations of ~ 200 fs (fiber) or < 0.4 ps-3.6 ps (thin-disk, Innoslab and cryogenic systems) and are rapidly proliferating as drivers for non-linear pulse compressors and OPCPA systems with kilowatts of average power [34, 35, 53].

In Yb-fiber systems implementation of CPA is essential due to their small mode area [126]. Transition to gigawatt peak powers and multi-millijoule pulse energies is possible but requires coherently combined systems [43, 133]. Chirped-pulse Yb:YAG Innoslab and thin-disk amplifiers can operate with larger modes, introduce less material and, therefore, amplification to pulses with gigawatt peak powers after compression is straightforward. Thin-disk amplifiers provide lower single-pass gain than the other systems and are commonly implemented in regenerative amplifiers to achieve high overall gain. Regenerative amplifiers, however, require an optical device that traps the pulses for the amplification process inside the resonator. Resonators in regenerative amplifiers have typical lengths of a few meters to provide enough time for changing the resonators state within one round trip of the pulse. Still the time scales on which the switch has to react is not more than ~ 10 -100 ns. Opening and closing the resonator at these time scales is commonly achieved with Pockels cells. Unfortunately, the switches suitable for high average power operation have lengths of 10-30 mm and clear apertures of only $\sim 12 \times 12$ mm

resulting in significant amount of material with a considerable non-linear refractive index. Despite the thin (~ 0.1 mm) gain medium, thin-disk regenerative amplifiers usually implement CPA to avoid non-linear optical effects introduced by the Pockels cell crystal. Implementing CPA in Yb:YAG amplifier systems is expensive and contributes to instabilities due to the required large-aperture gratings for stretching and/or compression. The grating compressor unit introduces timing jitter, which requires stabilization in optical parametric chirped-pulse amplification (OPCPA) systems [134] and carrier-envelope-phase (CEP) stable sources [135]. Despite the technological improvement of dielectric gratings that achieve efficiencies of $> 97\%$, the four reflections lead to losses of $\sim 10\%$.

In this context avoiding CPA in Yb:YAG amplifiers is worth considering to improve the cost-efficiency, stability and to provide a user-friendly system. Due to the thin gain medium, thin-disk amplifiers constitute an ideal basis for amplification without CPA [33, 58]. Regenerative amplifiers provide high gain and excellent beam quality. Therefore, a combination of the thin-disk concept with a regenerative amplifier is – despite the necessary optical switch (Sec. 2.3) – the ideal setup for CPA-free amplification of pulses with nanojoule pulse energy to the millijoule level.

The main focus of this chapter is set on the question whether amplification up to the multi-millijoule level avoiding chirped pulses is possible. It turns out that amplification of Fourier limited femtosecond pulses within the developed Yb:YAG thin-disk regenerative amplifier actually benefits from accumulation of non-linear phase overcoming the gain-narrowed spectral bandwidth limitation (~ 1 -2 nm) of Yb:YAG amplifiers.¹ This chapter provides a general description of the amplification process with repetition-rates in the kilohertz regime of pulses up to > 1 GW peak power. Details of the non-linear behavior of the amplifier without effects arising from average power contributions are discussed in the first part. Section (3.6) then focuses on scaling the repetition-rate and average power at constant output pulse energies and describes the developed amplifier in its current state.

3.1. The seed laser architecture and amplifier setup

The setup for seeding the amplifier (Fig. 3.1) consists of a commercial Menlo Orange fiber oscillator delivering 100 mW output power at 100 MHz repetition-rate. The corresponding pulse energy amounts to 1 nJ. A pulse picker reduces the repetition-rate of the seed pulses according to the desired value and allows switching with repetition-rates of up to 100 kHz. The pulse picker consists of a commercial

¹A similar concept was developed in parallel to this work and is described in [57] on the basis of negatively pre-chirping the input seed pulses.

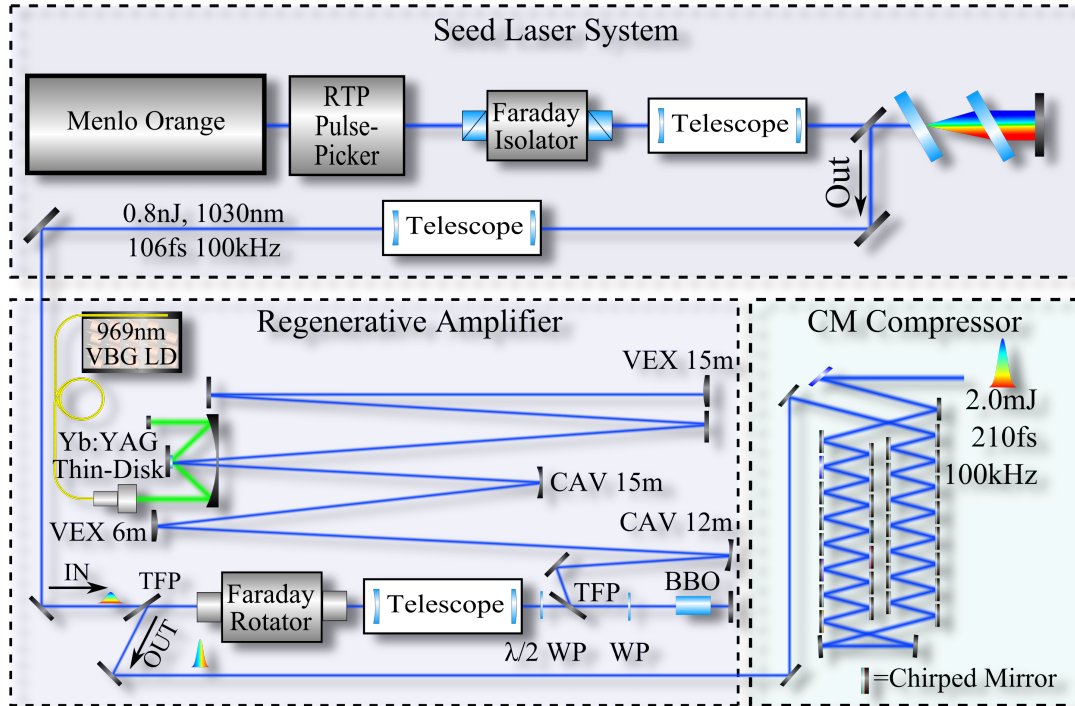


Figure 3.1.: Amplifier setup of the final 100 kHz system. Seed system based on a commercial Menlo Orange fiber laser. Pulse picker operates with repetition-rates between 5 kHz-100 kHz. Small grating compressor removes the chirp of the Yb-fiber oscillator. The amplifier input unit consists of a Faraday rotator a mirror telescope, a $\lambda/2$ waveplate, the thin-film polarizer of the resonator and the Pockels cell.

driver Bergmann Messgeräte Entwicklung KG including a 4x4 mm X-Cut rubidium titanyl phosphate (RTP) crystal. For protection against back reflection an optical isolator selects the pulses after the pulse picker.

To seed the amplifier with Fourier limited pulses, a small grating compressor with 1000 lines/mm removes the chirp of the seed laser pulses as provided by the manufacturer. This allows applicability of results to other laser sources emitting unchirped pulses. Figure (3.2) shows the retrieved second-harmonic frequency-resolved optical gating (SH-FROG) spectrum and the pulse of the seed after the grating compressor.

The second telescope enlarges the beam to a size of 9 mm ($1/e^2$) providing a large mode area in the Faraday rotator of the regenerative amplifier. This reduces the intensity after amplification to a minimum and exploits the 20 mm clear aperture of the device (Sec. 3.2.2). Mode matching to the resonators eigenmode is achieved with a mirror telescope after the rotator. The optical switch of the amplifier consists of a β -Ba (BO₂)₂ (BBO) Pockels cell in combination with a thin-film polarizer (TFP)

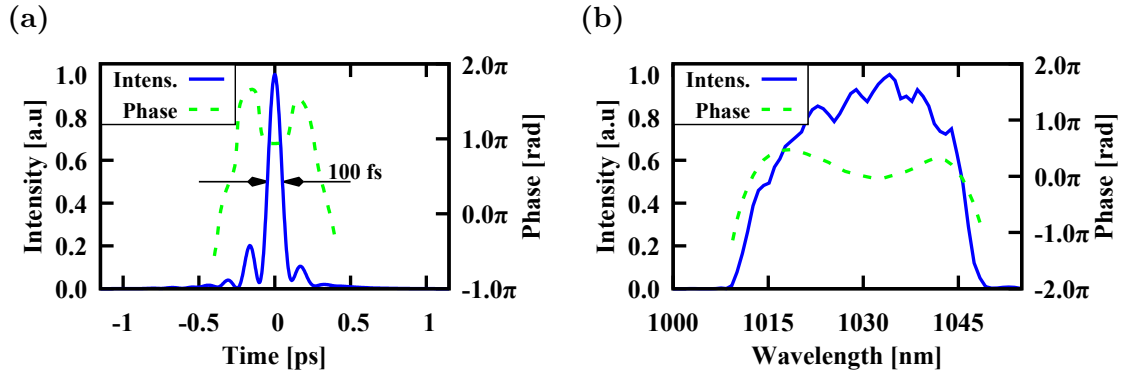


Figure 3.2.: Retrieved SH-FROG measurement of the compressed nearly Fourier limited seed pulse. (a) Field envelope and phase. (b) Spectrum and spectral phase.

and a wave plate and is capable of trapping the pulses with an extinction ratio of $>300:1$.

An optical isolator consisting of a Faraday rotator and a TFP separates the pulses entering the regenerative amplifier from those that exit. After the isolator the pulse passes a wave-plate to turn the polarization matching the transmissive state of the TFP of the resonator. For the low repetition rate experiments of a $12 \times 12 \times 15 \text{ mm}^3$ BBO Pockels cell was used. In the 100 kHz final system the Pockels cell crystal has the dimensions $12 \times 12 \times 20 \text{ mm}^3$. The reason for the to the larger crystal lies in industrial availability of the crystal with these dimensions that is commonly used in industry. The enhanced optical quality of the crystal as provided by TRUMPF Laser GmbH exceeded the advantages of shorter crystal with lower optical quality. In combination with a wave plate the Pockels cell traps the pulses inside the resonator by applying $\sim 12\text{-}14.5 \text{ kV}$ to the crystal. The Pockels cell driver is a commercial high voltage device provided by Bergmann Messgeräte Entwicklung KG that allows switching of the Pockels cell within $\sim 15 \text{ ns}$.

The thin-disk, provided by TRUMPF Laser GmbH, has a radius of curvature of $\sim 20 \text{ m}$ and is pumped into the zero-phonon line with a TRUMPF 969 nm Volume-Bragg-Grating stabilized pump diode module. The imaging system of the fiber collimation and the parabolic mirror of the pump light cavity produces a pump spot of $\sim 4.1 \text{ mm}$ on the thin-disk.

After the amplifier a compressor removes the introduced chirp resulting from the accumulated non-linear phase inside the amplifier. Pulse compression is realized with a chirped mirror compressor.

This is the basic amplifier scheme used throughout this work. The details of the amplifier configuration are explained in those parts where significant changes as compared to the system in (Fig. 3.1) are made.

3.2. Amplifier design considerations

Seeding a regenerative amplifier with femtosecond pulses requires careful consideration of critical design parameters. As described in section (2.1.3), the amplification bandwidth of Yb:YAG leads to narrowing of the spectrum. Considering the spectrum of the seed pulses it is obvious that gain narrowing reduces the spectral bandwidth and increases the transform limited pulse duration. For pulse energies lower than $100 \mu\text{J}$, the output pulse duration is $\sim 1\text{-}1.5$ ps.

It is important to obtain a quantitative measurement for the damage threshold of optical elements at these pulse durations. Knowledge of this quantity provides an important upper bound for acceptable fluences within the resonator of the regenerative amplifier.

3.2.1. Damage threshold of optics

Radiative damage of bulk dielectrics with laser pulses that exceed 20 ps pulse duration is generally accepted to be caused by energy transfer of heated conduction band electrons to the crystal lattice. The deposited heat ultimately causes destruction of the crystal lattice due to melting of the material. The energy per unit area (fluence) [Equ. (1.19)] that damages bulk dielectrics decreases with the square root, $\tau^{1/2}$, of the laser pulse duration τ . This decrease corresponds to the characteristic time scale of energy transfer from electrons to the lattice during the laser pulse [136, 137]. At the transition to the ultrashort regime (≤ 20 ps) fused silica exhibits a damage fluence of $\sim 6 \text{ J/cm}^2$ [136, 137]. On ultrashort time scales the mechanism differs fundamentally as the conduction band electrons gain energy much faster than they are able to transfer to the lattice. The damage of the material, results from field induced photoionization and the subsequent avalanche that is created by the heated electrons [136, 137]. The plasma formation subsequently leads to a coulomb explosion of the material and a strongly localized damaged region (Fig. 3.4b). In this region the damage fluence decreases slower as with $\tau^{1/2}$.

Damage threshold measurements of multilayer mirrors are often carried out with Q-Switched Nd:YAG lasers with 4-10 ns pulse duration. The results from these measurements are not directly transferable to the picosecond or femtosecond time scale due to the deviation from the $\tau^{1/2}$ scaling of the pulse duration. Correct design of the Yb:YAG laser amplifier requires the measurement of the damage fluences with laser pulses of duration similar to the femtosecond-picosecond pulses that appear during the amplification process.

The measurement of the damage threshold (Fig. 3.4) was carried out using the uncompressed 1.2 ± 0.1 ps pulses of the 5 kHz system that is described in the next sections of this chapter. The setup (Fig. 3.3) consists of a $\lambda/2$ -waveplate and a thin-film polarizer to control the power of the laser at the target position. The laser beam is focused with 1000 mm convex lens to a $1/e^2$ beam diameter of $200 \mu\text{m}$.

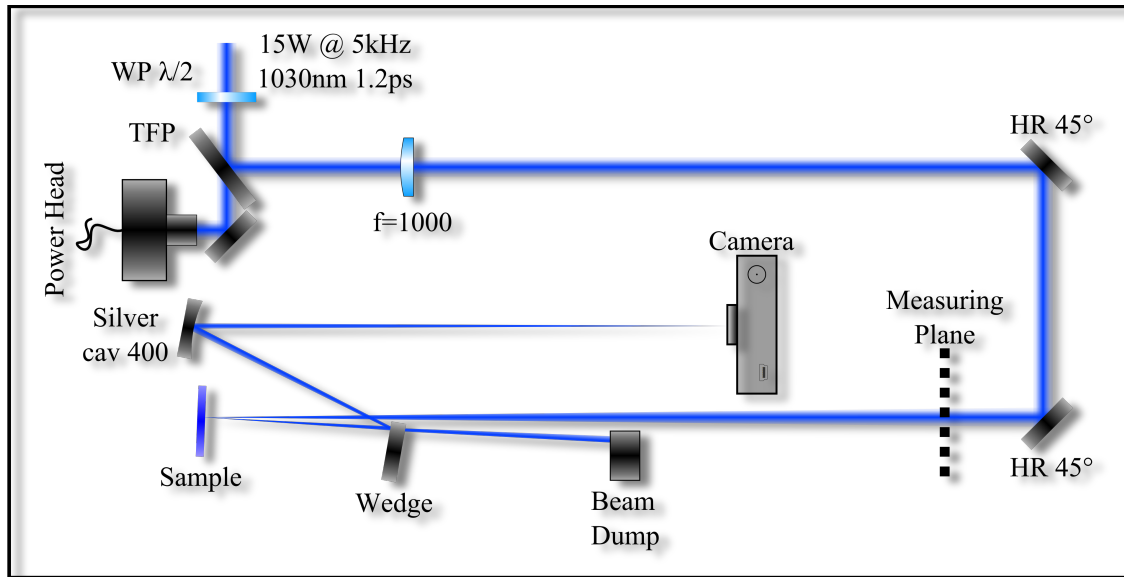


Figure 3.3.: Setup used for measuring the damage threshold. The fluence on the target is controlled by power adjustment with a $\lambda/2$ -waveplate (WP) and a TFP.

The laser beam profile in vicinity of the focus was recorded using a WinCamD beam profiler. The comparably weak focusing of the laser beam leads to a Rayleigh range of 3 cm, which reduces the systematical error emerging from inaccuracies of the sample position with respect to the recorded beam profile. This error is estimated from recordings of the beam profiles 5 mm in front and behind the target position. The resulting differences in the peak fluence give an upper limit of the error caused by misplacement of the optical element (Appx. C). Power monitoring behind the TFP allowed careful adjustment during the measurement. The measurement was performed by increasing the power stepwise every $\sim 20 - 30$ s until the optic was destroyed. After the damage occurred the power meter was placed at “measuring plane” (Fig. 3.3) to obtain an accurate power measurement at position of the target. Increasing the power until damage occurs defines a single value of the damage fluence at a specific spot of the optic. Moving the mirror and repeating the measurement leads to a set of data points that was used to determine the damage threshold. Figure (3.4) depicts the result for two high reflectors designed for an angle of incidence of 0° from different manufacturers and a highly dispersive chirped mirror. In this figure all measurements are summarized and for each mirror the probability of damage is defined as the number of damages at the given fluence relative to the total number of measurement points.

The high reflectors damage at fluences of $1.1 \pm 0.1 \text{ J/cm}^2$ and $1.60 \pm 0.07 \text{ J/cm}^2$. Interestingly, the optic with lower damage fluence also exhibits a less steep rise of the damage probability. This indicates inferior optical quality across the surface as

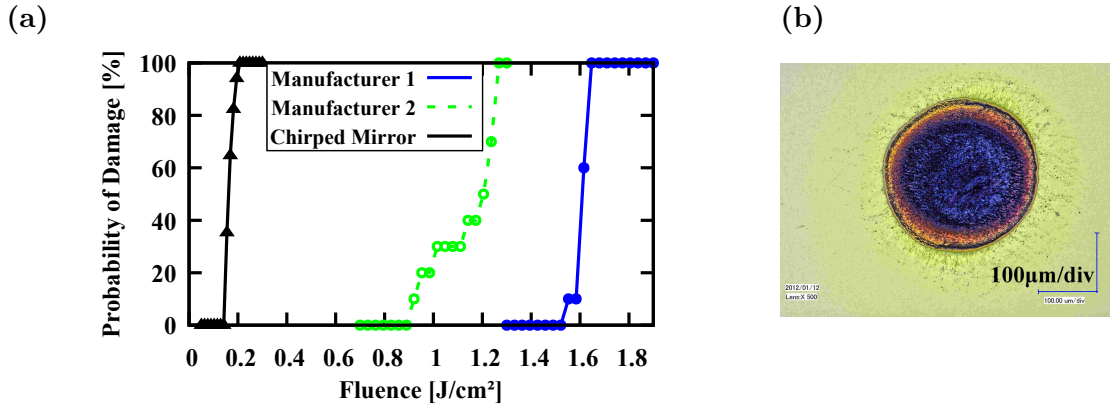


Figure 3.4.: (a) Measurement of the damage threshold of standard optical elements with picosecond pulses delivered by lasers in our laboratory. (b) Typical surface damage of a high reflector caused by picosecond pulses. The size of the damages spot is equal to the mode size of the laser.

compared the the other optic. With regard to the damage threshold of fused-silica (FS) the mirrors damage at comparable energies indicating good quality in both cases. The highly dispersive chirped mirror has a significant lower damage threshold $0.165 \pm 0.015 \text{ J/cm}^2$, which can be explained by the much higher complexity of the layer structure [138]. Still these mirrors exhibit sufficiently high damage fluences to be used in 4 mJ laser sources with beam diameters of $>2 \text{ mm}$. However, during compression experiments (Sec. 3.5) the mirrors damaged at lower fluences. The damage was caused by average powers effects at $\sim 10 \text{ W}$. The mirrors heated up and damaged within the time frame of 10 s - 30 s.

The measured fluences set an absolute upper limit to the acceptable fluences in the laser system at kilohertz repetition-rates. Within laser resonators of regenerative amplifiers, the pulses travels several (10 to >100) times over the same optic. Thus the optic experiences repetition-rate in the MHz level. Due to the higher repetition-rates the damage fluence significantly reduces due to average power effects that are caused by accumulated thermal heating of the lattice [139]. For a laser amplifier providing 2 mJ picosecond pulses a resonator based on high reflectors, therefore, should exceed a minimum beam diameter, d_{min} , of

$$E = 2 \text{ mJ}; \quad F = 1.6 \text{ J/cm}^2; \quad \kappa = 0.3 \quad (3.1)$$

$$d_{min} = 2 \cdot w_0 = 2 \cdot \sqrt{\frac{2 \cdot E}{\pi \kappa F}} = 1.0 \text{ mm}. \quad (3.2)$$

The factor κ accounts for the reduction of the damage fluence due to the MHz repetition-rate inside the laser resonator [139]. The factor of 2 in front of the pulse energy E results from the assumed a Gaussian intensity profile (Sec. D.2). In gene-

ral it is possible to achieve a single-mode beam with diameters of a few millimeters on every optic within a laser resonator. However, laser resonators operating at 1 μm wavelength easily tend to exhibit smaller beam diameters. This needs to be carefully considered in the resonator design and leads to increased length of the resonator [140].

The damage fluences of the mirrors are below the saturation fluences of Yb:YAG (Tab. 2.1), which means that energy extraction within a single pass through the material is not possible at these pulse durations. Therefore, it is necessary to extract the energy via several passes leading to average power saturation of the medium. Efficient extraction of the stored energy at amplifier repetition-rates below the kilohertz regime – picosecond pulses – is problematic because of the increasing pulse energy that is necessary to saturate the medium [18, p. 551].

3.2.2. Non-linear optical elements

The measured damage fluences correspond to intensities of $> 100 \text{ GW/cm}^2$. The accumulated non-linear phase of transmissive optical elements that are exposed to laser pulses with these intensities is significant and leads to self-phase modulation (SPM) and self-focusing (SF). Transmissive optics within the Yb:YAG thin-disk amplifier are:

- the host material of the gain medium, yttrium aluminium garnet (YAG),
- the optical switch, BBO,
- the material of the Faraday rotator (single pass), terbium gallium garnet (TGG),
- FS and quartz (TFP and wave plates)
- and the surrounding gas.

Table (3.1) summarizes the characteristic parameters of the different materials and gives values for the B-Integral [Equ. (1.97)] that a Gaussian pulse with 5 mJ, 1 ps duration and 4 mm $1/e^2$ -diameter (80 GW/cm^2) acquires. Clearly, BBO and TGG contribute the most to the non-linear phase. However, the pulse usually passes the TGG crystal only once with high energy after the amplification process. Fortunately, the clear apertures of the Faraday rotators reach 20 mm and adjusting the beam to match the aperture allows reduction of the non-linear phase contributed by this element. BBO does not allow an increase of the beam diameter (Sec. 2.3) and the pulse passes the crystal every resonator round trip leading to the main cause of non-linear phase. Experiments show that the actual contribution of the BBO is less severe (Sec. 3.4).

Medium	n_2 [10^{-16} cm ² /W]	λ [nm]	B(L)-Integral @ 80 GW/cm ²
YAG [141]	6.5	800	B(0.2 mm) = 0.063
BBO [142]	5.6(o) 2.3(e)	1064	B(40 mm) = 11(o)
TGG [143]	17.2	1064	B(20 mm) = 16.8
Fused Silica [144]	2.7	1064	B(10 mm) = 1.3
Air (1 bar) [145]	$2.4 \cdot 10^{-3}$	800	B(10 m) = 1.2

Table 3.1.: Non-linear refractive index of important optical components and the B-Integral for characteristic lengths. Assumed: Gaussian pulse with energy 5 mJ; mode diameter 4 mm; pulse duration 1 ps; $\lambda=1030$ nm.

From table (3.1) the contribution of air seems to affect the laser pulse only minorly, but the caustic of the resonator eigenmode usually has places where the diameter is much smaller than the assumed 4 mm. This can lead to large non-linear phase shifts particularly if the eigenmode exhibits a small focus. Section (3.4.1) uncovers this effect by directly comparing the output pulses under vacuum conditions and normal pressure in air.

3.3. Beneficial resonators and limitations

The measurements and thoughts carried out in the previous section contain all necessary information to choose a proper resonator design. The conditions in order of importance are:

1. a mode diameter at the active medium that matches the pump spot,
2. a mode diameter filling the aperture of the Pockels cell,
3. mode diameters as large as possible in between optics to reduce the non-linear contribution of air.

It is well known that the Gauss-Hermitian polynomials constitute solutions to resonator designs that fulfill the stability constraint discussed in section (2.1.2) [84, p. 643]. Consequently a resonator that supports a certain TEM₀₀ mode also supports all higher order Gauss-Hermitian modes. As the existence of higher order mode leads in most cases to instability and mode competition stable laser operation and a well defined mode is only possible if higher order modes are carefully suppressed.

Constraining laser resonators to the fundamental mode, requires a well matched fundamental mode to apertures within the resonator. Due to the increasing spatial spread of the Gauss-Hermitian eigenmodes with increasing order, apertures generally cause higher losses of higher order modes. Thus, matching the fundamental

mode to the approximate size of apertures within the resonator leads to fundamental mode operation. The pump spot embodies the most important aperture in the described system. A well matched resonator TEM₀₀ mode not only ensures operation with fundamental mode but also contributes to the final efficiency of the system.

The second constraint reduces the amount of non-linear phase contributed by the optical switch. Obviously, the amplifier runs below its capabilities if the eigenmode of the resonator is chosen smaller than the largest possible mode as supported by the optical switch. BBO of sufficiently high optical quality can be grown with apertures of 12x12 mm² and lengths of 20 mm. This limits the mode diameter to at most 5 mm-6 mm (1/e²). Operation with larger modes showed significant degradation in stability of the laser system at average powers > 20 W, which is caused by heating of the crystal holder. Crystals as short as 15 mm were used in the early stages of the system. Unfortunately, the optical quality of those crystals was too low to operate the laser with millijoule pulse energies and optical damage was observed much below 1 mJ. It would, however, be interesting to examine the laser performance with shorter crystals, as current Pockels cell drivers provide the necessary voltages for crystals of ~15 mm length and electrical breakdown in air is not expected up to 20 kV.

3.3.1. Large eigenmode resonators

In general, the mode shape within the resonator is arbitrary and only determined by the implemented optical elements. To develop and characterize resonator designs a numerical tool (Appx. B) has been developed that includes functions to analyze the resonator design using Monte-Carlo simulations to estimate the uncertainty resulting from imperfect optics and allows for adjustment of variable parameters.

Designing resonators that match the aforementioned constraints without introducing small beam waist on the mirrors or in the space between the mirrors is directly connected to using mirrors with large radii of curvature. This is based on basic properties of Gaussian beams and it is the purpose of this section to explain this fact.

Wavefronts of the fundamental mode are expressed via the radius of curvature (RoC) [Equ. (1.41)] that has its minimum

$$R_{min} = R(z_R) = \frac{2\pi w_0^2}{\lambda} \quad (3.3)$$

at one Rayleigh range, z_R , distance to the beam waist. This radius depends only on the wavelength and the waist diameter of the beam. For a beam of $w_0 = 1$ mm at $\lambda = 1030$ nm the minimal curvature is $R_{min} = 6.1$ m. Placing curved optics within a Gaussian beam leads to addition of the inverse RoC of the Gaussian beam and the inverse RoC ($1/R_{mirr}$) of the mirror. This directly leads to the conclusion that a

Gaussian beam with a flat wavefront possesses the radius of curvature of the optical element at this position and, therefore, the resulting beam has at most the waist size of

$$w_{0_{max}} = \sqrt{\frac{R_{mir}\lambda}{2\pi}}. \quad (3.4)$$

This most intuitively becomes visible at the end mirrors of linear resonators. At these positions the mode is – by definition – reflected back into itself and the end mirror defines the RoC of the beam. Hence, a concave mirror yields a focus in front of the optical element and a convex mirror does the opposite. The latter provides an effective method to avoid a beam waist shortly before the end mirror of the resonator. If the eigenmode to the configuration exists, the mirror also defines the largest waist $w_{0_{max}}$.

A more general picture is given in figure (3.5) that describes the most general case for a Gaussian beam with a focusing element and a fixed beam diameter at this position. In context of the resonator design that needs to match the conditions mentioned above, the pictures show a resonator eigenmode with the constraint that the beam radius at the mirror/disk w_D needs to be 1.8 mm.² This condition restricts the beam waist to a certain size at a defined distance whereby – without loss of generality – only the solutions having a waist position left of the focusing optical element are considered (the other half is obtained by switching left and right sides). In figure (3.5a) the situation for two beam waists at position d_1 and d_2 is shown. Clearly, the larger the distance to the focusing optical element, the larger the beam waist to match the beam radius constraint at the mirror/disk. The calculation of the resulting beam waist depending on three different values of the focal length f of the optical element (mirror/disk) and the input beam waist (Fig. 3.5b) reveals the mode behavior. Starting with the input beam waist versus the distance from the mirror/disk (Fig. 3.5b, blue) the output waist size for the different RoCs is increasing to reach a maximum equal to the waist size w_D . This corresponds to a collimation of the beam with the mirror/disk. For the two smaller radii, the point of collimation coincides with the focal length. For the last 10 m radius, the point is shifted due to the comparable values of the RoC of the optic and the Rayleigh range of the beam.

Considering the important question whether the optic is suitable for the resonator it is necessary to look at planes before (Fig. 3.5a, P1) and after (Fig. 3.5a, P2) the focusing element. These fictive planes can correspond to either optical elements or points of interest. As in experimental conditions, facing the aforementioned mode diameters and average powers, the distance between curved optics always reaches the order of ~50-70 cm. These planes are assumed to be fixed at 0.7 m distance from the focusing element. The beam waists at these planes are depicted in figure

²This is the aimed beam radius at the thin-disk for the 4.1 mm pump spot diameter.

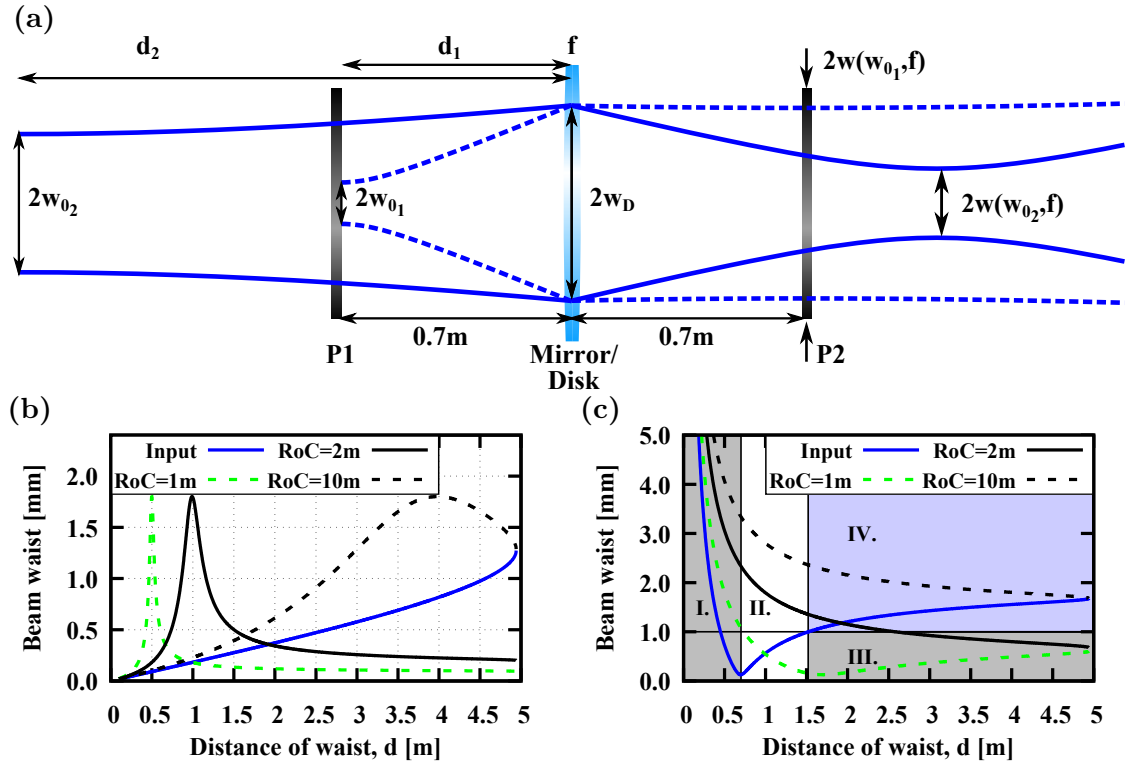


Figure 3.5.: (a) Schematic picture of the considered configuration. P1 and P2 define planes of interest the distance d is a free parameter defining the waists w_{0_x} with a fixed mode radius at a mirror or thin-disk w_D . (b) Calculated input beam waist (blue) depending on the distance of the waist to the mirror/disk d . The other curves show the output waist size for different curvatures of the mirror/disk element. (c) The beam radius in P1 for the input beam (blue). The other curves describe the mode at P2 depending on the distance d of the input waist to the optical element mirror/disk. Note that for the given mode size of 1.8 mm there exists no Gaussian beam with a waist further away than ~ 5 m.

(3.5c). The waist on the left side at P1 describes a decreasing mode size in area “I.”, which corresponds to a waist between the plane P1 and the mirror/disk. This, however, would violate the constraint that foci need to be avoided within air. In region “II.” waists are too small on P1 leading to damage of an optical element that is placed there. Within zones “III.” and “IV.” the beam waists at P1 are sufficiently large. In zone “III.”, however, the output beam waist at P2 exceeds the minimal diameter. Only zone “IV.” fulfills all conditions and shows that optical elements with less than 1 m RoC do not fulfill the conditions at all. For the 2 m mirror/disk a small region between 1.5 m and 2.5 m is acceptable but constrains the mode to < 1.5 mm radius. In conclusion, resonator designs that support large mode radii of > 1.5 mm require mirrors exceeding a RoC of 2 m.

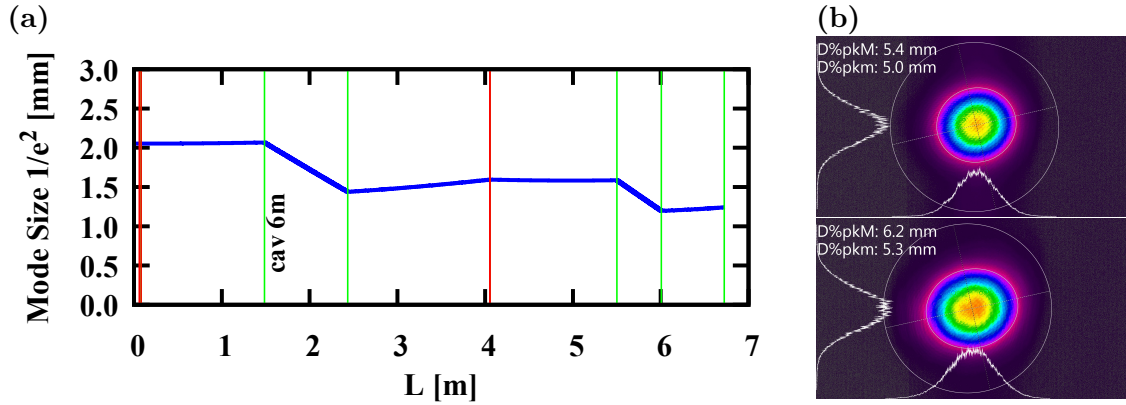


Figure 3.6.: Calculated resonator mode (a). Vertical lines: position of curved mirrors (green), the BBO (red, left) and the thin-disk (red, right). Low power CW output modes (b) exhibiting a significant mode change when the cav 6m optic is exchanged by an optic with the same specified value.

In the experiment resonator designs supportive for high energy operation always turned out to require optics with low refractive powers (5-20 m), which is justified by this arguments and also leads to the conclusion that flat thin-disks with RoC of ~ 20 m are necessary.³

3.3.2. Imperfect optics in optical resonators

Mirrors with radii of curvatures in the range of a few tens of meters are commercially available so that resonators of the required type can be easily constructed. Many years of building resonators have shown that this task is much more complicated due to one very important but rather obvious fact: The curvature of the mirrors deviates to some extent from the stated value. For this purpose a Michelson interferometer was built that had been calibrated with two mirrors of 4 m ($\pm 0.5\%$) RoC. Measurements of several optics reveal that curved mirrors deviate by up to 7% from the specified value. The tolerances of mirrors are usually specified by the manufacturer and vary from 4 m ($\pm 0.5\%$) (± 0.0025 dpt) to 15 m ($\pm 5\%$) (± 0.0067 dpt). Unspecified optics turn out to exhibit larger tolerances.

The uncertainty caused by implementing several curved optics has tremendous influence on the actual resonator properties. Figure (3.6) shows the resonator that has been used for testing the influence of two different mirrors on the resonator eigenmode. Exchanging the first curved optic (cav 6m #3 in (3.2)) from one manufacturer by a curved optic specified with cav 6m by another manufacturer led to a

³Standard thin-disks available in 2011 had RoCs of 2-4 m. It was quickly realized that resonator design is more flexible with thin-disks that have lower refractive powers.

#	Component	Shape	RoC [m]	Dist. [mm]	Beam \varnothing [μm]	Tol RoC [%]
01:	Mirror	flat	Inf	–	4105	0
02:	BBO	–	–	60	4106	–
03:	Mirror	cav	6	1406	4133	1.5
04:	Mirror	vex	4	948	2877	1
05:	Thin-Disk	cav	22	1621	3188	20
06:	Mirror	cav	4	1447	3173	1
07:	Mirror	vex	3	506	2393	0.75
08:	Mirror	cav	15	717	2482	3.75

Table 3.2.: Resonator parameters.

mode diameter significantly larger (Fig. 3.6, lower profile) than resulting from using the original mirror (Fig. 3.6, upper profile). As this test was performed with low average powers (~ 4 W) in continuous-wave (CW) operation, this change resembles the effect of the mirror, only.

This simple experiment impressively shows that deviations of the refractive power of optics can not be neglected. Thus, for analyzing a resonator that consists of several curved optics a Monte-Carlo simulation reveals helpful to estimate the success of a resonator design. Figure (3.7) depicts the distribution of the stability parameter and the beam diameter at the left side of the resonator described in figure (3.6) and (3.2). This distribution was calculated using 10000 normally distributed values of the refractive power having a standard deviation of 0.005 dpt. The tolerances of 0.005 dpt relate well to the stated values given by the manufacturer and result in the relative tolerances shown in table (3.2). The uncertainty of the thin-disk is estimated with 20 % accounting for changes produced by the pump light (thermal lensing and thermal expansion).

The resulting distribution shows the spread of the output mode reaching from 3.8 mm mode diameter up to 4.7 mm. The expected resonator design (without considering the tolerances) resulting in 4.1 ± 0.1 mm mode diameter is reached with only 37 % probability. In the experiment this reveals problematic as the design rarely hits resonator parameters of the physicist's volition.

It is important to note that the profiles as depicted in figure (3.6) are larger than the simulation predicts. Actually, the simulation has no configuration that fits the size of the measured eigenmode. This is a strong indicator for operation in multi-mode regime that might result from bad mode matching of the TEM_{00} mode at the thin-disk.

The sensitivity of the resonator to the uncertainty of the curved optics is indeed significant and requires careful measurement and adjustment of the resonator to reach the exact design parameters. For this purpose an interferometer and a M^2

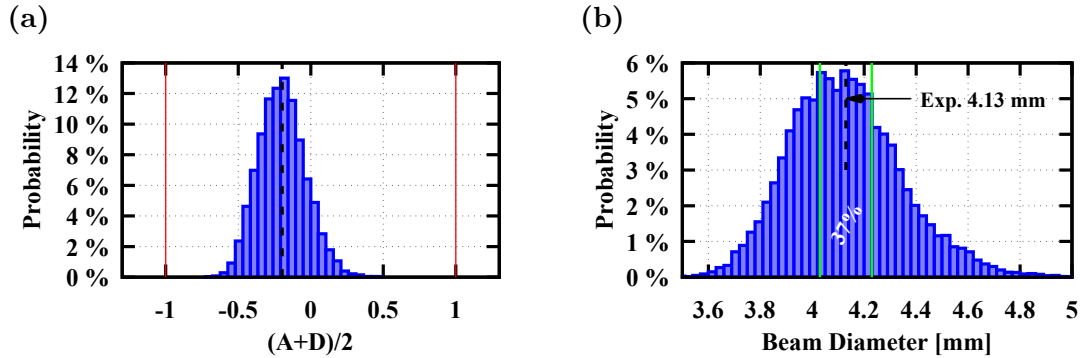


Figure 3.7.: Monte-Carlo simulation with 10000 values of normal distributed curvatures with the parameters of table (3.2). (a) Distribution of the stability parameter of the resonator. (b) Distribution of beam radii on the left side of the resonator (Fig. 3.6). Expectation value $2w_0=4.13$ mm.

meter are helpful tools to adjust the resonator. A reliable resonator design with curved optics in the 10 m range requires careful specification of the tolerances to decrease the spread of resonator output parameters. Furthermore, fine adjustment of the resonator design is necessary. Additionally, validation of single-mode operation is recommended to distinguish between multi-mode and single-mode operation.

The importance of achieving single-mode operation for a well working non-linear amplifier turned out to be fundamental for reasons of mode stability. Due to the non-linear character of the amplification process, it has been observed that the output mode can collapse to completely different shapes leading to unpredictable output. The increasing sensitivity in the non-linear regime could be caused by the non-linear lens (introduced by the Pockels cell) in combination with decreasing overlap of the laser eigenmode with the pumped region of the thin-disk. This increasing mismatch could then lead to a sudden transition from single-mode to multi-mode operation.

3.4. The amplification process

Seeding a regenerative amplifier with pulses well below the nanosecond level is the key difference of the system described in this thesis as compared to the standard chirped-pulse amplifier. In this section the properties of an Yb:YAG regenerative thin-disk amplifier are explained. The system boosts the pulses described in section (3.1), directly. Amplification of the 100 fs pulses to the multi-mJ level requires a good knowledge of the non-linear influences that are described in section (3.2.2). This section highlights the particular elements and the influences are discussed.

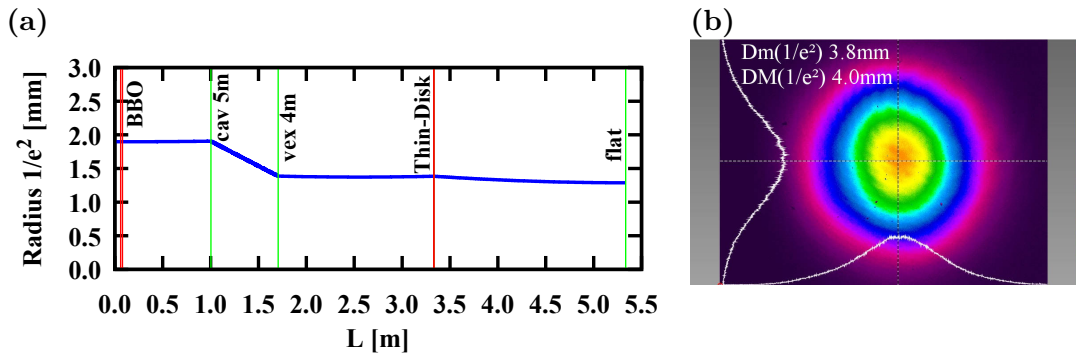


Figure 3.8.: Resonator used to analyze the influence of air. (a) Calculated resonator eigenmode. (b) Eigenmode of the resonator at low power at the position of the BBO crystal.

3.4.1. The influence of air

Amplifiers in our laboratory have been running within air so far. Due to the fact that pulses have not reached peak intensities triggering third-order non-linear processes in air during the amplification process the effects could be neglected. For pulses at the edge to the femtosecond regime this is not the case and air influences the amplification process significantly.

Quantifying the influence of air on the amplification process requires a vacuum chamber allowing for operation in both air and vacuum ($< 10^{-5}$ mbar). This allows direct comparison of the two states without changing the other parameters of the system. The experiment contains the measurement of the output pulses and their parameters for operation in both air and vacuum. Frequency-resolved optical gating (FROG) allows characterizing the the output pulse parameters. This technique ensures full information about the intensity and phase of the laser pulse at the output of the amplifier.

Figure (3.9a) summarizes the result of the measurement using the resonator depicted in figure (3.8) and 122 round trips. The graph shows the full width at half maximum (FWHM) of the Fourier limit calculated from the spectrum that is retrieved from the FROG measurement. Describing the spectral bandwidth with the FWHM pulse duration leads to easier interpretation than using the spectral bandwidth itself as the spectral FWHM is often a discontinuous function (Fig. 3.9b). The solid and dashed lines are fits that result from a pulse of 1 ps duration to which only SPM has been added. The fit then allows to quantify the introduced non-linear phase. Under vacuum conditions the total amount of non-linear phase of the 1 mJ pulse amounts to 1.5 rad. Amplification in ambient air leads to a non-linear phase of 2.9 rad for the same pulse energy. Obviously, for the resonator design shown in figure (3.8) 45% of the total non-linear phase is caused by air. This effect is

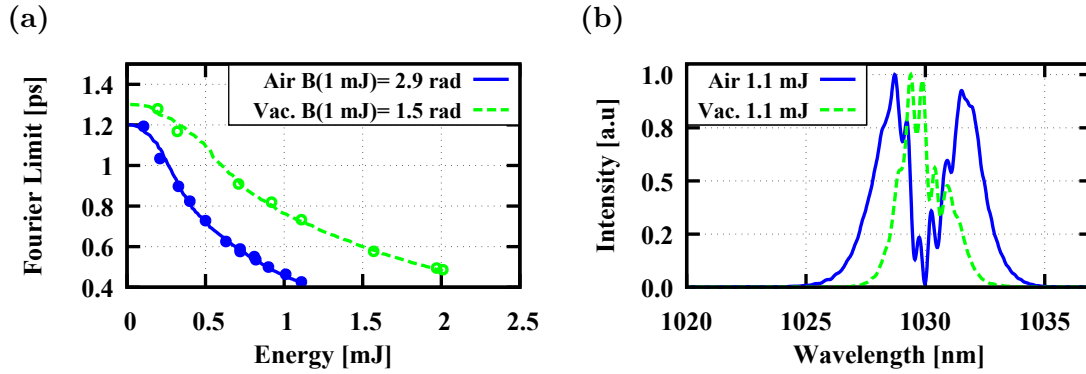


Figure 3.9.: (a) Fourier limits depending on the energy for operation in air and vacuum. The solid and dashed lines are fits using SPM as modulation parameter. (b) Retrieved spectra at 1.1 mJ for operation in air and in an evacuated environment.

visible even though the resonator exhibits a nearly collimated beam. Consequently, for operation in air resonators for non-linear amplification to the millijoule level require large ($>1\text{-}2\text{ mm}$) mode sizes at all positions within the resonator.

In case of large non-linear phase shifts, the amplification process interrupts (no increase of output power with increasing pump power). This interruption is attributed to a reduced overlap of the spectrum with the amplification bandwidth of Yb:YAG and by increased losses resulting from SF modulation. With the resonator shown in (3.10a) this effect was visible if the vacuum chamber was not evacuated. The pulse energy under ambient air was limited to $\sim 0.7\ \mu\text{J}$. The measured spectrum at this energy reached from 1020 nm-1038 nm, which is significantly different from the spectrum resulting from operating the same resonator under vacuum conditions (see spectrum for 0.6 mJ in figure (3.11), which exhibits almost no non-linear phase shift).

3.4.2. Pulse evolution within the amplifier

The details on the amplification process ranks among the most interesting features of the amplifier. To gain a deeper understanding in the details of the amplification process, a measurement system was set up to characterize the output pulses for different amplification cycles (round trips). The results of the measured pulses reveal the most dominant processes and allow distinguishing the amplification into three basic steps:

1. Adjustment of the spectrum to the amplification bandwidth of Yb:YAG
2. Gain narrowing
3. Non-linear pulse compression.

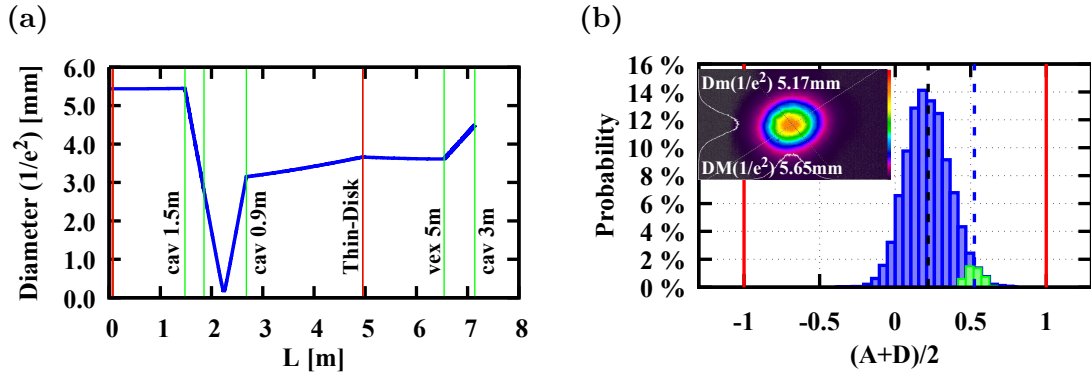


Figure 3.10.: (a) Resonator used to analyze the pulse evolution of the regenerative amplifier. (b) Histogram and measured mode of the resonator. The broader distribution corresponds to the calculated distribution. The smaller right shifted distribution contains all possible resonators that match to the measured eigenmode (assuming TEM₀₀).

The measurement of the output pulses to gain insight into these processes, involved two repeating steps:

1. Measurement of the
 - output pulses via SH-FROG
 - output power
 - spectrum with an Ocean Optics HR4000
2. Change the number of resonator round trips

The measurements were carried out simultaneously to reduce the influence on thermal drifts or mechanical influences during the measurement. The whole system was driven by a software (written by Moritz Ueffing and Tobias Pleyer) that controlled the Pockels cell driver to change the round-trip time and recorded the data from the SH-FROG-measurement, the spectrometer and the Ophir, L50(150)A-PF power head. With these tools the measurements lasted only a few minutes. The increase of the round-trip number was stopped at pulse energies of ~ 3.8 mJ to avoid damage to resonator optics.

The employed resonator contained a tightly focused waist (Fig. 3.10a) and required operation in vacuum. As the amplifier properties and the detailed influences of air and the BBO were unknown at this time the evacuated environment precluded air as an unknown variable. The major influence on the pulse and the dispersion is then solely effected by the BBO Pockels cell. The resonator has an (1/e²) eigenmode diameter of 5.17 mm (minor) and 5.6 mm (major) at the position of the Pockels cell. The Monte-Carlo simulation (tolerances of curved optics 0.5 mdpt) in combination with the measured beam waist predicts a stability value of 0.5 (Fig. 3.10b).

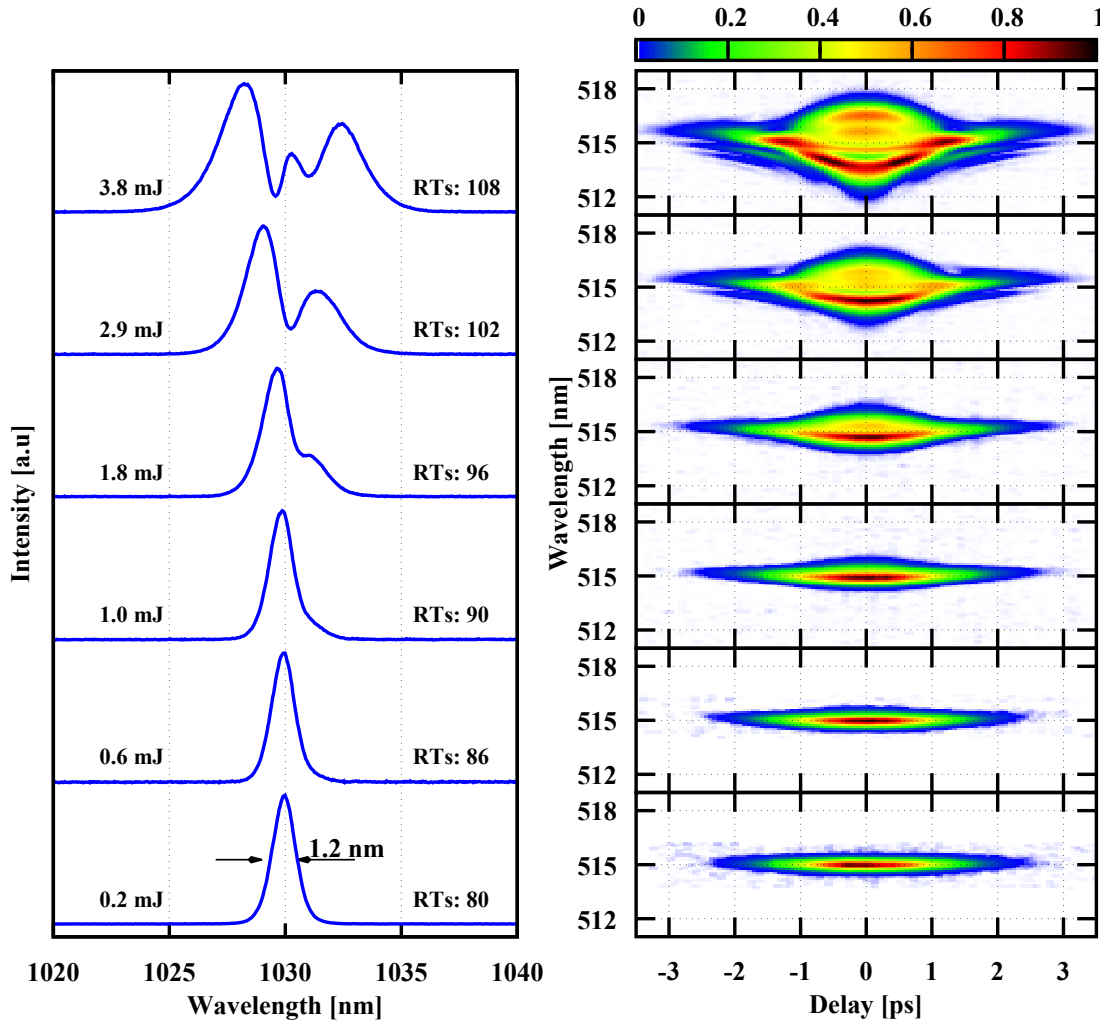


Figure 3.11.: Measured spectra and corresponding SH-FROG traces with 5 kHz repetition-rate at 200 W pump power with varying round trips (RTs) inside the laser resonator.

With increasing round trips inside the resonator the pulse energy grows and at a certain point reaches intensities at the Pockels cell crystal that trigger non-linear optical processes. As the Pockels cell crystal is non-centrosymmetric second harmonic generation is not entirely excluded but plays a minor role because the phase matching condition (Sec. 1.4.1) is not fulfilled. Therefore, the third order effects are the major cause for alteration of the output pulses. Considering the output spectra with increasing pulse energy (Fig. 3.11) spectral broadening of the pulse becomes visible. The spectral shape and the visible modulation is characteristic for SPM [79]. Also the corresponding SH-FROG traces show characteristics of

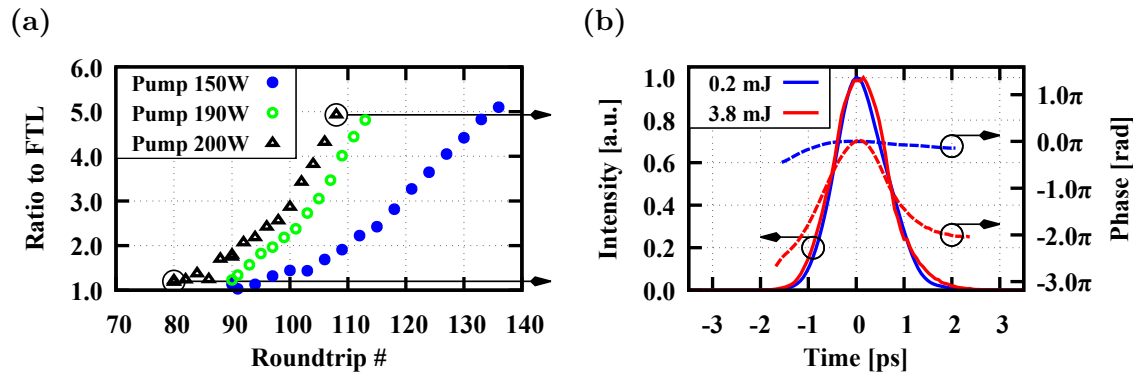


Figure 3.12.: (a) The ratio of the measured pulse duration relative to its FTL duration for different pump powers. (b) Temporal pulse intensity (solid) and phase (dashed) at two different energies (circles in (a)). The energetic pulse possesses a strong non-linear phase.

SPM. The minor deviations result from the introduced chirp and the slightly different spectrum. The spectrum of the 0.2 mJ pulse exhibits no modulation and the corresponding spectrogram indicates no signs of a non-linear phase shift. A retrieval of the pulse reveals that it is almost Fourier limited, which means that SPM has not yet set in. The output spectrum of 1.2 nm (FWHM) corresponds to a Fourier transform limit (FTL) pulse duration of 1.1 ± 0.1 ps. This gain narrowed (Sec. 2.1.3) pulse duration is quite typical for Yb:YAG regenerative amplifiers with gain of $\sim 10^6$ [35, 38, 95, 98]. Compared to the ~ 35 nm input spectrum (Fig. 3.2b) this corresponds to a significant increase of the pulse duration. The influence of the group velocity dispersion (GVD) of the BBO Pockels cell with $42 \text{ fs}^2/\text{mm}$ [146] amounts to $1.3 \cdot 10^5 \text{ fs}^2$ (0.24 ps/nm in the wavelength domain) after 80 RTs through the 20 mm crystal. This causes only minor changes to the temporal pulse shape. Thus, the pulses with energy of $< 0.2 \text{ mJ}$ are gain narrowed (nearly) Fourier limited pulses (Fig. 3.12a) that have not been influenced by non-linear optical effects. The only influence up to this point is the amplification process itself that monotonically increases the pulse duration due to the amplification bandwidth of Yb:YAG and the resulting gain narrowing. Accordingly it can be concluded that the FTL pulse duration for all pulses with less than 0.2 mJ energy is equal or less than the measured 1.1 ± 0.1 ps. From this analysis it turns out that the pulses evolve from the initial femtosecond pulses to picosecond pulses prior to the onset of the non-linear optical process. Subsequently, SPM introduces new spectral components to the gain narrowed pulse and provides the spectral bandwidth that later allows for shorter output pulses. The breathing of the spectrum is a unique property of non-linear regenerative amplifiers.

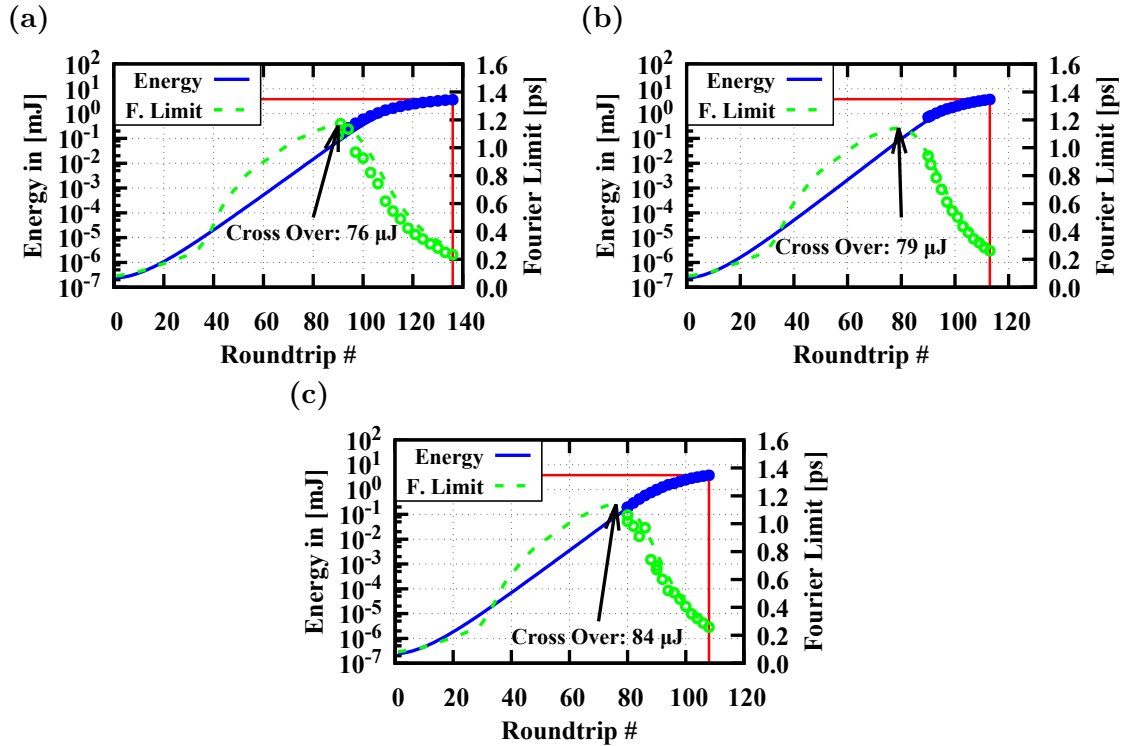


Figure 3.13.: Fourier limit and pulse energy of the output pulses depending on the number of round trips for (a) 150 W, (b) 190 W and (c) 200 W pump power. The solid and dashed lines depict data from the 2D-Split step simulation. Horizontal and vertical lines mark 3.8 mJ at the corresponding round trip number.

The measured pulse durations of the non-linear broadened pulses are with 1.1 ps–1.3 ps comparable to the pulse duration of the gain narrowed pulses prior to reaching the non-linear threshold. SPM introduces only a temporal phase [Equ. (1.92)] to the pulse, which leaves the pulse duration unchanged. The combined effect of SPM and GVD leads with increasing spectrum to altered temporal pulse profiles. However, the moderate amount of SPM and GVD of the BBO Pockels cell causes only minor effect on the temporal pulse shape (Fig. 3.12b).

The increased spectral bandwidth of the pulses can be characterized by calculating the ratios between the FWHM pulse duration and its FTL counterpart. Figure (3.12a) shows this ratio depending on the round trip number and the pump power. The main difference between operation at higher pump power lies in a higher gain that results in a shift of the non-linear processes to lower round trip numbers. The overall behavior of the pulse development from the initial seed pulse could not be measured for technical reasons. To gain insight into the process from the nano-joule level on, a 2D-Split step model (Appx. A) was implemented to simulate the whole amplification process. In order to gain best results the measurements for all

three pump powers served as benchmark for the free parameters that are not entirely known and needed to be adjusted. The simulation reveals a reduction of the effective non-linear refractive index by a factor of 0.3 with $n_{2_{BBO(o)}} = 5.6 \cdot 10^{-16} \text{ cm}^2/\text{W}$ or a factor of 0.7 with $n_{2_{BBO(e)}} = 2.3 \cdot 10^{-16} \text{ cm}^2/\text{W}$ (Tab. 3.1).⁴ As the measured threshold lies at pulse energies of 0.2 mJ, this reduction was adjusted accordingly as otherwise – with higher values of $n_{2_{BBO}}$ – the transition sets in at pulse intensities far below the measured values. The reduction of the non-linear refractive index confirms in a fit of the output spectra with a simpler 1D-Model [122]. Furthermore, $\sim 4\%$ /mJ losses had to be introduced to simulate the saturation behavior at higher energies to the measured data. Until now, the reason for the drop is not fully understood and might be located in parameters of the gain medium that do not fully resemble its performance. More likely, the effect is explained by the optical quality of the BBO crystal that was used as this time. It has turned out that some crystals heat with higher average powers. Further decrease of the performance might result from increasing importance of other parasitic non-linear effects that are not included into the model like second harmonic generation. However, as the model included SF in radial symmetry and includes the spatial information of the inversion of the gain medium it is unlikely that this loss channel is caused by contribution of SF and the resulting mismatch of the beam with the active volume of the gain medium.

Implementing these additional settings to the model leads to good agreement of the resulting data for all three pump powers (Fig. 3.13). The simulated data is calculated by changing the pump power within the model according to the measured values without changing any other parameters. The simulation of the amplification process shows the evolution of the input seed pulse. Starting from the nanojoule input pulse that is shown in figure (3.2b), the first amplification cycles (0-30) lead to an adjustment of the the amplification bandwidth of Yb:YAG. The following cycles are amplifying the pulse under normal linear conditions leading to spectral narrowing of the pulses. Once the energy reaches a level of $\sim 80 \mu\text{J}$ the transition to the non-linear regime is observed. The point of maximum Fourier limited pulse duration forms a cross over from the linear amplification part to the non-linear regime of amplifier. Considering the influence of the gain, the simulation reveals that the “cross over” to the non-linear regime also shifts to the left. This is caused by the steeper amplification curve and the lowered amount of passes through the non-linear medium, which effectively lowers the total amount of non-linear phase.

It is expected that larger round-trip numbers lead to increased spectral bandwidth and even shorter Fourier limited pulses. The temporal phase of the 3.8 mJ pulses (Fig. 3.12b) is well behaved and shows no signs of temporal pulse break up. The main limitation was set by the pulse energy that led to increased probability of damaging the BBO Pockels cell crystals that were used at this time. Increased

⁴Section (3.4.3) gives a possible explanation for the reduced non-linear refractive index.

damage threshold of this optic could lead to higher output pulse energies and even broader spectral bandwidths of the output pulses. Chirp compensation with chirped mirrors (CMs) inside the resonator becomes necessary to avoid pulse break up.

In summary, the measurement results in combination with the simulations show in detail three different amplification regimes. The first corresponds to the low energy limit at which the seed pulse adopts to the amplification bandwidth of the gain medium. The second describes the well known amplification in the linear regime that ends with pulse durations of 1-1.3 ps. The transition to the non-linear amplification process embodies the third regime, which is dominated by SPM. Thus, the 100 fs input pulses are via gain narrowing transformed to 1 ps pulses and afterwards shortened via SPM to 200 fs.

Influences of the seed pulse parameters

The simulation results and basic considerations allow to predict the amplification behavior depending on the input pulse energy. The same amplifier seeded with pulses of same duration but higher pulse energy will exhibit the cross over to the non-linear regime at lower pulse energies. Obviously, the lower necessary gain to reach the same intensities at the Pockels cell leads to less gain narrowing and a shorter pulse at the cross over. The pulse reaches the same intensity at lower pulse energies because of the shorter pulse duration. It is expected that the shorter pulses lead to increased output spectrum and, therefore, shorter pulses prior to reaching the threshold of pulse break up. Pulse durations of ~ 100 fs seem feasible in this case.

Seeding the amplifier with pulses possessing a narrower spectrum than the pulses used for the described experiments (Sec. 3.1), will reduce the intensity and the cross over will shift to higher energies and longer >1 ps pulse durations (the FTL at the cross over in figure (3.13) would shift upwards). As SF is expected to be pronounced equally in the amplifier, the intrinsically longer pulses will produce less spectrum under the influence of SPM at equal refractive power for the non-linear lens (Sec. 3.4.3). The result is a pulse with higher energy but less spectrum. From this consideration it is expected that the laser energy is scalable at the expense of output spectrum via spectral filtering to reduce the input spectrum of the seed pulses prior to amplification.

Current limits

The amplifier concept is capable of delivering up to 5 mJ pulse energy and provides a spectrum spanning over 1015-1045 nm (Fig. 3.14). The field at these output energies was strongly modulated resulting from the increasing spectral bandwidth of the pulse in interaction with the GVD of the Pockels cell crystal. The jumps of

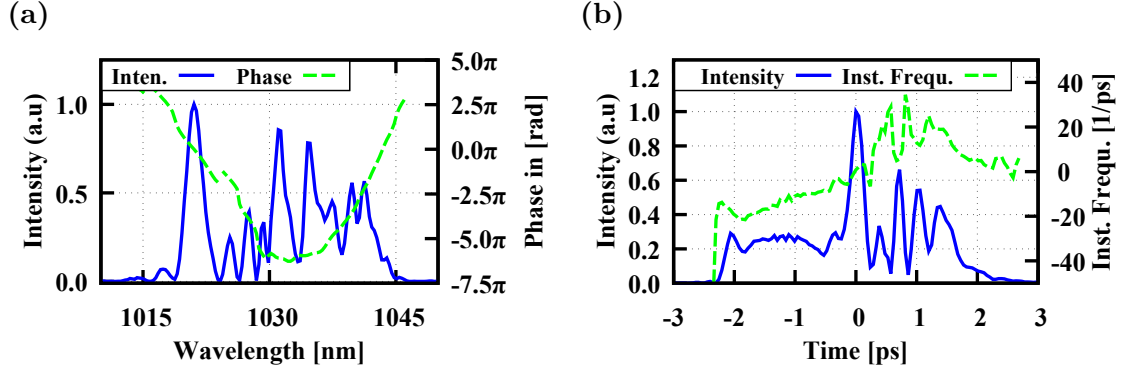


Figure 3.14.: Spectral intensity and phase (a) and temporal intensity profile with instantaneous frequency (b) of a 5 mJ pulse at 5 kHz repetition-rate.

the instantaneous frequency [Equ. (1.60)] in the back of the pulse are indications of optical wave breaking (Sec. 5.6.1) that might be compensated using intra-resonator dispersion management [147]. Higher pulse energy led to optical damage of the Pockels cell crystal or energy instability of the output pulses.

3.4.3. Self-focussing

Self-focusing constitutes the second non-linear effect that influences the system. At gigawatt peak power levels and the corresponding intensities of $\sim 6 \text{ GW/cm}^2$ SF caused by the BBO crystal gradually alters the wavefront during the amplification process. A quantitative value for the non-linear lens is important to design the resonator accordingly. Resonators with variable elements such as thermal lenses are usually designed to operate at optimized conditions in thermal equilibrium [91, 148]. Thus, a static change of the resonator optimized under the influence of the thermal lens is sufficient. For the fast non-linear lens a static optimization is a trade off and, consequently, the resonator needs to be stable over the full range of pulse energies during the whole amplification process. In a first approximation, the non-linear lens introduces an additional focusing element, the refractive power of which scales linearly with the peak power of the pulse [149],

$$D_{NL} \approx \frac{4n_{2_{eff}}L}{\pi w^4} \cdot P_{peak} \stackrel{Gauss}{=} \frac{4n_{2_{eff}}L}{\pi w^4} \cdot \sqrt{\frac{2E}{\pi\tau}} = c_{NL} \cdot E \quad (3.5)$$

where P_{peak} is the peak power of the pulse, w is the mode radius (4.5/2 mm), L is the length of the non-linear medium (BBO-crystal, 20 mm), E is the pulse energy, τ is the pulse duration (1.4 ps) and $n_{2_{eff}}$ represents an effective non-linear refractive index.

To get an estimate for D_{NL} , the focal position of the output laser beam was measured both in continuous wave operation and in 100 kHz pulsed mode (see section (3.6) for details on the amplifier and resonator). The higher repetition-rate is not necessary to perform this measurement but the system optimized for this repetition-rate was the most developed version of the amplifier at this time. As an accurate measurement of mode changes with changing pulse energy requires a well defined output mode and stable laser operation this measurement could not be performed at earlier stages of the amplifier.

The measurement was carried out with a Spiricon M²-200s M²-meter. An accurate measurement of the small refractive powers requires same settings and input average powers at the measurement device. To avoid the contribution of thermal heating of filters in front of the M²-meter, the average powers entering the device were below ~5 mW. Additionally, the output power in CW was adjusted to reach the same output power as in pulsed mode at 680 W pump power. The M²-device stayed at the same position and neither filters nor other parameters were altered as the effect was not visible otherwise. A 0.5% output coupler in front of the Faraday rotator provided the beam for the measurement to avoid any possible contribution of the TGG crystal to the measurement. Figure (3.15) depicts the change of the focal position behind the lens of the M²-Meter, d_{M^2} , for different output powers. Comparing the behavior of the laser operating in CW and at 100 kHz gives an estimate of the value for the non-linear lens according to equation (3.5). The ABCD-transition matrix for the setup is

$$\begin{pmatrix} A & B \\ C & D \end{pmatrix} = \begin{pmatrix} 1 & d_{M^2} \\ 0 & 1 \end{pmatrix} \begin{pmatrix} 1 & 0 \\ -\frac{1}{f_{M^2}} & 1 \end{pmatrix} \begin{pmatrix} 1 & d_{toM^2} \\ 0 & 1 \end{pmatrix} \begin{pmatrix} 1 & 0 \\ -D_{NL} & 1 \end{pmatrix} \quad (3.6)$$

$$d_{toM^2} = 3.8 \text{ m} \quad f_{M^2} = 0.29584 \text{ m} \quad (3.7)$$

where d_{toM^2} is the distance from the BBO crystal to the M²-meter and f_{M^2} is the focal length of the lens within the M²-device. A fit of the free parameter D_{NL} then yields the coefficient c_{NL} and the refractive power of the BBO crystal. The resonator design has a flat end mirror at the position of the Pockels cell leading to a collimated beam at this end. Therefore, the wavefront of the beam at this end mirror is flat to fulfill the eigenmode equation. Because of the short distance between end mirror and the BBO Pockels cell, it is assumed that the waist of the beam is located at the front surface of the crystal. This assumption then leads to

$$q_{in} = iz_R = i \frac{\pi w_0^2}{\lambda} \quad (3.8)$$

$$q_{out} = \frac{A \cdot q_{in} + B}{C \cdot q_{in} + D} = (d_{M^2} - z_{foc}) + iz_{R_{M^2}} \quad (3.9)$$

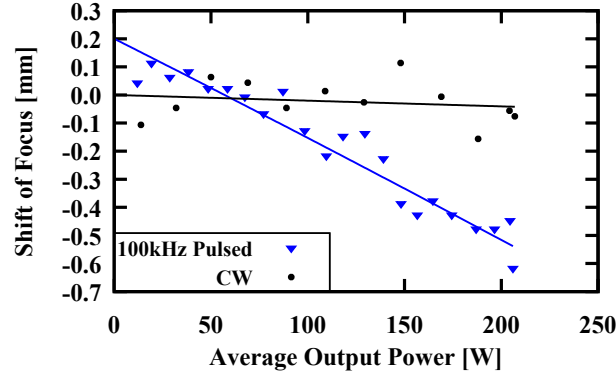


Figure 3.15.: Shift of the focus caused by non-linear lensing of the BBO crystal

where z_R is the Rayleigh length of the $w_0 = 4.5/2$ mm beam radius. As the position of the focus is equivalent to a vanishing real part of the q-parameter, q_{out} , solving the equation for $\text{Re}\{q_{out}\} = 0$ yields the focal position, d_{M^2} , depending on the non-linear lens with refractive power D_{NL} .

The fit to the solution of $\text{Re}\{q_{out}\} = 0$ reveals $n_{2_{eff}} = 0.15 \cdot n_{2_{BBO(o)}}$ or $c_{NL} = 4.6$ dpt/J (Tab. 3.1). Comparing this value to the results from the 2D-Split step model, however, a consistently reduced non-linear refractive index is observed (from section (3.4.2) SPM: $n_2 \approx 0.3n_{2_{BBO(o)}}$). The significant lower effective value of the non-linear refractive index is beneficial and supports higher output pulse energies than expected from the larger literature value. The refractive power calculated from this estimation is lower than 0.01 dpt at 2 mJ pulse energy.

In addition, a consistent reduction of the non-linear refractive index is found with an independent 1D-Split step simulation. In this model a simplified calculation in the time and spectral domain leads to a coefficient $c_{NL} = 0.24$ [122].

As the laser amplifier was operated under ambient air, the influence on the non-linear lens could not be excluded. However, the output mode of the laser has a $1/e^2$ -diameter of 4.5 mm at the position of the Pockels cell crystal, which also defines the output laser mode. A laser pulse with this mode diameter has a non-linear length [Equ. (1.95)] of > 25 m in air. For the measurement 0.5% of the beam was split off at ~ 0.4 m behind the laser resonator. The short propagation length of the beam, therefore, causes no significant contribution of air in between the laser output and the measurement device. Because of mode cleaning properties of the laser resonator in combination with the homogeneous distribution of the non-linear wavefront distortions over the full length of the laser resonator, the contribution of air to mode changes inside the laser resonator are neglected. This assumption is strengthened by the results presented on non-linear pulse compression in Herriott multi-pass cells that benefit from mode cleaning effects inside stable laser resonators [150, 151]. Additionally, the results presented in chapter (5) suggest

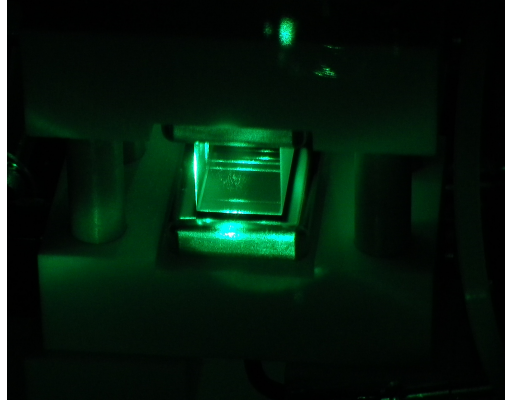


Figure 3.16.: Picture of the Pockels cell during operation. Green light corresponds to a small fraction of second harmonic generation from the 1030 nm fundamental beam.

mode cleaning effects for beam propagation in homogeneous non-linear media. For these reasons and the small influence of the exhibiting nonlinear lens ($f < 0.01$ dpt) on the eigenmode of the resonator (Fig. 3.20b) the mode at the position of the BBO crystal does not alter significantly and the influence of air is neglected.

Explanation for the reduced non-linear refractive index of BBO

The measurements presented in previous sections show a reduced non-linear refractive index of the BBO Pockels cell. The difference of the measured value compared to the literature value is attributed to the fact that the non-linear refractive index n_2 connects to the scalar non-linear susceptibility $\chi^{(3)}$ only if the incident electromagnetic wave is linearly polarized. In case of circular or elliptic polarization the susceptibility must be treated with the full tensor $\chi_{ijkl}^{(3)}$ description [62, p. 332]. This hypothesis is further supported by the two different literature values of n_2 for the ordinary $n_{2(o)}$ and the extraordinary $n_{2(e)}$ polarization states (Tab. 3.1). Furthermore, the applied voltage to the BBO crystal changes the properties of crystal and introduces a second optical axis. As the non-linear coefficients of BBO are not equal for the extraordinary and the ordinary ray this influence is expected to contribute to a change of the non-linear refractive index. Even though the conversion to the second harmonic is low (Fig. 3.16), the cascaded second order contribution to the non-linear refractive index [152, 153] might not be negligible. Examination of these effects might lead to technical optimization of the effective non-linearity in the regenerative amplifier.

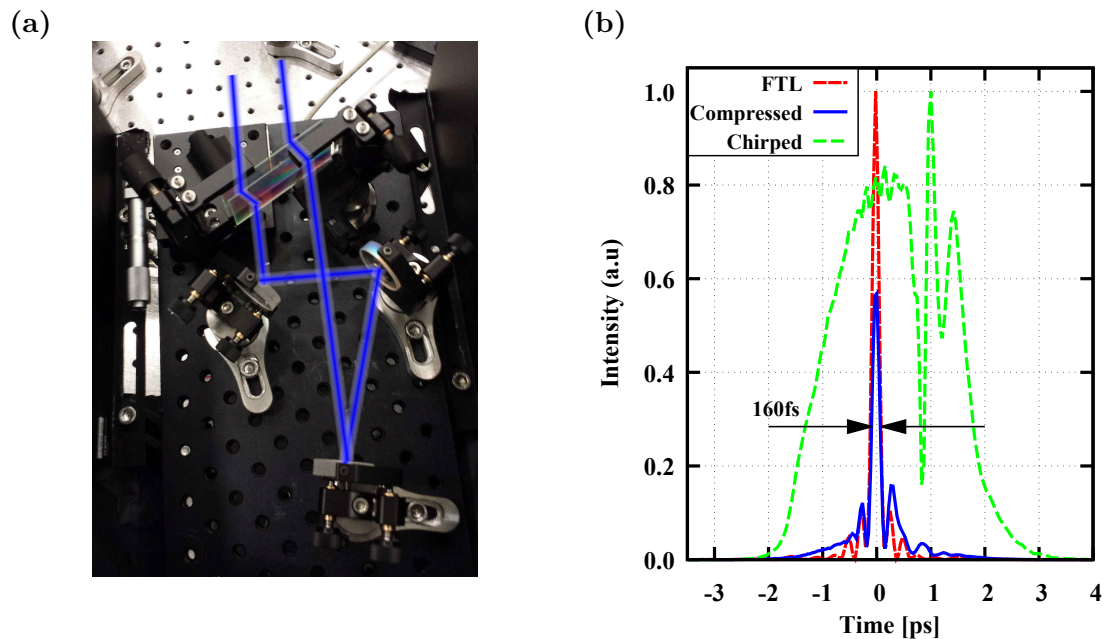


Figure 3.17.: (a) Transmission grating compressor and (b) shortest measured pulse and the corresponding Fourier limited pulse (peaks normalized to time integral). Uncompressed output pulse (dashed); not normalized.

3.5. Pulse compression

The increased spectrum of the amplifier leads to pulses with several millijoule energy that support pulse durations of ≤ 250 fs. In this section it is shown that pulse compression after the amplifier is possible and describes the path towards development of a highly efficient CM compressor.

3.5.1. Grating compressor

In the early stages of the amplifier a transmission grating compressor (Fig. 3.17a) led to pulses as short as 160 fs at 3 mJ (Fig. 3.17b) and thus to one of the shortest pulses out of an Yb:YAG regenerative amplifier at this time. However, significant amount of energy is distributed to side pulses leading to 57% of the peak power as compared to the Fourier limited pulse. The comparably low amount of group delay dispersion (GDD) was removed with transmission gratings with 9 ± 2 mm distance at a line density of 1000 lines/mm. Despite the comparably high single pass efficiency of 94% the overall efficiency amounts to only 80%. Highly efficient reflective gratings are accompanied with line densities in the order of the inverse wavelength [154, 155]. Therefore, implementation of highly efficient reflective gratings is not easily implemented due to the small separation distances of only a

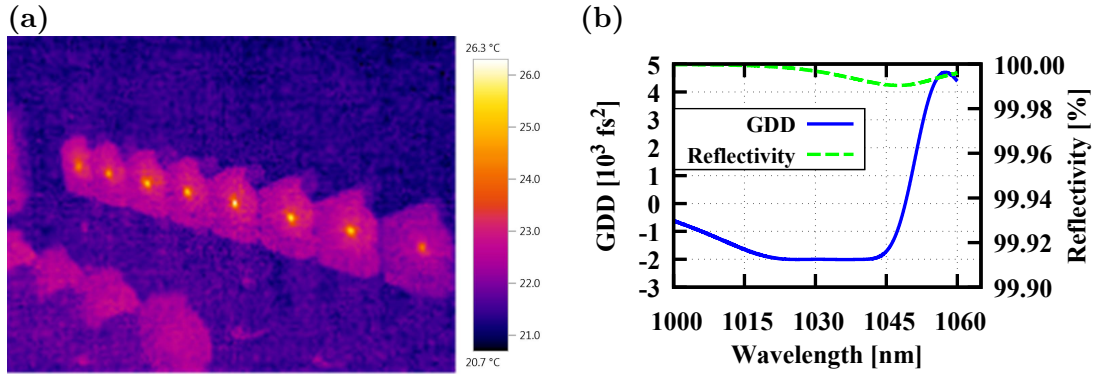


Figure 3.18.: (a) Heat distribution of the HD1602 chirped mirror with a beam diameter of 9 – 10 mm at 200 W input power at 100 kHz. (b) Theoretical GDD of a single bounce on a HD1602 chirped mirror (kindly provided by Dr. Vladimir Pervak).

few millimeters. Grating separation of a few millimeters with a beam as large as 5 mm-10 mm to avoid damage or non-linear optical effects in the compressor setup prevents the implementation of reflective gratings without further imaging components [156].

3.5.2. Chirped mirror compressor

Because of the more complex alignment, the reduced throughput after the grating compressors and the moderate amount of GDD (10^5 fs^2), a chirped mirror compressor is preferred.

The large progress in chirped mirror development during the last decades engendered optics with huge capabilities [157]. Mirrors introducing a GDD of more than 10^4 fs^2 in a single pass opened the path towards compression of the developed laser system. In combination with the high reflectivity ($> 99.9\%$) of these optics, chirped mirrors allow for pulse compression with throughput of $> 97\%$ of the pulse energy enabling pulse compression with nearly no losses.

In the experiment several iterations led to the conclusion that reliable operation of the chirped mirror compressor is indeed coupled very closely to the damage threshold of these optics. Thermal heating with subsequent damage of mirrors with powers between 10 W-15 W at 5 kHz prevented using highly dispersive optics with 10000 fs^2 and moderate beam sizes. However, this “soft” limit might be solved in future.

A compressor with 30 highly dispersive mirrors of type HD1602 (Fig. 3.19) that introduce less GDD (Fig. 3.18b) per pass led to reliable output and short pulses. The mirrors are less prone to thermal heating (Fig. 3.18a) permanently wit-



Figure 3.19.: Picture of the chirped mirror compressor (picture: Thorsten Naeser).

withstanding the high pulse energy. This compressor also opened the transition to repetition-rates of up to 100 kHz (Sec. 3.6) and showed excellent reliability during the last years.

3.6. 100 kHz non-linear regenerative thin-disk amplifier

This chapter focused so far the basic amplification process within the non-linear regenerative amplifier. Amplification reveals to be possible to a few millijoule prior to significant beam deteriorations and the resulting optical damage. Increasing the repetition-rate of the amplifier whilst maintaining the pulse energy is possible without the need for severe changes to the amplifier setup.

This section depicts the performance of the regenerative amplifier at 100 kHz repetition-rates with 2 mJ pulse energy. The obtained performance proves that non-linear regenerative amplification yields to stable output and can be utilized for use in experiments (Chap. 5).

3.6.1. Laser design

The seed system of the 100 kHz amplifier system is described in section (3.1) and the setup of the amplifier is depicted in figure (3.1). The laser is designed to allow operation in ambient air to avoid vacuum conditions. As seen in section (3.4.1) the contribution of air to non-linear phase shift is significant and requires beam diameters of a few millimeters to maintain the amplification process to the millijoule level.

Figure (3.20a) shows the calculated eigenmode of the implemented resonator. The resonator eigenmode has a minimum beam diameter of more than 2.6 mm ($1/e^2$). The corresponding non-linear length [Equ. (1.95)] in air at minimum mode diameter inside the resonator amounts to > 8 m at maximum pulse energy (2.1 mJ) and 1.2 ps pulse duration. This is comparable to the resonator length and finally

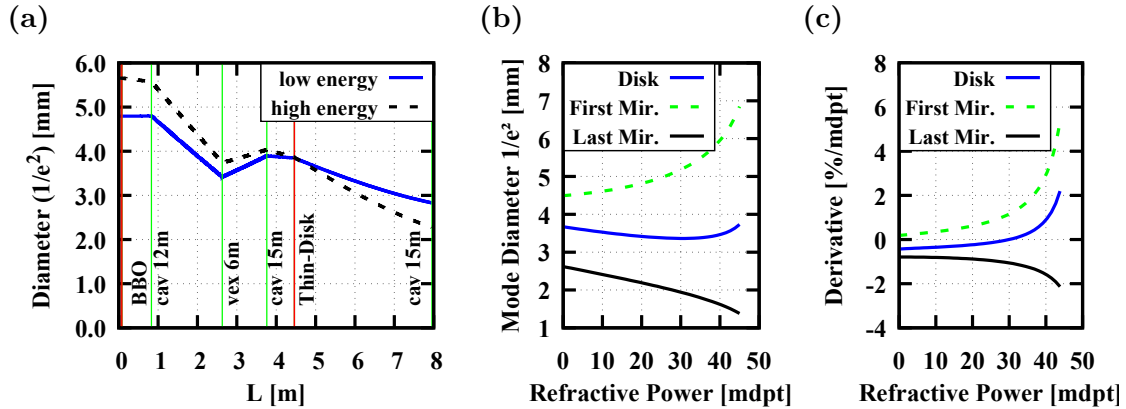


Figure 3.20.: (a) Resonator eigenmode of the amplifier (solid). (Dashed) change of the eigenmode with increased lensing of the BBO-crystal. (b) ABCD-Matrix calculation showing the change of the eigenmode diameter at the two end mirrors and the thin-disk with respect to a focusing element at the position of the BBO-crystal. (c) depicts the derivative of the relative change of the functions shown in (b) to the initial beam diameter without lensing.

leads to a non-linear phase shift caused by air. Furthermore, the resonator design exhibits low sensitivity of the mode diameter at the thin-disk with respect to an additional lens at the position of the BBO crystal. As the increasing pulse energy not only contributes to spectral broadening via SPM, but also leads to development of a non-linear lens, it is beneficial to design the resonator with a stability constraint at the position of the thin-disk. The dashed line in figure (3.20a) illustrates the effect of an increasing lens on the eigenmode. The increasing beam diameter at the BBO leads to a negative feedback reducing the intensity with increasing non-linear phase. This is important to avoid catastrophic collapse of the beam. At the position of the thin-disk the eigenmode features low changes of the mode size with respect to the lens. Comparing the refractive power to the measured value of the non-linear lens of section (3.4.3) at 2 mJ the approximate change of the refractive power is with ~ 10 mdpt well within the stability zones that reach up to 45 mdpt (Fig. (3.20b) and (3.20c)).

3.6.2. Performance

Figure (3.21a) depicts the output power of the amplifier (measured with an Ophir FL500A-BB-65 power head). The measurement shows 6 hours of operation starting from a cold system. After a time of approximately 2 hours the system stays at 207 W output power with less than 0.5 % root mean square (RMS) fluctuation. The pulse-to-pulse stability of the laser was measured by recording 5000 subsequent pulses with a photodiode and shows an upper bound of the RMS pulse-to-pulse noise of

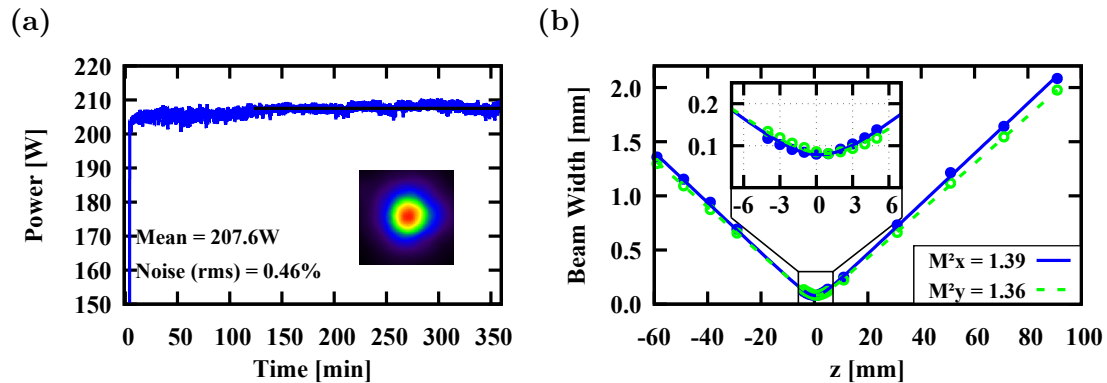


Figure 3.21.: (a) Measured stability of the system. The system was started in a cold state. After a 2 h warm up the system stayed at 207 W with a noise value of 0.46 % (RMS). The inset shows the beam profile of the output beam. (b) M^2 measurement of the 207 W output at 100 kHz

0.43 %. To achieve these parameters water cooled apertures removed stray light and temperature stability of the chillers for both the thin-disk and the pump diodes are optimized.

The output beam quality is with $M^2 < 1.4$ close to the diffraction limit. The beam quality was measured using a commercial Spiricon M^2 -200s taking the 4σ beam diameter (Fig. 3.21b). It is interesting to note that the M^2 value before the Faraday rotator can be accessed by replacing one of the guiding mirrors in between the resonator and the Faraday rotator with an output coupler of high reflectivity ($> 99.5\%$). At this position the beam quality factor was < 1.09 and thus much better than 1.4. This indicates thermal and/or non-linear contribution of the rotator or other optical elements and might lead to increased beam quality factors once the source is identified.

The non-linear spectral phase and the intracavity GDD (dominated by the BBO crystal) introduce a positive chirp to the 2.1 mJ output pulses. This results in an output FWHM pulse duration of 1.4 ps. The compressor (Sec. 3.5.2) consists of 30 chirped-mirrors (HD1602 manufactured by Dr. Vladimir Pervak and Dr. Michael Trubetskov). Each mirror has a group delay dispersion of -2000 fs^2 (Fig. 3.18b) leading to $\sim 6 \cdot 10^4 \text{ fs}^2$ in total. The characterization of the field using SH-FROG shows that the compressor removes the chirp of the output pulses almost perfectly (Fig. 3.22). The resulting pulse duration of 210 fs (FWHM) is close to the Fourier limit (205 fs (FWHM)) and shows only minor satellites. The retrieved spectrum of the SH-FROG measurement is in excellent agreement with the measured spectrum of the pulse at 2 mJ indicating good reconstruction. The ratio of the peak power

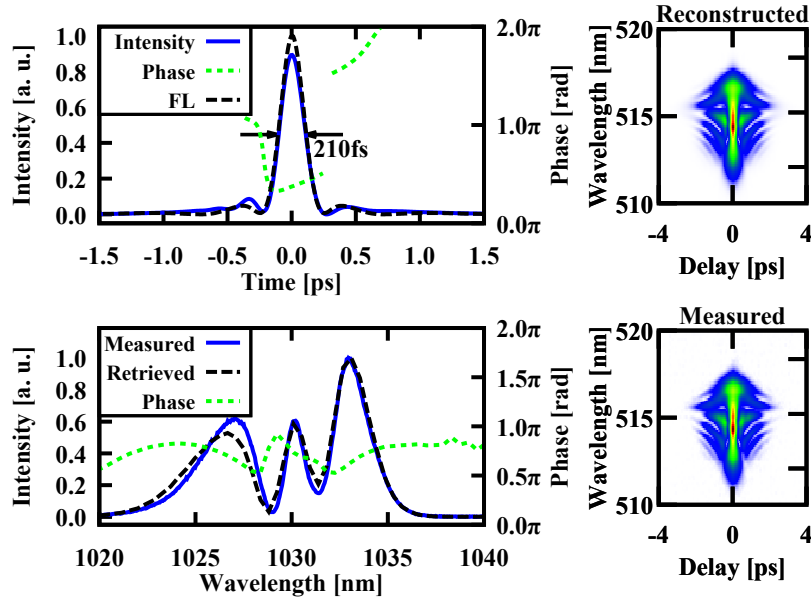


Figure 3.22.: FROG trace of the output pulses behind the chirped mirror compressor. The pulse reaches a peak power of 7.3 GW. FROG G-error 0.32 %.

between the Fourier limit and the compressed pulse is 89 %. The efficiency over the whole 35 mirrors in the compressor setup (chirped-mirrors + folding mirrors) amounts to 97 % leading to 2.0 mJ pulse energy and 7.3 GW peak power.

Even though chaotic output pulse energies at repetition-rates in the 0.1 MHz regime is not as pronounced as it is in the kHz regime it is still visible if the seed pulse energy is too low. This effect is observed if the seed beam is not well aligned with respect to the resonator of the amplifier. In this case a small energy splitting (Fig. 3.23) of the output pulses appears. However, with proper alignment of the seed beam this splitting vanishes and stable mono energetic output pulses are observed.

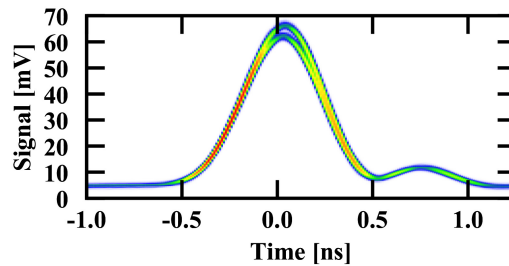


Figure 3.23.: Overlay of 5000 subsequent pulses showing the bifurcation at 100 kHz repetition-rate.

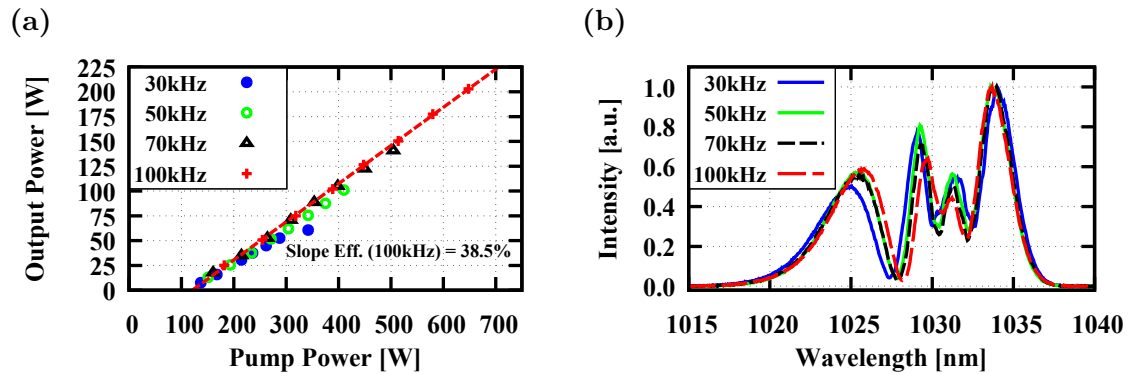


Figure 3.24.: (a) Output power depending on the pump power for different repetition-rates. (b) Spectra for different repetition-rates with same round trip number at 2 mJ output pulse energy.

3.6.3. Simple scaling of the repetition-rate

Scaling the regenerative amplifier in repetition-rate without optimizing the optical-to-optical efficiency for lower repetition-rates is simply achieved by electronic changes to the trigger system of the amplifier. The output of the amplifier vs. the pump power is shown in figure (3.24a). Here, 2 mJ pulse energy marked the point upon which the pump power was increased. At 100 kHz the system reaches an optical-to-optical efficiency of 31 % and a slope efficiency of 38.5 %. The output spectra for different repetition-rates (Fig. 3.24b) at same pulse energy are slightly different. This is attributed to thermal changes of the eigenmode, which grows slightly for higher pump powers due to changing refractive power of the thin-disk. The growing mode diameter results in reduced accumulation of non-linear optical phase with higher average (and pump powers) and, therefore, a narrower spectrum at high repetition-rates.

As thermal changes are static once the system reaches thermal equilibrium, these differences do matter only if the system is switched to different repetition-rates. If the experiment driven with such a laser source relies on precise and constant spectra this has to be considered and small changes to the resonator may be necessary to compensate for the differences.

3.7. Summary and conclusion

The sections in this chapter show the constraints and the design parameters that need to be considered for building a regenerative amplifier seeded with femtosecond light pulses. In detail, the contribution of the particular optical elements within the amplifier is shown highlighting that air considerably contributes to the non-linear amplification process.

The necessary conditions for stable operation of the resonator are explained showing that a reliable resonator design needs to follow three basic steps:

1. Calculation of the resonator,
2. Measuring the mode beam quality parameter,
3. Adjustment of the eigenmode.

Due to uncertainties of the refractive powers of the resonator optics, the M^2 parameter reveals if the laser runs in multi-mode operation. If the beam quality factor at low laser peak powers is worse than ~ 1.3 , the resonator TEM_{00} mode is most likely (if optical damage can be excluded) not well matched to the resonators hard and soft aperture constraints. In these resonators self-focusing effects are likely to be more pronounced and the output mode might follow unpredictable changes during operation.

Measurements of the field and simulations further explain that the spectrum of the seed pulses first adjust to the amplification bandwidth of the Yb:YAG gain medium that subsequently undergoes spectral narrowing due to the well known gain narrowing effect. After reaching the threshold intensity to trigger third-order non-linear processes, the spectral bandwidth increases.

It is demonstrated that compression of the SPM broadened pulses is possible, which proves that chirped mirrors lead to highly efficient output of the amplifier device.

Furthermore, a powerful CPA-free non-linear Yb:YAG thin-disk regenerative amplifier with high repetition-rate is presented. The system is capable of running for hours at stable output power of > 200 W at 100 kHz repetition-rate. Although the laser runs in a strongly non-linear regime, the M^2 of the output beam was measured to be < 1.4 indicating an efficient mode filtering and homogenizing effects (Chap. 5) inside the resonator. Furthermore, compression of the 2.1 mJ output pulses to nearly Fourier limited pulse duration is shown. The 210 fs pulse duration (FWHM) in combination with 97% efficiency of the chirped mirror compressor results in a pulse energy of 2.0 mJ and 7.3 GW peak power after compression. The measurements clearly show that the system is stable enough for further usage as a driving laser for non-linear optics as described in chapter (5).

Pulse energies of 5 mJ were obtained prior to causing optical damage to the Pockels cell crystal. Compression of a 3.5 mJ pulse to 160 fs shows unprecedented pulse duration out of an Yb:YAG non-linear regenerative amplifier. The minimum pulse duration is set by pulse break up caused by intra-resonator dispersion in combination with the non-linear broadening. Dispersion management in combination with larger non-linear phase shifts could reduce this effect. However, self-focusing still leads to mode changes with increasing pulse energy. This influences the resonator eigenmode and shifts the resonator towards its stability edge. The mode quality was observed to degrade in this case, which limited the output of the amplifier due to secondary effects such as optical damage or mode instabilities. As the contribution of self-focusing is primarily affected by the mode diameter at the BBO Pockels cell, higher pulse energies are possible with increased aperture of the BBO crystal. Therefore, the current limitation of pulse energy and spectral bandwidth is set by the limited availability of BBO Pockels cells with clear aperture of $>12 \times 12 \text{ mm}^2$ and sufficiently high optical quality.

Chapter 4

Energy Scaling of Non-linear Thin-Disk Amplifiers

Ultrafast amplifier systems providing high average powers ($>10\text{W}$) at repetition-rates in the kHz regime suffer from severe accumulation of non-linear phase inside the laser gain medium and other optical components within the amplifier. Implementation of chirped-pulse amplification (CPA) constitutes a well-established method to reduce the peak intensity of the laser pulse during the amplification process [21]. However, state of the art laser materials supporting high average output powers such as Yb:YAG have gain bands of 7-9 nm [36] and implementation of CPA in these systems is more challenging as compared to Ti:Sapphire (Ti:Sa) systems. The thin-disk technology in combination with a regenerative amplifier reduces the accumulation of non-linear effects in the laser gain medium to a minimum. The indispensable electro-optical switch (Pockels cell) in these systems, however, still demands CPA and, therefore, large and complex dispersive delay lines for amplification to the ten Joule level. Multi-pass thin-disk amplifiers allow amplification without the electro-optical switch and decrease the amount of material to a minimum but rely on geometric displacement to guide the beam several times (10 to ~ 40) through the gain medium. These amplifiers provide exceptional performance [33, 50] but are limited in overall gain. Amplification of oscillator pulses from nano/micro-joule energies to the multi-millijoule level is difficult to implement due to the tremendous amount of passes (~ 80 -200) through the gain medium.

The patented hybrid technology [158] overcomes this limitation exploiting the advantages of a thin-disk regenerative amplifier in combination with a multi-pass system. The system amplifies pulses within the cavity of a regenerative amplifier. Before accumulating destructive non-linear phase distortions, a multi-pass system using the same active amplification volume as the regenerative amplifier boosts the pulse energy to a level inaccessible inside the regenerative amplifier (Fig. 4.1). The absent electro-optical switch in the high-energy amplification process allows amplification without the need for CPA. Thus, this concept permits renouncing CPA leading to a compact setup including advantages in costs, stability and complexity of the system by abandoning stretcher and compressor units.

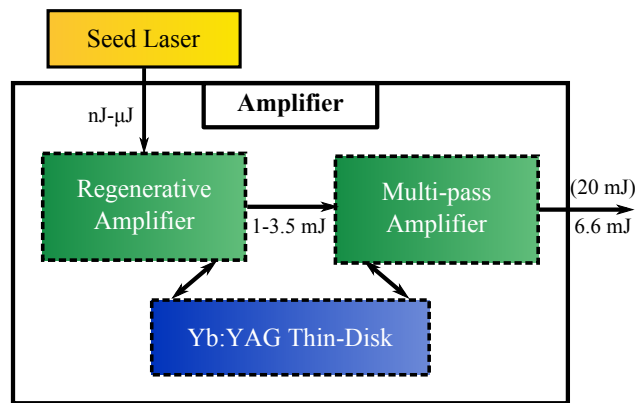


Figure 4.1.: The hybrid amplifier concept. Both the regenerative amplifier and the multi-pass amplifier share the same active gain volume of a thin-disk.

This chapter discusses the first steps in implementing this new type of amplifier and demonstrates the feasibility of the concept. Different aspects are discussed and further improvement is suggested. Considering the 6.6 mJ pulses that were achieved without implementing CPA, this amplifier delivers outstanding performance in terms of pulse energy in combination with a small footprint (1.0x1.5 m) [159]. The design of the amplifier theoretically supports 20 mJ, however, non-linear optical effects can limit the output. This topic is discussed and solutions for further improvement are given.

4.1. The hybrid setup

Figures (4.1) and (4.2) show the schematic overview of the laser amplifier. The amplification process starts with a seed oscillator described in section (3.1). The regenerative amplifier setup is described in chapter (3). Once the pulses leave the regenerative amplifier, the optical isolator separates input and output beam paths and sends the pulses to the multi-pass amplifier. Within several passes (2-40, depending on the needs) the remaining stored energy of the thin-disk is extracted boosting the pulse energy up.

4.2. Non-imaging multi-pass amplifier

Implementation of the concept requires an optical design compact enough to support both operation of the thin-disk regenerative amplifier and the multi-pass system. This requires an optical setup compact enough to merge the system into the same chamber. The design parameters with pulse energies of 20 mJ in combination

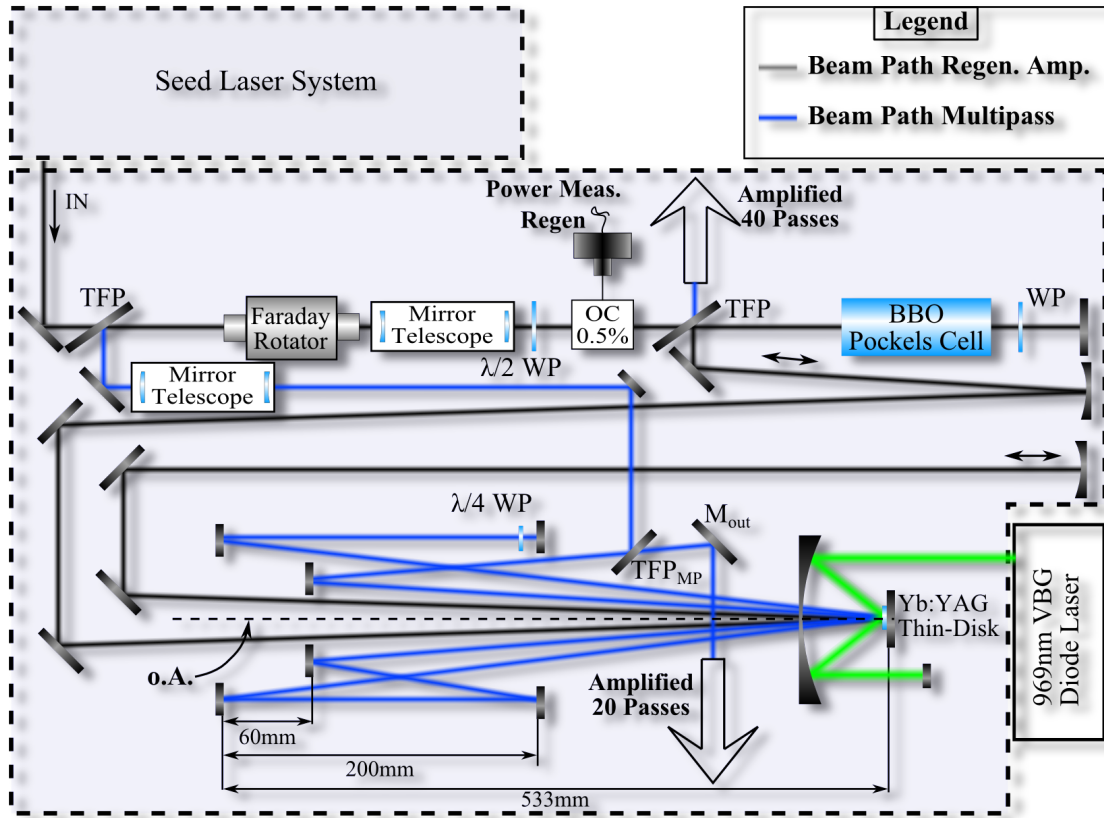


Figure 4.2.: Schematic overview of the hybrid amplifier. Regenerative amplifier and seed (black). Multi-pass amplifier (blue) with optical axis (o.A.). In the 40 pass configuration (beam at M_{out} is reflected back into itself) the rotator is passed three times (incoupling, after regenerative amplification and after multi-pass amplification) leading to output coupling at position of the thin-film polarizer of the resonator. Power measurement of the regenerative amplifier is implemented with a high-reflective output coupler that splits 0.5% from the regenerative amplifier output.

with the picosecond pulse duration necessitates a vacuum chamber to avoid critical self-focusing in air. The following sections describe the implementation of the multi-pass system with a simple guidance of the beam of the gain medium, which allows a comparably compact setup.

4.2.1. Design

The multi-pass setup contains 30 mirrors arranged in rotational symmetry around the optical axis. Figure (4.3a) shows a picture of the system as it was used in the laboratory. Figure (4.3c) schematically depicts the beam path through the system from the perspective of the thin-disk (D). The implementation incorporates two

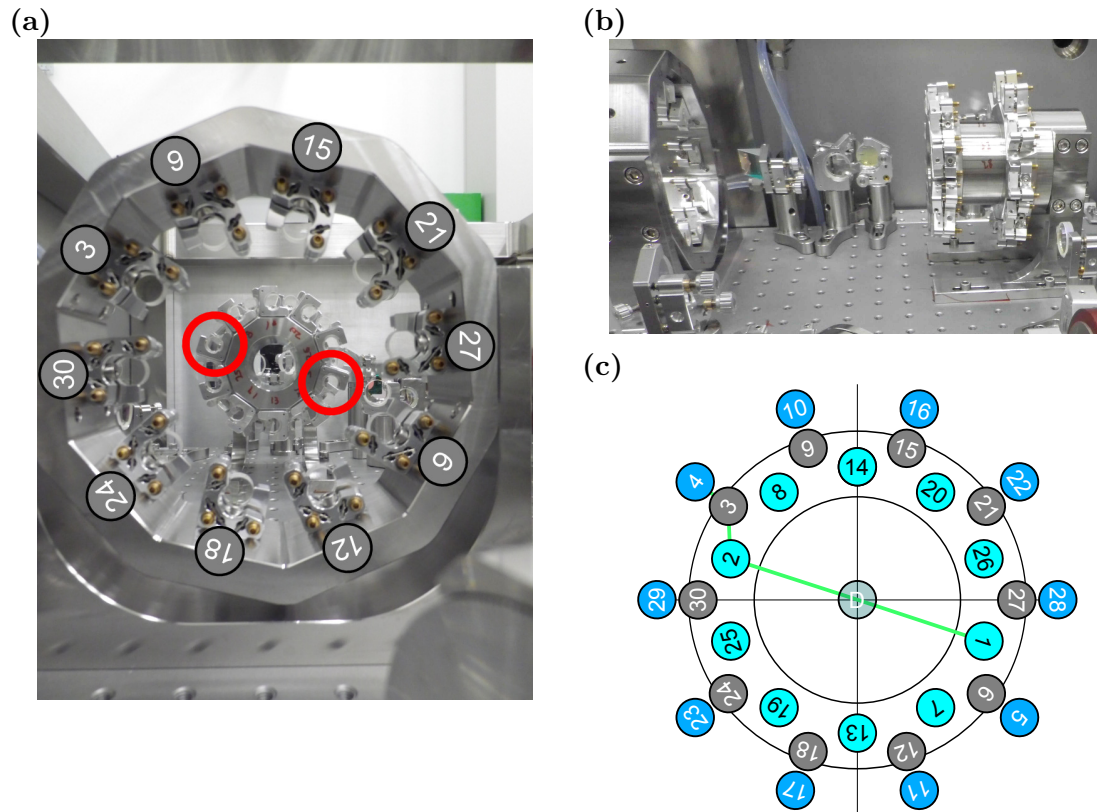


Figure 4.3.: (a) Picture of the multi-pass system from the perspective of the thin-disk. Mirrors 1, 2 (red circles) and the second wheel are labeled. (b) Side view of the system. (c) Numbering of the mirrors within the multi-pass system from the perspective of the thin-disk.

components. One for guiding the beam over the disk, the second for shifting the beam from one mirror to the next. In the schematic view the inner and the outer rings (cyan and blue) represent mirrors fixed on the first holder and the middle ring (grey) represents the mirrors on the folding mechanic. Starting with mirror 1 the setup guides the beam over the disk to mirror 2 and mirror 3 shifts the beam to mirror 4 that repeats the cycle. The blue beam path in figure (4.2) depicts system from a top view showing the system along the optical axis. A single pass through the whole system introduces 10 passes through the gain medium and 30 passes over 1/2" mirrors. Folding the beam back doubles the passes through the system without extra efforts. Separation of the beam is achieved using a quarter wave-plate in front of the last mirror to turn the polarization from "s" to "p" leading to transmittance at the thin-film polarizer (TFP), TFP_{MP} , in the beginning of the multi-pass setup. In total this configuration allows 20 passes through the thin-disk with a total optical path length of ~ 36 m. During the experiments it turned

out that a higher number of passes would be beneficial. Doubling of the 20 pass geometry to allow 40 passes over the thin-disk is achieved by sending the beam that passes the polarizer, TFP_{MP}, with “p”-polarization back into itself. The beam then follows the multi-pass configuration once again in backward direction reaching the isolation stage of the regenerative amplifier. As the beam is “s”-polarized before entering the Faraday rotator the polarization remains “s” after passing the wave-plate behind the rotator. This leads to a reflection at the TFP of the resonator. This method, however, contains significant amount of material due to the additional pass through the 20 mm terbium gallium garnet (TGG) crystal of the rotator and the TFPs. Therefore, this method is used for proof of principle experiments, only. The section (4.3.1) discusses in detail a setup allowing for at least 40 passes without the need for passing transmissive elements in the high energy part of the multi-pass amplifier.

4.2.2. Amplification and output

Ideally, the multi-pass system provides constant mode sizes at the thin-disk matching the pump spot diameter to approximately 80% leading to an ideal spot diameter of 3.2 mm ($1/e^2$) on the thin-disk. A beam size slightly smaller than the active region in the laser material supports homogeneous amplification across the beam profile. Considering the damage threshold of the implemented optical elements ($< 1 \text{ J/cm}^2$) (Sec. 3.2.1), this spot diameter directly leads to a maximum output energy,

$$E_{\text{damage}} = \frac{1}{2} F \pi w_0^2 = 40 \text{ mJ}, \quad (4.1)$$

for a Gaussian beam. In terms of provided pump power (700 W) and based on experiences from CPA Yb:YAG thin-disk laser amplifiers that provide optical-to-optical efficiencies of $\simeq 30\%$ [35, 95], the system can provide output powers of $\simeq 200 \text{ W}$. The average power in combination with the damage energy yields to a repetition-rate of $\sim 5 \text{ kHz}$ that would lead towards the limits of laser pulse amplifier. With respect to these estimations the goal of the amplifier is the crossing of the 10 mJ pulse energy limit, which would be comparable to state of the art CPA based amplifier systems.

To reach this goal, the regenerative amplifier needs to deliver pulses with enough energy so that the limited number of amplification cycles as provided by the multi-pass system suffice to boost the energy to the desired level. As described in chapter (3), the regenerative amplifier provides energies of up to $\sim 2 \text{ mJ}$ - 5 mJ . Thus, the gain of the multi-pass needs to reach at least a factor of 5 to reach the desired pulse energies. The necessary gain directly determines the required number of amplification passes in the multi-pass system. In addition, due to the non-linear broadening in the regenerative amplifier it is beneficial to seed the multi-pass amplifier with

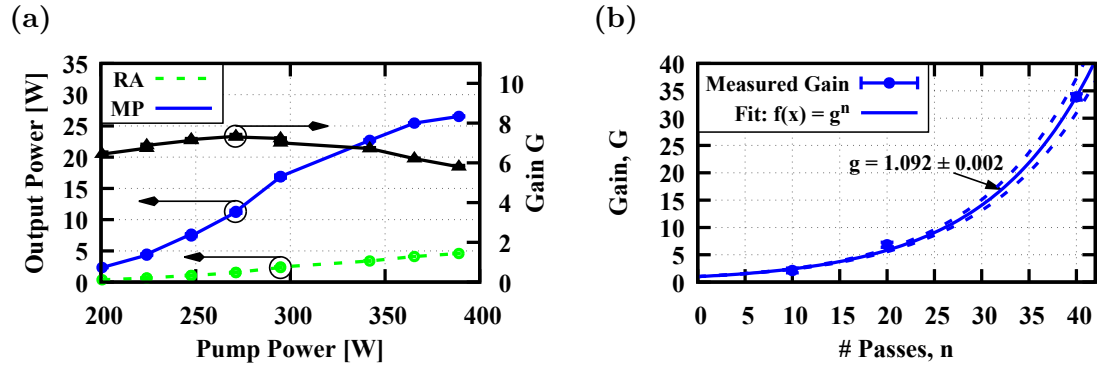


Figure 4.4.: (a) Power measurement of multi-pass (MP), regenerative amplifier (RA) and the calculated gain. (b) average gain evaluated from three measurements as shown in (a) for different number of passes through the thin-disk. The x-axis represents the number of passes through the thin-disk. Dashed: Upper and lower bounds of the fit.

pulses of ~ 1 mJ to avoid intensive reduction of the single pass gain due to gain narrowing. Being influenced by the regenerative amplifier, the total gain within the multi-pass system needs to be measured to determine the number of passes needed to fulfill the requirements. In the following, the gain is accessed via the ratio of the output power, P_{MP} , of the whole amplifier (regenerative + multi-pass amplifier) depending on the output power of the regenerative amplifier P_{RA} . The total gain of the multi-pass is defined as:

$$G = \frac{P_{MP}}{P_{RA}}. \quad (4.2)$$

To measure the power of the regenerative amplifier without influencing the amplification process in the multi-pass system, an output coupler with 99.5% reflectivity guided the beam towards the multi-pass amplifier (Fig. 4.2). The transmitted 0.5% of the power were recorded with a 3 W power head (Ophir 3A-P-V1) that was calibrated prior to the measurements. The round trip time was set to $3.28 \mu\text{s}$ corresponding to 84 full amplification round trips inside the laser resonator. The total number of passes over the thin-disk prior to entering the multi-pass amplifier is $2 \cdot 84 = 168$ because of the linear resonator.

Figure (4.4a) shows the power measurement for 20 extra passes through the thin-disk that are realized with the multi-pass system. As both system are optically coupled, the powers of both the regenerative amplifier and the multi-pass amplifier increase at the same time. The calculated gain of the multi-pass (black, right y-axis) increases with moderate and decreases at higher pump powers. The decrease of the gain with higher pump power is attributed to several processes. The system was not optimized for efficiency, which leads to an optical-to-optical efficiency of only 7% at the highest tested pump power. The high pump intensities with the low power

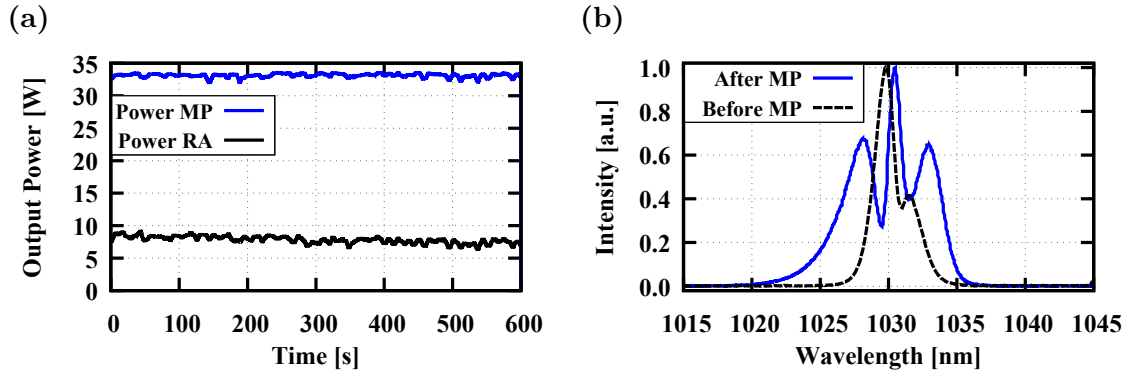


Figure 4.5.: (a) Power stability of regenerative (green) and multi-pass amplifier (blue). (b) Spectrum of the input and output pulses. The increased spectral bandwidth results from non-linear phase within the multi-pass.

extraction might lead to increased amplified spontaneous emission (ASE) or heat storage in the thin-disk that can reduce the gain. Misalignment of the system due to the increasing average powers and thermal heating could not entirely be excluded. Furthermore, the output pulses of the regenerative amplifier start to accumulate non-linear phase shifts, which results in a broader spectral bandwidth prior to entering the multi-pass amplifier. The larger spectral bandwidth contributes to reduction of the total gain due to reduced overlap with the peak of the emission cross section of Yb:YAG.

The measurement was repeated for the 10 pass and the 40 pass configuration. The average gain that was achieved with the different number of passes through the thin-disk is shown in figure (4.4b). An exponential fit gives a single pass gain of 1.092 ± 0.002 at 5 kHz. From the results it can be derived that the simple 20 pass configuration yields to a gain of 8, which would allow for amplification of a 1-2 mJ pulse to 8-16 mJ. The measured gain in the 40 pass configuration amounted to 33 and similar energies could be achieved with an input energy of 0.25-0.5 mJ.

Although the system was not fully optimized with respect to efficiency, it was capable of reaching the damage threshold of the implemented high-reflective (HR) mirrors. With 20 transitions through the thin-disk the hybrid system delivered up to 6.6 mJ (Fig. 4.5a) prior to optical damage of the high reflective mirrors was observed. To achieve these energies the mode within the multi-pass amplifier was adjusted at the folding components (Fig. 4.3, grey) with convex mirrors to compensate for the ~ 20 m concave radius of curvature (RoC) of the thin-disk.

The output spectrum after the multi-pass system is significantly broader than the input spectrum that is provided by the regenerative amplifier (Fig. 4.5b). The difference can be attributed to self-phase modulation (SPM) within the multi-pass amplifier. At pulse energies of ~ 6 mJ the ~ 3 mm mode diameter leads to intensi-

ties of $> 150 \text{ GW/cm}^2$ on the optical elements. Table (4.1) summarizes the non-linear parameters and the effective propagation lengths inside the multi-pass system for the involved optical components. The calculated values for non-linear lengths [Equ. (1.95)] of the implemented TFP, the thin-disk and air reveal that the main contribution to the non-linear phase is given by air. The achieved pulse energy is close to the critical power of air leading to pulse energy limitation because of the long propagation distance within the multi-pass. As optical damage was always observed within the system at these pulse energies the damage mechanism is attributed to the self-focusing (SF) of air. The resulting output pulse and second-harmonic frequency-resolved optical gating (SH-FROG) spectrogram (Fig. 4.6) is significantly different to those observed in chapter (3) (Fig. 3.12b and 3.11), which is mainly attributed to the higher pulse energy and the increased influence of air in the system. The full width at half maximum (FWHM) of the pulse is 670 fs, which is slightly less than the 1.2 ps input pulses. This is also considered as an indication of more complex non-linear influence on the pulse caused by the diatomic molecules (oxygen and nitrogen) of air. Effects similar to this but with slightly different parameters have been observed in context of the spectral broadening scheme described in chapter (5).

Evacuation of the system would be an effective solution to avoid the non-linear phase accumulation. Unfortunately, the mechanical setup misaligned during evacuation and the small aperture of the implemented mirrors led to clipping of the beam. This instability prevented the usage under vacuum conditions and is one of the reasons for the suggested imaging system that is described in section (4.3.1).

The system has also been operated at 10 kHz with 40 passes leading to similar output energy of 6.5 mJ and 65 W output power prior to reaching the limit of optical damage. Thus, the concept is easily scalable in average power, as expected.

10 mJ pulse energy with a 3.2 mm beam diameter in combination with the 4.1 mm pump spot at the $\sim 0.1 \text{ mm}$ Yb:YAG thin-disk leads to well known chaotic effects of the output pulse energy (Sec. 2.1.4). In the described hybrid system chaotic effects set in at pulse energies comparable to $\sim 5 \text{ mJ}$. At these pulse energies bifurcations have been observed, which led to pulses carrying distributed amounts of energy. Operation of the amplifier at these energy levels often led to optical damage when

	L [mm]	$n_2 [10^{-20} \text{ m}^2/\text{W}]$	L_{NL} [mm]
Air	35600	$2.9 \cdot 10^{-3}$ [160]	3330
FS	22	2.7 [144]	3.6
YAG	4.5	6.5 [141]	1.5

Table 4.1.: Non-linear lengths, L_{NL} , for fused silica, YAG and air for 1 ps pulses carrying 6 mJ energy.

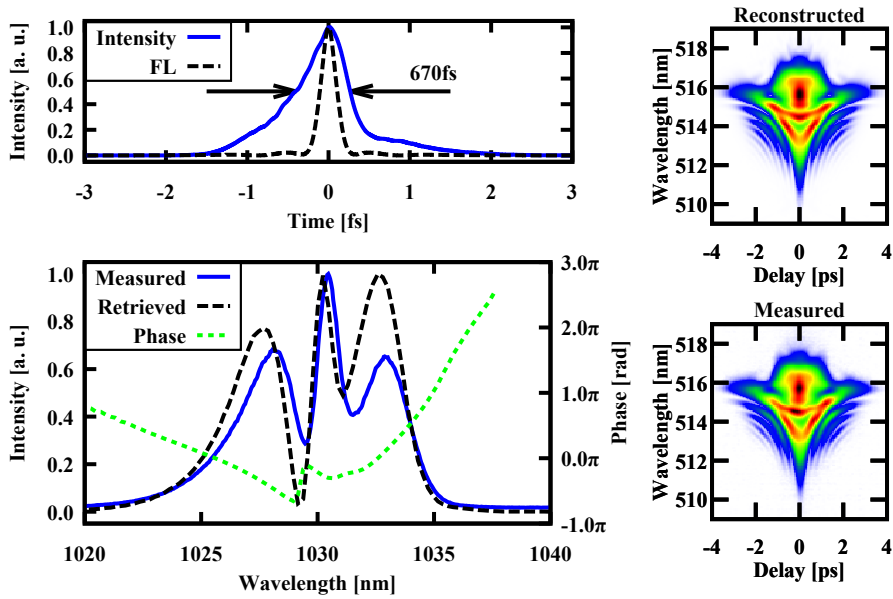


Figure 4.6.: SH-FROG measurement of the 6.6 mJ output pulses from the hybrid amplifier realized with a 20 pass multi-pass configuration.

splitting of the pulse energy occurred. This is because the average output power remains constant but one pulse suddenly carries significantly more energy than 6 mJ energy and damages the multi-pass mirrors. At average powers of 55 W an energy distribution of $\sim 3:1$ at 10 kHz was visible prior to damaging the system. The resulting pulse energy distribution is then 1.4 mJ in one pulse and 4.1 mJ in the other pulse. Splitting of this kind is introduced by increasing the pump power and can in combination with mechanical instabilities lead to sudden changes of the pulse energy.

In spite of these effects, the next section focuses on improvement of the multi-pass system. Special attention is directed on the multi-pass caustic being the origin for the pulse energy limitation. The analysis leads to the conclusion that a simple non-imaging multi-pass amplifier prevents the system from reaching the limits set by the damage threshold at 3.2 mm beam size. Therefore, an imaging multi-pass is suggested. The analysis illustrates that this approach is more robust to changes and offers control of the beam caustic and fluences under the influence of changing pulse energy.

4.2.3. Limitations and further design analysis

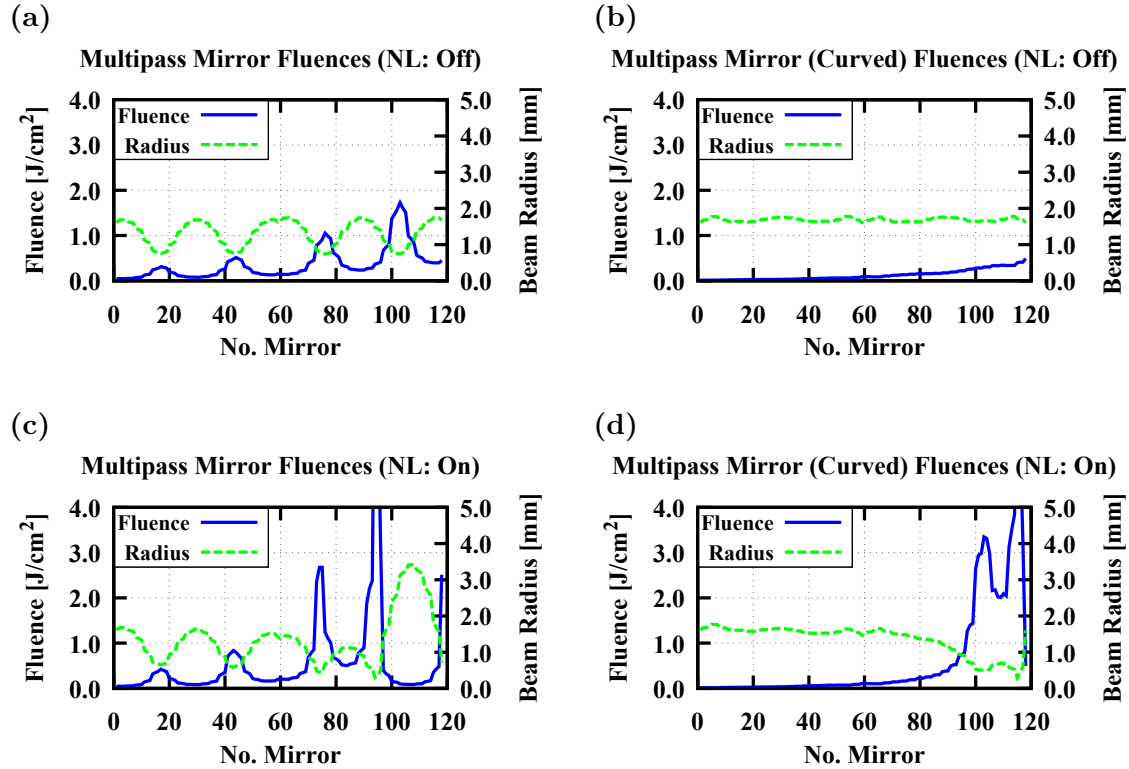


Figure 4.7.: Simulation of the beam caustic (dashed) and fluences (solid) on each mirror within the multi-pass assuming constant gain of the thin-disk up to 20 mJ pulse energy. (a) multi-pass contains only flat optics and the non-linear lens is switched off. (c) same as (a) but the non-linear lens is switched on. (b) multi-pass corrected with convex mirrors, non-linear lens is switched off. (d) same as (b) with non-linear lens.

In a first attempt the multi-pass incorporated just flat HR mirrors to transport the beam. The beam caustic is then determined by the focal length of the thin-disk being the only (linear) refractive component in the system. The resulting beam caustic shows oscillations depending on the initial beam size and radius of curvature of the wavefront. In the experiment, the qualitative behavior of the mode could only be observed with an IR-card. The observed changes of the mode size build the basis for the following calculation of the beam caustic. Figure (4.7a) is the result of a calculation based on ABCD-matrix propagation of Gaussian beams. The model assumes a RoC of the thin-disk of 22 m and an input beam $1/e^2$ -radius of 1.6 mm with a flat wavefront. In addition, the calculation assumes simple exponential growth of the pulse energy to include the effect of amplification. The beam path lengths are matched to the distances of the experiment (Fig. 4.2).

The resulting beam waist shrinks until it reaches a minimum. In this model the minimum corresponds to mirror #17 (Fig. 4.7a). Diffraction then leads to beam expansion until the refractive power of the thin-disk compensates the divergence. The fluences follow the beam size and increase steadily due to the exponential increase of the energy. At a certain point the fluence exceeds the damage threshold of $\sim 1 \text{ J/cm}^2$ (Sec. 3.2.1). According to the calculations the energy of the pulse at point of reaching the damage threshold amounts to 8-9 mJ. As compared to the experiment this is almost 5 times higher than the energy achieved in this configuration.

Compensation of the steady focusing led to output pulses with $> 6 \text{ mJ}$ energy. In accordance with the experiment, the simulation compensates the refractive power of the thin-disk with convex mirrors that have large radii of curvature ($> 15 \text{ m}$). Figure (4.7b) shows that the caustic describes a well defined beam waist that alters only within acceptable values. In the experiment, however, implementation of curved mirrors always led to random results in the beam behavior which was later confirmed to be the accuracy of the radii of curvatures as produced by the manufacturer. Interferometric measurements revealed a deviation of the RoC of the mirrors from the specified value with up to $> 20 \%$.

Further analysis exposes another optical property of the multi-pass configuration that might lead to optical damage prior to reaching the 20 mJ output even if the system is operated in vacuum. The increasing energy during the amplification process is likely to cause a non-linear lens introduced by the thin-disk. Although the thickness is with $\sim 0.1 \text{ mm}$ comparably thin the pulse energies suffices to introduce a non-linear lens large enough to cause focusing of the beam. The refractive power of the non-linear lens is [149]

$$D = \frac{4n_2L}{\pi w^4} \cdot P_{peak} = \frac{4n_2L}{\pi w^4} \cdot \sqrt{\frac{4 \ln 2}{\pi}} \frac{E}{\tau_{FWHM}}. \quad (4.3)$$

Assuming a beam diameter of 3.2 mm, 2 mJ pulse energy, $\tau_{FWHM} = 1 \text{ ps}$ and $n_{2YAG} = 6.5 \cdot 10^{-16} \text{ cm}^2/\text{W}$ (Tab. 3.1), the refractive power of 0.1 mm YAG amounts to 10% of the refractive power introduced by the 22 m RoC of the thin-disk. Consequently, the non-linear lens contributes, once the energy exceeds a few millijoule. Figures (4.7c) and (4.7d) depict the influence for the different configurations. Choosing only flat mirrors leads to an increased amplitude of the beam size oscillations that lead to fluences exceeding the damage threshold after mirror ~ 40 . This corresponds to a full double pass through the multi-pass amplifier and a pulse energy of 4.5 mJ. Compensation of the refractive power of the thin-disk with convex curved mirrors leads to a constantly larger beam and to a shift of the predicted damage to mirror 95 (≤ 3 passes) and $\sim 10 \text{ mJ}$ pulse energy.

The calculation applies to any other distortion that leads to changing focal lengths of the thin-disk. A thermal or stress induced lens can not be well compensated. In this system the changing focal length leads to accumulation of the

effect and causes either higher losses because of a diverging beam or oscillations of the beam waist on the HR mirrors. The latter reduces the achievable output energy. The first situation is unwanted because of beam profile distortions caused by clipping on finite apertures.

The calculated threshold values for a non-linear lens are close to the measured 6.6 mJ being the highest pulse energy achieved with this setup. The calculations do not include the influence of air, although the effect might be dominating due to the large propagation distances in the medium. Experimental data did not allow to distinguish between the contribution of air and the thin-disk as operation of the multi-pass system in vacuum was not reliable, for stated reasons.

In summary, the multi-pass design based on flat optics leads to a good control over the beam diameter. In this configuration the beam did not grow to sizes above the clear aperture of the 1/2"-mirrors. However, the repetitive focusing caused by the finite RoC of the thin-disk leads to increased fluences and, therefore, to optical damage. Adjustment of the mode inside the multi-pass with mirrors of low refractive power turns out to be complicated and not reliable due to optical tolerances and sensitivity of the mode with respect to the exact choice of the implemented optics. Gaussian beam propagation further reveals the instability of the setup with introduced non-linear lenses that are expected for the desired pulse energy range. The multi-pass system as designed and implemented in the laboratory has, therefore, been operated as its limits and further optical design improvement of the setup is necessary. Pulse energy limitations caused by the stored energy inside the thin-disk could not be observed, so far.

4.3. Outlook

The solution to the observed restrictions is one of the challenges that is described in this section. Together with Robert Lange an imaging multi-pass system was developed that is thought to handle all mentioned effects and is less prone to non-linear optical changes.

4.3.1. Imaging multi-pass amplifier

Using an imaging system has two very important advantages

1. constant mode size on the thin-disk,
2. controllable mode size on the imaging optics.

The ideal optical system possesses both characteristics and transports the beam over the thin-disk whilst being stable against the discussed dynamic parameters. Considering the 4f-configuration (Fig. 2.7) and knowing that thin lenses resemble the Fourier transform of the field in the focus, the system applies the Fourier twice.

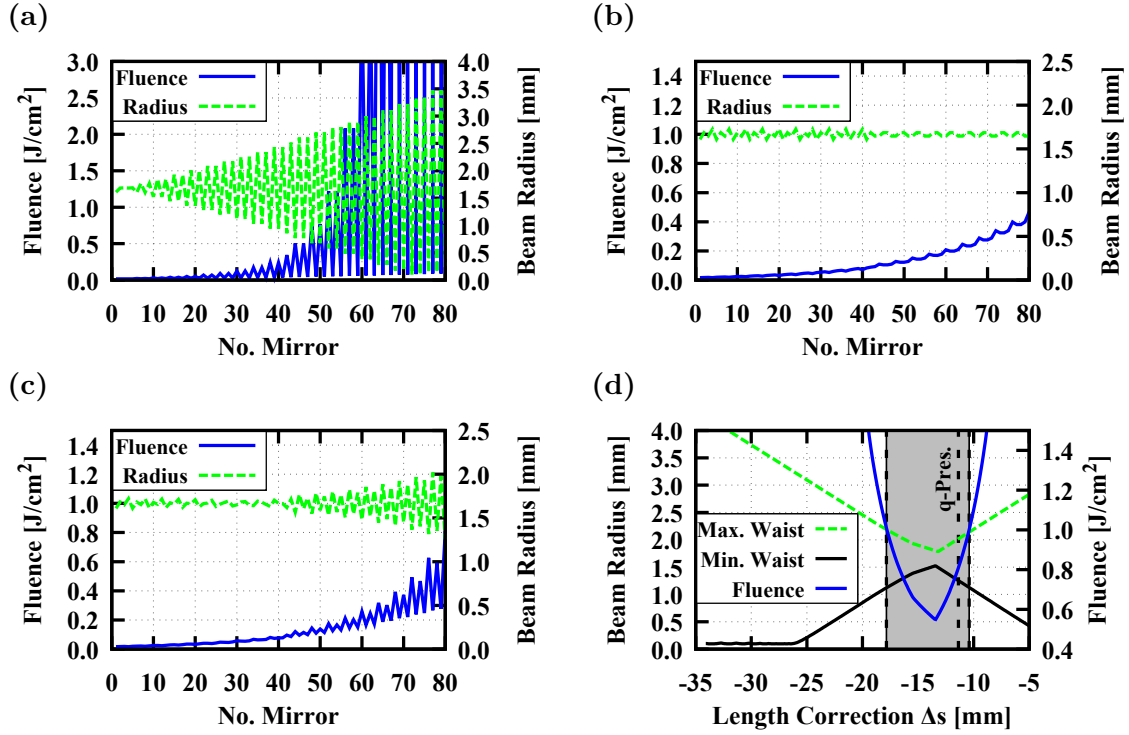


Figure 4.8.: (a) Beam caustic (dashed) and corresponding fluences (solid) of a 4f-imaging system with a curved optic every second imaging plane ($RoC_{disk}=22$ m). (b) same imaging system as (a) with decreased telescope length. (c) Effect of an increasing (non-linear) lens at the position of the thin-disk. (d) Minimum and maximum beam waist on the mirrors depending on Δs (here $2f = 1.0$ m). Operation below the damage threshold (shaded area). “q-Pres.” marks the q-preserving distance without non-linear lensing (b).

Once with the first lens and a second time with the second lens. This means that the field is resembled in the imaging plane at distance equal to the focal length f behind the two lenses. Because of this property the ideal 4f-imaging system can be applied many times without changing the field characteristic. The field at other planes within the system is defined by the exact phase and shape of the input field. A collimated Gaussian beam ($z_R \gg f$) propagates to the first imaging optic, is focused and the focus is located at as distance f behind the optic. Reaching the second imaging optic the beam possesses its initial size and is collimated by the second imaging optic. The field with its initial parameters emerges at distance f from the second imaging optic.

4f relay-imaging systems that implement one and the same optic at the imaging planes tend to degrade the beam quality and/or alter the beam propagation parameters. This is often directly visible at planes different from the imaging plane.

The distortion of the beam and its wavefront caused by the optic in the imaging plane results from deviations from an ideal flat shape of the optic. The phase shifts imprinted on the wavefront add up, which depending on the optic leads to degraded beam quality or mode radii oscillations. Perfect curved optics introduce a constant parabolic phase to the wavefront of the beam that results in increasing mode radii on one imaging optic, whilst developing decreasing mode radii at the other (Fig. 4.8a). The calculation used for figure (4.8a) propagates the beam through an imaging system equal to figure (2.7) with the difference that a curved optic with $\text{RoC}=22\text{ m}$ is located at the left imaging plane and a flat optic is located in the other imaging plane. The imaging system is constructed to repeatedly image the fields from one plane to the other and vice versa. The calculation shows the mode size of a Gaussian beam on the imaging optics. As described above the beam starts growing and shrinking on the imaging optics resulting from the focusing element. The slight but repeated focusing at one imaging plane shifts the focus from the center of the imaging system to the first imaging optic. Defocussing of the beam leads then to a larger mode size on the second imaging optic. The situation aggravates and leads to small modes on the second imaging optic, which would limit the output energy of the system. The imaging system allows for correcting these oscillations if the involved optical elements introduce parabolic phases to the beam (ideal parabolic mirrors or perfect thin lenses). This is achieved by adjusting the distances of the imaging system so that it incorporates the distance f from the imaging plane to the imaging optic, $L_{Tele} = 2f - \Delta s$ (Fig. 2.7) and f from the second imaging optic to the second imaging plane. The distance Δs is calculated from the q-preserving condition [Equ. (2.20)] [161, 162]. A system that implements an optical component with refractive power D_{ref} in every second imaging plane the solution of the q-preserving condition gives

$$\Delta s = \frac{1}{2}f^2 D_{ref} = \frac{1}{4} \frac{R_{im}^2}{R_{disk}} \quad (4.4)$$

where f is the focal length of the imaging components. The correction factor for a multi-pass system based on HR mirrors with RoC of R_{im} in combination with a thin-disk with RoC of R_{disk} is then given by the right side of equation (4.4). The effect of the corrected telescope length is shown in figure (Fig. 4.8b). The imaging system without any other distortion obviously leads to a well controlled mode.

High intensities and the increasing refractive power due to non-linear lensing of the thin-disk leads to decreasing beam waists on the imaging mirrors (4.8b). As the non-linear lens develops dynamically during the amplification cycle, full compensation of the refractive power is not possible with linear optical elements. It is possible, however, to adjust the system for optimized mode behavior even with the non-linear lens. Figure (4.8d) shows the mode maxima and minima for the 4f-imaging system depending on the deviation from the ideal 2f-distance of the imaging mirrors (here $2f = 1.0\text{ m}$). Clearly, the minimum and maximum waists

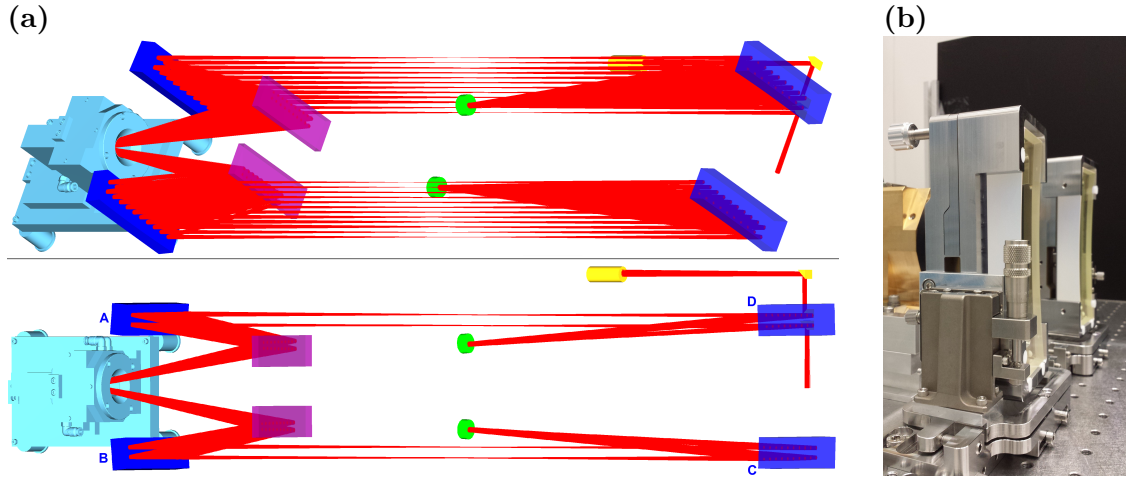


Figure 4.9.: (a) Image of the imaging system as implemented in Zemax by Robert Lange within the scope of his Master thesis. (b) The mechanical setup as developed by me and Florian Saran.

reach a point of least deviation at a distance $\Delta s \approx -14$ mm. This corresponds to a telescope distance of $1.0 - 0.014$ m that is slightly shorter than the q-preserving distance without the non-linear lens. Within the gray shaded region the multi-pass amplifier operates well within the damage threshold of the optical elements for all passes through the amplifier including the effect of non-linear lensing caused by the ~ 0.1 mm thin-disk.

These calculations reveal that the imaging system is by far less prone to dynamic changes as compared to the tested non-imaging system. Adjustment of the telescope length provides a simple method for compensation of both the refractive power of the thin-disk and the developing non-linear lens. Notice that compensation of the system is also possible using curved optics in the imaging planes.

Design

Together with Robert Lange a 4f-imaging multi-pass system was developed [163] that both fulfills the discussed requirements and the restrictions resulting from finite space in the laboratory. The imaging system as depicted in figure (4.9) uses only 4 curved, concave 1 m, imaging mirrors to implement more than 20 passes over the thin-disk. This is possible with a beam of ≤ 4 mm diameter and rectangular mirrors with 40×140 mm² clear aperture that guide the beam through the setup. Sending the beam after 20 passes back through the system permits 40 passes over the thin-disk without the need for an additional isolation stage as in case of the

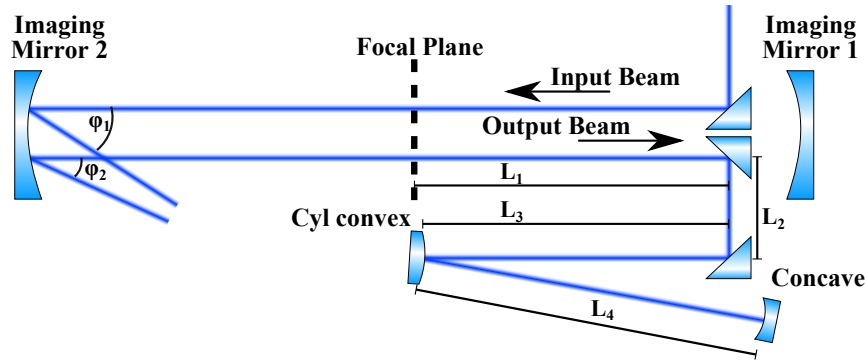


Figure 4.10.: Setup to compensate the astigmatism of the imaging multi-pass setup. Picture shows the lowest plane of the upper half of the imaging system of figure (4.9a).

multi-pass described in the previous sections. With the results presented in the previous sections the system should be capable of reaching > 100 W at 10 kHz repetition rate.

The system embodies a 4f-imaging using both lateral coordinates to guide the beam over the thin-disk. The thin-disk is located in one of the imaging planes (Fig. 4.9, left). The second imaging plane consists of flat mirrors but might be used to adjust the mode with curved optics. To change the beam path through the system the beam is shifted with the mirrors in the second imaging plane to another position on the curved imaging optic. Being in the imaging plane a change of the beam direction leaves the position in the imaging planes unaffected but relocates the beam on the imaging optics. Correct adjustment of the system leads to a rectangular beam pattern on the imaging optics. In- and output beams are coupled to the system on the lowest plane with mirrors located in front of the imaging mirrors (Fig. 4.10).

Due to the asymmetry in x- and y-direction the system suffers from increasing astigmatism. A combination of a cylindrical with a concave mirror, however, suffices to fully compensate for the astigmatism at the output of the system. This configuration is based on a concentric retro reflection of the beam into itself. Ideally, the beam then propagates through the imaging system with its predefined caustic. Different effective curvatures along x- and y-direction resulting from the finite angle of incidence (AOI) lead to different focal planes of the beam in both directions. A retro reflection with a fixed concave optic of RoC, R_{end} , is then only possible for one of the two distinct axis. The cylindrical convex optic in front of the concave mirror allows for an effective reduction of the optical power in one axis (here x-axis) by adjusting its distance to the concave end mirror (Fig. 4.10). The former stays at fixed distance to the focal plane of the beam on the y-axis (sagittal) meaning that $\sum_i L_i = R_{end}$.

The setup of the imaging system allowed to prove that compensation of the

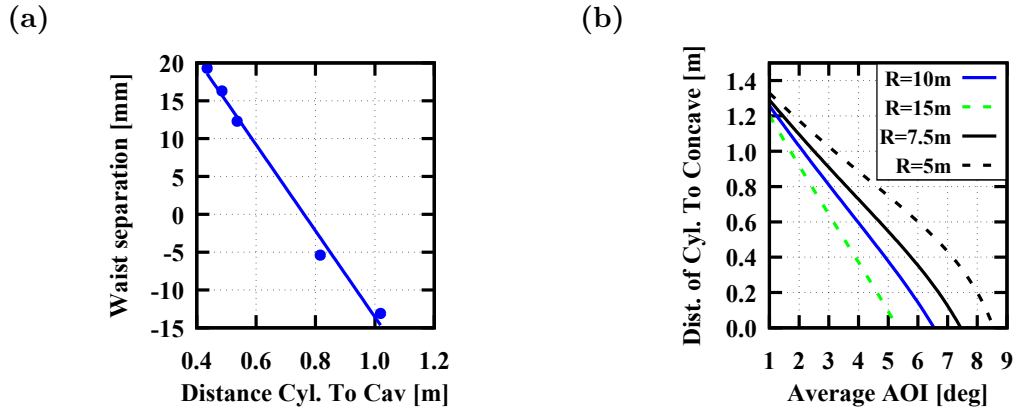


Figure 4.11.: Characterization of the astigmatism. (a) Measurement of the different waist positions for x- and y-direction of the beam with respect to the distance L_4 . (b) Calculated optimum distance of the cylindrical to the spherical mirror depending on the average AOI on the curved imaging optics.

introduced astigmatism is well working. To characterize the behavior of the astigmatic beam with respect to the distance L_4 , a Spiricon M-200 M²-meter was used to measure the positions of the waists for both x- and y-direction. A distance, L_4 , of approximately 720-740 mm leads to compensation of the astigmatism with a cylindrical, convex 10 m and a spherical concave 1.5 m mirror (Fig. 4.11a). The compensation is most sensitive to the average AOI on the curved optics. The implementation in the laboratory showed an AOI of approximately 3.2° . The simulation predicts 733 mm for this angle, which is good agreement with the experimental setup and results retrieved from the intersection of the fit (Fig. 4.11a) with the abscissa at 760 mm. Figure (4.11b) shows the solutions for different radii of the cylindrical mirror depending on the average AOI. Clearly, the system allows compensation up to 8° with a convex, cylindrical 5 m mirror. Lower angles should be compensated with radii exceeding 10 m to avoid proximity to the focal plane and small beam diameters on the cylindrical optic.

The system has successfully been tested under vacuum conditions during the experiments presented in chapter (5). Mechanical instability of the components or misalignment have not been observed. As compared to the other non-imaging multi-pass system this configuration holds promise to allow reliable operation of the hybrid amplifier under vacuum conditions.

4.3.2. Summary

This chapter discussed the amplification of femtosecond laser pulses within a hybrid amplifier. This amplifier concept provides gain in with $> 10^7$ whilst relying

on a simple design without the need for CPA. It has been proven to work up to 6.6 mJ within a multi-pass setup based on simple geometrical displacement of the beam. The detailed analysis of the limiting effects illustrates that a design based on an imaging multi-pass system might reach pulse energies limited by the damage threshold of the optical elements, only. It has been shown that control over the non-linear, dynamic, lens is gained with an adjusted, astigmatism compensated setup. The imaging system has not yet been tested in the amplifier but promises outstanding performance. Pulse energies of more than 10 mJ are feasible. Therefore, the amplifier concept is at the edge of reaching pulse energies and amplification factors that otherwise are only realized with CPA.

Chapter 5

Pulse Compression in Gas Filled Multi-pass Cells

Non-linear pulse compression constitutes the key technology in state of the art laser systems to produce optical pulses well below durations that are supported by the amplification gain medium [22, 164]. Different schemes based on bulk compression [165], cascaded second order non-linear effects [153, 166] and hollow core fibers have been presented. All of which have their limitations. Bulk compressors using a single pass through the non-linear medium usually suffer from bad beam quality requiring a spatial filter that leads to high losses. Cascaded second order non-linear effects provide better beam qualities but are not useful for pulse energies above 1 mJ because of the large crystal apertures required for such systems. Hollow core fibers [22] still reach unprecedented pulse durations and high beam quality factors. For high average powers this scheme has recently been adopted to a fiber laser system resulting in 6.3 fs at 216 W and 170 μ J [30]. However, scaling this concept to higher pulse energies and average powers in the kW scale is complicated. Other pulse compression techniques for pulse energies of more than 1 mJ at average powers > 100 W providing reasonably good conversion efficiency maintaining high beam quality factors have been missing so far.

This chapter discusses non-linear pulse compression based on gas filled multi-pass cells. In detail, non-linear properties of different gases are enlightened and it is shown which gas is the most suitable to compress the laser described in section (3.6). In argon, a factor of 5.6 compression to 37 fs (full width at half maximum (FWHM)) is achieved. The results gained in this chapter are connected to the wave propagation equation used to describe the process with a 2D-split-step [78] simulation (Appx. A). Simulations and measurements of the fields in the experiment reveal that it is possible to give detailed information of the processes involved.

5.1. Introduction

Shortening laser pulses involves the application of non-linear optical effects that lead to a few undesirable effects that require good control over the process to avoid destruction of the pulse or the beam profile. The main non-linear process involved in most non-linear compression schemes is self-phase modulation (SPM) [22, 30, 167]. The effect introduces a phase to the laser pulse depending on the non-linear refractive index, n_2 , the laser intensity and the length, L , of the medium. The temporal variation of the intensity profile, $I(r, t)$, of the laser pulse then leads to a phase shift of,

$$\phi_{NL}(r, t) = \frac{2\pi}{\lambda} n_2 \int_0^L I(r, t, z) dz, \quad (5.1)$$

which introduces new spectral components to the laser pulse. In state of the art laser systems, pulse compression based on this effect is applied in fibers giving good control over the beam profile of the output. In free space this control is lost and the non-linear phase also follows the spatial intensity profile. As most laser systems provide Gaussian shaped beams $I(r, t, z) \propto e^{-r^2}$, the resulting phase shift is significantly larger in the center of the beam as compared to its edges. This leads to self-focusing (SF) which is considered undesirable as it causes a distorted spatial wave front and in the worst case causes damage to implemented optics. In the temporal domain, this intensity profile is the source for an inhomogeneous spectrum across the beam profile, which translates into a variation of the pulses temporal profile.

Because of this phenomenon a simple pass through a non-linear medium with a collimated beam leads to significant degradation of the beam quality resulting in useless output if significant compression factors are aimed for. In spite of these issues, the community is working on methods that deliver homogeneous spectral broadening in combination with a process that keeps the initial beam quality factor of the laser.

The authors of [150] proposed a bulk compression scheme that is based on introducing multiple, small non-linear phase shifts (< 0.1 rad) to the pulse whilst the beam propagates in between the single passes. Propagation inside a Herriott-cell [168] provides a compact setup to trap the beam and allows more than 50 passes through the bulk [151]. Herriott-cells fulfill the resonator stability condition (Sec. 3.3.1) and consist of two mirrors in between which the laser beam travels on a predefined off-axis beam path. Introducing small non-linear phase shifts followed by beam propagation shows well behaved beam profiles and leads to homogeneous spectral broadening [150, 151]. These setups incorporate only high reflective mirrors and thin bulk (fused silica) plates whilst using a moderate beam size well below

the damage threshold of the optical elements. Thus, it easily supports average powers of more than 200 W. However, the schemes aim for compression of pulses in the μJ -level.

Supporting non-linear pulse compression for lasers with multi-millijoule pulse energy is the topic of the following sections. A compression scheme is developed that benefits from introducing moderate phase shifts in a medium which is longer than the Rayleigh range of the focusing laser beam [169]. Propagation in combination with SPM supports homogeneous spectral broadening and avoids distortions that appear in setups solely relying on large non-linear phase shifts in a single non-linear medium. The authors of [170] published a theoretical analysis of this method also confirming the validity of the aforementioned properties. The developed setup allows pulse compression with high average powers $> 200\text{ W}$ as it is based on high reflective mirrors that easily support average powers of several kW. Furthermore, the method supports pulse energies over several tens of millijoules depending on the peak intensity in the focus of the system and the ionization potential of the gas. Scaling the setup to larger mode sizes within a setup of several meters in length easily allows mode sizes large enough to avoid ionization of He supporting several hundreds of millijoule pulse energy.

5.2. Simulation results

Interesting attributes of the non-linear affected pulses arise if their path is sliced into small sections whilst observing its properties. The observables that describe the beam to very good extend are the beam quality factor and the spectral inhomogeneity, IH , of the laser pulse. The latter can be described by the relative deviation of the extreme points of the Fourier transform limit (FTL) across the beam profile,

$$IH = \frac{\max FTL(r) - \min FTL(r)}{\min FTL(r)} = \frac{FTL_{max}}{FTL_{min}} - 1. \quad (5.2)$$

This quantity vanishes if the beam exhibits a homogeneous spectrum across its profile and increases with increasing spectral differences. As the FTL describes the theoretical limit of the pulse duration, the quantity IH provides a measure that describes the compressibility of the pulse with respect to its spatial variation.

Beam propagation was performed with a 2D-Split step simulation (Appx. A) that uses a Fourier transform limited $\tau_{\text{FWHM}} = 200\text{ fs}$ pulsed-Gaussian-beam [171] with quality factor of $M^2=1$, a homogeneous FTL across the profile and $1/e^2$ -beam-diameter of 3 mm. The focusing mirror is an ideal parabolic optic with 0.5 m focal length resulting in the beam caustic as shown in figure (5.1) and figure (5.2). The

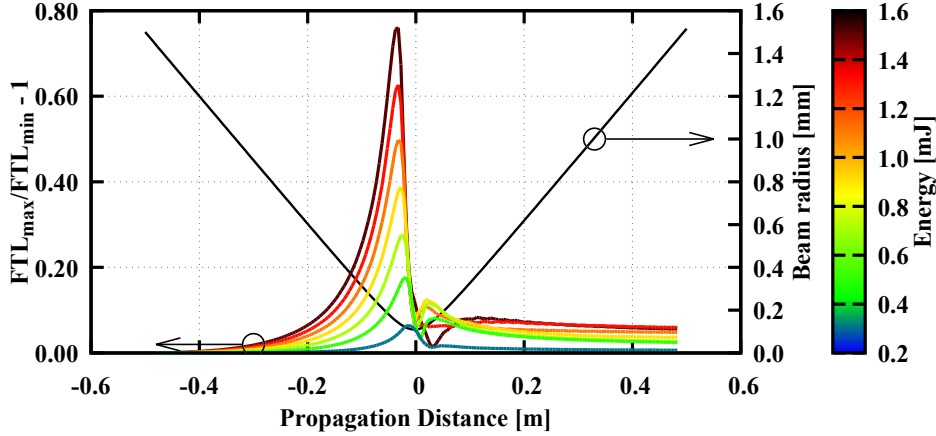


Figure 5.1.: Calculated spectral inhomogeneity, IH , of the beam in lateral direction vs. the propagation distance in a non-linear medium. Undistorted beam caustic (black).

non-linear refractive index is $n_2 = 2 \cdot 10^{-23} \text{ m}^2/\text{W}$ and the simulation applies solely intensity dependent phase shifts neglecting dispersion and self-steepening effects or other higher order contributions of any kind.¹

From equation (5.1) it is obvious that the central part of the Gaussian beam accumulates more non-linear phase than the outer regions with lower intensity. Consequently, the central region of the beam develops more spectral components and the inhomogeneity increases. Figure (5.1) shows this effect for the regions in front of the focus (negative values). Approaching the focus the inhomogeneity increases rapidly and reaches a maximum shortly before reaching the beam waist. The crucial point in the evolving propagation is reached behind the focus. Here, the homogeneity increases which is expressed in a decreasing inhomogeneity, IH . The origin of this effect lies in the spatial non-linear accumulated phase shift that increases the curvature of the central spectral broadened region of the pulse. The increased curvature in the central parts of the beam leads to larger convergence and a focus shifted to the left as compared to the undistorted beam. As the central part of the beam focuses earlier than the outer parts, spectral components in the center of the beam propagate towards the outer parts and vice versa. The spectral broadened parts are suddenly in the outer, less intense, regions of the beam profile whilst the components less affected by the non-linear phase shift are found in the central, high intense, part of the beam. With further propagation through the non-linear medium the beam restores the homogeneity by spectral broadening of the now centered, spectral narrower, part of the beam to very good extend. After propagation through the focus the beam resembles only minor variations of the spectrum across the profile.

¹The value of n_2 corresponds to one of the literature values of argon (Tab. 5.1)

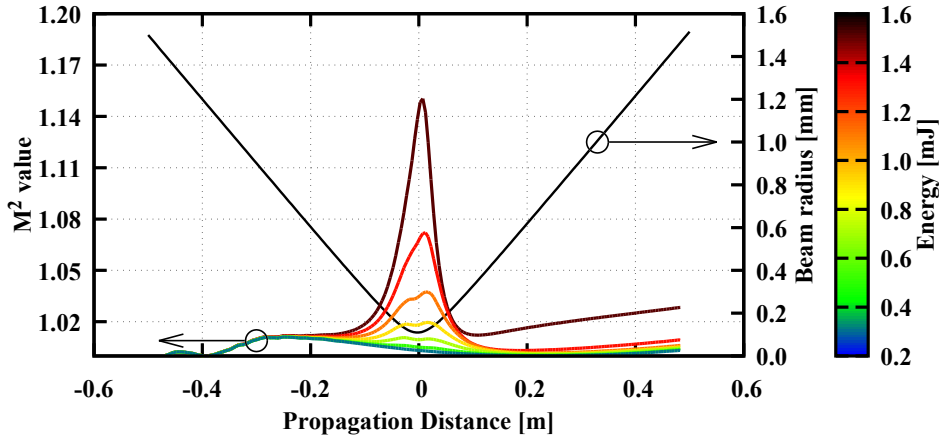


Figure 5.2.: Calculated beam quality factor (M^2) vs. propagation distance in a non-linear medium. Undistorted beam caustic (black).

The beam quality factor exhibits a similar behavior as the inhomogeneity of the beam (Fig. 5.2). With increasing proximity to the focal point the beam quality degrades (increasing M^2). Shortly behind the focus, the beam restores the spatial wavefronts by introducing non-linear phase to parts of the beam that were not affected before the focus.

Considering the final M^2 and IH values, a fundamental difference is observed. Whilst the inhomogeneity approaches a defined value, the M^2 parameter increases more quickly after the process. The rapid degradation of the beam quality sets a limit to the acceptable non-linear phase shift within a single focus. Therefore, large non-linear pulse compression factors maintaining the beam quality factor demand propagation through multiple foci with moderate non-linear phase shifts. It is likely that this effect is identical to the observations in Herriott-cells with bulk materials [150, 151].

The following sections explain the experimental results obtained with a multi-pass cell setup allowing for compact implementation of many foci to benefit from this result.

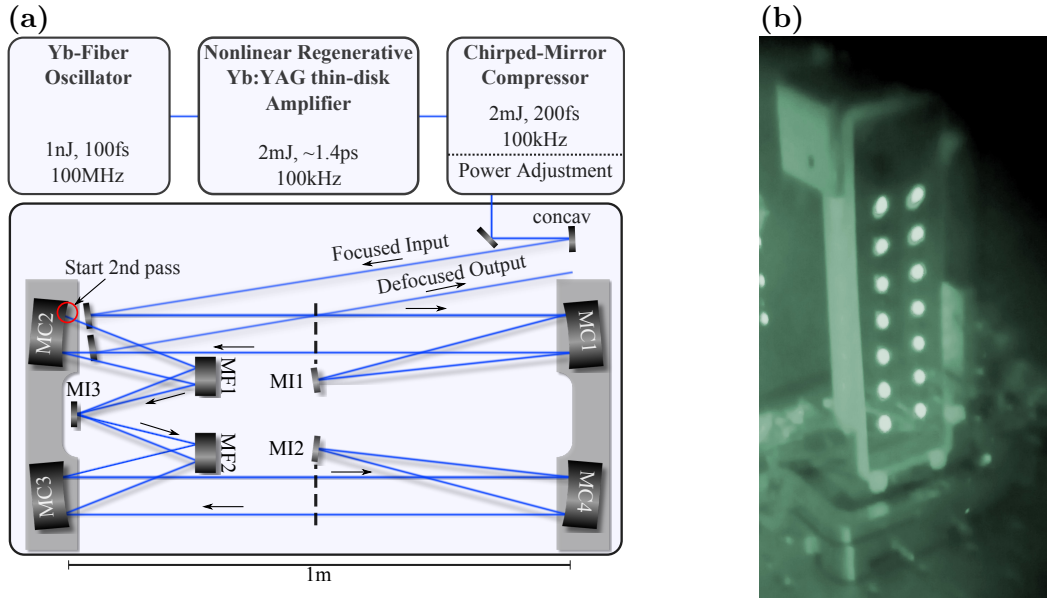


Figure 5.3.: (A) Schematic picture of the setup. (B) Beam pattern on a high reflective imaging mirror

5.3. Multi-pass cell setup

The setup is based on the non-linear regenerative Yb:YAG thin-disk amplifier described in (Sec. 3.6). The amplifier emits 210 fs pulses after compression carrying 2 mJ pulse energy. At 100 kHz repetition-rate this corresponds to 200 W average power. The peak power of the pulses amount to 7.3 GW. After the chirped mirror compressor the laser beam passes a half-wave plate and a thin-film polarizer allowing power adjustment and control over the intensity inside the multi-pass system.

The considerable power of the laser and the resulting fluences easily reach the damage threshold of applied optics. Having in mind that the damage fluences of the mirrors are $\sim 1 \text{ J/cm}^2$ (Sec. 3.2.1), the beam caustic should exhibit beam profile diameters in the order of 3 mm at the locations of optical elements to be significantly below this value. In the experiment a mirror with 3 m radius of curvature focuses the beam to 200 μm leading to a $1/e^2$ -beam-diameter of 3.2 mm and 0.05 J/cm^2 fluence on the optics.

Within the 4f-imaging multi-pass cell the beam propagates in three dimensions through the optical setup (Fig. 5.3a). The setup incorporates four concave mirrors (MC1-MC4) with a radius of curvature of 1 m separated by 1 m. The concave mirrors have a size of $140 \times 40 \text{ mm}^2$ supporting enough aperture to guide the 3.2 mm beam up to ~ 20 times over a single mirror. Three 1 " mirrors (MI1-MI3) are located at the imaging planes in 0.5 m distance from the curved optics. Tilting one of these

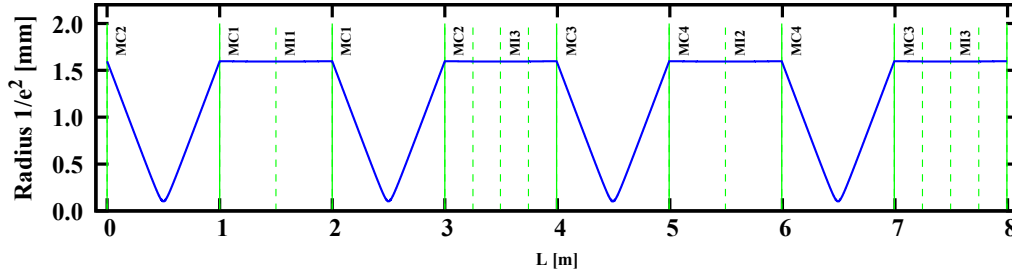


Figure 5.4.: Beam caustic of one round-trip inside the multipass cell.

mirrors increases or decreases the number of passes through the multi-pass cell. Additionally, two mirrors with an aperture of $100 \times 30 \text{ mm}^2$ (MF1, MF2) are folding the beam pulling the left and right imaging planes apart.

The setup focuses the beam 4 times during one full round trip (Fig. 5.4) leading to 26 foci for the implemented 6 passes. Additionally, input and output introduce 2 foci so that the setup contains 28 foci, in total. Figure (5.3b) shows the beam pattern on one of the imaging mirrors. The number of reflections on the high-reflective (HR) mirrors add up to $16 \cdot 6 + 2 \cdot 3 = 102$. The considerable amount of reflections lead to a loss of $\Lambda \approx 1 - 0.9995^{102} \approx 5\%$.

The repeating focusing of the beam leads to weak plasma channels within the gas (Fig. 5.5b). The length of the visible plasma channels corresponds to twice the Rayleigh length of the focusing beam and thus to places of highest intensity. These channels are at constant position within the cell.

5.4. Comparisson of different gases

Implementation of non-linear pulse compression based on gases is connected to the question which gas is the most suitable for the 2 mJ, 210 fs pulses of the laser system and at which pressure. Knowing that the non-linear mechanism is mainly based on SPM, it is important to consider the non-linear refractive indices (n_2) of the different gases. Table (5.1) shows a summary of measurements of this value for noble gases and the values for the instantaneous response of selected of molecular gases and air. All those values are of the order $10^{-23} \text{ m}^2/\text{W}$. However, considering the variation of the values it is necessary to benchmark the non-linear process.

Measuring the influence of the different gases demands good knowledge of the input beam intensity along the propagation direction. To determine the input beam characteristics, the beam caustic was measured along the beam propagation direction with a beam profiler. Based on these measurements the input peak intensity in the focal plane for the first pass is calculated to $60 \text{ TW}/\text{cm}^2$. The $1/e^2$ -

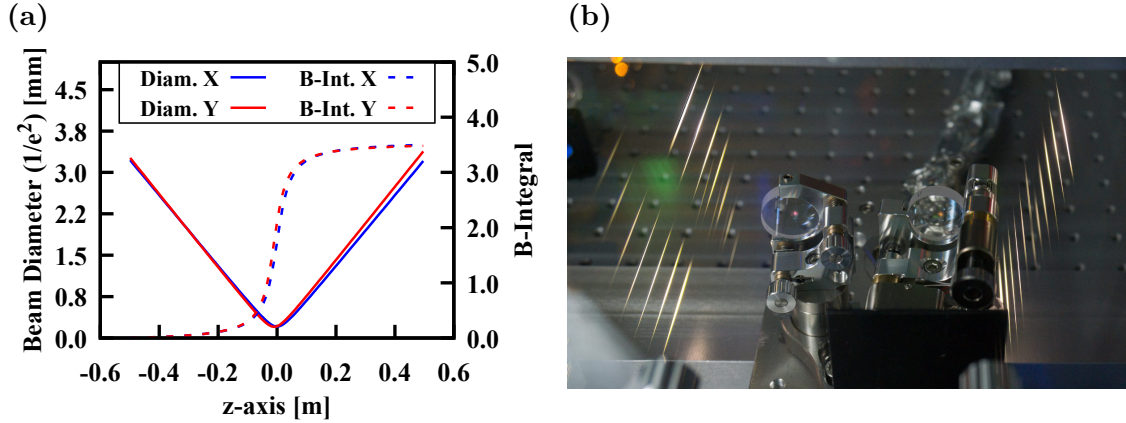


Figure 5.5.: (a) Measured input beam caustic (y-axis, left) and the calculated B-Integral (y-axis, right) for $n_2 = 10^{-23} \text{ m}^2/\text{W}$. (b) Picture of the plasma channels. Two rows on the left and two rows on the right corresponding to the rectangular beam pattern of the setup (picture: Kilian Fritsch).

diameter of the focus is $200 \mu\text{m}$ and a fit to the measured beam profiles along the propagation axis yields the beam caustic (Fig. 5.5a) and the beam diameter at the imaging mirror MC1 (3.2 mm). Figure (5.5a) also shows the B-Integral,

$$B_{peak} = \frac{2\pi}{\lambda} \int n_2 \max_{r,t} I(r, t, z) dz \quad (5.3)$$

for a paradigmatic non-linear refractive index of $10^{-23} \text{ m}^2/\text{W}$. The accumulation of a non-linear phase shift of this amount significantly alters both temporal and spatial properties of the pulsed laser beam. Additionally, the 7.3 GW peak power of the driving laser exceeds the critical power [60, 176, 177],

$$P_{cr} = \alpha \frac{\lambda^2}{4\pi n_0 n_2}; \quad \alpha = 1.8962 \quad (\text{Gaussian beam [177]}) \quad (5.4)$$

for all gases except for argon ($\sim 9 \text{ GW}$), neon (110 GW) and helium (270 GW) at normal pressure (Tab. 5.1). Laser pulses with peak powers equal to or exceeding the critical power of a gas propagate under strong influence of SF. This can quickly lead to self-trapping [176] or break up [60, 178] of the laser beam consequently leading to damage of the multi-pass optics. The macroscopic quantity n_2 , however, is proportional to the gas pressure [173] permitting direct control over critical power and the non-linear phase shift. For this reason, the experimental setup is surrounded by a vacuum chamber that supports gas pressures between $\sim 10^{-2} \text{ mbar}$ and normal pressure.

The spectral bandwidths obtained with the different gases (Fig. 5.6) represent the non-linear indices of the different noble gases very well. Helium (not shown here) leads to only minor spectral broadening of the aforementioned pulses. Neon

Gas	n_2 [10^{-23} m ² /W]	P_{cr} [GW]	λ_0 [nm]	τ	Ref.
He	0.06	270	1030 ^a	150 ns	[172, 173]
	0.34	47	800	theo	[174]
Ne	0.14	114	1030 ^a	150 ns	[172, 173]
	0.85	19	800	theo	[174]
Ar	1.55	9.2	1030 ^a	150 ns	[172, 173]
	1.4 ± 0.2	11	800	120 fs	[160]
	0.97 ± 0.12	17	800	40 fs	[175]
	2.0 ± 0.12	8.0	800	90 fs	[145]
Kr	7.96	2.0	800	theo	[174]
	3.53	4.0	1030 ^a	150 ns	[172, 173]
Xe	18.9	0.85	800	theo	[174]
	9.53	1.4	1030 ^a	150 ns	[172, 173]
	8.1 ± 0.8	2.0	800	120 fs	[160]
N ₂	54.8	0.29	800	theo	[174]
	1.21	12	1030 ^a	150 ns	[172, 173]
	2.3 ± 0.3	7.0	800	120 fs	[160]
	0.74 ± 0.09	22	800	40 fs	[175]
O ₂	2.4 ± 0.4	6.7	800	90 fs	[145]
	1.28	11	1030 ^a	150 ns	[172, 173]
	5.1 ± 0.7	3.1	800	120 fs	[160]
	0.95 ± 0.12	17	800	40 fs	[175]
Air	3.2 ± 0.7	5.0	800	90 fs	[145]
	2.9 ± 0.4	5.5	800	120 fs	[160]
	2.4 ± 0.5	6.7	800	90 fs	[145]

Table 5.1.: Non-linear properties of selected gases. Critical power calculated for $\lambda=1.03 \mu\text{m}$ using equation (5.4). “theo”: theoretical prediction. ^aCalculated from the dispersion relation of given in Table II and Table IV in [172].

introduces less non-linear phase than argon. Aiming for the shortest possible pulse duration, neon is not suitable because the low non-linear refractive index does not provide enough spectral bandwidth at normal pressure to allow pulse compression to durations shorter than ~ 100 fs. Higher pressures or more passes inside the multi-pass cell are possible, however, the comparably high costs for operating the multi-pass cell with neon suggest other gases. The remaining gases, argon and nitrogen support the spectral bandwidths leading to Fourier limited pulse durations (Fig. 5.6b) of even less than 30 fs prior to observing instabilities of the broadening process.

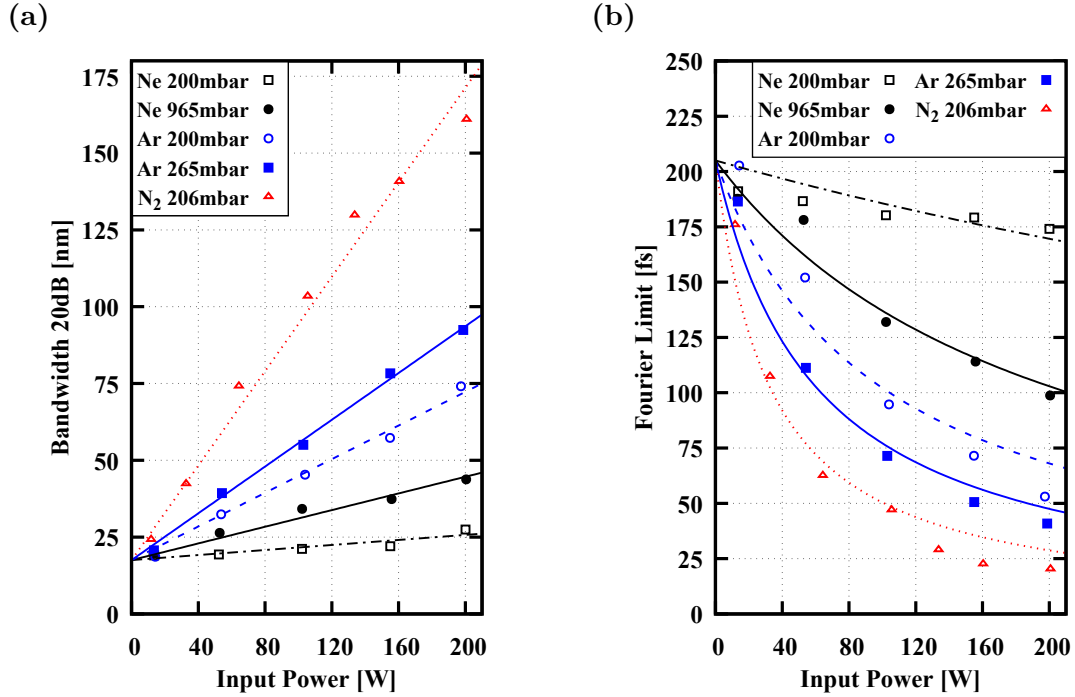


Figure 5.6.: (A) 20 dB spectral bandwidth for different pressures of neon, argon and nitrogen. (B) The corresponding calculated Fourier limits. Dashed and solid lines represent fitted linear (A) and the inverse (B) function to the data points.

The linear increase of the spectral bandwidth enables a relative comparison between the non-linear refractive indices of neon, argon and nitrogen. A linear fit of the function $a_{(gas)} \cdot p \cdot P + const.$ to the data of the whole set of measurements reveals

$$\begin{aligned}
 a_{Ne} &= (0.129 \pm 0.035) \frac{\text{nm}}{\text{W} \cdot \text{bar}} &= (12.9 \pm 3.5) \frac{\text{nm}}{\text{mJ} \cdot \text{bar}}, \\
 a_{Ar} &= (1.32 \pm 0.17) \frac{\text{nm}}{\text{W} \cdot \text{bar}} &= (132 \pm 17) \frac{\text{nm}}{\text{mJ} \cdot \text{bar}}, \\
 a_{N_2} &= (3.74 \pm 0.34) \frac{\text{nm}}{\text{W} \cdot \text{bar}} &= (374 \pm 34) \frac{\text{nm}}{\text{mJ} \cdot \text{bar}},
 \end{aligned}$$

where p is the gas pressure and P is the laser average power. The identities on the right are calculated via the repetition-rate r_{rep} of the laser amplifier $E[\text{mJ}] = P[\text{W}]/r_{rep}[\text{kHz}]$. The ratio of these coefficients agrees well with the literature values for neon and argon ($a_{Ne}/a_{Ar} \approx 0.1$) (Tab. 5.1). Comparing argon and nitrogen ($a_{N_2}/a_{Ar} \approx 2.8$) a significant difference is visible which is attributed to the slow Raman response of the diatomic nitrogen molecule. The influence of the Raman contribution to the final output field is discussed in section (5.6.2).

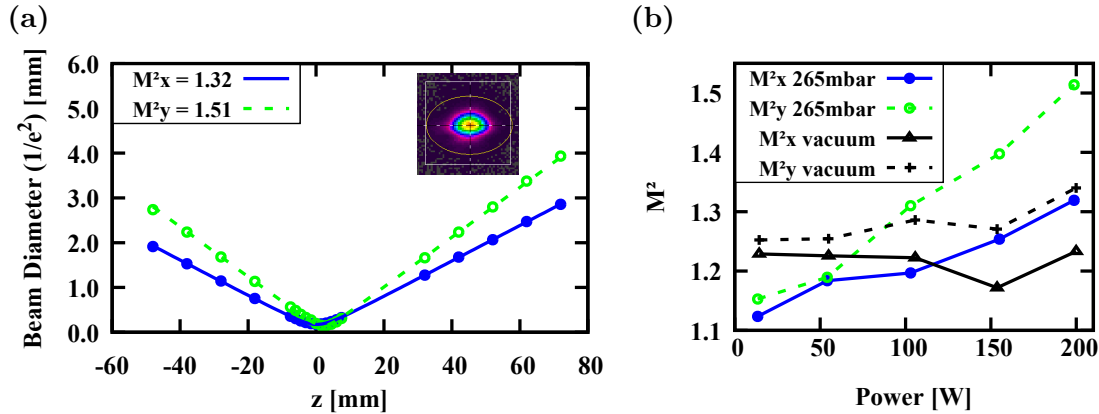


Figure 5.7.: (a) Measurement of the beam quality factor (M^2) at 200 W input power and 265 mbar argon pressure. The inset shows the beam profile in the focus ($z=0$). (b) M^2 parameter depending on the input power

The throughput after the broadening process shows excellent values of $\sim 93\%$ and is independent of the used gases for moderate pressures. Only if the pressure in combination with the non-linear index of the gas is large enough to support spectral bandwidths surpassing the supported bandwidth of the high reflective mirrors losses can exceed 10%. This regime, however, becomes visible for pressures above 200 mbar in nitrogen. Increasing the pressure above this value led already to unstable plasma channels within the Rayleigh range of the focus in between the imaging optics indicating close proximity to critical SF. Further increase of the pressure is not implemented to avoid damage to the optics.

5.5. Beam quality

5.5.1. Beam quality factor

Characterized with a commercial M^2 -Meter (Spiricon M200), the beam quality factor was measured for different pressures and selected gases. The measurements reveal an increase of the beam quality factor raises with increasing non-linear phase shifts. Thereby the beam quality factors of the different axis (x- and y-axis) show different behavior. This could be caused by the differences of the setup resulting from the introduced astigmatism of the multi-pass cell and the different input beam quality factors for the different directions.

In nitrogen it was observed that the beam quality factor increases with increasing spectral bandwidth, at first and then starts decreasing again. The beam quality factor for moderate non-linear phase shifts was, therefore, worse as for larger non-

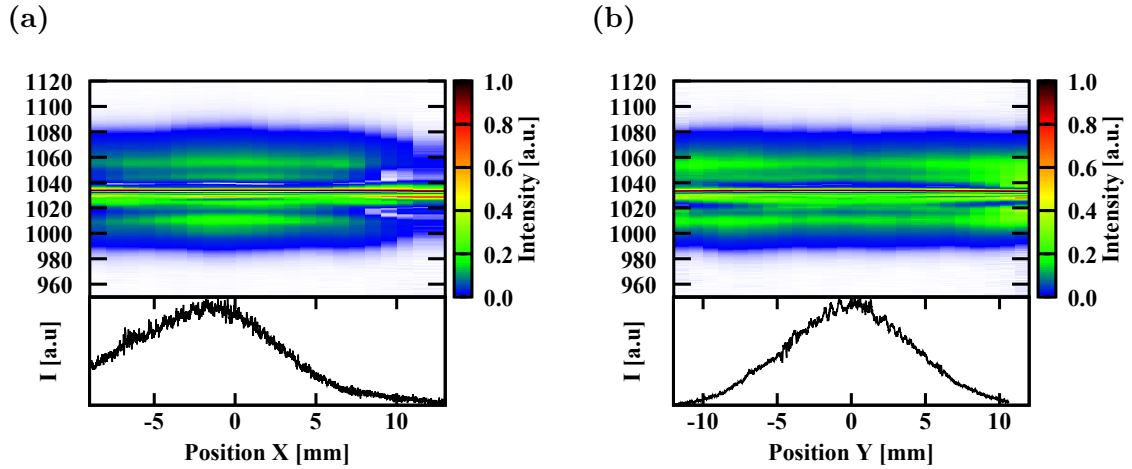


Figure 5.8.: Measured spectra at different positions of the beam profile along the (a) x- and the (b) y-axis. Spectra are normalized to the peak. Bottom: Measured beam profile.

linear phase shifts. An accurate explanation for this behavior is not yet found but might be resulting from increasing plasma defocussing [179]. Combined effects caused by SF and the increased intensity on the high reflective mirrors are also considered possible.

Best results in combination with good compressibility of the output pulses was achieved with pressures of 265 mbar in argon. The beam quality of the 200 W output beam at this pressure is 1.3(X) and 1.5(Y) (Fig. 5.7a). Considering the differences in the different directions of the laser it is observed that the x-direction possesses a better beam quality factor than the y-direction. This holds promise for improvement of the y-direction in future.

Considering the behavior with increasing average power, figure (5.7b) shows a linear increase of the beam quality factor depending on the input power at 265 mbar. The better beam quality at low powers for the beam propagating through argon is considered an artifact resulting from pressure induced differences on the mechanical alignment of the beam leading to differences on the input optics. This increase is strongly reduced in vacuum leading to the conclusion that the increase is indeed caused by the applied non-linearity. It is also observed that the slope for x- and y-direction is different which might be caused by the astigmatism of the system.

5.5.2. Spectral homogeneity of the beam

The simulation in section (5.2) shows that the spectral homogeneity is ensured, to good extend, if the pulse propagates through the focus. To exclude significant deviations from these results the spectral homogeneity of the output beam was analyzed.

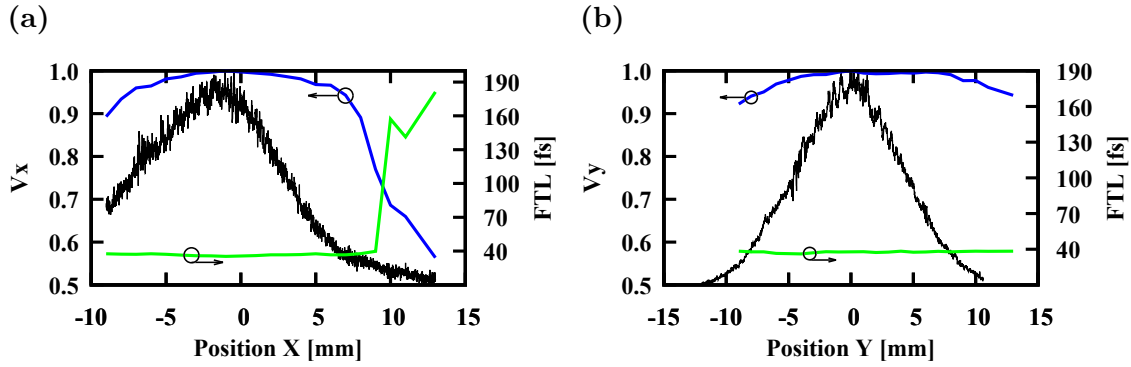


Figure 5.9.: Characteristic values for the spectral homogeneity V and the Fourier transform limited pulse duration of the beam in x- (a) and y-direction (b). Measured beam profile (black).

The experiment was performed with a beam diameter of ~ 15 mm. An aperture selected sections with 0.5 mm diameter that were coupled into a single-mode fiber. The spectra across x- and y-direction of the beam were then recorded in 1 mm steps with an optical spectrum analyzer (Anritsu MS9740A, Res: 0.057 nm).

Figure (5.8) shows the normalized recorded spectra with varying positions in x- and y-direction (Fig. 5.8a and 5.8b). It is observed that the spectrum along the x-direction is indeed broadest in the center of the beam. On the outermost edge $x > 8$ mm it narrows but still exceeds the input spectrum (Fig. 3.22) of the laser pulse indicating the spectral broadening of the outermost parts of the beam. The situation of the spectrum in y-direction is qualitatively different. The outer parts of the spectrum possess a spectrum of approximately the same bandwidth but the spectrum is slightly altered. Considering the resulting FTLs the observed spectra show very homogenous durations only on the edges of the beam in horizontal (x-) direction the increase is measurable. Within the tolerances of the measurement the FTLs are constant across the y-direction. According to the definition [151]

$$V := \frac{\left[\int \sqrt{S(\lambda)S_0(\lambda)} d\lambda \right]^2}{\int S(\lambda) d\lambda \int S_0(\lambda) d\lambda} \quad (5.5)$$

which describes the overlap of the spectra $S(\lambda)$ observed at different positions relative to a reference spectrum $S_0(\lambda)$. Figure (5.9) presents the values of V for both directions and includes the calculated FTLs. The spectrum at the peak of the beam profile represents the reference $S_0(\lambda)$. The parameter V_x drops to 89% from the center to the outer region of the beam. In the outermost part a drop to 56% is visible. The FTL across the main part of the beam stays at ~ 37 fs. The step rise of the FTL at the outer part of the beam in x-direction ($x > 8$ mm) corresponds to less spectral bandwidth in this region. In y-direction the homogeneity level is higher as

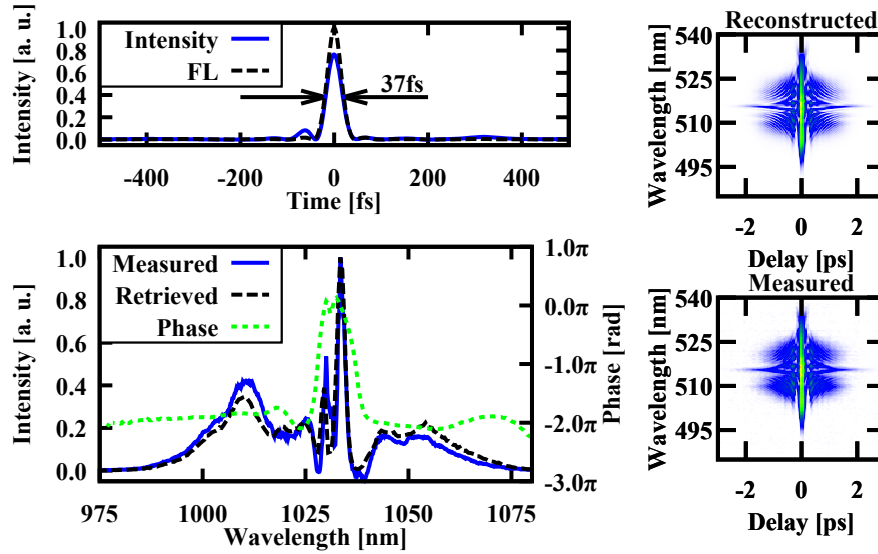


Figure 5.10.: SH-FROG measurement of the compressed output pulse (G-error: 0.32 %) at 265 mbar in argon and 1.9 mJ output energy. Upper left graph: Fourier limited pulse (red dashed line) and the measured pulse (solid blue). Lower left graph: measured (solid blue) and retrieved (dashed red) spectra.

compared to the x-direction. The parameter V_y stays above 92 % over the whole beam profile. The FTL represents this behavior equally. The calculated intensity weighted average of these quantities amounts to $V_x = 97.6 \%$ and $V_y = 98.6 \%$. The measured parameters are comparable to $V_x = 99.5 \%$ and $V_y = 99.2 \%$, which are presented by the authors of [151] in a non-linear pulse compression scheme based on fused silica and μJ pulse energy.

The reason of the different behavior of the spectrum in the two directions is not yet understood. Gaining knowledge on the origin of these differences might lead to equal homogeneity in both directions. The measurements of the beam quality and the homogeneity show that both quantities are preserved to good extend at least for one direction of the beam. Further experiments aiming for optimizing the system are likely to reveal the hidden mechanisms.

5.6. Pulse compression after the multi-pass cell

Pulse compression after the multi-pass cell is realized with chirped mirrors (CMs). The internal multilayer research group provided all mirrors for the experiment. Dr. Vladimir Pervak and his group manufactured the mirrors and the design of the multilayer stack was calculated by Dr. Michael Trubetskov.

The manufactured chirped mirrors for pulse compression (PC547) have a group delay dispersion (GDD) of -700 fs^2 . Four of these mirrors compressed the 210 fs pulses of the non-linear regenerative amplifier to 37 fs at 265 mbar gas pressure in argon corresponding to a compression ratio of 5.6. The total amount of group delay dispersion amounts to -2800 fs^2 . The main pulse contains 80 % of the energy as compared to the Fourier limited pulse (Fig. 5.10). The power throughput of the multi-pass cell amounts to $> 93 \%$ with these parameters. The resulting peak power of the pulse amounts to 35 GW. The high accuracy of the frequency-resolved optical gating (FROG) retrieval (G-error = 0.32 %) indicates high spatial homogeneity of the focus within the FROG device and supports the measurement of the previous section.

The root mean square (RMS) pulse-to-pulse stability of the output pulses is below 1 % for $18 \cdot 10^3$ pulses and is well suitable for driving subsequent non-linear processes.

Pulse compression beyond this pulse duration turns out to be difficult. Both argon and nitrogen at higher pressures (Ar: $> 300 \text{ mbar}$ and N_2 : $> 150 \text{ mbar}$) showed phase distortions at full power that could not be fully removed with chirped mirrors. Durations $< 35 \text{ fs}$ could be achieved, however, significant amount ($> 40 \%$) of energy is distributed in wings of the pulse. This leads to an effective reduction of the peak power as compared to the pulse shown in (5.10). Analysis of the measured FROG traces revealed quite complicated phases that can not be compensated even with more sophisticated CM designs [180]. The next section investigates on the reasons for this behavior.

The non-linear processes involved in the multi-pass compression stage are summarized in the ultrashort-pulse equation (5.6). This equation is derived from [60, equ. (13.2.23)] in (A.2),

$$\begin{aligned} \frac{\partial}{\partial z'} \tilde{A}(\mathbf{r}, t) \approx & \left[\frac{i}{2k_0} \left(1 + \frac{ik_1}{k_0} \frac{\partial}{\partial \tau} \right)^{-1} \nabla_{\perp}^2 + i\tilde{D} + i\gamma_1 |\tilde{A}(\mathbf{r}, t)|^2 \right] \tilde{A}(\mathbf{r}, t) \\ & - \gamma_2 \frac{1}{\omega_0} \frac{\partial}{\partial \tau} |\tilde{A}(\mathbf{r}, t)|^2 \tilde{A}(\mathbf{r}, t) \end{aligned} \quad (5.6)$$

where $\tilde{A}(\mathbf{r}, t)$ is the slowly varying complex field amplitude, k_0 is the wave vector at the carrier frequency ω_0 , $k_1 = 1/v_g = \partial k(\omega)/\partial \omega|_{\omega=\omega_0}$ is the inverse group velocity, $\tau = t - z/v_g$ is the retarded time and c is the speed of light in vacuum. The coefficient \tilde{D} [60]

$$D = \sum_{n=2}^{\infty} \frac{k_n}{n!} (\omega - \omega_0)^n \xrightarrow[(\omega - \omega_0) \rightarrow i \frac{\partial}{\partial \tau}]{\mathcal{FT}} \tilde{D} = \sum_{n=2}^{\infty} \frac{k_n}{n!} \left(i \frac{\partial}{\partial \tau} \right)^n \quad (5.7)$$

describes dispersive effects and is defined by the Taylor expansion of the wave vector starting from the second order term [Equ. (5.7)]. The non-linear parts of the equation are related to the physical constants via

$$\gamma_1 = \frac{3}{2} \frac{\omega_0}{cn_0} \chi^{(3)}(\omega_0) = 2\omega_0 n_0 \epsilon_0 n_2 \quad (5.8)$$

$$\gamma_2 = \frac{3}{2} \frac{\omega_0}{cn_0} \chi^{(3)}(\omega_0) \left(1 + \frac{\omega_0}{\chi^{(3)}(\omega_0)} \frac{d\chi^{(3)}}{d\omega} \right) = \gamma_1 \left(1 + \frac{\omega_0}{\chi^{(3)}(\omega_0)} \frac{d\chi^{(3)}}{d\omega} \right) \quad (5.9)$$

$$n_2 = \frac{3}{4} \frac{\chi^{(3)}}{n_0^2 \epsilon_0 c}. \quad (5.10)$$

The coefficients γ_1 [Equ. (5.8)] and γ_2 [Equ. (5.9)] represent the non-linear response caused by the the third order non-linear susceptibility $\chi^{(3)}$ and its dispersion. In case of a vanishing non-linear susceptibility $\chi^{(3)}(\omega_0)$, γ_1 and γ_2 vanish and equation (5.6) turns into the linear wave equation including dispersion and diffraction.

To understand the underlying physics behind the spectral broadening process within the multi-pass cell, the next sections consider the non-linear coefficients and their contribution to the shape and phase of the output electric field. This short overview shows why noble gases tend to show better results after compression than molecular gases. The non-linear coefficients γ_1 and γ_2 allow distinguishing three different types of non-linear optical effects. Thereby, γ_1 is the source for SPM and SF. Together with dispersion \tilde{D} this leads to optical wave-breaking [181–183] if the introduced non-linear phase is large enough. The second coefficient carries information of the dispersive character of the third order susceptibility and, thus, the information on slower time dependent processes [78].

5.6.1. Optical wave-breaking and shock formation

Optical pulse compression using the multi-pass setup with 2 mJ, 210 fs pulses at 200 W quickly leads to compression factors of 5 or more. The spectral bandwidth then exceeds 100 nm and dispersive effects become relevant. It is known that SPM in combination with dispersion leads to optical shock formation. An optical shock develops due to the shape of the instantaneous frequency that results from the SPM induced temporal phase. As the instantaneous frequency shift follows the intensity of the pulse, the leading and trailing edges of the pulse experience almost no frequency shift while the central part of the pulse is essentially linearly chirped. In normal dispersive media the leading edge of the pulse travels slower than the red shifted front. On the blue shifted back of the pulse the trailing edge will be traveling faster and closes up. Depending on the group velocity dispersion (GVD) of the medium the pulse will develop a rectangular pulse shape and the instantaneous frequency shows step edges on the sides of the pulse. This process is known as optical-shock formation or optical wave-breaking [181–183].

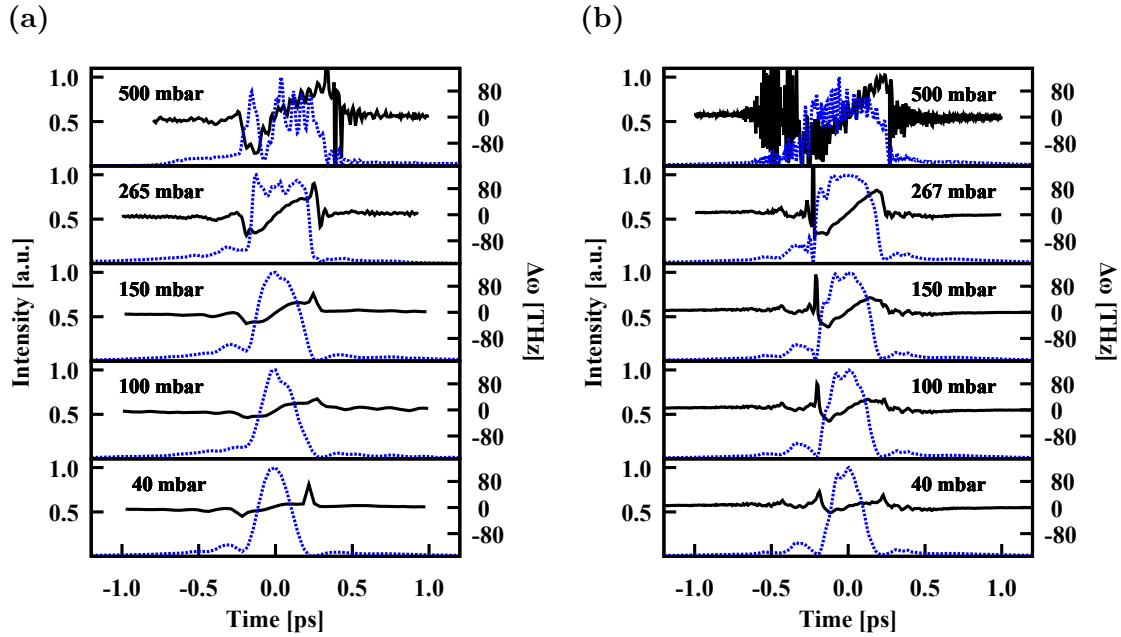


Figure 5.11.: Illustration of optical wave-breaking. (a) Measured pulse intensity (dashed) and instantaneous angular frequency (solid) at 200 W input power for different pressures of argon. (b) Calculated intensity (dashed) and instantaneous angular frequency (solid) ($n_2 = 1.2 \cdot 10^{-23} \frac{\text{m}^2}{\text{W}}$)

In the experiment the formation of an optical shock wave is undesirable as it leads to fast oscillations in the instantaneous frequency which lead to significant reduction of the compressibility of the pulse. Because of this, spectral broadening of our pulses has a limitation that results from both the GVD of the utilized gas and the GDD of the mirrors.

The formation of an optical shock wave was recorded by measuring the output pulses with second-harmonic frequency-resolved optical gating (SH-FROG). Calculation of the instantaneous angular frequency reveals optical shock formation as it shows the increasing frequency jump at the edges of the pulse. Figure (5.11a) (solid) depicts the instantaneous angular frequency for increasing pressures of argon at 2 mJ input energy. Up to 265 mbar the instantaneous frequency increases almost linearly with time. At higher pressures the instantaneous frequency starts oscillating and pulse compression reveals to be impossible. Figure (5.11a) shows this effect at 500 mbar in argon.

To simulate this effect both the GDD of the high reflective mirrors (8 fs^2) and the GVD of argon were included. The dispersion of argon for low pressures ≤ 1 bar is according to the Clausius-Mosotti equation [184, 185] linear with the gas pressure. Argon at normal pressure possesses a GVD of $14.5 \text{ fs}^2/\text{m}$ [186]. For pressures

between 40 mbar and 500 mbar the accumulated GDD for one round-trip (8 m) (Fig. 5.4) takes values between 4.6 fs^2 (40 mbar) and $\sim 60 \text{ fs}^2$ (500 mbar). The 16 reflections on HR mirrors the GDD accumulates to 128 fs^2 for one round-trip leading to the main contribution of GDD for one round-trip. Including the two parameters into the simulation, the data (Fig. 5.11a) agrees excellently with the measured data if a non-linear refractive index of $1.2 \cdot 10^{-23} \text{ m}^2/\text{W}$ is assumed. This is in good agreement with literature values (Tab. 5.1).

Compensation of the introduced chirp is helpful to shift the point of optical wave-breaking towards larger non-linear phase shifts and, therefore, larger spectral bandwidths of the pulse. In combination with a well behaved phase, pulses as short as 20 fs are feasible. With chirp compensation wings of the pulse can be effectively reduced and the pulse carries the main part of its energy in the center of the pulse. Even larger non-linear phase shifts might be possible with increasing number of foci in the multi-pass cell or slightly higher gas pressures (below the critical power). Limits are then set by the supported spectral bandwidth of the HR mirrors. Reaching a super-continuum with this cell might be possible but careful dispersion management is necessary to ensure good pulse compression results after the broadening process. Starting from the 200 fs input pulse duration it is likely that pulse compression prior to entering a second gas filled multi-pass cell leads to better results than direct pulse compression with a single multi-pass cell. The choice of different gases and pressures then holds promise for crossing the sub-10 femtosecond regime.

5.6.2. Differences between nitrogen and argon

Measurements of the output pulses resulting from the non-linear response of nitrogen reveals differences between the pulse shapes observed in the simulation. The GVD and third order dispersion (TOD) for nitrogen and argon at $\lambda=1.03 \mu\text{m}$ and normal pressure are

$$GVD_{N_2} = 0.0156 \frac{\text{fs}^2}{\text{mm}} \quad \text{and} \quad TOD_{N_2} = 0.0891 \frac{\text{fs}^3}{\text{mm}} \quad [187] \quad \text{and} \quad (5.11)$$

$$GVD_{Ar} = 0.0145 \frac{\text{fs}^2}{\text{mm}} \quad \text{and} \quad TOD_{Ar} = 0.0154 \frac{\text{fs}^3}{\text{mm}} \quad [186], \quad (5.12)$$

showing that the TOD of nitrogen is by a factor of 7 higher as the TOD of argon. However, compared to the GVD and the spectral bandwidth of the pulses that corresponds to $\tau_{FTL} \approx 40 \text{ fs}$ the influence of TOD on the pulse shape is negligible because $\tau_{FTL} \cdot GVD_{N_2}/TOD_{N_2} = 7 > 1$ [78, p. 77]. This argument is further supported by simulation results, which show no significant differences between the two gases.

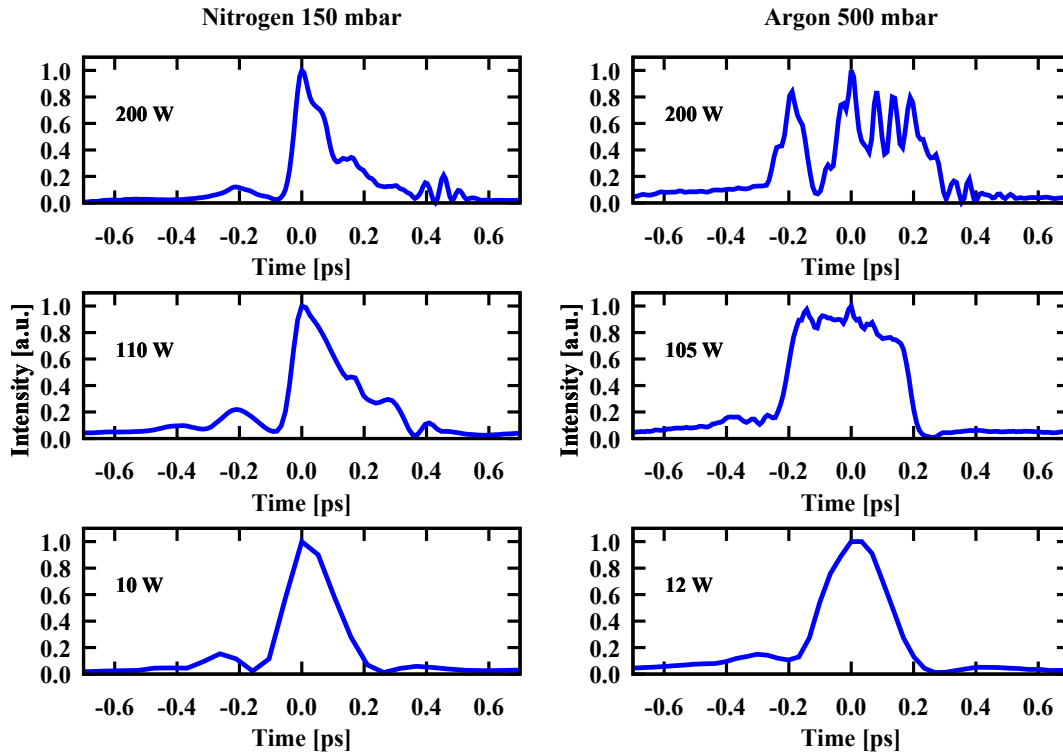


Figure 5.12.: Effects resulting from the Raman response of nitrogen at 150 mbar (left). (Right) Temporal profiles resulting from argon (500 mbar). The pressures are chosen to match the same effective values of n_2 in both cases. Multi-pass cell input power is increased from bottom to top.

This suggests that non-linear processes are involved, which are not included in the simulation. As the term, $\gamma_2 \frac{1}{\omega_0} \frac{\partial}{\partial \tau} |\tilde{A}(\mathbf{r}, t)|^2 \tilde{A}(\mathbf{r}, t)$ is not included, the differences are attributed to sources described by the dispersion of the non-linear susceptibility and the time derivative of the non-linear field $|\tilde{A}(\mathbf{r}, t)|^2 \tilde{A}(\mathbf{r}, t)$. This part of equation (5.6) is the source for self-steepening (see [60, sec. (13.3.1)]). As the coefficient γ_2 [Equ. (5.9)] has two terms it is possible to distinguish between an instantaneous, frequency independent, process and a response resulting from time dependent, slower, mechanism of the non-linear medium. To see how self-steepening influences the process it is useful to relate it to the non-linear lengths L_{NL} [Equ. (1.95)]. The lengths for SPM and SF [Equ. (1.95)] and the characteristic length for self-steepening L_{SS} ,

$$L_{SS} = \frac{cT}{2n_2I}; \quad \frac{L_{SS}}{L_{NL}} = \frac{T}{\frac{1}{2}\omega_0} \quad (5.13)$$

show that both effects will contribute equally if the characteristic pulse duration

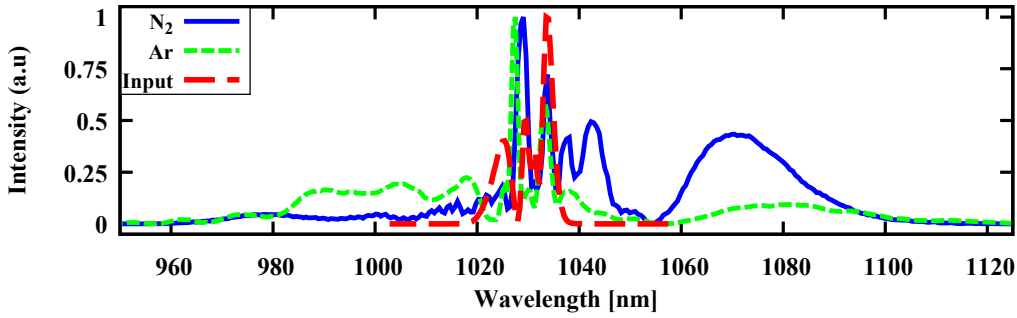


Figure 5.13.: Spectra of output pulses at 200 W input power for 150 mbar nitrogen and 500 mbar argon.

T is equal to $2/\omega_0 = \lambda/\pi c$. Clearly, for pulses with durations > 30 fs at 1030 nm ($T=1$ fs) the process of self-steepening is difficult to observe for media exhibiting a fast electronic response, only [60, 188].

The frequency dependent term in γ_2 describes dispersive effects of the non-linear susceptibility $\chi^{(3)}$. The dispersion of this quantity is interpreted as a non-instantaneous response of the non-linear medium. Effects of this kind are well known from pulse propagation in fibers and are attributed to the Raman effect [78]. Figure (5.12) shows a measurement of the pulse with increasing power from bottom to top in nitrogen in comparison with the output fields resulting from argon. To keep the data comparable, the pressures were adjusted to show the same spectral bandwidth with both gases ideally leading to the same effective non-linear refractive index of both gases if other effects are excluded. Clearly, the right, trailing, edge of the pulse develops a long tail with increasing intensity. The pulse shapes resulting from broadening in argon are different and the tail is not visible. In contrast to nitrogen, argon shows the typical rectangular pulse shape as known from the combination of SPM with dispersion [78]. The corresponding spectrum is symmetrically distributed around the central frequency and the input spectrum. The spectrum of the 2 mJ pulse propagating through 150 mbar nitrogen has a strong shift to the red (Fig. 5.13). This is a property known from intense ultrashort pulses that propagate through gases consisting of diatomic molecules [160]. The strong red shift results from the rotational response of the diatomic nitrogen molecule and, therefore, is caused by the Raman effect. The influence of the molecules lies in a non-linear refractive index change caused by rotational alignment of the molecules in the laser field. This response is slow (~ 150 fs [160]) and effectively leads to an additional time dependent term in the description of the refractive index change [160]

$$\Delta n(t) = n_{2_{instant}} I(t) + n_{2_{Raman}}(t). \quad (5.14)$$

Nibbering et al. [160] have described this effect and calculated the time response

of nitrogen. The time scale of the processes (~ 150 fs) matches the pulse duration of the used laser pulses [160, 175] explaining the strong influence on the shape (Fig. 5.12). As opposed to self-steepening caused by the instantaneous response of the medium, the leading part is slightly steepened in nitrogen (Fig. 5.12, right). This might be caused by the negative Kerr-like response ($\Delta n(t) < 0$) of nitrogen that develops ~ 200 fs behind the peak of the laser pulse [160].

In summary, pulse compression in argon leads to better results because of the instantaneous response and the well controlled phase of the output pulses. The influence of SPM and GVD on the pulse imprints a linear instantaneous frequency sweep across the main part of the pulse prior to reaching the limits of optical wave breaking. The slow Raman response of nitrogen is more complex and leads to lower performance in the compression of the output pulses with respect to obtaining highest peak powers.

5.7. Scaling laws

To scale this concept to higher or lower pulse energy, the parameters for adjustment are the

1. non-linear medium (gas),
2. gas pressure,
3. number of passes/foci,
4. focal length of the imaging optics and
5. the dispersion.

Adjustment of these parameters allows tweaking the output for best performance. Implementation to other laser sources requires consideration of the

- damage threshold of the used optics ~ 1 J/cm²,
- peak power of the laser pulse,
- initial spectrum of the laser pulse.

The damage threshold determines the minimum beam size on the mirrors. The initial beam size in combination with the focal length of the imaging optics yields the peak intensity of the laser in the focal plane. Adjustment of the non-linear refractive index using the gas pressure allows precise setting of the non-linear phase shift for a single pass through the focus. The gas is easily selected requiring that the critical power is larger than the peak power of the laser pulse.

Implementation of the concept to pulse energies above 2 mJ can be realized without the need for increasing the size of the setup, in the first place. Due to the 4f-imaging system, the input beam size on the optics is scalable and reducing the

fluence on the mirrors links to an increasing intensity in the focus of the multi-pass cell. Adjustment of the gas pressure to compensate this effect is easily implemented. In case of intensities permitting strong ionization of argon, neon and helium become suitable gas choices. For lower pulse energies the system benefits from heavier noble gases such as krypton or xenon allowing compression of pulses with energies $< 70 \mu\text{J}$ (Xe, normal pressure). High-pressure cells allow larger non-linear optical coefficients for pulse energies in the μJ -range.

The simulation results shown in section (5.6.1) reveal a non-linear refractive index of $1.2 \cdot 10^{-23} \text{ m}^2/\text{W}$ for argon which is very close to the values presented by [172] (Tab. 5.1). According to the presented values energy scaling of the system is straight forward.

5.8. Conclusion

This chapter outlined a detailed analysis of the spectral pulse compression based on a 4f-imaging multi-pass cell. The setup allows compression of the 200 W amplifier (Sec. 3.6) to 37 fs and increases the peak power by a factor of 4.8 to 35 GW. It is demonstrated that the output pulse-to-pulse stability is better than 1 %.

Discussion of the important physical mechanism behind the pulse compression opens the path for further improvement of the system using dispersion controlled setups that are less prone to optical shock formation, which is considered the limiting factor of the demonstrated compression scheme. Because of the promising results it is believed that the setup paves the way towards new scalable high-power non-linear compression schemes.

Summary and Outlook

This thesis demonstrates amplification of femtosecond laser pulses to the millijoule level with a non-linear thin-disk Yb:YAG regenerative amplifier. The understanding of linear and non-linear processes during the amplification process not only permits average output powers of hundreds of watts but also leads to stable operation within the non-linear regime and unique output parameters of the amplifier. The highly stable output laser pulses have been proven to be suitable as driver for subsequent non-linear optical processes.

The developed thin-disk regenerative amplifier provides pulses with 100 kHz repetition-rate that now last only 210 fs and carry 2 mJ energy. Constraints and influences of the resonator design, the damage threshold of optics and the influences of non-linear optical elements have been discussed (Chap. 3). It has been demonstrated that large mode volume resonator designs based on optics with large radii of curvatures (RoCs) (> 5 m) are necessary for high pulse energy operation of the laser system. The challenges of building these resonators have been outlined and a strategy for running these resonators with single-mode output beams is presented. It is shown how self-phase modulation (SPM) and self-focusing (SF) influence the output pulses of the amplifier. Detailed measurements in the high energy passes of the regenerative amplifier give insight into the evolution of the output pulses. With this knowledge gain-narrowing in the regenerative amplifier is overcome and pulse compression could be optimized. The non-linear phase introduced within the amplifier is removed with a chirped mirror compressor after the amplifier facilitating highly efficient pulse compression without the need for gratings.

Further efforts were made to scale the pulse energy of the amplifier. In this context a new amplification method is presented. This method connects a multi-pass amplifier and a regenerative amplifier through coupling of both devices to the same active gain volume of a thin-disk. This effectively avoids the crystal of the optical switch in the high pulse energy amplification cycles. The concept has proven to deliver up to 6.6 mJ pulse energy. The limiting mechanisms are explained and a new multi-pass concept based on a 4f-relay imaging is suggested. The system holds promise for scaling by at least a factor of two to 10-20 mJ output energy. Systems delivering ultrashort pulses with these energies usually base on chirped-pulse amplification (CPA). As the suggested system directly amplifies the pulses it allows for compact implementation and, thus, leads to higher stability and cost efficiency.

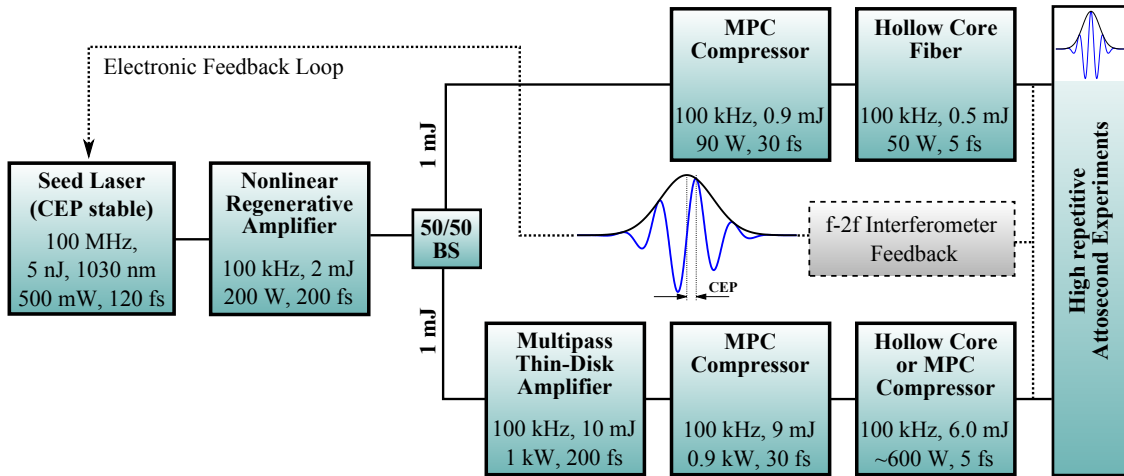


Figure 5.14.: Laser architecture for future CEP-stable high pulse energy, high repetition-rate attosecond beam lines. Multi-pass cell (MPC).

Always aiming for single-cycle pulses with highest possible pulse energy in combination with high repetition-rates leads to challenges in terms of available techniques to generate the necessary spectral bandwidth. In the last chapter of this thesis non-linear pulse compression within a gas filled multi-pass cell is demonstrated. A compression factor of 5.6 at 200 W average input power is demonstrated. The resulting 37 fs pulses with 1.9 mJ energy build an excellent basis for further pulse shortening in a hollow-core fiber or even a second gas filled multi-pass cell. The high-reflector based 4f-imaging cell is extremely stable against misalignment and provides an excellent throughput of 93 %. It is shown that the dispersion in combination with the low but existing group delay dispersion (GDD) of the mirrors leads to optical wave breaking that finally sets limitations on the pulse contrast of the compressed output pulses. Dispersion control within the multi-pass cell will lead to increased compression factors. Best performance in throughput and pulse contrast after compression was shown with 265 mbar in argon. The measurements presented in this chapter provide a benchmark for systems with altered input parameters. As the system is scalable in both pulse energy and average power it holds promise for supporting kilowatts average powers and joule scale energies.

The presented laser technology lays the foundation for a 100 kHz high-repetitive driving laser for attosecond metrology. The suggested architecture (Fig. 5.14) is based on a carrier-envelope-phase (CEP) stable frontend that delivers pulses for the non-linear regenerative amplifier. After amplification the system splits the 2 mJ output pulses into two 1 mJ pulses that seed two channels. The first (upper) channel directly compresses the pulses with a multi-pass cell (MPC) to ~30 fs followed by a second hollow-core fiber based compression stage. The first channel will provide ~0.5 mJ pulse energy with single-cycle pulse duration. The second chan-

nel introduces a multi-pass amplifier prior to the pulse compressors to boost the energy to 10 mJ corresponding to 1 kW average power. The following MPC based compression stage holds promise to be implemented without significant changes to the system shown in this thesis. The performed measurements (Sec. 5.4) suggest that neon at normal pressure leads to similar spectral broadening with the 10 mJ input pulses. Further research is necessary for implementing the last compression stage. This stage might be realized either with a hollow-core fiber or another MPC compressor. Compression with hollow-core fibers at these pulse energies has not been shown at 1030 nm wavelength so far and feasibility of this method needs to be elicited. The MPC has less restrictions to the pulse energy and scaling the current setup to support the 10 mJ pulse energy is thought to be straight forward. The challenge, however, lies in the increased spectral bandwidth of the single cycle pulses that quickly exceeds the reflectivity of GDD controlled high reflective mirrors. Actively cooled silver mirrors remedy this issue but the comparably high losses ($\sim 2\%$) require a dramatically decreased number of bounces on the optics as compared to the described MPC setup.

The CEP of the pulses for both channels is measured with an f-2f interferometer and feedback is given to the laser frontend to remove phase noise introduced by the amplifier chains. This system will provide kilowatt scale few-cycle pulses and paves the way to new frontiers in attosecond metrology. Thereby, the increased repetition-rate of the driving laser leads to better statistics on the observable of interest and gives access to observing and describing low-cross-section events on the atomic time scale [27].

List of Publications

Peer reviewed journal articles

- Moritz Ueffing, Simon Reiger, Martin Kaumanns, Vladimir Pervak, Michael Trubetskov, Thomas Nubbemeyer, and Ferenc Krausz. “Nonlinear pulse compression in a gas filled multipass cell”. In: *Optics Letters* doc. ID 322807 (posted 28 March 2018, in press). <http://www.osapublishing.org/abstract.cfm?msid=322807>

The main work was done by me. Design of the optical imaging system was done together with Robert Lange.

- Moritz Ueffing, Robert Lange, Tobias Pleyer, Vladimir Pervak, Thomas Metzger, Dirk Sutter, Zsuzsanna Major, Thomas Nubbemeyer, and Ferenc Krausz. “Direct regenerative amplification of femtosecond pulses to the multimillijoule level”. In: *Optics Letters* 41.16 (Aug. 2016), p. 3840. ISSN: 0146-9592, 1539-4794. DOI: 10.1364/OL.41.003840

I did the design, mechanical setup, analysis software and the simulations.

- Thomas Nubbemeyer, Martin Kaumanns, Moritz Ueffing, Martin Gorjan, Ayman Alismail, Hanieh Fattahi, Jonathan Brons, Oleg Pronin, Helena G. Barros, Zsuzsanna Major, Thomas Metzger, Dirk Sutter, and Ferenc Krausz. “1 kW, 200 mJ picosecond thin-disk laser system”. In: *Optics Letters* 42.7 (Apr. 2017), p. 1381. ISSN: 0146-9592, 1539-4794. DOI: 10.1364/OL.42.001381

Involved in construction and developed the laser during the whole time of the development. Build the laser chain, parts of the laser design and software used for the system was developed by me.

- Hanieh Fattahi, Helena G. Barros, Martin Gorjan, Thomas Nubbemeyer, Bidoor Alsaif, Catherine Y. Teisset, Marcel Schultze, Stephan Prinz, Matthias Haefner, Moritz Ueffing, Ayman Alismail, Lénárd Vámos, Alexander Schwarz, Oleg Pronin, Jonathan Brons, Xiao Tao Geng, Gunnar Arisholm, Marcelo Ciappina, Vladislav S. Yakovlev, Dong-Eon Kim, Abdallah M. Azzeer, Nicholas Karpowicz, Dirk Sutter, Zsuzsanna Major, Thomas Metzger, and Ferenc Krausz. “Third-generation femtosecond technology”. In: *Optica* 1.1 (July 2014), p. 45. ISSN: 2334-2536. DOI: 10.1364/OPTICA.1.000045

Development of the thin-disk regenerative amplifiers for OPCPA.

- Yunpei Deng, Alexander Schwarz, Hanieh Fattahi, Moritz Ueffing, Xun Gu, Marcus Ossiander, Thomas Metzger, Volodymyr Pervak, Hideki Ishizuki, Takunori Taira, Takayoshi Kobayashi, Gilad Marcus, Ferenc Krausz, Reinhard Kienberger, and Nicholas Karpowicz. “Carrier-envelope-phase-stable, 12 mJ, 15 cycle laser pulses at 21 μm ”. In: *Optics Letters* 37.23 (Dec. 1, 2012), p. 4973. ISSN: 0146-9592, 1539-4794. DOI: 10.1364/OL.37.004973

Contributed in development of the OPCPA system.

- Alexander Schwarz, Moritz Ueffing, Yunpei Deng, Xun Gu, Hanieh Fattahi, Thomas Metzger, Marcus Ossiander, Ferenc Krausz, and Reinhard Kienberger. “Active stabilization for optically synchronized optical parametric chirped pulse amplification”. In: *Optics Express* 20.5 (Feb. 27, 2012), p. 5557. ISSN: 1094-4087. DOI: 10.1364/OE.20.005557

Build the system and significantly contributed to the analysis of the data.

Patent

- “Amplifier device and method for amplifying laser pulses”. EP2873123 (B1). Moritz Ueffing, Thomas Metzger, and Ferenc Krausz

I am one of the inventors of the system. Implementation of the concept is presented in chapter (4)

Selected conference talk

- M. Ueffing, T. Pleyer, R. Lange, H. G. Barros, D. Sutter, T. Metzger, Zs. Major, and F. Krausz. “Compact Sub-Picosecond Multi-mJ Multi-kHz Yb:YAG Amplifier”. In: *2015 European Conference on Lasers and Electro-Optics - European Quantum Electronics Conference*. Optical Society of America, 2015, CA_12_3

Appendix A

Split-Step model

A.1. Split-step method

The 2D-Model used for modeling the nonlinear behavior of the regenerative amplifier and data acquired in context of developing the multi-pass cell (MPC) is based on solving the nonlinear wave equation in space and time. The equation is generally of the form

$$\frac{\partial A(r, t, z')}{\partial z'} = (\hat{D} + \hat{N}) A(r, t, z'), \quad (\text{A.1})$$

where \hat{D} is an operator known in the frequency domain and \hat{N} is an operator known in the time domain. The formal solution for a small step h is represented by [78]

$$A(r, t, z' + h) = e^{(\hat{D} + \hat{N})h} A(r, t, z') \quad (\text{A.2})$$

and can be approximated by [78]

$$A(r, t, z' + h) \approx e^{\hat{D}h} e^{\hat{N}h} A(r, t, z'). \quad (\text{A.3})$$

In the last step terms resulting from the non-commuting property of the two operators are neglected. The method implemented with this approximation is of first order in h [78], which requires step sizes small enough to approximate correct solutions. The simulation results shown in figures (5.1) and (5.2) are calculated with a step-size of $h = 10$ mm that was adopted if the phase shift of a single step exceeded $\pi/50$.

The scheme of the calculation is listed in figure (A.1). Starting with an input field in the time domain the program applies the phase introduced by self-phase modulation (SPM). In a following step the field is transformed to the frequency domain. The gain is applied in the space-frequency domain. After the gain is applied the field is transformed to the spatial-frequency domain. The transformation to the spatial frequency domain is implemented in rotational symmetry using a quasi-discrete Hankel transform [189]. Both dispersion and propagation operators

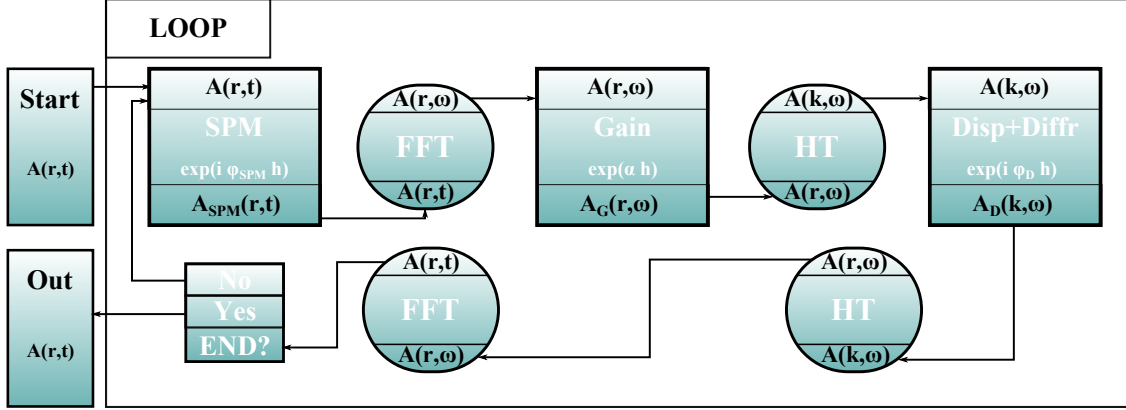


Figure A.1.: Illustration of the implemented beam propagation algorithm. FFT: Fast Fourier Transform, HT: Hankel Transform.

are applied in the k - ω -representation of the field envelope A . The output field is transformed back to space and time coordinates. These steps are repeated until the $\sum_i h_i = L$, where L is the length of the medium. Subsequent other propagation steps are applied in different media, if necessary.

A.2. Implementation

According to the definitions of the field envelope [Equ. (1.10)] and the approximations described in chapter (1) the wave equation for ultra-short pulses is given by [60, equ. (13.2.23)]

$$\begin{aligned} & \left[\nabla_{\perp}^2 + 2ik_0 \frac{\partial}{\partial z'} \left(1 + \frac{ik_1}{k_0} \frac{\partial}{\partial \tau} \right) + 2k_0 \tilde{D} \left(1 + \frac{ik_1}{k_0} \frac{\partial}{\partial \tau} \right) \right] A_{rt} \\ & = - \frac{3}{c^2} \omega_0^2 \left(1 + \frac{i}{\omega_0} \frac{\partial}{\partial \tau} \right)^2 \left[\chi^{(3)}(\omega_0) + i \frac{d\chi^{(3)}}{d\omega} \frac{\partial}{\partial \tau} \right] |A_{rt}|^2 A_{rt}. \end{aligned} \quad (\text{A.4})$$

The nonlinear factor on the right side of the equation is further approximated to keep only the first order time derivative. In addition, the approximation

$$\frac{k_1}{k_0} = \frac{1}{k_0} \left[\frac{n(\omega_0)}{c} + \frac{\omega_0}{c} \frac{\partial n}{\partial \omega} \Big|_{\omega=\omega_0} \right] = \frac{1}{\omega_0} + \frac{1}{n(\omega_0)} \frac{\partial n}{\partial \omega} \Big|_{\omega=\omega_0} \quad (\text{A.5})$$

is included

$$\begin{aligned} \left(1 + \frac{ik_1}{k_0} \frac{\partial}{\partial \tau} \right)^{-1} \left(1 + \frac{i}{\omega_0} \frac{\partial}{\partial \tau} \right)^2 & \approx \left(1 + \frac{i}{\omega_0} \frac{\partial}{\partial \tau} \right) - i \frac{1}{n} \frac{\partial n}{\partial \omega} \frac{\partial}{\partial \tau} \\ & \approx 1 + \frac{i}{\omega_0} \frac{\partial}{\partial \tau}, \end{aligned} \quad (\text{A.6})$$

where the Taylor series $a^2/(a + \Delta x) \approx a - \Delta x$ with

$$a = \left(1 + \frac{i}{\omega_0} \frac{\partial}{\partial \tau}\right) \quad \text{and} \quad (\text{A.7})$$

$$\Delta x = \frac{1}{n(\omega_0)} \frac{\partial n}{\partial \omega} \frac{\partial}{\partial \tau} \quad (\text{A.8})$$

is applied in the first step. The equation then simplifies to:

$$\begin{aligned} \frac{\partial}{\partial z'} \tilde{A}(\mathbf{r}, t) &\approx \left[\frac{i}{2k_0} \left(1 + \frac{ik_1}{k_0} \frac{\partial}{\partial \tau}\right)^{-1} \nabla_{\perp}^2 + i\tilde{D} \right. \\ &\quad \left. + i\frac{3}{2} \frac{\omega_0}{cn(\omega_0)} \left(1 + \frac{i}{\omega_0} \frac{\partial}{\partial \tau}\right) \left[\chi^{(3)}(\omega_0) + i \frac{d\chi^{(3)}}{d\omega} \frac{\partial}{\partial \tau} \right] |\tilde{A}(\mathbf{r}, t)|^2 \right] \tilde{A}(\mathbf{r}, t) \\ &\approx \left[\frac{i}{2k_0} \left(1 + \frac{ik_1}{k_0} \frac{\partial}{\partial \tau}\right)^{-1} \nabla_{\perp}^2 + i\tilde{D} + i\frac{3}{2} \frac{\omega_0}{cn(\omega_0)} \chi^{(3)}(\omega_0) |\tilde{A}(\mathbf{r}, t)|^2 \right] \tilde{A}(\mathbf{r}, t) \\ &\quad - \frac{3}{2} \frac{1}{cn(\omega_0)} \chi^{(3)}(\omega_0) \left(1 + \frac{\omega_0}{\chi^{(3)}(\omega_0)} \frac{d\chi^{(3)}}{d\omega}\right) \frac{\partial}{\partial \tau} |\tilde{A}(\mathbf{r}, t)|^2 \tilde{A}(\mathbf{r}, t), \end{aligned} \quad (\text{A.9})$$

where ∇_{\perp}^2 is the transverse Laplace operator. The terms independent of the time derivative are implemented in the propagation code following the steps shown in (A.1). The last term containing the time derivative is neglected throughout the work presented in this thesis.

Appendix B

Resonator Calculation

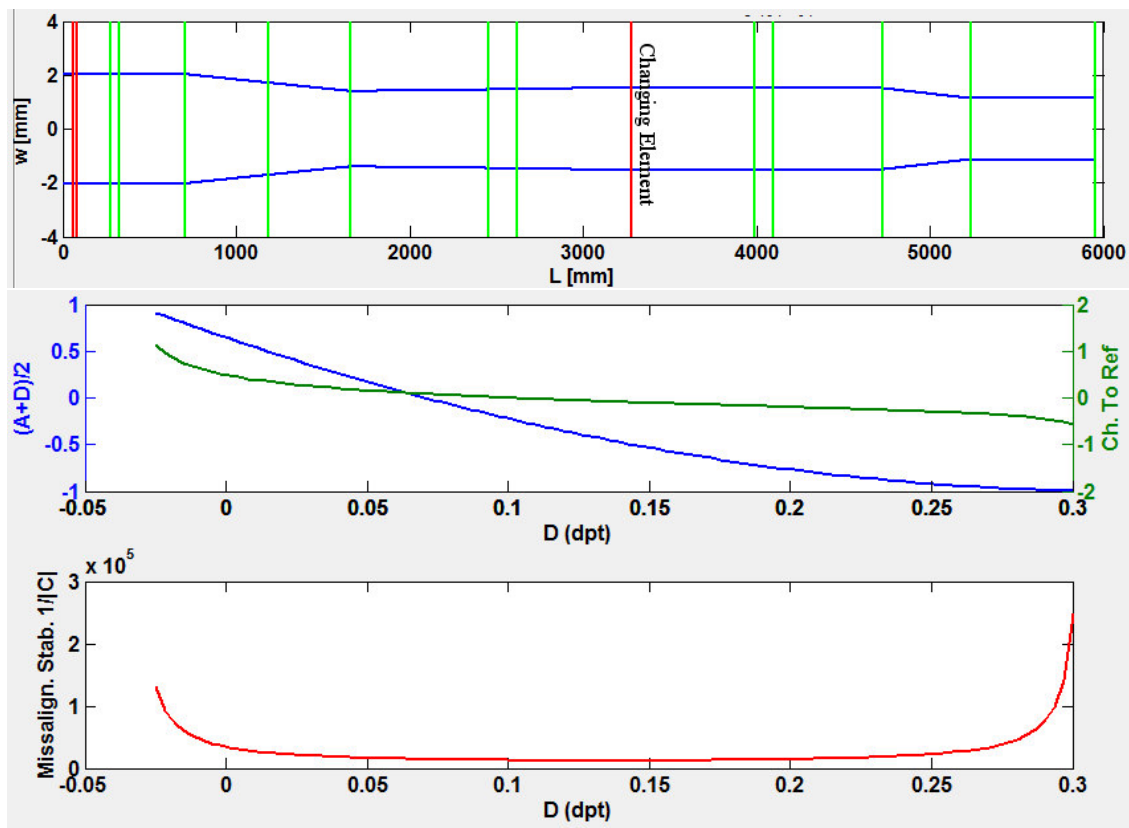


Figure B.1.: Top: Resonator with optical elements represented as vertical lines (green: reflective; red: transmissive) and resonator parameters depending on changes of the marked optical element.

Calculation of the resonator configurations for the regenerative amplifier are implemented with an ABCD-matrix calculation. The application includes both calculation of ring and linear resonators with predefined optical elements. The program calculates the resonator parameters and plots the eigenmode (Fig. B.1, upper

graph) according to the solution of equation (2.13). Furthermore, the program provides several tools to analyze the resonator depending on variable parameters. Changes of the properties of an implemented optical element leads to changing resonator parameters. These changes are illustrated with three different graphs

1. stability parameter $(A + D)/2$,
2. change of the mode size according to equation (B.1),
3. the stability parameter $1/|C|$,

vs. the changing parameter (Fig. B.1, middle and lower graph). Figure (B.1) displays the three parameters. The middle plot shows the stability parameter (blue) [Equ. (2.15)] with respect to a changing optical power of an optical element within the resonator. The variation of the parameter is chosen to range over the whole stability range, $-1 < (A + D)/2 < 1$ of the resonator. The green parameter illustrates the relative change of the mode size according to a selected optical element. This parameter is defined as

$$\delta y = \frac{d - d_0}{d_0}, \quad (\text{B.1})$$

where d is the diameter resulting from the value printed on the x-axis and d_0 is the initial diameter of the eigenmode prior to calculating the dynamics of the resonator. The quantity $1/|C|$ is plotted in the graph below and gives a measure for the misalignment sensitivity of the resonator [91].

The basic operations of the code are based on 2x2-matrix multiplication

$$M_{out} = M_n \cdot M_{n-1} \dots M_2 \cdot M_1 \quad (\text{B.2})$$

with the matrices listed in table (B.1).

Element	ABCD-matrix	Explanation
Propagation	$\begin{pmatrix} 1 & d \\ 0 & 1 \end{pmatrix}$	propagation by distance d
Lens	$\begin{pmatrix} 1 & 0 \\ -\frac{1}{f} & 1 \end{pmatrix}$	lens with focal length f
Mirror	$\begin{pmatrix} 1 & 0 \\ -\delta\frac{2}{R} & 1 \end{pmatrix}$	mirror with radius R (cav: $R>0$; vex $R<0$) $\delta = \cos(\theta)$ (sagittal), $\delta = \cos^{-1}(\theta)$ (tangential); θ is the angle of incidence
NLlens	$\begin{pmatrix} 1 & 0 \\ -D & 1 \end{pmatrix}$	$D_{NL} = \sqrt{\frac{\ln 2}{\pi}} \frac{8n_2L}{\pi w^4 \tau_{FWHM}} E$ L : length of medium; w : beam waist; n_2 : non-linear refractive index; τ_{FWHM} : pulse duration; E : Pulse energy

Table B.1.: List of ABCD-matrices as implemented in the resonator calculation. NL-lens: Non-linear lens

Appendix C

Damage Threshold Calculation

The total energy E on the sample is related to the peak fluence on the target F_0

$$E = \int_{-\infty}^{\infty} \int_{-\infty}^{\infty} dx dy \quad F_0 f(x, y) \quad (\text{C.1})$$

via the distribution function $f(x, y)$ that describes the measured beam profile if it is normalized so that

$$\max_{x, y \in \mathbb{R}} (f(x, y)) = 1. \quad (\text{C.2})$$

The integration over the beam profile f yields to an effective area

$$A_{eff} = \int_{-\infty}^{\infty} \int_{-\infty}^{\infty} dx dy \quad f(x, y) \quad (\text{C.3})$$

which relates the total energy on the sample to the peak fluence F_0 . The damage fluence F_0 is

$$F_0 = \frac{P}{R \cdot A_{eff}} \quad (\text{C.4})$$

where P is the power at which damage occurs and R is the repetition-rate of the laser system.

The effective area A_{eff} is calculated from the recorded raw data of the measured beam profile. As integration over the whole data set leads to a significant contribution of noise the mean value of the noise level outside the area of the beam profile is subtracted from each measured pixel. To fulfill constraint (C.2) the peak is normalized to 1. Integration over the two dimensional array is realized by executing the trapezoidal quadrature twice (for x and y values). Finally the mean value and the standard deviation of the damage threshold is determined. The systematic error produced by inaccuracies of the optics position relative to the position of the focus is estimated using data from a second beam profile measurement 5 mm away from the focal position. The uncertainty caused by differences of the effective area defines systematical error of the measurement and is added to the standard deviation using

$$\Delta F = \sqrt{\Delta F_{sys}^2 + \Delta F_{stat}^2}. \quad (\text{C.5})$$

Appendix D

Conversion of Parameters

D.1. The nonlinear refractive index

Conversion of the hyperpolarizability γ to the third order non-linear susceptibility is given by [172, 173]

$$\chi^{(3)} \simeq \frac{\rho_{at}}{4\epsilon_0} \langle \gamma \rangle \quad (\text{D.1})$$

$$n_2 = \frac{3}{4} \frac{\chi^{(3)}}{n_0^2 \epsilon_0 c} \quad (\text{D.2})$$

with the gas density ρ_{at} and the refractive index n_0 at the given wavelength. The density ρ_{at} is the number density, which for an ideal gas calculates to

$$\rho_{at} = \frac{p}{k_B T}, \quad (\text{D.3})$$

with k_B is the Boltzmann constant, T is the temperature and p is the pressure.

D.2. Gaussian laser pulses

The intensity profile Gaussian laser pulses in time and space is defined as

$$I(r, t) = I_0 e^{-\frac{2t^2}{\tau^2}} e^{-\frac{2r^2}{w^2}}, \quad (\text{D.4})$$

where I_0 is the peak intensity, τ the pulse width in time and w is the beam size in transverse direction. The intensity profile of this pulse has a full width at half maximum (FWHM) temporal width of

$$\tau_{FWHM} = \sqrt{2 \ln 2} \tau \quad (\text{D.5})$$

and a spatial profile that drops to $1/e^2$ at distance w from the center. This intensity profile gives the time dependent power of the pulse according to

$$P(t) = \int_0^\infty I(r, t) 2\pi r dr = 2\pi I_0 e^{-\frac{2t^2}{\tau^2}} \int_0^\infty e^{-\frac{2r^2}{w^2}} r dr = \frac{\pi w^2}{2} I_0 e^{-\frac{2t^2}{\tau^2}} \quad (\text{D.6})$$

showing the peak at $t = 0$ with magnitude

$$P_{Peak} = P(0) = \frac{\pi w^2}{2} I_0. \quad (\text{D.7})$$

Integration over time gives the total amount of energy contained within the pulse, which relates the energy to the peak intensity

$$E = \int_{-\infty}^{\infty} P(t) dt = \int_{-\infty}^{\infty} \frac{\pi w^2}{2} I_0 e^{-\frac{2t^2}{\tau^2}} dt = \frac{\pi w^2 \tau}{2} \sqrt{\frac{\pi}{2}} I_0 \quad (\text{D.8})$$

$$I_0 = \frac{2E}{\pi w^2} \frac{\sqrt{2}}{\sqrt{\pi \tau}} = F \frac{\sqrt{2}}{\sqrt{\pi \tau}} \quad (\text{D.9})$$

$$(\text{D.10})$$

The fluence F of the pulse is defined as

$$F = \frac{2E}{\pi w^2}. \quad (\text{D.11})$$

Appendix E

Data Archiving

Every plot has its own “*.bat” file named after the “*.pdf” or “*.jpeg” file listed in the “FigureArchive.txt”. To produce the plot run the “*.bat” file. All “*.bat” files can be opened in any text-editor and point the user towards the plot and data files. Extra information is included, if necessary. For detailed information read “ReadmeFirst.txt” located in the main archive folder for this thesis. The data archive is:

```
/afs/ipp-garching.mpg.de/mpq/lap/publication_archive/Theses/2018/
```


Bibliography

- [1] Alhazen and A. I. Sabra. *The Optics of Ibn al-Haytham. Books I-III: On direct vision*. Studies of the Warburg Institute v. 40. OCLC: ocm24910015. London: Warburg Institute, University of London, 1989. 2 pp. ISBN: 978-0-85481-072-7.
- [2] J. C. Maxwell. "A Dynamical Theory of the Electromagnetic Field". In: *Philosophical Transactions of the Royal Society of London* 155.0 (Jan. 1, 1865), pp. 459–512. ISSN: 0261-0523. DOI: 10.1098/rstl.1865.0008.
- [3] A. Einstein. "Über einen die Erzeugung und Verwandlung des Lichtes betreffenden heuristischen Gesichtspunkt". In: *Annalen der Physik* 322.6 (1905), pp. 132–148. ISSN: 00033804, 15213889. DOI: 10.1002/andp.19053220607.
- [4] Albert Einstein. "Zur Quantentheorie der Strahlung". In: *Mitteilungen der Physikalischen Gesellschaft Zürich* 18 (1916), pp. 121–128.
- [5] T. H. Maiman. "Stimulated Optical Radiation in Ruby". In: *Nature* 187.4736 (Aug. 1960), pp. 493–494. ISSN: 0028-0836, 1476-4687. DOI: 10.1038/187493a0.
- [6] P. A. Franken, A. E. Hill, C. W. Peters, and G. Weinreich. "Generation of Optical Harmonics". In: *Physical Review Letters* 7.4 (Aug. 15, 1961), pp. 118–119. ISSN: 0031-9007. DOI: 10.1103/PhysRevLett.7.118.
- [7] L. E. Hargrove, R. L. Fork, and M. A. Pollack. "LOCKING OF He-Ne LASER MODES INDUCED BY SYNCHRONOUS INTRACAVITY MODULATION". In: *Applied Physics Letters* 5.1 (July 1964), pp. 4–5. ISSN: 0003-6951, 1077-3118. DOI: 10.1063/1.1754025.
- [8] D. E. Spence, P. N. Kean, and W. Sibbett. "60-fsec pulse generation from a self-mode-locked Ti:sapphire laser". In: *Optics Letters* 16.1 (Jan. 1, 1991), p. 42. ISSN: 0146-9592, 1539-4794. DOI: 10.1364/OL.16.000042.
- [9] U. Keller, G. W. 'tHooft, W. H. Knox, and J. E. Cunningham. "Femtosecond pulses from a continuously self-starting passively mode-locked Ti:sapphire laser". In: *Optics Letters* 16.13 (July 1, 1991), p. 1022. ISSN: 0146-9592, 1539-4794. DOI: 10.1364/OL.16.001022.

- [10] Luis Spinelli, Bernard Couillaud, Norman Goldblatt, and Daniel K. Negus. “Starting and Generation of Sub-100fs Pulses in Ti:Al₂O₃ by Self-Focusing”. In: *Conference on Lasers and Electro-Optics*. Conference on Lasers and Electro-Optics. Vol. 10. OSA Technical Digest. Optical Society of America, May 12, 1991, CPD7.
- [11] Michel Piché. “Beam reshaping and self-mode-locking in nonlinear laser resonators”. In: *Optics Communications* 86.2 (Nov. 1991), pp. 156–160. ISSN: 00304018. DOI: 10.1016/0030-4018(91)90552-0.
- [12] François Salin, Michel Piché, and Jeff Squier. “Mode locking of Ti:Al₂O₃ lasers and self-focusing: a Gaussian approximation”. In: *Optics Letters* 16.21 (Nov. 1, 1991), p. 1674. ISSN: 0146-9592, 1539-4794. DOI: 10.1364/OL.16.001674.
- [13] H. A. Haus, J. G. Fujimoto, and E. P. Ippen. “Structures for additive pulse mode locking”. In: *Journal of the Optical Society of America B* 8.10 (Oct. 1, 1991), p. 2068. ISSN: 0740-3224, 1520-8540. DOI: 10.1364/JOSAB.8.002068.
- [14] T. Brabec, Ch. Spielmann, P. F. Curley, and F. Krausz. “Kerr lens mode locking”. In: *Optics Letters* 17.18 (Sept. 15, 1992), p. 1292. ISSN: 0146-9592, 1539-4794. DOI: 10.1364/OL.17.001292.
- [15] H.A. Haus, J.G. Fujimoto, and E.P. Ippen. “Analytic theory of additive pulse and Kerr lens mode locking”. In: *IEEE Journal of Quantum Electronics* 28.10 (Oct. 1992), pp. 2086–2096. ISSN: 00189197. DOI: 10.1109/3.159519.
- [16] U. Keller, W. H. Knox, and H. Roskos. “Coupled-cavity resonant passive mode-locked Ti:sapphire laser”. In: *Optics Letters* 15.23 (Dec. 1, 1990), p. 1377. ISSN: 0146-9592, 1539-4794. DOI: 10.1364/OL.15.001377.
- [17] Ursula Keller. “Recent developments in compact ultrafast lasers”. In: *Nature* 424.6950 (Aug. 14, 2003), pp. 831–838. ISSN: 0028-0836. DOI: 10.1038/nature01938.
- [18] Thomas Brabec and Ferenc Krausz. “Intense few-cycle laser fields: Frontiers of nonlinear optics”. In: *Reviews of Modern Physics* 72.2 (Apr. 1, 2000), pp. 545–591. ISSN: 0034-6861, 1539-0756. DOI: 10.1103/RevModPhys.72.545.
- [19] Ahmed H. Zewail. “Femtochemistry. Past, present, and future”. In: *Pure and Applied Chemistry* 72.12 (Jan. 2000). ISSN: 1365-3075, 0033-4545. DOI: 10.1351/pac200072122219.
- [20] Ferenc Krausz and Misha Ivanov. “Attosecond physics”. en. In: *Reviews of Modern Physics* 81.1 (Feb. 2009), pp. 163–234. ISSN: 0034-6861, 1539-0756. DOI: 10.1103/RevModPhys.81.163.

- [21] Donna Strickland and Gerard Mourou. “Compression of amplified chirped optical pulses”. In: *Optics communications* 55.6 (1985), pp. 447–449.
- [22] M. Nisoli, S. De Silvestri, and O. Svelto. “Generation of high energy 10 fs pulses by a new pulse compression technique”. en. In: *Applied Physics Letters* 68.20 (May 1996), pp. 2793–2795. ISSN: 0003-6951, 1077-3118. DOI: 10.1063/1.116609.
- [23] B. Schenkel, J. Biegert, U. Keller, C. Vozzi, M. Nisoli, G. Sansone, S. Stagira, S. De Silvestri, and O. Svelto. “Generation of 3.8-fs pulses from adaptive compression of a cascaded hollow fiber supercontinuum”. In: *Optics letters* 28.20 (2003), pp. 1987–1989.
- [24] A L Cavalieri, E Goulielmakis, B Horvath, W Helml, M Schultze, M Fieß, V Pervak, L Veisz, V S Yakovlev, M Uiberacker, A Apolonski, F Krausz, and R Kienberger. “Intense 1.5-cycle near infrared laser waveforms and their use for the generation of ultra-broadband soft-x-ray harmonic continua”. In: *New Journal of Physics* 9.7 (July 2007), pp. 242–242. ISSN: 1367-2630. DOI: 10.1088/1367-2630/9/7/242.
- [25] Isao Matsushima, Hidehiko Yashiro, and Toshihisa Tomie. “10 kHz 40 W Ti:sapphire regenerative ring amplifier”. en. In: *Optics Letters* 31.13 (July 2006), p. 2066. ISSN: 0146-9592, 1539-4794. DOI: 10.1364/OL.31.002066.
- [26] T. Südmeyer, C. Kränkel, C. R. E. Baer, O. H. Heckl, C. J. Saraceno, M. Golling, R. Peters, K. Petermann, G. Huber, and U. Keller. “High-power ultrafast thin disk laser oscillators and their potential for sub-100-femtosecond pulse generation”. In: *Applied Physics B* 97.2 (Oct. 2009), pp. 281–295. ISSN: 0946-2171, 1432-0649. DOI: 10.1007/s00340-009-3700-z.
- [27] G. Sansone, F. Kelkensberg, F. Morales, J. F. Perez-Torres, F. Martín, and M. J. J. Vrakking. “Attosecond Time-Resolved Electron Dynamics in the Hydrogen Molecule”. In: *IEEE Journal of Selected Topics in Quantum Electronics* 18.1 (Jan. 2012), pp. 520–530. ISSN: 1077-260X, 1558-4542. DOI: 10.1109/JSTQE.2011.2155624.
- [28] Stephen R. Leone, C. William McCurdy, Joachim Burgdörfer, Lorenz S. Cederbaum, Zenghu Chang, Nirit Dudovich, Johannes Feist, Chris H. Greene, Misha Ivanov, Reinhard Kienberger, Ursula Keller, Matthias F. Kling, Zhi-Heng Loh, Thomas Pfeifer, Adrian N. Pfeiffer, Robin Santra, Kenneth Schaffer, Albert Stolow, Uwe Thumm, and Marc J. J. Vrakking. “What will it take to observe processes in ‘real time’?” In: *Nature Photonics* 8.3 (Feb. 28, 2014), pp. 162–166. ISSN: 1749-4885, 1749-4893. DOI: 10.1038/nphoton.2014.48.

- [29] Cesar Jauregui, Jens Limpert, and Andreas Tünnermann. “High-power fibre lasers”. In: *Nature Photonics* 7.11 (Oct. 20, 2013), pp. 861–867. ISSN: 1749-4885, 1749-4893. DOI: 10.1038/nphoton.2013.273.
- [30] Steffen Hädrich, Marco Kienel, Michael Müller, Arno Klenke, Jan Rothhardt, Robert Klas, Thomas Gottschall, Tino Eidam, András Drozdy, Péter Jójárt, Zoltán Várallyay, Eric Cormier, Károly Osvay, Andreas Tünnermann, and Jens Limpert. “Energetic sub-2-cycle laser with 216 W average power”. en. In: *Optics Letters* 41.18 (Sept. 2016), p. 4332. ISSN: 0146-9592, 1539-4794. DOI: 10.1364/OL.41.004332.
- [31] Peter Russbueldt, Dieter Hoffmann, Marco Hofer, Jens Lohring, Jorg Luttmann, Ansgar Meissner, Johannes Weitenberg, Martin Traub, Thomas Sartorius, Dominik Esser, Rolf Wester, Peter Loosen, and Reinhart Poprawe. “Innoslab Amplifiers”. In: *IEEE Journal of Selected Topics in Quantum Electronics* 21.1 (Jan. 2015), pp. 447–463. ISSN: 1077-260X, 1558-4542. DOI: 10.1109/JSTQE.2014.2333234.
- [32] A. Giesen, H. Hügel, A. Voss, K. Wittig, U. Brauch, and H. Opower. “Scalable concept for diode-pumped high-power solid-state lasers”. In: *Applied Physics B* 58.5 (May 1994), pp. 365–372. ISSN: 0946-2171, 1432-0649. DOI: 10.1007/BF01081875.
- [33] Jan-Philipp Negel, André Loescher, Andreas Voss, Dominik Bauer, Dirk Sutter, Alexander Killi, Marwan Abdou Ahmed, and Thomas Graf. “Ultrafast thin-disk multipass laser amplifier delivering 1.4 kW (4.7 mJ, 1030 nm) average power converted to 820 W at 515 nm and 234 W at 343 nm”. en. In: *Optics Express* 23.16 (Aug. 2015), p. 21064. ISSN: 1094-4087. DOI: 10.1364/OE.23.021064.
- [34] Michael Müller, Marco Kienel, Arno Klenke, Thomas Gottschall, Evgeny Shestaev, Marco Plötner, Jens Limpert, and Andreas Tünnermann. “1 kW 1 mJ eight-channel ultrafast fiber laser”. In: *Optics Letters* 41.15 (Aug. 1, 2016), p. 3439. ISSN: 0146-9592, 1539-4794. DOI: 10.1364/OL.41.003439.
- [35] Thomas Nubbemeyer, Martin Kaumanns, Moritz Ueffing, Martin Gorjan, Ayman Alismail, Hanieh Fattahi, Jonathan Brons, Oleg Pronin, Helena G. Barros, Zsuzsanna Major, Thomas Metzger, Dirk Sutter, and Ferenc Krausz. “1 kW, 200 mJ picosecond thin-disk laser system”. en. In: *Optics Letters* 42.7 (Apr. 2017), p. 1381. ISSN: 0146-9592, 1539-4794. DOI: 10.1364/OL.42.001381.
- [36] Joerg Koerner, Christian Vorholt, Hartmut Liebetrau, Martin Kahle, Diethard Kloeppel, Reinhard Seifert, Joachim Hein, and Malte C. Kaluza. “Measurement of temperature-dependent absorption and emission spectra of Yb:YAG, Yb:LuAG, and Yb:CaF₂ between 20 °C and 200 °C and predicti-

- ons on their influence on laser performance”. en. In: *Journal of the Optical Society of America B* 29.9 (Sept. 2012), p. 2493. ISSN: 0740-3224, 1520-8540. DOI: 10.1364/JOSAB.29.002493.
- [37] Catherine Teisset, Marcel Schultze, Robert Bessing, Matthias Haefner, Stefan Prinz, Dirk Sutter, and Thomas Metzger. “300 W Picosecond Thin-Disk Regenerative Amplifier at 10 kHz Repetition Rate”. In: OSA, 2013, JTh5A.1. ISBN: 978-1-55752-983-1. DOI: 10.1364/ASSL.2013.JTh5A.1.
- [38] Hanieh Fattahi, Helena G. Barros, Martin Gorjan, Thomas Nubbemeyer, Bidoor Alsaif, Catherine Y. Teisset, Marcel Schultze, Stephan Prinz, Matthias Haefner, Moritz Ueffing, Ayman Alismail, Lénárd Vámos, Alexander Schwarz, Oleg Pronin, Jonathan Brons, Xiao Tao Geng, Gunnar Arisholm, Marcelo Ciappina, Vladislav S. Yakovlev, Dong-Eon Kim, Abdallah M. Azzeer, Nicholas Karpowicz, Dirk Sutter, Zsuzsanna Major, Thomas Metzger, and Ferenc Krausz. “Third-generation femtosecond technology”. en. In: *Optica* 1.1 (July 2014), p. 45. ISSN: 2334-2536. DOI: 10.1364/OPTICA.1.000045.
- [39] Catherine Teisset, Marcel Schultze, Robert Bessing, Matthias Häfner, Jens Rauschenberger, Dirk Sutter, and Thomas Metzger. “Picosecond Thin-Disk Regenerative Amplifier with High Average Power for Pumping Optical Parametric Amplifiers”. In: OSA, 2013, CTh5C.6. ISBN: 978-1-55752-972-5. DOI: 10.1364/CLEO_SI.2013.CTh5C.6.
- [40] Jonathan Fischer, Alexander-Cornelius Heinrich, Simon Maier, Julian Jungwirth, Daniele Brida, and Alfred Leitenstorfer. “615 fs pulses with 17 mJ energy generated by an Yb:thin-disk amplifier at 3 kHz repetition rate”. In: *Optics Letters* 41.2 (Jan. 15, 2016), p. 246. ISSN: 0146-9592, 1539-4794. DOI: 10.1364/OL.41.000246.
- [41] Tino Eidam, Stefan Hanf, Enrico Seise, Thomas V. Andersen, Thomas Gähler, Christian Wirth, Thomas Schreiber, Jens Limpert, and Andreas Tünnermann. “Femtosecond fiber CPA system emitting 830 W average output power”. In: *Optics letters* 35.2 (2010), pp. 94–96.
- [42] Arno Klenke, Sven Breilkopf, Marco Kienel, Thomas Gottschall, Tino Eidam, Steffen Hädrich, Jan Rothhardt, Jens Limpert, and Andreas Tünnermann. “530 W, 13 mJ, four-channel coherently combined femtosecond fiber chirped-pulse amplification system”. In: *Optics Letters* 38.13 (July 1, 2013), p. 2283. ISSN: 0146-9592, 1539-4794. DOI: 10.1364/OL.38.002283.
- [43] Arno Klenke, Steffen Hädrich, Tino Eidam, Jan Rothhardt, Marco Kienel, Stefan Demmler, Thomas Gottschall, Jens Limpert, and Andreas Tünnermann. “22 GW peak-power fiber chirped-pulse-amplification system”. In: *Optics Letters* 39.24 (Dec. 15, 2014), p. 6875. ISSN: 0146-9592, 1539-4794. DOI: 10.1364/OL.39.006875.

- [44] Katie Kowalewski, Jason Zembek, Victoria Envid, and David C. Brown. “201 W picosecond green laser using a mode-locked fiber laser driven cryogenic Yb:YAG amplifier system”. In: *Optics Letters* 37.22 (Nov. 15, 2012), p. 4633. ISSN: 0146-9592, 1539-4794. DOI: 10.1364/OL.37.004633.
- [45] K. F. Wall, D. E. Miller, and T. Y. Fan. “Cryo-Yb:YAG lasers for next-generation photoinjector applications”. In: ed. by W. Andrew Clarkson and Ramesh K. Shori. Feb. 9, 2012, p. 823512. DOI: 10.1117/12.907419.
- [46] Shigeki Tokita, Junji Kawanaka, Yasukazu Izawa, Masayuki Fujita, and Toshiyuki Kawashima. “23.7-W picosecond cryogenic-Yb:YAG multipass amplifier”. In: *Optics Express* 15.7 (2007), p. 3955. ISSN: 1094-4087. DOI: 10.1364/OE.15.003955.
- [47] Darren A. Rand, Scot E. J. Shaw, Juan R. Ochoa, Daniel J. Ripin, Andrew Taylor, Tso Yee Fan, Hector Martin, Scott Hawes, Jim Zhang, Samvel Sarkisyan, Eric Wilson, and Paul Lundquist. “Picosecond pulses from a cryogenically cooled, composite amplifier using Yb:YAG and Yb:GSAG”. In: *Optics Letters* 36.3 (Feb. 1, 2011), p. 340. ISSN: 0146-9592, 1539-4794. DOI: 10.1364/OL.36.000340.
- [48] Kyung-Han Hong, Juliet T. Gopinath, Darren Rand, Aleem M. Siddiqui, Shu-Wei Huang, Enbang Li, Benjamin J. Eggleton, John D. Hybl, Tso Yee Fan, and Franz X. Kärtner. “High-energy, kHz-repetition-rate, ps cryogenic Yb:YAG chirped-pulse amplifier”. In: *Optics Letters* 35.11 (June 1, 2010), p. 1752. ISSN: 0146-9592, 1539-4794. DOI: 10.1364/OL.35.001752.
- [49] L. E. Zapata, F. Reichert, M. Hemmer, and F. X. Kärtner. “250 W average power, 100 kHz repetition rate cryogenic Yb:YAG amplifier for OPCPA pumping”. In: *Optics Letters* 41.3 (Feb. 1, 2016), p. 492. ISSN: 0146-9592, 1539-4794. DOI: 10.1364/OL.41.000492.
- [50] Cory Baumgarten, Michael Pedicone, Herman Bravo, Hanchen Wang, Liang Yin, Carmen S. Menoni, Jorge J. Rocca, and Brendan A. Reagan. “1 J, 0.5 kHz repetition rate picosecond laser”. In: *Optics Letters* 41.14 (July 15, 2016), p. 3339. ISSN: 0146-9592, 1539-4794. DOI: 10.1364/OL.41.003339.
- [51] Brendan A. Reagan, Cory Baumgarten, Michael Pedicone, Herman Bravo, Liang Yin, Hanchen Wang, Carmen Menoni, and Jorge Rocca. “Development of High Repetition Rate, High Energy Diode-Pumped Short Pulse Lasers and Applications”. In: OSA, 2017, ATh1A.1. ISBN: 978-0-9600380-7-7. DOI: 10.1364/ASSL.2017.ATh1A.1.
- [52] P. Russbuedt, T. Mans, G. Rotarius, J. Weitenberg, H. D. Hoffmann, and R. Poprawe. “400W Yb:YAG Innoslab fs-Amplifier”. In: *Optics Express* 17.15 (July 20, 2009), p. 12230. ISSN: 1094-4087. DOI: 10.1364/OE.17.012230.

- [53] P. Russbueldt, T. Mans, J. Weitenberg, H. D. Hoffmann, and R. Poprawe. “Compact diode-pumped 1.1 kW Yb:YAG Innoslab femtosecond amplifier”. In: *Optics Letters* 35.24 (Dec. 15, 2010), p. 4169. ISSN: 0146-9592, 1539-4794. DOI: 10.1364/OL.35.004169.
- [54] Tl Mans, Jan Dolkemeyer, P. Russbüldt, and Claus Schnitzler. “Highly flexible ultrafast laser system with 260W average power”. In: ed. by W. Andrew Clarkson, Norman Hodgson, and Ramesh Shori. Feb. 10, 2011, p. 79120M. DOI: 10.1117/12.874417.
- [55] M. Schulz, R. Riedel, A. Willner, T. Mans, C. Schnitzler, P. Russbueldt, J. Dolkemeyer, E. Seise, T. Gottschall, S. Hädrich, S. Duesterer, H. Schlarb, J. Feldhaus, J. Limpert, B. Faatz, A. Tünnermann, J. Rossbach, M. Drescher, and F. Tavella. “Yb:YAG Innoslab amplifier: efficient high repetition rate subpicosecond pumping system for optical parametric chirped pulse amplification”. In: *Optics Letters* 36.13 (July 1, 2011), p. 2456. ISSN: 0146-9592, 1539-4794. DOI: 10.1364/OL.36.002456.
- [56] R. Riedel, A. Stephanides, M. J. Prandolini, B. Gronloh, B. Jungbluth, T. Mans, and F. Tavella. “Power scaling of supercontinuum seeded megahertz-repetition rate optical parametric chirped pulse amplifiers”. In: *Optics Letters* 39.6 (Mar. 15, 2014), p. 1422. ISSN: 0146-9592, 1539-4794. DOI: 10.1364/OL.39.001422.
- [57] Julien Pouysegur, Martin Delaigue, Clemens Honninger, Yoann Zaouter, Patrick Georges, Frederic Druon, and Eric Mottay. “Numerical and Experimental Analysis of Nonlinear Regenerative Amplifiers Overcoming the Gain Bandwidth Limitation”. In: *IEEE Journal of Selected Topics in Quantum Electronics* 21.1 (Jan. 2015), pp. 212–219. ISSN: 1077-260X, 1558-4542. DOI: 10.1109/JSTQE.2014.2321520.
- [58] Mikhail Larionov, Frank Butze, Detlef Nickel, and Adolf Giesen. “High-repetition-rate regenerative thin-disk amplifier with 116 μ J pulse energy and 250 fs pulse duration”. In: *Optics Letters* 32.5 (Mar. 1, 2007), p. 494. ISSN: 0146-9592, 1539-4794. DOI: 10.1364/OL.32.000494.
- [59] Guenter Huber, Christian Kränkel, and Klaus Petermann. “Solid-state lasers: status and future [Invited]”. In: *Journal of the Optical Society of America B* 27.11 (Nov. 1, 2010), B93. ISSN: 0740-3224, 1520-8540. DOI: 10.1364/JOSAB.27.000B93.
- [60] Robert W. Boyd. *Nonlinear optics*. 3rd ed. Amsterdam ; Boston: Academic Press, 2008. ISBN: 978-0-12-369470-6.

- [61] Thomas Brabec and Ferenc Krausz. “Nonlinear Optical Pulse Propagation in the Single-Cycle Regime”. In: *Physical Review Letters* 78.17 (Apr. 28, 1997), pp. 3282–3285. ISSN: 0031-9007, 1079-7114. DOI: 10.1103/PhysRevLett.78.3282.
- [62] Georg A. Reider. *Photonik: eine Einführung in die Grundlagen*. 2., überarb. und erw. Aufl. Springer-Lehrbuch Technik. OCLC: 249445916. Wien: Springer, 2005. 386 pp. ISBN: 978-3-211-21901-0.
- [63] L.G. Gouy. *Sur une propriété nouvelle des ondes lumineuses*. Mélanges scientifiques. Gauthier-Villars, 1890.
- [64] G.A. Deschamps. “Gaussian beam as a bundle of complex rays”. In: *Electronics Letters* 7.23 (1971), p. 684. ISSN: 00135194. DOI: 10.1049/e1:19710467.
- [65] Marc Couture and Pierre-A. Belanger. “From Gaussian beam to complex-source-point spherical wave”. In: *Physical Review A* 24.1 (July 1, 1981), pp. 355–359. ISSN: 0556-2791. DOI: 10.1103/PhysRevA.24.355.
- [66] H. Kogelnik and T. Li. “Laser Beams and Resonators”. In: *Applied Optics* 5.10 (Oct. 1, 1966), p. 1550. ISSN: 0003-6935, 1539-4522. DOI: 10.1364/AO.5.001550.
- [67] Anthony E. Siegman. “New developments in laser resonators”. In: ed. by Dale A. Holmes. June 1, 1990, p. 2. DOI: 10.1117/12.18425.
- [68] Norman Hodgson and Horst Weber. *Laser resonators and beam propagation: fundamentals, advanced concepts and applications*. 2nd ed. Springer series in optical sciences v. 108. OCLC: ocm60564637. New York: Springer, 2005. 793 pp. ISBN: 978-0-387-40078-5.
- [69] Robert Szipöcs, Christian Spielmann, Ferenc Krausz, and Kárpát Ferencz. “Chirped multilayer coatings for broadband dispersion control in femtosecond lasers”. In: *Optics Letters* 19.3 (Feb. 1, 1994), p. 201. ISSN: 0146-9592, 1539-4794. DOI: 10.1364/OL.19.000201.
- [70] Valentin G. Dmitriev, Gagik G. Gurzadjan, and David N. Nikogosjan. *Handbook of nonlinear optical crystals*. 3. rev. ed., softcover reprint of the hardcover 3rd ed. 1999. Springer series in optical sciences 64. OCLC: 837781122. Berlin: Springer, 2010. 413 pp. ISBN: 978-3-540-65394-3.
- [71] Richard Lee Sutherland, Daniel Garth McLean, and Sean Kirkpatrick. *Handbook of nonlinear optics*. 2nd ed., rev. and expanded. Optical engineering 82. New York: Marcel Dekker, 2003. 971 pp. ISBN: 978-0-8247-4243-0.
- [72] Max Born and Emil Wolf. *Principles of optics: electromagnetic theory of propagation, interference and diffraction of light*. 4th ed. Oxford, New York: Pergamon Press, 1969. 808 pp. ISBN: 978-0-08-013987-6.

- [73] H. Nakatani, W. Bosenberg, L. K. Cheng, and C. L. Tang. “Linear electro-optic effect in barium metaborate”. In: *Applied Physics Letters* 52.16 (Apr. 18, 1988), pp. 1288–1290. ISSN: 0003-6951, 1077-3118. DOI: 10.1063/1.99680.
- [74] M. Abarkan, J.P. Salvestrini, M.D. Fontana, and M. Aillerie. “Frequency and wavelength dependences of electro-optic coefficients in inorganic crystals”. In: *Applied Physics B: Lasers and Optics* 76.7 (July 1, 2003), pp. 765–769. ISSN: 0946-2171, 1432-0649. DOI: 10.1007/s00340-003-1196-5.
- [75] D. N. Nikogosyan. *Nonlinear optical crystals: a complete survey*. OCLC: ocm55502652. New York: Springer-Science, 2005. 427 pp. ISBN: 978-0-387-22022-2.
- [76] Castech. *RTP Crystal*. 2017.
- [77] M. Roth, M. Tseitlin, and N. Angert. “Oxide crystals for electro-optic Q-switching of lasers”. In: *Glass Physics and Chemistry* 31.1 (Jan. 2005), pp. 86–95. ISSN: 1087-6596, 1608-313X. DOI: 10.1007/s10720-005-0028-6.
- [78] G. P. Agrawal. *Nonlinear fiber optics*. 3rd ed. Optics and photonics. San Diego: Academic Press, 2001. 466 pp. ISBN: 978-0-12-045143-2.
- [79] Rick Trebino, Kenneth W. DeLong, David N. Fittinghoff, John N. Sweetser, Marco A. Krumbügel, Bruce A. Richman, and Daniel J. Kane. “Measuring ultrashort laser pulses in the time-frequency domain using frequency-resolved optical gating”. In: *Review of Scientific Instruments* 68.9 (Sept. 1997), pp. 3277–3295. ISSN: 0034-6748, 1089-7623. DOI: 10.1063/1.1148286.
- [80] Rick Trebino. *Frequency-Resolved Optical Gating: The Measurement of Ultrashort Laser Pulses*. OCLC: 906705593. Boston, MA: Springer US, 2000. ISBN: 978-1-4615-1181-6.
- [81] R. Kienberger, E. Goulielmakis, M. Uiberacker, A. Baltuska, V. Yakovlev, F. Bammer, A. Scrinzi, Th. Westerwalbesloh, U. Kleineberg, U. Heinzmann, M. Drescher, and F. Krausz. “Atomic transient recorder”. In: *Nature* 427.6977 (Feb. 26, 2004), pp. 817–821. ISSN: 0028-0836, 1476-4679. DOI: 10.1038/nature02277.
- [82] Michelle Rhodes, Günter Steinmeyer, and Rick Trebino. “Standards for ultrashort-laser-pulse-measurement techniques and their consideration for self-referenced spectral interferometry”. In: *Applied Optics* 53.16 (June 1, 2014), p. D1. ISSN: 0003-6935, 1539-4522. DOI: 10.1364/AO.53.0000D1.

- [83] Ioachim Pupeza, Tino Eidam, Jens Rauschenberger, Birgitta Bernhardt, Akira Ozawa, Ernst Fill, Alexander Apolonski, Thomas Udem, Jens Limpert, Zeyad A. Alahmed, Abdallah M. Azzeer, Andreas Tünnermann, Theodor W. Hänsch, and Ferenc Krausz. “Power scaling of a high-repetition-rate enhancement cavity”. In: *Optics Letters* 35.12 (June 15, 2010), p. 2052. ISSN: 0146-9592, 1539-4794. DOI: 10.1364/OL.35.002052.
- [84] Anthony E. Siegman. *Lasers*. OCLC: 14525287. Mill Valley, Calif: Univ. Science Books, 1986. 1283 pp. ISBN: 978-0-935702-11-8.
- [85] N.P. Barnes and B.M. Walsh. “Amplified spontaneous emission-application to Nd:YAG lasers”. In: *IEEE Journal of Quantum Electronics* 35.1 (Jan. 1999), pp. 101–109. ISSN: 00189197. DOI: 10.1109/3.737626.
- [86] Jochen Speiser. “Scaling of thin-disk lasers—influence of amplified spontaneous emission”. In: *Journal of the Optical Society of America B* 26.1 (Jan. 1, 2009), p. 26. ISSN: 0740-3224, 1520-8540. DOI: 10.1364/JOSAB.26.000026.
- [87] R. Paschotta, J. Nilsson, P.R. Barber, J.E. Caplen, A.C. Tropper, and D.C. Hanna. “Lifetime quenching in Yb-doped fibres”. In: *Optics Communications* 136.5 (Apr. 1997), pp. 375–378. ISSN: 00304018. DOI: 10.1016/S0030-4018(96)00720-1.
- [88] The LIGO Scientific Collaboration et al. “Advanced LIGO”. In: *Classical and Quantum Gravity* 32.7 (Apr. 9, 2015), p. 074001. ISSN: 0264-9381, 1361-6382. DOI: 10.1088/0264-9381/32/7/074001.
- [89] Vittorio Magni. “Multielement stable resonators containing a variable lens”. In: *Journal of the Optical Society of America A* 4.10 (Oct. 1, 1987), p. 1962. ISSN: 1084-7529, 1520-8532. DOI: 10.1364/JOSAA.4.001962.
- [90] Henning Carstens, Simon Holzberger, Jan Kaster, Johannes Weitenberg, Volodymyr Pervak, Alexander Apolonski, Ernst Fill, Ferenc Krausz, and Ioachim Pupeza. “Large-mode enhancement cavities”. In: *Optics Express* 21.9 (May 6, 2013), p. 11606. ISSN: 1094-4087. DOI: 10.1364/OE.21.011606.
- [91] V. Magni, G. Valentini, and S. De Silvestri. “Recent developments in laser resonator design”. In: *Optical and Quantum Electronics* 23.9 (Nov. 1991), pp. 1105–1134. ISSN: 0306-8919, 1572-817X. DOI: 10.1007/BF00619980.
- [92] Sylvain Gigan, Laurent Lopez, Nicolas Treps, Agnès Maître, and Claude Fabre. “Image transmission through a stable paraxial cavity”. In: *Physical Review A* 72.2 (Aug. 5, 2005). ISSN: 1050-2947, 1094-1622. DOI: 10.1103/PhysRevA.72.023804.
- [93] Jochen Dörring, Alexander Killi, Uwe Morgner, Alexander Lang, Max Lederer, and Daniel Kopf. “Period doubling and deterministic chaos in continuously pumped regenerative amplifiers”. In: *Optics Express* 12.8 (2004), p. 1759. ISSN: 1094-4087. DOI: 10.1364/OPEX.12.001759.

- [94] M. Grishin, V. Gulbinas, and A. Michailovas. “Dynamics of high repetition rate regenerative amplifiers”. In: *Optics Express* 15.15 (2007), p. 9434. ISSN: 1094-4087. DOI: 10.1364/OE.15.009434.
- [95] Thomas Metzger, Alexander Schwarz, Catherine Yuriko Teisset, Dirk Sutter, Alexander Killi, Reinhard Kienberger, and Ferenc Krausz. “High-repetition-rate picosecond pump laser based on a Yb:YAG disk amplifier for optical parametric amplification”. en. In: *Optics Letters* 34.14 (July 2009), p. 2123. ISSN: 0146-9592, 1539-4794. DOI: 10.1364/OL.34.002123.
- [96] Hanieh Fattahi, Alexander Schwarz, Xiao Tao Geng, Sabine Keiber, Dong Eon Kim, Ferenc Krausz, and Nicholas Karpowicz. “Decoupling chaotic amplification and nonlinear phase in high-energy thin-disk amplifiers for stable OPCPA pumping”. In: *Optics Express* 22.25 (Dec. 15, 2014), p. 31440. ISSN: 1094-4087. DOI: 10.1364/OE.22.031440.
- [97] J Rothhardt, S Hädrich, Jc Delagnes, E Cormier, and J Limpert. “High Average Power Near-Infrared Few-Cycle Lasers”. In: *Laser & Photonics Reviews* 11.4 (July 2017), p. 1700043. ISSN: 18638880. DOI: 10.1002/lpor.201700043.
- [98] Oliver H. Heckl, Jochen Kleinbauer, Dominik Bauer, Sascha Weiler, Thomas Metzger, and Dirk H. Sutter. “Ultrafast Thin-Disk Lasers”. In: *Ultrashort Pulse Laser Technology*. Ed. by Stefan Nolte, Frank Schrepel, and Friedrich Dausinger. Vol. 195. Cham: Springer International Publishing, 2016, pp. 93–115. ISBN: 978-3-319-17659-8.
- [99] Aldo Antognini, Karsten Schuhmann, Fernando D. Amaro, François Biraben, Andreas Dax, Adolf Giesen, Thomas Graf, Theodor W. Hansch, Paul Indelicato, Lucile Julien, Cheng-Yang Kao, Paul E. Knowles, Franz Kottmann, Eric Le Bigot, Yi-Wei Liu, Livia Ludhova, Niels Moschuring, Françoise Mulhauser, Tobias Nebel, François Nez, Paul Rabinowitz, Catherine Schwob, David Taqqu, and Randolph Pohl. “Thin-Disk Yb:YAG Oscillator-Amplifier Laser, ASE, and Effective Yb:YAG Lifetime”. In: *IEEE Journal of Quantum Electronics* 45.8 (Aug. 2009), pp. 993–1005. ISSN: 0018-9197. DOI: 10.1109/JQE.2009.2014881.
- [100] C. J. Saraceno, F. Emaury, C. Schriber, A. Diebold, M. Hoffmann, M. Golling, T. Südmeyer, and U. Keller. “Toward Millijoule-Level High-Power Ultrafast Thin-Disk Oscillators”. In: *IEEE Journal of Selected Topics in Quantum Electronics* 21.1 (Jan. 2015), pp. 106–123. ISSN: 1077-260X. DOI: 10.1109/JSTQE.2014.2341588.

- [101] B. L. Volodin, S. V. Dolgy, E. D. Melnik, E. Downs, J. Shaw, and V. S. Ban. “Wavelength stabilization and spectrum narrowing of high-power multimode laser diodes and arrays by use of volume Bragg gratings”. In: *Optics Letters* 29.16 (Aug. 13, 2004), p. 1891. ISSN: 0146-9592, 1539-4794. DOI: 10.1364/OL.29.001891.
- [102] A. Brenier, Y. Guyot, H. Canibano, G. Boulon, A. Ródenas, D. Jaque, A. Eganyan, and A. G. Petrosyan. “Growth, spectroscopic, and laser properties of Yb³⁺-doped Lu₃Al₅O₁₂ garnet crystal”. en. In: *Journal of the Optical Society of America B* 23.4 (Apr. 2006), p. 676. ISSN: 0740-3224, 1520-8540. DOI: 10.1364/JOSAB.23.000676.
- [103] Jun Dong, Michael Bass, Yanli Mao, Peizhen Deng, and Fuxi Gan. “Dependence of the Yb³⁺ emission cross section and lifetime on temperature and concentration in yttrium aluminum garnet”. In: *Journal of the Optical Society of America B* 20.9 (Sept. 1, 2003), p. 1975. ISSN: 0740-3224, 1520-8540. DOI: 10.1364/JOSAB.20.001975.
- [104] Jasbinder Sanghera, Woohong Kim, Guillermo Villalobos, Brandon Shaw, Colin Baker, Jesse Frantz, Bryan Sadowski, and Ishwar Aggarwal. “Ceramic laser materials: Past and present”. In: *Optical Materials* 35.4 (Feb. 2013), pp. 693–699. ISSN: 09253467. DOI: 10.1016/j.optmat.2012.04.021.
- [105] Kolja Beil, Susanne T. Fredrich-Thornton, Friedjof Tellkamp, Rigo Peters, Christian Kränkel, Klaus Petermann, and Günter Huber. “Thermal and laser properties of Yb: LuAG for kW thin disk lasers”. In: *Optics express* 18.20 (2010), pp. 20712–20722.
- [106] M. Siebold, M. Loeser, F. Roeser, M. Seltmann, G. Harzendorf, I. Tsybin, S. Linke, S. Banerjee, P. D. Mason, P. J. Phillips, K. Ertel, J. C. Collier, and U. Schramm. “High-energy, ceramic-disk Yb:LuAG laser amplifier”. In: *Optics Express* 20.20 (Sept. 24, 2012), p. 21992. ISSN: 1094-4087. DOI: 10.1364/OE.20.021992.
- [107] Hiroaki Nakao, Akira Shirakawa, Ken-ichi Ueda, Hideki Yagi, Takagimi Yanagitani, Birgit Weichelt, Katrin Wentsch, Marwan Abdou Ahmed, and Thomas Graf. “Demonstration of a Yb³⁺-doped Lu₃Al₅O₁₂ ceramic thin-disk laser”. In: *Optics Letters* 39.10 (May 15, 2014), p. 2884. ISSN: 0146-9592, 1539-4794. DOI: 10.1364/OL.39.002884.
- [108] Shotaro Kitajima, Hiroaki Nakao, Akira Shirakawa, Hideki Yagi, and Takagimi Yanagitani. “Kerr-lens mode-locked Yb³⁺-doped Lu₃Al₅O₁₂ ceramic laser”. In: *Optics Letters* 41.19 (Oct. 1, 2016), p. 4570. ISSN: 0146-9592, 1539-4794. DOI: 10.1364/OL.41.004570.

- [109] Cyrill Roman Emmanuel Baer, Christian Kränkel, Clara Jody Saraceno, Oliver Hubert Heckl, Matthias Golling, Rigo Peters, Klaus Petermann, Thomas Südmeyer, Günter Huber, and Ursula Keller. “Femtosecond thin-disk laser with 141 W of average power”. In: *Optics Letters* 35.13 (July 1, 2010), p. 2302. ISSN: 0146-9592, 1539-4794. DOI: 10.1364/OL.35.002302.
- [110] I. J. Graumann, A. Diebold, C. G. E. Alfieri, F. Emaury, B. Deppe, M. Golling, D. Bauer, D. Sutter, C. Kränkel, C. J. Saraceno, C. R. Phillips, and U. Keller. “Peak-power scaling of femtosecond Yb:Lu₂O₃ thin-disk lasers”. In: *Optics Express* 25.19 (Sept. 18, 2017), p. 22519. ISSN: 1094-4087. DOI: 10.1364/OE.25.022519.
- [111] P. A. Loiko, K. V. Yumashev, R. Schödel, M. Peltz, C. Liebald, X. Mateos, B. Deppe, and C. Kränkel. “Thermo-optic properties of Yb:Lu₂O₃ single crystals”. In: *Applied Physics B* 120.4 (Sept. 2015), pp. 601–607. ISSN: 0946-2171, 1432-0649. DOI: 10.1007/s00340-015-6171-4.
- [112] Rosalind Wynne, John L. Daneu, and Tso Yee Fan. “Thermal coefficients of the expansion and refractive index in YAG”. In: *Applied Optics* 38.15 (May 20, 1999), p. 3282. ISSN: 0003-6935, 1539-4522. DOI: 10.1364/AO.38.003282.
- [113] U. Griebner, V. Petrov, K. Petermann, and V. Peters. “Passively mode-locked Yb:Lu₂O₃ laser”. In: *Optics Express* 12.14 (2004), p. 3125. ISSN: 1094-4087. DOI: 10.1364/OPEX.12.003125.
- [114] Rigo Peters, Christian Kränkel, Klaus Petermann, and Günter Huber. “Broadly tunable high-power Yb:Lu₂O₃ thin disk laser with 80% slope efficiency”. In: *Optics Express* 15.11 (2007), p. 7075. ISSN: 1094-4087. DOI: 10.1364/OE.15.007075.
- [115] Frédéric Druon, Sandrine Ricaud, Dimitris N. Papadopoulos, Alain Pellegrina, Patrice Camy, Jean Louis Doualan, Richard Moncorgé, Antoine Courjaud, Eric Mottay, and Patrick Georges. “On Yb:CaF₂ and Yb:SrF₂: review of spectroscopic and thermal properties and their impact on femtosecond and high power laser performance [Invited]”. In: *Optical Materials Express* 1.3 (July 1, 2011), p. 489. ISSN: 2159-3930. DOI: 10.1364/OME.1.000489.
- [116] P. F. Moulton. “Spectroscopic and laser characteristics of Ti:Al₂O₃”. In: *Journal of the Optical Society of America B* 3.1 (Jan. 1, 1986), p. 125. ISSN: 0740-3224, 1520-8540. DOI: 10.1364/JOSAB.3.000125.
- [117] R. S. Nagymihaly, H. Cao, D. Papp, G. Hajas, M. Kalashnikov, K. Osvay, and V. Chvykov. “Liquid-cooled Ti:Sapphire thin disk amplifiers for high average power 100-TW systems”. In: *Optics Express* 25.6 (Mar. 20, 2017), p. 6664. ISSN: 1094-4087. DOI: 10.1364/OE.25.006664.

- [118] Jan-Hinnerk Wolter, Marwan Abdou Ahmed, and Thomas Graf. “Thin-disk laser operation of Ti:sapphire”. In: *Optics Letters* 42.8 (Apr. 15, 2017), p. 1624. ISSN: 0146-9592, 1539-4794. DOI: 10.1364/OL.42.001624.
- [119] M. D. Perry, J. Weston, and F. G. Patterson. “Spectral shaping in chirped-pulse amplification”. In: *Optics Letters* 15.7 (Apr. 1, 1990), p. 381. ISSN: 0146-9592, 1539-4794. DOI: 10.1364/OL.15.000381.
- [120] Charles G. Durfee, Sudipta Bera, A.J. Sabbah, Jeff A. Squier, and Michael Ellison. “Spectral shaping filter for broadband amplifiers”. In: *Optics Communications* 263.2 (July 2006), pp. 256–260. ISSN: 00304018. DOI: 10.1016/j.optcom.2006.01.036.
- [121] Sandro Klingebiel, Christoph Wandt, Mathias Siebold, Zsuzsanna Major, Izhar Ahmad, Sergei Trushin, Rainer Hörlein, Tie-Jun Wang, Ferenc Krausz, and Stefan Karsch. “Counteracting Gain Narrowing Using Spectral Amplitude Shaping in a High-Energy Diode-Pumped CPA System Based on Yb-Doped Materials”. In: OSA, 2009, TuB9. ISBN: 978-1-55752-864-3. DOI: 10.1364/ASSP.2009.TuB9.
- [122] Moritz Ueffing, Robert Lange, Tobias Pleyer, Vladimir Pervak, Thomas Metzger, Dirk Sutter, Zsuzsanna Major, Thomas Nubbemeyer, and Ferenc Krausz. “Direct regenerative amplification of femtosecond pulses to the multimillijoule level”. In: *Optics Letters* 41.16 (Aug. 2016), p. 3840. ISSN: 0146-9592, 1539-4794. DOI: 10.1364/OL.41.003840.
- [123] N. F. Andreev, A. A. Babin, V. S. Davydov, A. Z. Matveev, S. G. Garanin, Yu. V. Dolgoplov, S. M. Kulikov, S. A. Sukharev, and S. V. Tyutin. “Wide-aperture plasma-electrode pockels cell”. In: *Plasma Physics Reports* 37.13 (Dec. 2011), pp. 1219–1224. ISSN: 1063-780X, 1562-6938. DOI: 10.1134/S1063780X1106002X.
- [124] Dinguo Chen. “Anti-reflection (AR) coatings made by sol-gel processes: A review”. In: *Solar Energy Materials and Solar Cells* 68.3 (June 2001), pp. 313–336. ISSN: 09270248. DOI: 10.1016/S0927-0248(00)00365-2.
- [125] N. F. Andreev. *Plasma Pockels Cell (request)*. E-mail. Nov. 21, 2013.
- [126] Sven Breilkopf, Tino Eidam, Arno Klenke, Lorenz von Grafenstein, Henning Carstens, Simon Holzberger, Ernst Fill, Thomas Schreiber, Ferenc Krausz, Andreas Tünnermann, Ioachim Pupeza, and Jens Limpert. “A concept for multiterawatt fibre lasers based on coherent pulse stacking in passive cavities”. In: *Light: Science & Applications* 3.10 (Oct. 10, 2014), e211. ISSN: 2047-7538. DOI: 10.1038/lisa.2014.92.
- [127] M. Yu. “Strength and Breaking Mechanism of Multiwalled Carbon Nanotubes Under Tensile Load”. In: *Science* 287.5453 (Jan. 28, 2000), pp. 637–640. ISSN: 00368075, 10959203. DOI: 10.1126/science.287.5453.637.

- [128] Giedrius Sinkevicius and Algirdas Baskys. “Investigation of frequency response of pockels cells based on beta barium borate crystals”. In: IEEE, Apr. 2017, pp. 1–4. ISBN: 978-1-5386-3998-6. DOI: 10.1109/eStream.2017.7950307.
- [129] J. Tümmeler, R. Jung, H. Stiel, P. Nickles, and W. Sandner. “High repetition rate diode pumped thin disk laser of the Joule class”. In: IEEE, June 2009, pp. 1–1. ISBN: 978-1-4244-4079-5. DOI: 10.1109/CLEOE-EQEC.2009.5192752.
- [130] J. Tümmeler, R. Jung, H. Stiel, P. V. Nickles, and W. Sandner. “High-repetition-rate chirped-pulse-amplification thin-disk laser system with joule-level pulse energy”. In: *Optics Letters* 34.9 (May 1, 2009), p. 1378. ISSN: 0146-9592, 1539-4794. DOI: 10.1364/OL.34.001378.
- [131] Sandro Klingebiel, Marcel Schultze, Catherine Y. Teisset, Robert Bessing, Matthias Haefner, Stephan Prinz, Martin Gorjan, Dirk H. Sutter, Knut Michel, Helena G. Barros, zsuzsanna Major, Ferenc Krausz, and Thomas Metzger. “220mJ Ultrafast Thin-Disk Regenerative Amplifier”. In: OSA, 2015, STu4O.2. ISBN: 978-1-55752-968-8. DOI: 10.1364/CLEO_SI.2015.STu4O.2.
- [132] W. Schneider, A. Ryabov, Cs. Lombosi, T. Metzger, Zs. Major, J. A. Fülöp, and P. Baum. “800-fs, 330- μ J pulses from a 100-W regenerative Yb:YAG thin-disk amplifier at 300 kHz and THz generation in LiNbO₃”. en. In: *Optics Letters* 39.23 (Dec. 2014), p. 6604. ISSN: 0146-9592, 1539-4794. DOI: 10.1364/OL.39.006604.
- [133] Arno Klenke, Enrico Seise, Stefan Demmler, Jan Rothhardt, Sven Breitkopf, Jens Limpert, and Andreas Tünnermann. “Coherently-combined two channel femtosecond fiber CPA system producing 3 mJ pulse energy”. In: *Optics Express* 19.24 (Nov. 21, 2011), p. 24280. ISSN: 1094-4087. DOI: 10.1364/OE.19.024280.
- [134] Sandro Klingebiel, Izhar Ahmad, Christoph Wandt, Christoph Skrobol, Sergei A. Trushin, Zsuzsanna Major, Ferenc Krausz, and Stefan Karsch. “Experimental and theoretical investigation of timing jitter inside a stretcher-compressor setup”. In: *Optics Express* 20.4 (Feb. 13, 2012), p. 3443. ISSN: 1094-4087. DOI: 10.1364/OE.20.003443.
- [135] Lorenzo Canova, Xiaowei Chen, Alexandre Trisorio, Aurélie Jullien, Andreas Assion, Gabriel Tempea, Nicolas Forget, Thomas Oksenhendler, and Rodrigo Lopez-Martens. “Carrier-envelope phase stabilization and control using a transmission grating compressor and an AOPDF”. In: *Optics Letters* 34.9 (May 1, 2009), p. 1333. ISSN: 0146-9592, 1539-4794. DOI: 10.1364/OL.34.001333.

- [136] B. C. Stuart, M. D. Feit, A. M. Rubenchik, B. W. Shore, and M. D. Perry. “Laser-Induced Damage in Dielectrics with Nanosecond to Subpicosecond Pulses”. In: *Physical Review Letters* 74.12 (Mar. 20, 1995), pp. 2248–2251. ISSN: 0031-9007, 1079-7114. DOI: 10.1103/PhysRevLett.74.2248.
- [137] B. C. Stuart, M. D. Feit, S. Herman, A. M. Rubenchik, B. W. Shore, and M. D. Perry. “Nanosecond-to-femtosecond laser-induced breakdown in dielectrics”. In: *Physical Review B* 53.4 (Jan. 15, 1996), pp. 1749–1761. ISSN: 0163-1829, 1095-3795. DOI: 10.1103/PhysRevB.53.1749.
- [138] V. Pervak, M. Trubetskov, and A. Tikhonravov. “Design consideration for high damage threshold UV-Vis-IR mirrors”. In: ed. by Gregory J. Exarhos, Vitaly E. Gruzdev, Detlev Ristau, M. J. Soileau, and Christopher J. Stolz. Oct. 7, 2009, 75040A. DOI: 10.1117/12.835787.
- [139] B. J. Nagy, L. Gallais, L. Vámos, D. Oszetzky, P. Rácz, and P. Dombi. “Direct comparison of kilohertz- and megahertz-repetition-rate femtosecond damage threshold”. en. In: *Optics Letters* 40.11 (June 2015), p. 2525. ISSN: 0146-9592, 1539-4794. DOI: 10.1364/OL.40.002525.
- [140] Norman Hodgson and Horst Weber. *Optical resonators: fundamentals, advanced concepts, and applications*. London ; New York: Springer, 1997. 659 pp. ISBN: 978-3-540-76137-2.
- [141] Yasuki Takeuchi, Junji Kawanaka, and Masayuki Fujita. “Nonlinear refractive index of a YAG crystal at low temperature”. In: IEEE, June 2009, pp. 1–1. ISBN: 978-1-4244-4079-5. DOI: 10.1109/CLEOE-EQEC.2009.5192480.
- [142] R. A. Ganeev, I. A. Kulagin, A. I. Rysanyanskii, R. I. Tugushev, and T. Usmanov. “The nonlinear refractive indices and nonlinear third-order susceptibilities of quadratic crystals”. en. In: *Optics and Spectroscopy* 94.4 (Apr. 2003), pp. 561–568. ISSN: 0030-400X, 1562-6911. DOI: 10.1134/1.1570482.
- [143] Northrop Gumman. *Terbium Gallium Garnet - TGG Terbium*.
- [144] David Milam. “Review and assessment of measured values of the nonlinear refractive-index coefficient of fused silica”. In: *Applied optics* 37.3 (1998), pp. 546–550.
- [145] Vincent Loriot, Edouard Hertz, Olivier Faucher, and Bruno Lavorel. “Measurement of high order Kerr refractive index of major air components”. en. In: *Optics Express* 17.16 (Aug. 2009), p. 13429. ISSN: 1094-4087. DOI: 10.1364/OE.17.013429.
- [146] D. Eimerl, L. Davis, S. Velsko, E. K. Graham, and A. Zalkin. “Optical, mechanical, and thermal properties of barium borate”. In: *Journal of Applied Physics* 62.5 (Sept. 1987), pp. 1968–1983. ISSN: 0021-8979, 1089-7550. DOI: 10.1063/1.339536.

- [147] Joerg Neuhaus, Florian Fink, and Mikhail Larionov. “Generation of high-energy femtosecond pulses by use of spectral broadening effects in Yb:YAG thin-disk regenerative amplifiers”. In: *Journal of the Optical Society of America B* 34.5 (May 1, 2017), p. 959. ISSN: 0740-3224, 1520-8540. DOI: 10.1364/JOSAB.34.000959.
- [148] S. De Silvestri, P. Laporta, and V. Magni. “Rod thermal lensing effects in solid-state laser ring resonators”. In: *Optics Communications* 65.5 (Mar. 1988), pp. 373–376. ISSN: 00304018. DOI: 10.1016/0030-4018(88)90106-X.
- [149] G. H. Kim, J. Yang, A. V. Kulik, E. G. Sall, S. A. Chizhov, V. E. Yashin, and U. Kang. “Power limitations and pulse distortions in an Yb : KGW chirped-pulse amplification laser system”. In: *Quantum Electronics* 43.8 (Aug. 31, 2013), pp. 725–730. ISSN: 1063-7818, 1468-4799. DOI: 10.1070/QE2013v043n08ABEH015094.
- [150] Jan Schulte, Thomas Sartorius, Johannes Weitenberg, Andreas Vernaleken, and Peter Russbuehdt. “Nonlinear pulse compression in a multi-pass cell”. en. In: *Optics Letters* 41.19 (Oct. 2016), p. 4511. ISSN: 0146-9592, 1539-4794. DOI: 10.1364/OL.41.004511.
- [151] Johannes Weitenberg, Andreas Vernaleken, Jan Schulte, Akira Ozawa, Thomas Sartorius, Vladimir Pervak, Hans-Dieter Hoffmann, Thomas Udem, Peter Russbuehdt, and Theodor W. Hänsch. “Multi-pass-cell-based nonlinear pulse compression to 115 fs at 75 μ J pulse energy and 300 W average power”. In: *Optics Express* 25.17 (Aug. 21, 2017), p. 20502. ISSN: 1094-4087. DOI: 10.1364/OE.25.020502.
- [152] Ch. Bosshard, R. Spreiter, M. Zgonik, and P. Günter. “Kerr Nonlinearity via Cascaded Optical Rectification and the Linear Electro-optic Effect”. In: *Physical Review Letters* 74.14 (Apr. 3, 1995), pp. 2816–2819. ISSN: 0031-9007, 1079-7114. DOI: 10.1103/PhysRevLett.74.2816.
- [153] George I Stegeman. “cascading: nonlinear phase shifts”. In: *Quantum and Semiclassical Optics: Journal of the European Optical Society Part B* 9.2 (Apr. 1997), pp. 139–153. ISSN: 1355-5111, 1361-6625. DOI: 10.1088/1355-5111/9/2/003.
- [154] Kiyoshi Yokomori. “Dielectric surface-relief gratings with high diffraction efficiency”. In: *Applied Optics* 23.14 (July 15, 1984), p. 2303. ISSN: 0003-6935, 1539-4522. DOI: 10.1364/AO.23.002303.
- [155] B. W. Shore, M. D. Perry, J. A. Britten, R. D. Boyd, M. D. Feit, H. T. Nguyen, R. Chow, G. E. Loomis, and Lifeng Li. “Design of high-efficiency dielectric reflection gratings”. In: *Journal of the Optical Society of America A* 14.5 (May 1, 1997), p. 1124. ISSN: 1084-7529, 1520-8532. DOI: 10.1364/JOSAA.14.001124.

- [156] Sterling Backus, Charles G. Durfee, Margaret M. Murnane, and Henry C. Kapteyn. “High power ultrafast lasers”. In: *Review of Scientific Instruments* 69.3 (Mar. 1998), pp. 1207–1223. ISSN: 0034-6748, 1089-7623. DOI: 10.1063/1.1148795.
- [157] V. Pervak, V. Fedorov, Yu. A. Pervak, and M. Trubetskov. “Empirical study of the group delay dispersion achievable with multilayer mirrors”. In: *Optics Express* 21.15 (July 29, 2013), p. 18311. ISSN: 1094-4087. DOI: 10.1364/OE.21.018311.
- [158] “Amplifier device and method for amplifying laser pulses”. EP2873123 (B1). Moritz Ueffing, Thomas Metzger, and Ferenc Krausz.
- [159] M. Ueffing, T. Pleyer, R. Lange, H. G. Barros, D. Sutter, T. Metzger, Zs. Major, and F. Krausz. “Compact Sub-Picosecond Multi-mJ Multi-kHz Yb:YAG Amplifier”. In: *2015 European Conference on Lasers and Electro-Optics - European Quantum Electronics Conference*. Optical Society of America, 2015, CA_12_3.
- [160] E. T. J. Nibbering, G. Grillon, M. A. Franco, B. S. Prade, and A. Mysyrowicz. “Determination of the inertial contribution to the nonlinear refractive index of air, N₂, and O₂ by use of unfocused high-intensity femtosecond laser pulses”. en. In: *Journal of the Optical Society of America B* 14.3 (Mar. 1997), p. 650. ISSN: 0740-3224, 1520-8540. DOI: 10.1364/JOSAB.14.000650.
- [161] Dominik Bauer. “Modengekoppelte Scheibenzillatoren für Materialbearbeitung”. PhD thesis. Konstanz: Universität Konstanz, 2012.
- [162] Jörg Neuhaus. “Passively mode-locked Yb:YAG thin-disk laser with active multipass geometry”. PhD thesis. Konstanz: Universität Konstanz, 2009.
- [163] Robert Lange. “Design & Characterization of a Yb:YAG Thin-Disk Multipass Amplifier for 20 mJ, Sub-Picosecond Laser Pulses”. Master Thesis. Ludwig-Maximilians-Universität München, Aug. 12, 2015.
- [164] T. Inoue and S. Namiki. “Pulse compression techniques using highly nonlinear fibers”. In: *Laser & Photonics Review* 2.1 (Apr. 25, 2008), pp. 83–99. ISSN: 18638880, 18638899. DOI: 10.1002/lpor.200710029.
- [165] Claude Rolland and P. B. Corkum. “Compression of high-power optical pulses”. en. In: *Journal of the Optical Society of America B* 5.3 (Mar. 1988), p. 641. ISSN: 0740-3224, 1520-8540. DOI: 10.1364/JOSAB.5.000641.
- [166] Marcus Seidel, Jonathan Brons, Gunnar Arisholm, Kilian Fritsch, Vladimir Pervak, and Oleg Pronin. “Efficient High-Power Ultrashort Pulse Compression in Self-Defocusing Bulk Media”. en. In: *Scientific Reports* 7.1 (Dec. 2017). ISSN: 2045-2322. DOI: 10.1038/s41598-017-01504-x.

- [167] D. E. Rivas, A. Borot, D. E. Cardenas, G. Marcus, X. Gu, D. Herrmann, J. Xu, J. Tan, D. Korman, G. Ma, W. Dallari, G. D. Tsakiris, I. B. Földes, S.-w. Chou, M. Weidman, B. Bergues, T. Wittmann, H. Schröder, P. Tzallas, D. Charalambidis, O. Razskazovskaya, V. Pervak, F. Krausz, and L. Veisz. “Next Generation Driver for Attosecond and Laser-plasma Physics”. In: *Scientific Reports* 7.1 (Dec. 2017). ISSN: 2045-2322. DOI: 10.1038/s41598-017-05082-w.
- [168] D. Herriott, H. Kogelnik, and R. Kompfner. “Off-Axis Paths in Spherical Mirror Interferometers”. en. In: *Applied Optics* 3.4 (Apr. 1964), p. 523. ISSN: 0003-6935, 1539-4522. DOI: 10.1364/AO.3.000523.
- [169] Nenad Milosevic, Gabriel Tempea, and Thomas Brabec. “Optical pulse compression: bulk media versus hollow waveguides”. In: *Optics Letters* 25.9 (May 1, 2000), p. 672. ISSN: 0146-9592, 1539-4794. DOI: 10.1364/OL.25.000672.
- [170] Marc Hanna, Xavier Délen, Loic Lavenu, Florent Guichard, Yoann Zaouter, Frédéric Druon, and Patrick Georges. “Nonlinear temporal compression in multipass cells: theory”. In: *Journal of the Optical Society of America B* 34.7 (July 7, 2017), p. 1340. ISSN: 0740-3224, 1520-8540. DOI: 10.1364/JOSAB.34.001340.
- [171] Miguel A. Porras. “Ultrashort pulsed Gaussian light beams”. In: *Physical Review E* 58.1 (July 1, 1998), pp. 1086–1093. ISSN: 1063-651X, 1095-3787. DOI: 10.1103/PhysRevE.58.1086.
- [172] D. P. Shelton. “Nonlinear-optical susceptibilities of gases measured at 1064 and 1319 nm”. In: *Physical Review A* 42.5 (1990), p. 2578.
- [173] Arnaud Couairon, Himadri S. Chakraborty, and Mette B. Gaarde. “From single-cycle self-compressed filaments to isolated attosecond pulses in noble gases”. en. In: *Physical Review A* 77.5 (May 2008). ISSN: 1050-2947, 1094-1622. DOI: 10.1103/PhysRevA.77.053814.
- [174] Carsten Bree, Ayhan Demircan, and Günter Steinmeyer. “Method for Computing the Nonlinear Refractive Index via Keldysh Theory”. In: *IEEE Journal of Quantum Electronics* 46.4 (Apr. 2010), pp. 433–437. ISSN: 0018-9197, 1558-1713. DOI: 10.1109/JQE.2009.2031599.
- [175] J. K. Wahlstrand, Y.-H. Cheng, and H. M. Milchberg. “Absolute measurement of the transient optical nonlinearity in N_2 , O_2 , N_2O , and Ar”. en. In: *Physical Review A* 85.4 (Apr. 2012). ISSN: 1050-2947, 1094-1622. DOI: 10.1103/PhysRevA.85.043820.
- [176] R. Y. Chiao, E. Garmire, and C. H. Townes. “Self-Trapping of Optical Beams”. In: *Physical Review Letters* 13.15 (Oct. 12, 1964), pp. 479–482. ISSN: 0031-9007. DOI: 10.1103/PhysRevLett.13.479.

- [177] Gadi Fibich and Alexander L. Gaeta. “Critical power for self-focusing in bulk media and in hollow waveguides”. en. In: *Optics Letters* 25.5 (Mar. 2000), p. 335. ISSN: 0146-9592, 1539-4794. DOI: 10.1364/OL.25.000335.
- [178] V. I. Bespalov and V. I. Talanov. “Filamentary Structure of Light Beams in Nonlinear Liquids”. In: *JETP Letters* 3.11 (June 15, 1966), pp. 471–476.
- [179] T. Auguste, P. Monot, L.-A. Lompré, G. Mainfray, and C. Manus. “Defocusing effects of a picosecond terawatt laser pulse in an underdense plasma”. In: *Optics communications* 89.2 (1992), pp. 145–148.
- [180] Michael Trubetskov. *Design CM*. E-mail. May 17, 2017.
- [181] W. J. Tomlinson, R. H. Stolen, and A. M. Johnson. “Optical wave breaking of pulses in nonlinear optical fibers”. en. In: *Optics Letters* 10.9 (Sept. 1985), p. 457. ISSN: 0146-9592, 1539-4794. DOI: 10.1364/OL.10.000457.
- [182] B.P. Nelson, D. Cotter, K.J. Blow, and N.J. Doran. “Large nonlinear pulse broadening in long lengths of monomode fibre”. en. In: *Optics Communications* 48.4 (Dec. 1983), pp. 292–294. ISSN: 00304018. DOI: 10.1016/0030-4018(83)90218-3.
- [183] Joshua E. Rothenberg. “Femtosecond optical shocks and wave breaking in fiber propagation”. en. In: *Journal of the Optical Society of America B* 6.12 (Dec. 1989), p. 2392. ISSN: 0740-3224, 1520-8540. DOI: 10.1364/JOSAB.6.002392.
- [184] Pierre Van Rysselberghe. “Remarks concerning the Clausius-Mossotti Law”. In: *The Journal of Physical Chemistry* 36.4 (Jan. 1931), pp. 1152–1155. ISSN: 0092-7325, 1541-5740. DOI: 10.1021/j150334a007.
- [185] P. W. Atkins and Julio De Paula. *Atkins’ Physical chemistry*. 8th ed. Oxford ; New York: Oxford University Press, 2006. 1064 pp. ISBN: 978-0-19-870072-2.
- [186] Edson R. Peck and Donald J. Fisher. “Dispersion of Argon”. en. In: *Journal of the Optical Society of America* 54.11 (Nov. 1964), p. 1362. ISSN: 0030-3941. DOI: 10.1364/JOSA.54.001362.
- [187] Edson R. Peck and Baij Nath Khanna. “Dispersion of Nitrogen”. In: *Journal of the Optical Society of America* 56.8 (Aug. 1, 1966), p. 1059. ISSN: 0030-3941. DOI: 10.1364/JOSA.56.001059.
- [188] Ding Wang, Yuxin Leng, and Zhizhan Xu. “Measurement of nonlinear refractive index coefficient of inert gases with hollow-core fiber”. In: *Applied Physics B* 111.3 (May 2013), pp. 447–452. ISSN: 0946-2171, 1432-0649. DOI: 10.1007/s00340-013-5354-0.

- [189] Li Yu, Meichun Huang, Mouzhi Chen, Wenzhong Chen, Wenda Huang, and Zhizhong Zhu. “Quasi-discrete Hankel transform”. en. In: *Optics Letters* 23.6 (Mar. 1998), p. 409. ISSN: 0146-9592, 1539-4794. DOI: 10.1364/OL.23.000409.

Acknowledgments

First of all I would like to thank Prof. Ferenc Krausz for giving me the great opportunity to join his research group. I would like to thank him for providing an ideal research environment, his continuous support and his valuable advice.

I thank Thomas Metzger and Zsuzsana Major for their support particularly in the beginning of this work. Thanks to Thomas for introducing me into the world of lasers, water connections and scientific laser material processing of stones.

I would like to thank Oleg Pronin and Jonathan Brons for their help and the valuable discussions.

Furthermore, I thank Dirk Sutter, Dominik Bauer and the TRUMPF team for their support.

Thanks goes to Martin Gorjan who supported me in many ways with his profound knowledge in laser science. I thank Thomas Nubbemeyer for his willingness to help and the important support during the laser development. I thank him for his calm and objective way of handling the project coordination.

Thanks to Vladimir Pervak, Michael Trubetskov and Olga Razskazovskaya for the high-tech mirrors.

Thanks to Prof. Reinhard Kienberger who initiated the connection to this fantastic research group.

Thanks to Hanieh Fattahi and Roswitha Graf for their support. For obvious reasons I thank Hanieh for being the “best colleague ever”.

I thank Martin Schmidberger for his support in the very early stages of the laser development. Without him, equipping the empty laboratory would have been much harder. I thank Martin for his tireless commitment! I would also like to thank Robert Lange for his support in developing the imaging multi-pass system. Furthermore, I would like to thank Tobias Pleyer and Simon Reiger for their important help in many ways that finally contributed to the success of this project.

My special thanks goes to Kilian Fritsch for the nice photos of the multi-pass cell setup. I appreciate his readiness to help.

Thanks to Pawel Wnuk and Maximilian Seeger for the support in the last steps of this thesis.

Thanks to Jakub Novák, Martin Kaumanns, Ayman Alismail, Haochuan Wang, Marcus Seidel, Dimitry Kormin and Henning Carstens for their help, support and the interesting discussions.

Thanks to Florian Saran and Klaus Wirgler for the important support in developing mechanical setups for the laser concepts. Thanks to Florian for the culinary presents during Christmas time. Thanks to the MPQ and LMU workshop!

For administrative support I thank Tanya Bergues, Franziska Hoss, Simone Mann, Renate Sailer, Klaus Franke, Nils Haag and Thorsten Naeser.

I would also like to thank Simon Holzner and Annkatrin Sommer. Thanks for your support and the good times we had during the last years. Special thanks to Annkatrin for the rebuke that became famous at our institute. I'm still afraid of staying to long on the ski slopes... I would also like to thank Martin Schultze, Wolfram Helml, Konrad Hütten, Nick Karpowicz, Sabine Keiber and all others that contributed to many joyful hours.

A very special thanks goes to my parents for their continuous support. Thank you! And last but not least the biggest thanks goes to Miriam. Without her support I would have been lost!